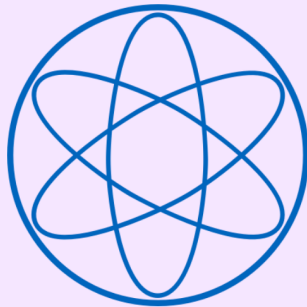


LEHRSTUHL E15  
PHYSIK - DEPARTMENT



**Towards the Detection of the  
Diffuse Supernova Neutrino  
Background in the Large Volume  
Scintillator Experiment JUNO**

Dissertation  
von

Julia Sawatzki



TECHNISCHE UNIVERSITÄT MÜNCHEN



# TECHNISCHE UNIVERSITÄT MÜNCHEN

Fakultät für Physik  
Lehrstuhl für Experimentelle Astroteilchenphysik, E15  
Prof. Dr. Lothar Oberauer

## **Towards the Detection of the Diffuse Supernova Neutrino Background in the Large Volume Scintillator Experiment JUNO**

Julia Sawatzki

Vollständiger Abdruck der von der Fakultät für Physik der Technischen  
Universität München zur Erlangung des akademischen Grades eines

Doktors der Naturwissenschaften (Dr. rer. nat.)

genehmigten Dissertation.

Vorsitzende/-r: Prof. Dr. Alejandro Ibarra  
Prüfende/-r der Dissertation: Prof. Dr. Lothar Oberauer  
Prof. Dr. Elisa Resconi (schriftliche Beurteilung)  
Prof. Dr. Susanne Mertens (mündliche Prüfung)

Die Dissertation wurde am 07.04.2020 bei der Technischen Universität München  
eingereicht und durch die Fakultät für Physik am 07.09.2020 angenommen.





---

## Abstract

The diffuse supernova neutrino background (DSNB) is the average cumulate neutrino flux of all past core-collapse supernovae in the visible universe. A perspective measurement would provide information on the average explosion mechanism of stars, giving access to the fraction of failed explosions, the mass threshold of black hole formation, and the rate of supernovae. Within this work, the detection potential for the DSNB flux was studied for the Chinese multipurpose neutrino experiment named Jiangmen Underground Neutrino Observatory (JUNO). The 20 kt liquid scintillator detector will allow a precise measurement of  $\bar{\nu}_e$ 's via the inverse  $\beta$ -decay and could be one of the first experiments to measure the DSNB successfully with a signal prediction of 5.5 events per year. Although the coincidence event signature provides high-grade background suppression, a variety of backgrounds are still present. The two  $\bar{\nu}_e$  background sources of reactor and atmospheric neutrinos are indistinguishable from the signal and define the low and high energy thresholds for DSNB detection at  $\sim 10$  MeV and  $\sim 35$  MeV, respectively. Although the detector will be located underground,  $\sim 3.5 \mu/s$  reach the central detector volume and can produce relatively long-lived radioactive isotopes with a Q-value large enough to reach in the DSNB signal. Moreover, muons traversing the rock material can produce high-energetic neutrons, which can enter the inner detector volume without being tagged. This background can be reduced significantly, as most of the events concentrate on the verge of the scintillator volume. Neutral current (NC) reactions of atmospheric neutrinos pose the primary background source when nucleons are knocked out of the  $^{12}\text{C}$  nucleus. Signal and background events were simulated, and backgrounds overwhelm the DSNB signal by a factor of  $\sim 16$ . Therefore an efficient active background identification is essential. Pulse shape discrimination was used to disentangle background and signal events, and the atmospheric NC background can be reduced to  $\sim 1.5\%$  of its initial rate, ensuring 86% signal efficiency. Additionally, the proposed triple coincidence veto searches for a third signal after the coincidence, and reduces the overall signal efficiency by 6%, but allows for an additional atmospheric NC background reduction of 30%. A DSNB discovery strategy was proposed, and the detection significance was calculated to  $4\sigma$ , with  $\sim 21$  expected signal and  $\sim 12$  background events after ten years of data taking. Supplementary, a new technique of neutrino detection, utilizing water-based liquid scintillators, was introduced for the proposed Theia detector. Finally, existing and future neutrino experiments (JUNO, SuperK-Gd, HyperK, Theia, DUNE) using different detection techniques (LS, WCD, WbLS, LAr) were discussed and compared in terms of their DSNB detection potential. Several neutrino experiments are ready to start within the next years, also sensitive to complementary neutrino channels. With the studied methods of background rejection, and the proposed strategy, a successful first discovery of the DSNB is in reach of the JUNO experiment.



---

## Zusammenfassung

Der diffuse Supernova-Neutrino-Hintergrund (DSNH) ist der gemittelte kumulierte Neutrino-Fluss aller vergangenen Kernkollaps-Supernovae im sichtbaren Universum. Eine perspektivische Messung würde gemittelte Informationen über Sternexplosionen liefern, wie beispielsweise der Supernova-Rate. Zudem könnte eine Messung Auskunft zur Häufigkeit fehlgeschlagener Sternexplosionen und zur kritischen Masse zur Bildung von schwarzen Löchern geben. Im Rahmen dieser Arbeit wurde das Nachweispotential des DSNH-Flusses für das chinesische Neutrino-Experiment namens Jiangmen Underground Neutrino Observatory (JUNO) untersucht. Der 20-kt-Flüssigszintillator-Detektor ermöglicht eine präzise Messung von  $\bar{\nu}_e$ 's über den inversen  $\beta$ -Zerfall. JUNO könnte, mit einer erwartenden Ereignisrate von 5,5 Neutrino-Signalen pro Jahr, eines der ersten Experimente sein, welches den DSNH misst. Obwohl die Koinzidenz-Signatur des inversen  $\beta$ -Zerfalls eine hervorragende Unterdrückung von unerwünschten Hintergrundereignissen garantiert, sind dennoch Hintergrundquellen präsent. Reaktor- und atmosphärische  $\bar{\nu}_e$ 's sind vom Signal nicht zu unterscheiden und definieren somit die niedrige und hohe Energieschwelle bei  $\sim 10$  MeV bzw.  $\sim 35$  MeV. Obwohl sich der Detektor unter der Erde befindet, erreichen circa  $3.5 \mu/s$  das zentrale Detektorvolumen. Myonen können langlebige radioaktive Isotope mit einem Q-Wert erzeugen, welcher groß genug ist, um das DSNH-Signal zu überlagern. Darüber hinaus können Myonen, die das umliegende Gesteinsmaterial durchqueren, hochenergetische Neutronen erzeugen, welche unbemerkt in das innere Detektorvolumen gelangen. Da sich die meisten dieser Neutronenereignisse im äußeren Bereich des Szintillatorvolumens konzentrieren, kann dieser Untergrund erheblich reduziert werden. Atmosphärische Neutrinos, die Nukleonen aus dem  $^{12}\text{C}$ -Kern herausschlagen, sind die primäre Quelle für Untergrundereignisse. Sowohl Signal- als auch Untergrundereignisse wurden simuliert. Es zeigte sich, dass der Untergrund das DSNH-Signal um das 16-fache übersteigt. Daher ist eine effiziente aktive Identifikation des Untergrunds unerlässlich. Eine Möglichkeit bietet die Pulsformanalyse, welche den atmosphärischen Untergrund auf  $\sim 1.5\%$  seiner Rate reduziert und eine Signaleffizienz von 86% garantiert. Die zusätzliche Möglichkeit der Untersuchung von Ereignissen auf Dreifach-Koinzidenz, ermöglicht eine zusätzliche Reduzierung des atmosphärischen Untergrunds um 30%, bei Verringerung der Signaleffizienz um 6%. Eine Strategie zur Messung des DSNH in JUNO wurde anschließend entwickelt. Der DSNH kann mit einer Signifikanz von  $4\sigma$  detektiert werden, ausgehend von  $\sim 21$  Signal- und  $\sim 12$  Untergrunderereignissen nach zehnjähriger Messung. Zusätzlich wurde die Verwendung von Flüssigszintillatoren auf Wasserbasis als Detektor-Technik diskutiert und für den vorgeschlagenen Detektor Theia die Möglichkeit einer DSNH Messung untersucht. Abschließend wurden bestehende und zukünftige Neutrino-Experimente (JUNO,

---

SuperK-Gd, HyperK, Theia, DUNE) mit verschiedenen Detektionstechniken diskutiert und hinsichtlich ihres DSNH-Detektionspotentials verglichen. Verschiedene Neutrino-Experimente, mit Empfindlichkeit auf unterschiedliche Neutrino-Arten, beginnen in den nächsten Jahren ihre Messung. Mit den untersuchten Methoden zur Identifizierung des Untergrunds und der vorgeschlagenen Detektionsstrategie ist eine erste Entdeckung des DSNH in Reichweite des JUNO-Experiments.

# Contents

<b>Introduction</b> . . . . .	1
<b>NEUTRINOS AS ASTROPHYSICAL MESSENGERS</b> . . . . .	
<b>1 Neutrino Physics</b> . . . . .	5
1.1 Neutrinos in the Standard Model . . . . .	6
1.2 Neutrinos beyond the Standard Model . . . . .	8
1.2.1 Vacuum Oscillations . . . . .	9
1.2.2 Oscillations in Matter . . . . .	15
1.3 Neutrino Nucleon Interactions . . . . .	20
1.4 Neutrinos as Astrophysical Messengers . . . . .	23
1.4.1 Solar Neutrinos . . . . .	23
1.4.2 Atmospheric Neutrinos . . . . .	26
1.4.3 Supernova Neutrinos . . . . .	29
1.4.4 Diffuse Supernova Neutrino Background . . . . .	33
<b>2 Large Volume Neutrino Detectors</b> . . . . .	37
2.1 Water Cherenkov Detectors . . . . .	40
2.1.1 Super-Kamiokande . . . . .	42
2.1.2 IceCube . . . . .	43
2.2 Liquid Scintillator Detectors . . . . .	45
2.2.1 Borexino . . . . .	48
2.2.2 SNO+ . . . . .	48
2.2.3 KamLAND . . . . .	49

<b>THE JUNO DETECTOR</b>	.....	
<b>3 Jiangmen Underground Neutrino Observatory</b>	.....	53
3.1 Detector Concept	.....	54
3.2 Liquid Scintillator	.....	57
3.3 Detector Simulation	.....	60
3.4 Physics Potential	.....	61
3.4.1 Neutrino Mass Ordering	.....	61
3.4.2 Determination of Oscillation Parameters	.....	65
3.4.3 Solar Neutrinos	.....	66
3.4.4 Supernova Burst Neutrinos	.....	68
3.4.5 Geoneutrinos	.....	69
3.4.6 Sterile Neutrinos	.....	70
3.4.7 Proton Decay	.....	71
3.4.8 Dark Matter	.....	73
<b>THE DSNB SIGNAL</b>	.....	
<b>4 Diffuse Supernova Neutrino Signal</b>	.....	79
4.1 Neutrino Signals from Successful and Failed Core-Collapse Supernovae	.....	80
4.2 Cosmic Core-Collapse Supernova Rate	.....	84
4.3 Signal Expectation in JUNO	.....	87
4.4 Simulation and Event Selection	.....	90
<b>THE BACKGROUND SOURCES</b>	.....	
<b>5 Reactor Neutrino Background</b>	.....	95
<b>6 Atmospheric Neutrino Background</b>	.....	101
6.1 Atmospheric Neutrino Flux	.....	102
6.2 Charged Current Reactions	.....	106
6.3 Neutral Current Reactions	.....	108
6.4 Simulation Setup	.....	112
<b>7 Muon-Induced Background</b>	.....	115
7.1 In-Situ Produced Cosmogenic Isotopes	.....	117
7.2 Fast Neutrons	.....	121

<b>BACKGROUND IDENTIFICATION</b>	.....	
<b>8 Pulse Shape Discrimination</b>	.....	125
8.1 Obtaining Pulse Shapes within the Simulation Process	.....	128
8.2 Discrimination Efficiency using the Tail-to-Total Method	.....	133
<b>9 Delayed Decay Triple Coincidence</b>	.....	139
9.1 Size of the Vetoed Volume	.....	143
9.2 Signal Efficiency	.....	148
9.3 Atmospheric Background Reduction	.....	151
<b>DSNB DETECTION POTENTIAL</b>	.....	
<b>10 DSNB Detection Potential in JUNO</b>	.....	157
10.1 Proposal for Detection Strategy	.....	160
10.2 Detection Significance	.....	165
10.3 Constraining the Astrophysical Parameter Space	.....	170
<b>11 DSNB Detection in the Proposed Water-Based Liquid Scintillator</b>		
<b>Detector Theia</b>	.....	175
11.1 Detector Concept	.....	177
11.2 Signal and Background Estimation	.....	179
11.2.1 Charged Current Background	.....	179
11.2.2 Muon-Induced Background	.....	182
11.2.3 Neutral Current Atmospheric Background	.....	185
11.3 Background Identification	.....	188
11.3.1 Cherenkov Ring Counting	.....	189
11.3.2 Cherenkov-to-Scintillation Ratio	.....	190
11.3.3 Delayed Decay Triple Coincidence	.....	193
11.4 Detection Significance	.....	194
<b>12 Comparison of Detection Techniques</b>	.....	197
12.1 Gd-loaded Super-Kamiokande	.....	198
12.2 Hyper-Kamiokande	.....	199
12.3 Deep Underground Neutrino Experiment	.....	200
12.4 Comparison	.....	201
<b>Conclusions</b>	.....	205

<b>APPENDIX</b> . . . . .	
<b>Additional Figures and Tables</b> . . . . .	215
<b>Atmospheric Charged Current Background on <sup>12</sup>C</b> . . . . .	223
<b>List of Abbreviations</b> . . . . .	225
<b>List of Figures</b> . . . . .	229
<b>List of Tables</b> . . . . .	233
<b>Bibliography</b> . . . . .	235



# Introduction

The first neutrino detection in 1956 established a new field of experimental particle physics [1]. Since then, many experiments have been built to detect neutrinos and examine their properties. Even after 60 years of neutrino physics, still, some unknown properties remain, motivating ongoing research in this field.

Since neutrinos interact only little with matter, large detectors are necessary to enhance the interaction probability. As they are less affected by matter nor by electromagnetic fields on their passage, they are well suited as messenger particles, as they carry valuable information on the environment in which they were created. Exemplary, neutrino signals from a supernova explosion contain information on the supernova explosion mechanism itself and the dying star. A supernova was successfully observed with neutrinos in 1987, but a measurement of the so-called diffuse supernova neutrino background (DSNB) is still pending [2]. The DSNB is the average cumulative neutrino emission of all past core-collapse supernova in the universe. Such a future measurement provides average information on supernovae of all stars. Up to now, only upper limits exist on the DSNB flux determined by the Super-Kamiokande experiment [3]. Hence, future experiments would like to perform a first measurement of the DSNB.

A promising experiment is the Chinese Jiangmen Underground Neutrino Observatory (JUNO) experiment, which is a 20 kt liquid scintillator detector currently under construction in southern China [4]. Due to its large target mass and unprecedented energy resolution, JUNO is capable of performing high statistic measurements of reactor neutrinos, which are produced at the nuclear power plants distanced  $\sim 53$  km to the detector. Precise measurement of the oscillation probability opens up the possibility to determine the neutrino mass ordering. Besides the measurement of geoneutrinos and possibly supernova neutrinos, JUNO could be one of the first experiments to detect the DSNB. Even in such a colossal detector, only a few DSNB events per year are expected, making its detection very challenging. Under the presence of background signals, background suppression represents a decisive issue for this measurement.

The present work comprises an analysis performed in the scope of DSNB detection with the JUNO detector and is divided into six main parts. After an introduction of neutrino properties, several astrophysical neutrino sources are presented in the

first chapter. The two main techniques applied in real-time neutrino detectors, the water Cherenkov and liquid scintillator detector technology, are described in chapter 2.

The second part, chapter 3, illustrates the experimental setup of the JUNO detector and outlines JUNO's physics program.

Chapter 4 focusses on the DSNB signal in the JUNO detector and discusses the influence of astrophysical parameters on the expected DSNB signal strength.

Besides the desired signal, there is a variety of backgrounds present, which are presented in part four of this thesis. The background topic is divided into three chapters according to the background origin. Chapter 5 and chapter 6 investigate interactions of the reactor and atmospheric neutrinos, respectively. Besides neutrinos, also muons can cause a possible background, which is appraised in chapter 7. Techniques to identify background interactions are presented in the subsequent part, consisting of chapter 8 and chapter 9. The powerful tool of pulse shape discrimination is of particular interest and presented in chapter 8. Additionally, a triple coincidence veto method is presented in chapter 9, which allows further suppression of the atmospheric neutrino background. Based on the signal and background expectations, and the background suppression techniques, the detection potential for the JUNO detector is determined in chapter 10.

Supplementary, a future neutrino detector technique, water-based liquid scintillator detectors, is introduced and discussed in chapter 11 on the example of the proposed Theia detector. The possibility of a future DSNB detection with the combined detector technique is discussed. Finally, chapter 12 compares the DSNB detection sensitivity of existing and future neutrino experiments and show the potential of a future joint DSNB analysis.

The last part concludes the results of the present work.

# **NEUTRINOS AS ASTROPHYSICAL MESSENGERS**



# Chapter 1

## Neutrino Physics

The neutrino started in 1930 as a new and purely hypothetical particle, postulated by Wolfgang Pauli [5]. It was introduced to fix the problem of the measured continuous energy spectra and the missing spin observed in  $\beta$ -decay experiments. After its postulation, the first detection of electron antineutrinos by Cowan and Reines in 1956, started a new era in experimental particle physics [1]. Only six years later, Lederman, Schwartz, and Steinberg discovered the muon neutrino [6]. After the first discoveries, Weinberg and Salam proposed 1967 the standard electroweak model, which served as an accurate description for almost all phenomena below the electroweak scale to this date [7]. Later, measurements immediately implied the existence of the third neutrino flavor, the tau neutrino, which was finally detected by the DONUT experiment in 2000 [8,9]. The success of discovering neutrinos lead to many experiments in order to detect these particles and investigate their properties.

The role of neutrinos within the Standard Model of particle physics is introduced in the following section. Section 1.2 discusses the neutrino properties going beyond the Standard Model, manifest in the effect of neutrino oscillations. Subsequently, section 1.3 introduces the possibilities for neutrinos to interact with matter, where the last part of this chapter, section 1.4, discusses neutrinos as astrophysical messengers, arising from the Sun, the atmosphere, and supernovae.

## 1.1 Neutrinos in the Standard Model

The Standard Model (SM) of particle physics connects three of the four fundamental interactions, where the strong, weak and electromagnetic interactions are correlated to  $SU(3)$ ,  $SU(2)$ , and  $U(1)$  gauge groups, respectively [10]. Electromagnetic and weak interactions can further be combined in a  $SU(2) \times U(1)$  gauge group, introducing the theory of electroweak interactions [7]. The SM is capable of treating the three interaction forces at energies within the electroweak scale very precisely. However, it does not yet include gravitation as the fourth fundamental interaction [11]. Due to the smallness of gravitational effects compared to effects supplied by the other three forces, gravitation can be neglected in the following, still providing accurate predictions of particle interactions through the SM

Within the SM, neutrinos ( $\nu_e, \nu_\mu, \nu_\tau$ ) are described as massless and electrically neutral partners of the charged leptons ( $e, \mu, \tau$ ), describing the so-called family or flavor of the particle [10]. Assuming that the lepton number is conserved in all processes<sup>1</sup>, weak charged current reactions convert charged leptons into their neutrino-partners of the same flavor and vice versa. After the discovery of parity violation in the weak interaction, the two-component theory of the neutrino was introduced, in which by assumption only left-handed neutrinos and right-handed antineutrinos exist [12-14]. The exchange particles of weak interactions, the  $W^\pm$  and  $Z^0$  vector bosons, couple exclusively to left-handed particles (or right-handed antiparticles), while left-handed antiparticles (or right-handed particles) remain inactive. Therefore by assumption, the left-handed fermion fields transform as doublets under  $SU(2)$ , and the right-handed fields are understood as singlets in the SM:

$$\begin{pmatrix} \nu_e \\ e^- \end{pmatrix}_L, \begin{pmatrix} \nu_\mu \\ \mu^- \end{pmatrix}_L, \begin{pmatrix} \nu_\tau \\ \tau^- \end{pmatrix}_L, e_R, \mu_R, \tau_R, \quad (1.1)$$

where the indices L and R denote the left- and right-handed fields, respectively [10]. As the chirality of neutrinos is the same as their helicity, the SM only includes left-handed neutrinos with negative helicity and right-handed antineutrinos with positive helicity. Hence, it is not possible to generate masses via the standard Higgs-mechanism, which requires a change in handedness for a particle that interacts with the Higgs boson, which is per definition not allowed for neutrinos within the SM [15]. Consequently, neutrinos are assumed to be massless and are treated as eigenstates of helicity within the SM.

<sup>1</sup> Within the SM lepton number conservation is assumed, but, e.g., an observation of the proposed neutrinoless double  $\beta$ -decay would signal a violation of total lepton number conservation.

The coupling strengths of  $W^\pm$  and  $Z^0$  bosons to the weak charge of fermions are comparable to electromagnetic interactions. However, the mass of the weak exchange bosons ( $m_W = 80 \text{ GeV}$ ,  $m_Z = 92 \text{ GeV}$ ) lower the effective reach, and thus the observable strength of the force at low energies is significantly decreased. In this regime, neutrino interactions can, therefore, be described as being point-like, which was first introduced by Enrico Fermi [16]. The Fermi coupling constant  $G_F \cong 90 \text{ eV fm}^3$  enters neutrino scattering cross-sections quadratically, leading to rather small cross-sections in the order of  $\sim 10^{-43} \text{ cm}^2$  [10].

In contrast to the above-introduced neutrino properties in the SM, neutrino flavor oscillations, a process that violates lepton family number, is only possible if neutrinos do possess mass. Motivated by its observation, physics beyond the SM has to be considered in the case of describing neutrino physics correctly and will be discussed in the following section.

## 1.2 Neutrinos beyond the Standard Model

The Standard Model (SM) of particle physics integrates neutrinos and their antiparticles as massless and exclusively weakly interacting particles [10]. However, there have been several experiments, which hinted at neutrino properties beyond the SM [17, 18].

Inspired by the work of Gell-Mann and Pais in 1957, Bruno Pontecorvo suggested first the possibility of quantum mechanical mixing in a neutral particle: the neutrino [19, 20]. Even though the idea that the neutrino may oscillate into its antiparticle later turned out to be wrong, the idea of neutrino oscillation was born. After that, the oscillation among the three different neutrino flavors was proposed by Maki, Nakagawa, and Sakata in 1962 [21].

Since then, various exotic and unanticipated properties of the neutrino were revealed in the following decades. One of the most prominent cases was the so-called *solar neutrino problem* describing the unexpectedly low rate of solar neutrinos observed in terrestrial neutrino detectors [22–26]. The concept of neutrino flavor oscillations could explain the missing amount of neutrinos, and oscillations were first observed in the atmospheric neutrino experiment Super-Kamiokande [27].<sup>2</sup> Meanwhile, solar neutrino experiments, reactor neutrino experiments, and experiments using long-baseline neutrino beams observed this phenomenon additionally [28–33].

However, even after the discovery of neutrino oscillations, many properties of the neutrino remain unknown. Notably, the absolute neutrino mass scale, the neutrino mass ordering, the nature of neutrinos as Dirac or Majorana particles, and the size of the CP-violating phase of the mixing matrix are still unresolved, motivating ongoing research in the field of neutrino physics [10, 34, 35].

The next section introduces the phenomenon of neutrino oscillations in a vacuum, presenting the oscillation mixing parameters and facing the open question of neutrino mass ordering. Subsequently, section 1.2.2 explains how the oscillation effect changes when neutrinos traverse matter instead of vacuum.

---

<sup>2</sup> The Nobel Prize 2015 in Physics was awarded for the discovery of neutrino oscillations.



### 1.2.1 Vacuum Oscillations

Generally, flavor oscillations of particles can be studied when a known mixture of flavor states are produced, and it is possible within a particular experiment to detect the resulting flavor state. The weak neutrino flavor eigenstates  $|\nu_\alpha\rangle$ ,  $\alpha \in \{e, \mu, \tau\}$  can be described as a coherent, linear superposition of the orthogonal and left-handed neutrino mass eigenstates  $|\nu_i\rangle$ ,  $i \in \{1, 2, 3\}$ :

$$\begin{pmatrix} \nu_e \\ \nu_\mu \\ \nu_\tau \end{pmatrix} = U \cdot \begin{pmatrix} \nu_1 \\ \nu_2 \\ \nu_3 \end{pmatrix}, |\nu_\alpha\rangle = \sum_{i=1}^n U_{\alpha i}^* |\nu_i\rangle, \quad (1.2)$$

where  $U$  is the unitary  $n \times n$  Pontecorvo-Maki-Nakagawa-Sakata (PMNS) mixing matrix [21, 36]. Throughout this part, only active neutrino flavors are considered, fixing the number of neutrino families to three.<sup>3</sup> A convenient parameterization of the  $3 \times 3$  PMNS mixing matrix  $U$  is proposed in [38]:

$$U = \begin{pmatrix} 1 & 0 & 0 \\ 0 & c_{23} & s_{23} \\ 0 & -s_{23} & c_{23} \end{pmatrix} \times \begin{pmatrix} c_{13} & 0 & s_{13}e^{-i\delta} \\ 0 & 1 & 0 \\ -s_{23}e^{-i\delta} & 0 & c_{13} \end{pmatrix} \times \begin{pmatrix} c_{12} & s_{12} & 0 \\ -s_{12} & c_{12} & 0 \\ 0 & 0 & 1 \end{pmatrix} \times P, \quad (1.3)$$

with  $c_{ij} = \cos \theta_{ij}$ ,  $s_{ij} = \sin \theta_{ij}$ , and  $\delta$  as the CP-violating phase. The diagonal matrix  $P$  is the identity matrix if neutrinos are Dirac fermions, and it contains two additional CP-violating phases,  $P = \text{diag}(e^{i\alpha_1}, e^{i\alpha_2}, 1)$ , if they are Majorana fermions. As the Majorana phases,  $\alpha_1$  and  $\alpha_2$ , do not affect the measurable survival probability in neutrino flavor oscillations, they are omitted in the ongoing discussion [39, 40].

In the following, the neutrino mass eigenstates are treated as plane waves<sup>4</sup>, and the Schrodinger equation gives the time evolution of the neutrino mass eigenstates [10]:

$$|\nu_i(t)\rangle = e^{-iE_i t} |\nu_i(0)\rangle, \quad (1.4)$$

where  $E_i$  represents the energy of the mass eigenstate  $|\nu_i(t)\rangle$ .<sup>5</sup>

<sup>3</sup> A measurement of the  $Z^0$ -decay width at the Large Electron-Positron Collider determined the number of active neutrino flavors to be three [37]. Additional neutrino states, like sterile neutrinos, are not part of the following work. A short overview of the concept of sterile neutrinos is given in section 3.4.6

<sup>4</sup> Although this is an approach, it has also been shown that a wave packet formalism or the treatment in the framework of quantum field theory, lead to the same oscillation probability [41, 42].

<sup>5</sup> In the following  $\hbar = c = 1$ .

If the neutrino flavor eigenstate  $|\nu_\alpha\rangle$  is produced at  $t = 0$ , the time evolution is given by [36]:

$$|\nu_\alpha\rangle(t) = \sum_{\beta \in \{e, \mu, \tau\}} |\nu_\beta\rangle \langle \nu_\beta | e^{-iE_\beta t} | \nu_\alpha \rangle. \quad (1.5)$$

Accordingly, the probability  $P_{\alpha \rightarrow \beta}$  of detection a neutrino in the flavor eigenstate  $|\nu_\beta\rangle$ , which was produced in the flavor eigenstate  $|\nu_\alpha\rangle$  can be expressed as [43]:

$$\begin{aligned} P_{\alpha \rightarrow \beta} &= |\langle \nu_\beta | e^{-iE_\beta t} | \nu_\alpha \rangle|^2 = \left| \sum_{i=1}^3 \langle \nu_\beta | \nu_i \rangle e^{-iE_i t} \langle \nu_i | \nu_\alpha \rangle \right|^2 \\ &= \left| \sum_{i=1}^3 U_{\beta i} e^{-iE_i t} U_{\alpha i}^* \right|^2. \end{aligned} \quad (1.6)$$

It is evident that the factor  $U_{\alpha i}^*$  represents the amplitude of the transition from the initial flavor state  $|\nu_\alpha\rangle$  into the state with definite mass  $|\nu_i\rangle$ . The factor  $e^{-iE_i t}$  describes the time propagation of the mass eigenstate  $|\nu_i\rangle$  and the factor  $U_{\beta i}$  is related to the amplitude of the transition from the state with definite mass into the final state  $|\nu_\beta\rangle$ .

Assuming the relativistic approximation for light neutrinos with a small but finite mass ( $p \gg m_i$ ), the neutrino energy  $E_i$  can be approximated as [36]:

$$\begin{aligned} E_i &= \sqrt{p^2 + m_i^2} = p \sqrt{1 + \left(\frac{m_i}{p}\right)^2} = p \left[ 1 + \frac{1}{2} \left(\frac{m_i}{p}\right)^2 - \frac{1}{8} \left(\frac{m_i}{p}\right)^4 + \dots \right] \\ &\simeq p + \frac{m_i^2}{2p} \simeq E + \frac{m_i^2}{2E}, \end{aligned} \quad (1.7)$$

where  $E = p$  is the energy at  $m_i \rightarrow 0$ . The ultrarelativistic condition implies  $L \approx t$ , with the distance  $L$  the neutrino traveled from its point of creation, transforming Eq. (1.6) to

$$P_{\alpha \rightarrow \beta} = \left| \sum_{i=1}^3 U_{\beta i} e^{-\frac{m_i^2 L}{2E}} U_{\alpha i}^* \right|^2. \quad (1.8)$$

Consequently, the probability of detecting a neutrino in the same flavor eigenstate  $|\nu_\alpha\rangle$ , as it was produced, can be rearranged to [36]:

$$\begin{aligned}
 P_{\alpha \rightarrow \alpha} &= \left| \sum_{i=1}^3 |U_{\alpha i}|^2 e^{-2i\Delta p_{ij}} \right|^2 \\
 &= 1 - 4 \sum_{i < j} |U_{\alpha i} U_{\alpha j}|^2 \sin^2 \left( \frac{\Delta m_{ij}^2 L}{4E} \right),
 \end{aligned} \tag{1.9}$$

with  $\Delta p_{ij} = (E_i - E_j)t \simeq \frac{\Delta m_{ij}^2 L}{4E}$  and  $\Delta m_{ij}^2 = m_i^2 - m_j^2$ . Eq. (1.9) demonstrates that the probability of detecting a neutrino in the same flavor eigenstate as it was produced is generally smaller than one and oscillating in  $L/E$ , calling this phenomenon *neutrino oscillation*. It follows directly that neutrino oscillations are only possible if the neutrino masses are not equal ( $\exists i, j \in \{1, 2, 3\} : \Delta m_{ij}^2 \neq 0$ ), and the mixing matrix  $U$  is not diagonal, demanding for non-zero mixing angles ( $\theta_{ij} \neq 0$ ). As a result, the measurement of neutrino oscillations demands not conserved lepton flavor number and at least two neutrino mass eigenstates that are not massless, contrary to the predictions of the SM.

Furthermore, as neutrino oscillations depend on the squared mass differences  $\Delta m_{ij}^2$ , no information about the absolute neutrino mass scale can be gained from neutrino oscillation experiments. The KATRIN experiment achieved the current best direct limit  $m_{\nu_e} < 1.1$  eV (90% C.L.) by measuring the endpoint of the Tritium  $\beta$ -decay spectrum [44]. More stringent but indirect limits can be set by cosmology [45, 46] and measurements of the neutrinoless double  $\beta$ -decay [47].

Up to now, the knowledge of the mixing angles  $\theta_{12}$ ,  $\theta_{13}$  and  $\theta_{23}$  and the quadratic mass differences  $\Delta m_{12}^2$  and  $|\Delta m_{23}^2|$  were gained in several experiments. Their latest best fit values obtained from a global analysis on all available oscillation data performed in 2018 are summarized in Tab. 1.1 [10].

While the  $^8\text{B}$  neutrino measurements performed by the Super-Kamiokande (SuperK) experiment, mainly fixed the value of the solar mixing angle  $\theta_{12}$  [49], the mass difference  $\Delta m_{12}^2$  is essentially determined by the results of the KamLAND reactor experiment [50]. SuperK has also measured the atmospheric mixing angle  $\theta_{23}$  to high precision in the T2K experiment and giving the currently best value for  $|\Delta m_{23}^2|$  [48]. While the sign of  $\Delta m_{21}^2 > 0$  has been inferred from solar neutrino experiments and the observation of the Mikheyev-Smirnov-Wolfenstein effect in solar neutrinos, the sign of  $\Delta m_{23}^2$  is still unknown, as vacuum neutrino oscillations are not sensitive to signs in mass differences [28, 49, 50]. Finally, the best direct limit on the reactor mixing angle  $\theta_{13}$  is determined by the Daya Bay experiment and showed that it is significantly non-zero [51]. Since the unknown CP-violating

Oscillation Parameter	Value
$\sin^2(\theta_{12})$	$0.307^{+0.013}_{-0.012}$
$\Delta m_{21}^2$	$7.53 \pm 0.18 \times 10^{-5} \text{ eV}^2$
$\sin^2(\theta_{23})$	$0.417^{+0.025}_{-0.028}$ (NO)
	$0.421^{+0.033}_{-0.025}$ (IO)
$\Delta m_{32}^2$	$+2.51 \pm 0.05 \times 10^{-3} \text{ eV}^2$ (NO)
	$-2.56 \pm 0.04 \times 10^{-3} \text{ eV}^2$ (IO)
$\sin^2(\theta_{13})$	$0.0212 \pm 0.008$
$\delta_{CP}$	$1.45^{+0.27}_{-0.26}$ (NO)
	$1.54^{+0.22}_{-0.23}$ (IO)

Table 1.1: Global best fit values for the neutrino squared mass differences  $\Delta m_{ij}^2$ , mixing angles  $\theta_{ij}$  [10] and CP violating phase  $\delta_{CP}$  [48].

phase does not affect the survival probability as well, it cannot be measured in disappearance experiments.

Due to the unknown sign of the mass difference  $\Delta m_{23}^2$  in contrast to the solar case, only two independent mass squared differences are present in the three-neutrino mixing case. The correlation

$$\Delta m_{31}^2 = \Delta m_{32}^2 + \Delta m_{21}^2, \quad (1.10)$$

allows for two possible neutrino mass ordering (NMO) scenarios of the neutrino mass eigenstates: the so-called normal ordering (NO) and the inverted ordering (IO). Their characteristics are summarized and illustrated in Fig. 1.1. The bars indicate the mass of the mass eigenstates  $\nu_i$  ordered from the bottom up due to their masses. The colors represent the fractions of the neutrino flavor eigenstates contained in the mass eigenstates. As  $|\Delta m_{31}^2|$  is larger (smaller) than  $|\Delta m_{32}^2|$  for NO (IO), the NMO can be determined in principle by precision measurements of these two parameters. This approach is followed in the Jiangmen Underground Neutrino Observatory experiment, which is currently under construction and introduced in more detail in chapter 3. To answer the open question of NMO, oscillations of the reactor electron antineutrinos ( $\bar{\nu}_e$ 's) arriving from nuclear power plants will be analyzed via a precision spectral measurement. This reactor neutrino disappearance experiment focuses on the survival probability of  $\bar{\nu}_e$ .

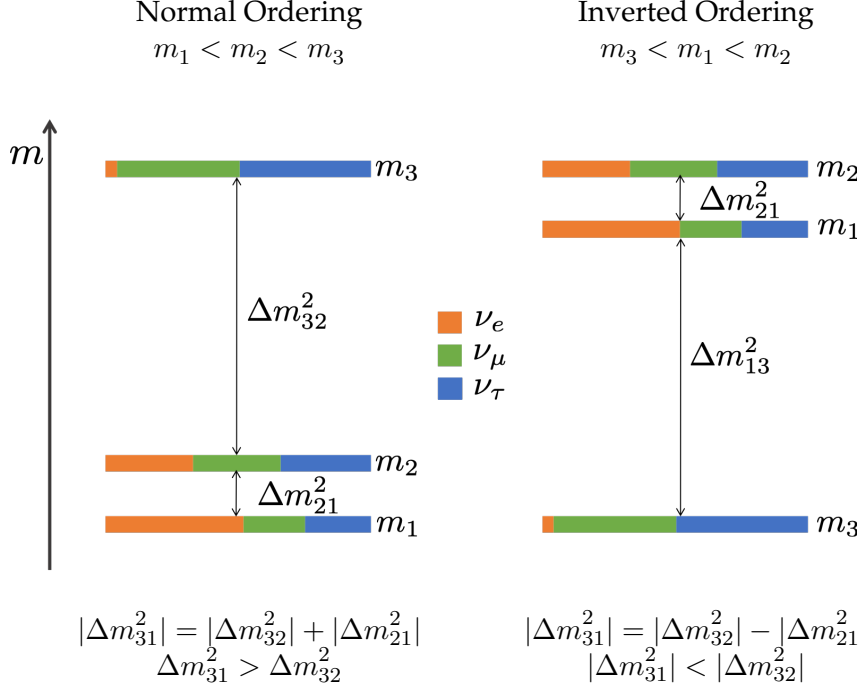


Figure 1.1: Schematic representation of the neutrino mass ordering. The color-coding indicates the fraction  $|U_{\alpha i}|^2$  of each distinct flavor  $\nu_\alpha$ ,  $\alpha \in (e, \mu, \tau)$  contained in each mass eigenstate  $\nu_i$ ,  $i \in (1, 2, 3)$ . For **NO**, the small mass difference is between the two lightest mass eigenstates, while for **IO** it is between the massive eigenstates.

Outgoing from Eq. (1.9) and using the standard parametrization of the **PMNS** mixing matrix, the survival probability in the vacuum that an  $\bar{\nu}_e$  is detected in the same flavor state as it was produced is reduced by three terms [52]:

$$\begin{aligned}
 P_{\bar{\nu}_e \rightarrow \bar{\nu}_e}(E) &= 1 - P_{21} - P_{31} - P_{32}, \text{ with} \\
 P_{21} &= \cos^4(\theta_{13}) \sin^2(2\theta_{12}) \sin^2(\Delta_{21}) \\
 P_{31} &= \cos^2(\theta_{12}) \sin^2(2\theta_{13}) \sin^2(\Delta_{31}) \\
 P_{32} &= \sin^2(\theta_{12}) \sin^2(2\theta_{13}) \sin^2(\Delta_{32}),
 \end{aligned} \tag{1.11}$$

with  $\Delta_{ij} \propto (m_i^2 - m_j^2) \times \frac{L}{E}$  and the mixing angles  $\theta_{12}$  and  $\theta_{13}$ . The three terms  $P_{21}$ ,  $P_{31}$ , and  $P_{32}$  oscillate each with a "frequency" in L/E space specified by  $\Delta_{ij}$ , while the mixing angles  $\theta_{12}$  and  $\theta_{13}$  determine the amplitude of each term. The term  $P_{21}$  with the lowest frequency ( $\propto \Delta_{21}$ ), dominates the suppression, due to the small value of mixing angle  $\theta_{13}$  appearing in  $P_{31}$  and  $P_{32}$ . The relative amplitude of the three oscillation components  $P_{21}$ ,  $P_{31}$ , and  $P_{32}$  is  $\sim 40:2:1$ , respectively.

Therefore, to resolve the difference in parameters due to **NMO** in experiments is exceptionally challenging as the difference in the measured neutrino energy spectra is suppressed by the small value of the mixing angle  $\theta_{13}$ . The energy resolution of the experiment has to be good enough, in the same order as the size of the ratio  $|\Delta m_{21}^2/\Delta m_{32}^2| \sim 3\%$  [53]. The survival probability as a function of  $L/E$  with  $L$  as the traveled distance and  $E$  as neutrino energy is depicted in Fig. 1.2 for **NO** (blue) and **IO** (orange).

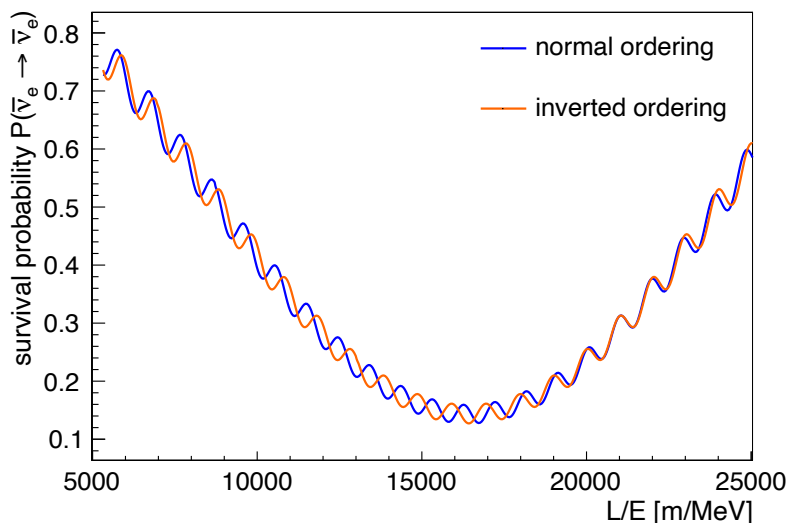


Figure 1.2: Survival probability  $P_{\bar{\nu}_e \rightarrow \bar{\nu}_e}$  for **NO** (blue) and **IO** (orange) as a function of the detector-source distance  $L$  divided by neutrino energy  $E$ . The range of the  $x$ -axis corresponds to the accessible parameter space for the **JUNO** experiment (cf. chapter 3), with a baseline of  $\sim 53$  km and reactor neutrinos with energies between  $1.8$  MeV and  $\sim 8$  MeV.

Whether the **NMO** is normal or inverted represents one of the remaining unmeasured fundamental questions in the neutrino sector, and its nature has profound implications in the development of models of particle physics with significant implications for cosmology and astrophysics [54, 55]. A measurement of the mass ordering would also impact ongoing and future research of other crucial neutrino properties, e.g., in accelerator neutrino oscillation experiments with sensitivity to unknown leptonic CP-violating phases, where a known **NMO** would significantly reduce the uncertainty. Besides, knowledge on the **NMO** will influence the interpretation of non-oscillation experiments, like neutrinoless double  $\beta$ -decay ( $0\nu\beta\beta$ -decay) experiments, which are sensitive to the particle nature of the neutrino (Dirac vs. Majorana) and the absolute mass, by limiting the domain for

observation of a signal [56]. While the chances of observing  $0\nu\beta\beta$ -decay for an IO are realistic with planned experiments, new techniques are needed to cover the whole parameter space of NO [57].

The effect of the above-explained neutrino oscillations changes if neutrinos traverse matter instead of vacuum, which is explained in the next section.

### 1.2.2 Oscillations in Matter

When traversing ordinary matter, neutrinos may scatter coherently off the weak potential created by nucleons and electrons. Usually, the effect is negligible, but if the density is large enough, an observable effect, named the Mikheyev-Smirnov-Wolfenstein (MSW) effect, is present. While muon neutrinos ( $\nu_\mu$ 's) and tau neutrinos ( $\nu_\tau$ 's) can only scatter elastically by neutral current (NC) reactions, electron neutrinos ( $\nu_e$ 's) can additionally interact elastically with electrons via charged current (CC) reactions, leading to an enhanced overall cross-section for  $\nu_e$  interactions compared to  $\nu_\mu$ 's and  $\nu_\tau$ 's. This enlarged  $\nu_e$  cross-section can be interpreted as an additional potential,

$$V = \sqrt{2}G_F n_e(\mathbf{x}), \quad (1.12)$$

altering the oscillation mechanism for  $\nu_e$  compared to the vacuum case. Here  $G_F$  is the Fermi coupling constant and  $n_e(\mathbf{x})$  the electron density of the traversing material [58]. The potential  $V$  is seen as an addition to the mass terms introduced in the Hamiltonian, which describes the propagation of the neutrino mass eigenstates. If the matter potential  $V$  is large enough, the change of the Hamiltonian could influence the mixing angles and the mass differences compared to the vacuum case significantly. Since only differences in the mass terms drive the oscillations, the same shift of all neutrino masses by the NC interactions can be neglected. Accordingly, the CC interaction term  $V$  only affects the  $\nu_e$  flavor proportion of the mass eigenstates. In general, the mass eigenstate  $\nu_1$  is affected the most as its proportion of the flavor  $\nu_e$  is the largest.

A prominent example of neutrinos traversing matter is given through the solar neutrino flux. The solar neutrino flux arriving at the Earth is an incoherent sum of the fluxes of mass eigenstate neutrinos, resulting in a generally written  $\nu_e$  survival probability [59],

$$P_{ee} = P_{e1}^\odot P_{1e}^0 + P_{e2}^\odot P_{2e}^0 + P_{e3}^\odot P_{3e}^0, \quad (1.13)$$

with  $P_{ei}^\odot$  ( $i \in 1, 2, 3$ ) as the probability of an  $\nu_e \rightarrow \nu_i$  conversion in the Sun.  $P_{ie}^0$  represents the projection of the  $i$ th mass eigenstate onto  $\nu_e$  via  $P_{ie}^0 = |U_{ei}|^2$  with  $U$  as the leptonic mixing matrix in the vacuum from Eq. (1.3).

The third matter eigenstate  $\nu_{3m} \sim \nu_3$  is practically not affected by solar or Earth matter, leading to

$$P_{e3}^{\odot} \simeq P_{3e}^0 \sim \sin^2(\theta_{13}) \ll 1, \quad (1.14)$$

that decouples  $\nu_{3m}$  from  $\nu_{1m}$  and  $\nu_{2m}$  [60]. This transfers Eq. (1.13) into

$$P_{ee} = c_{13}^4 P_{2f}(\theta_{12}, \Delta m_{21}^2, c_{13}^2 V) + s_{13}^4, \quad (1.15)$$

with  $P_{2f}$  as the  $\nu_e$  survival probability for the two flavor case [59]. The effective potential  $c_{13}^2 V$  substitutes the neutrino potential in the Sun  $V$ , defining the instantaneous effective mixing angle in matter  $\theta_{12m}$  [61]

$$\cos(2\theta_{12m})(V, E_\nu) = \frac{\cos 2\theta_{12} - 2E_\nu V / \Delta m_{12}^2}{\sqrt{(\cos 2\theta_{12} - 2E_\nu V / \Delta m_{12}^2)^2 + \sin^2 2\theta_{12}}}. \quad (1.16)$$

Here,  $E_\nu$  being the neutrino energy,  $\theta_{12}$  the vacuum mixing angle, and  $\Delta m_{12}^2$  the squared vacuum mass difference between the mass eigenstates  $\nu_1$  and  $\nu_2$ . Eq. (1.16) leads to three specific scenarios:

1. For low electron densities, the mixing angle is almost unaffected by the matter, called the vacuum region.  
 $2EV / \Delta m_{12}^2 \ll \cos 2\theta_{12} \rightarrow \cos 2\theta_{12m} \simeq \cos 2\theta_{12}$
2. Reaching the maximal mixing effect between the two neutrino mass eigenstates, independent of  $\theta_{12}$ , is called the transition region.  
 $2EV / \Delta m_{12}^2 \simeq \cos 2\theta_{12} \rightarrow \theta_{12m} \simeq 45^\circ$
3. Almost no mixing occurs if an  $\nu_e$  mainly consists of the matter eigenstate  $\nu_{2m}$ , called the matter-dominated region.  
 $2EV / \Delta m_{12}^2 \gg \cos 2\theta_{12} \rightarrow \theta_{12m} \simeq 90^\circ$

The matter-dominated case applies for  $\nu_e$ 's that are generated in fusion processes in the core of the Sun at energies above  $\sim 10$  MeV. Thus, these produced  $\nu_e$ 's consist mainly of the mass eigenstate  $\nu_{2m}$  for the given electron density. When these neutrinos propagate towards the surface of the Sun, the electron density decreases accompanied by a change of the mixing angle  $\theta_{12m}$ . The implications of the matter effect during the propagation of an  $\nu_e$  from the core to the surface of the Sun are depicted in Fig. 1.3. Due to the small gradient of the electron density inside the Sun compared to the oscillation length of the neutrino in matter, an adiabatic conversion<sup>6</sup> may occur at a resonance point, leaving the neutrino in the mass

<sup>6</sup> Since non-adiabatic corrections to that mechanism are very small, they are neglected in the evaluations given here [61].



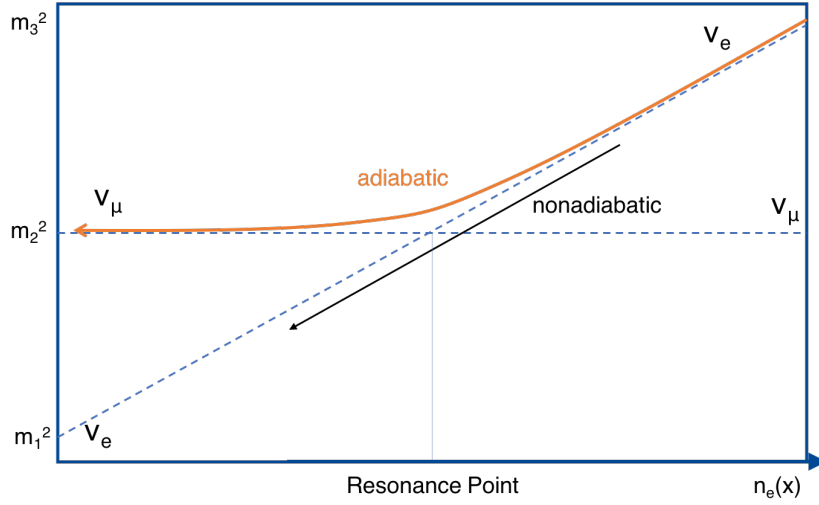


Figure 1.3: Illustration of the **MSW** effect. An  $\nu_e$  created in the core of the Sun (right upper corner) propagates through the solar matter with a decreasing electron density  $n_e(x)$  towards the vacuum. If the adiabatic conversion takes place, the  $\nu_e$  leaves the Sun in the mass eigenstate  $\nu_2$  that in vacuum basically forms  $\nu_\mu$ .

eigenstate  $\nu_{2m}$ . When the neutrino reaches the vacuum region, the vacuum **PMNS** mixing matrix applies, and mostly  $\nu_\mu$ , which dominantly consist of  $\nu_2$ , remain. The resonant conversion of  $\nu_e$  into  $\nu_\mu$  is referred to as the **MSW** effect, named after its discoverers [62, 63].

Since the neutrinos are in the mass eigenstate  $\nu_{2m}$  when leaving the Sun, they do not oscillate on their way to the Earth. The so-called Earth-matter effect describes the transition  $\nu_{2m} \rightarrow \nu_{1m}$  for neutrinos passing through the Earth and affects the  $\nu_e$  survival probability by  $\sim 1-2\%$  [59]. Therefore, the Earth-matter effect is neglected, and the solar  $\nu_e$  survival probability ascertains to be

$$P_{ee} = |\langle \nu_{2m} | \nu_e \rangle|^2 \sim \sin^2(2\theta_{12}) \sim 30\%. \quad (1.17)$$

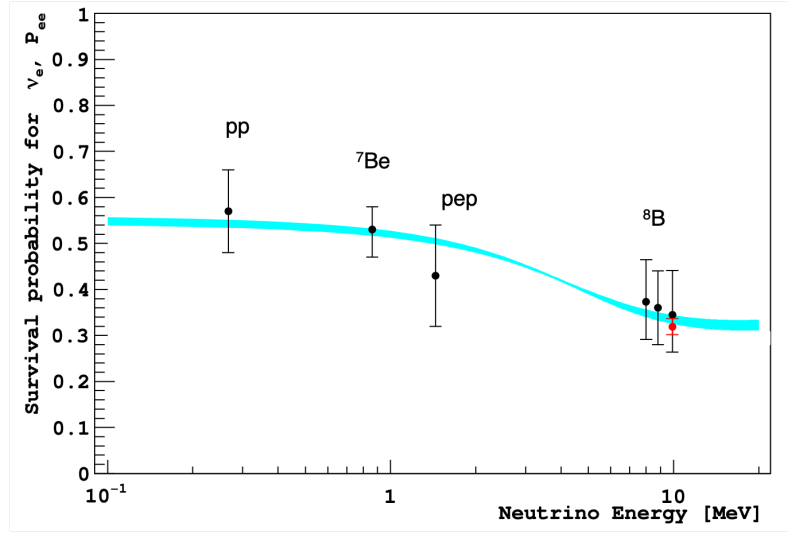


Figure 1.4: The energy-dependent survival probability for  $\nu_e$  produced in the Sun. The black points represent, from left to right, the Borexino pp,  $^7\text{Be}$ , pep, and  $^8\text{B}$  data, while red points correspond to SNO+SK  $^8\text{B}$  data [64, 65]. The electron neutrino survival probabilities from experimental points are determined using a high metallicity Standard Solar Model [66]. The error bars represent the  $\pm 1\sigma$  experimental and theoretical uncertainties. The blue band corresponds to the  $\pm 1\sigma$  errors of the survival probability as theoretically predicted by the MSW-LMA solution [67]. Figure from [10].

Considering all possible production points of neutrinos in the Sun and upon averaging over fast neutrino oscillations inside the Sun, the two flavor  $\nu_e$  survival probability  $P_{2f}$  appearing in Eq. (1.15), can be expressed as [60]

$$P_{2f}(\theta_{12}, \Delta m_{21}^2, c_{13}^2 V) = \frac{1}{2}(1 + \cos 2\theta_{12} \langle \cos 2\theta_{12m} \rangle). \quad (1.18)$$

Here,  $\langle \cos 2\theta_{12m} \rangle$  denotes the value of  $\cos 2\theta_{12m}$  averaged over all possible production points

$$\langle \cos 2\theta_{12m} \rangle = \int_0^{R_\odot} f(r) \times \cos 2\theta_{12m}(r) dr, \quad (1.19)$$

with the radius of the Sun  $R_\odot$  and the normalized spatial distribution function  $f(r)$  of the neutrino source in the Sun. As  $\langle \cos 2\theta_{12m} \rangle$  depends on the neutrino energy, the survival probability is also energy-dependent, as depicted in Fig. 1.4, where the two oscillation regimes can be visibly distinguished.

While the oscillations of the low-energetic pp,  ${}^7\text{Be}$ , and pep neutrinos are vacuum dominated, the oscillations of the high-energetic  ${}^8\text{B}$  neutrinos are matter-dominated. Since this effect is only possible for  $m_2 > m_1$ , the presence of the MSW effect determines the sign of  $\Delta m_{12}^2$  to be positive [68]. Until today, all measurements of the solar  $\nu_e$  survival probability have been performed in either the vacuum or the matter-dominated region while the transition region between  $\sim 2\text{MeV}$  and  $\sim 5\text{MeV}$  remains mostly unexplored so far. However, measurements in this region might yield important implications as non-standard neutrino interactions could influence the survival probability at these energies.<sup>7</sup>

---

<sup>7</sup> Besides non-standard interactions of neutrinos, also the existence of sterile neutrinos, which are neutrinos that do not interact weakly, could alter the survival probability of solar  $\nu_e$  in the transition region [69].

### 1.3 Neutrino Nucleon Interactions

As the thesis mainly focusses on the detection of neutrinos through the interaction with matter, a short overview of possible interactions of neutrinos with nucleons is given in the following. The four main possible interactions:

- elastic- and quasielastic scattering,
- resonant neutrino scattering,
- deep inelastic scattering, and
- coherent neutrino-nucleus scattering

are discussed and delineated in the following. Corresponding exemplary Feynman diagrams are depicted in Fig. 1.5 and their interaction cross-sections are plotted in Fig. 1.6

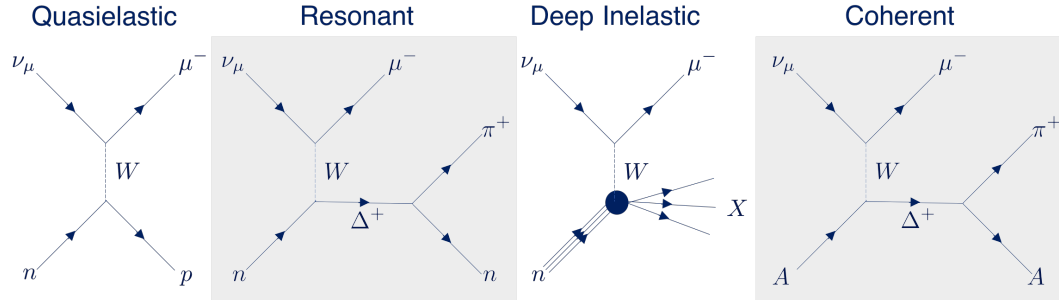


Figure 1.5: Feynman diagrams of exemplary charged current neutrino-nucleon interactions: quasielastic scattering, resonance single-pion interaction, deep inelastic scattering, and coherent neutrino scattering.

The nucleon interactions possible for neutrinos with low energies are the ones in which the nucleons stays intact. All neutrinos and antineutrinos can scatter off both neutrons and protons in what is referred to as neutral current (NC) elastic scattering:

$$\bar{\nu} + p/n \rightarrow \bar{\nu} + p/n. \quad (1.20)$$

Once neutrinos acquire sufficient energy, they can also undergo the analogous charged current (CC) interactions:

$$\bar{\nu}_l + p/n \rightarrow n/p + l^\pm, \quad (1.21)$$

where the flavor is denoted by  $l \in (e, \mu, \tau)$ . Because of the need to create the charged lepton's mass, this is referred to as quasielastic (QEL) scattering. As exemplarily

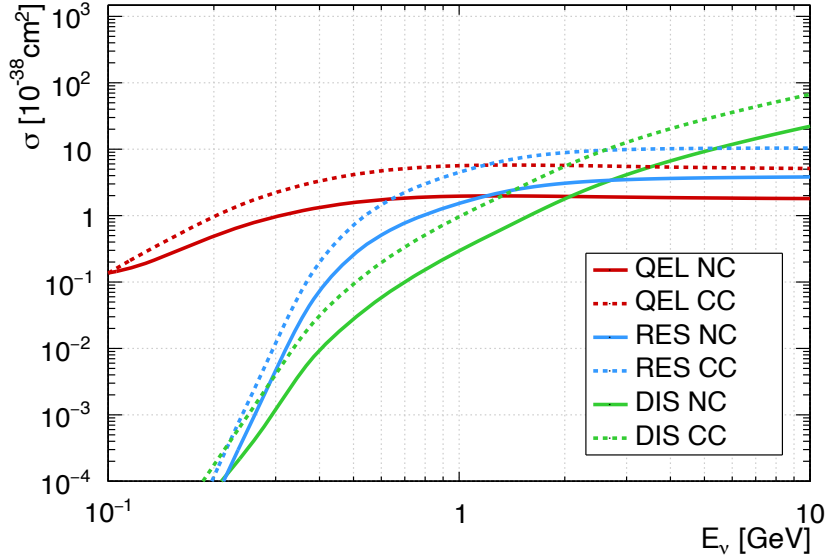


Figure 1.6: Energy-dependent neutral current (NC) (solid) and charged current (CC) (dotted) cross-section per nuclei for  $\nu_e$  reactions on  $^{12}\text{C}$  [70]. Quasielastic (QEL), resonant interaction (RES) and deep inelastic scattering (DIS) cross-sections are compared.

shown for electron neutrino ( $\nu_e$ ) in Fig. 1.6, the dominant interaction below  $\sim 1$  GeV neutrino energy is the CCQEL scattering.

As the energy transfer scales with incoming neutrino energy  $E_\nu$ , it becomes increasingly unlikely for the nucleon to remain intact, and neutrinos gain access to inelastic scattering processes. The target nucleon is knocked into a baryonic resonance, which is determined by the neutrino's energy. Subsequently, these resonances decay back down to a nucleon, most often accompanied by pions, kaons, or radiative photons, depending on the resonance channel. All combinations of neutrinos and anti-neutrinos, scattering off neutrons and protons, via CC or NC, which obey charge conservation, can occur in resonant scattering reactions. For example, CC single pion production can occur on both neutrons and protons:

$$\nu_1^{(-)+} \text{ n/p} \rightarrow \text{l}^\pm + \text{n/p} + \pi^\mp. \quad (1.22)$$

Resonance production is most significant in the transition region between QEL and deep inelastic scattering dominance between  $\sim 0.5$  GeV and  $\sim 10$  GeV.

At even higher energies, the neutrino can transfer sufficient momentum to resolve the internal structure of the nucleon. Now, neutrinos can scatter directly off the quarks inside the nucleons. This process is known as deep inelastic scattering. The neutrino can scatter off any quark that appears inside the nucleon, including those which form the sea of quarks and anti-quarks that are continually popping in and out of existence. At lower values, the nucleons contain mostly up, down, and some strange quarks, but higher momenta can access the higher-mass and shorter-lived quarks, too. As the struck quark recoils the nucleon fragments, the strong force between the quarks results in hadronization, resulting in a jet of strongly interacting particles.

The coherent neutrino-nucleus scattering was measured in 2017 for the first time after more than four decades of postulation [71]. The feature of coherent neutrino-nucleus interaction is that the nucleus recoils as a whole, which increases the cross-section significantly [72]. The nucleus does not break up and stays unfragmented and unexcited. To avoid the destruction of the nucleus, this can only be achieved if the momentum transfer to the nucleus is kept small. This strongly constrains the kinematics of coherent scattering such that the final-state lepton, and any additional particles created, are produced at small-scattering angles with respect to the incoming neutrino. Therefore this effect only plays a role for energies below  $\sim 50$  MeV. At low neutrino energies, a neutrino can undergo **NC** coherent scattering, resulting only in very low recoil energies ( $\mathcal{O}(\text{keV})$ ). At higher neutrino energies, both **CC** and **NC** coherent scattering becomes possible, which also results in the creation of an additional final-state forward going particles, e.g., **CC** and **NC** coherent pion production

$$\begin{aligned} \bar{\nu}_1^{(-)+} + A &\rightarrow \bar{\nu}_1^{(-)} + \pi^{0+} + A \\ \bar{\nu}_1^{(-)} + A &\rightarrow l^{\mp} + \pi^{\pm} + A, \end{aligned} \tag{1.23}$$

respectively, in which the neutrino scatters off the nucleus  $A$ , and produces a single pion of the appropriate charge.

This section should give a short overview of the different interaction possibilities. As the present thesis focusses on neutrino detection for neutrinos below 40 MeV, the following mainly concentrates on **QEL** neutrino interactions.

## 1.4 Neutrinos as Astrophysical Messengers

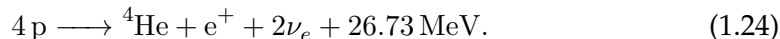
Besides the determination of neutrino properties, neutrinos offer an essential advantage in the observation of astrophysical objects. As they only interact weakly, they are marginally affected by matter and offer the possibility to look at and into their source directly. Contrary to the charged particles of cosmic radiation, neutrinos are not deflected by galactic and intergalactic magnetic fields. Photons that reach an optical telescope are mostly emitted from the surface of stellar objects and have a spectrally dependent probability of being absorbed by intermediary gas and dust clouds or by the Earth's atmosphere. Therefore, light channel observations provide limited information from the inside of dense objects.

In this respect, neutrinos can be used analogously to conventional photon astronomy as astrophysical messengers. As they carry valuable information on the environment in which they were created, this allows to investigate the happenings deep inside of an astrophysical object, e.g., the formation of a proto-neutron star in a core-collapse supernova, fusion processes in the center of the Sun or the production of thermal energy in the deep layers of Earth itself. Contrariwise, due to their minuscule interaction with matter originating from the small interaction cross-sections, detection is cumbersome and requires large detector masses. Large volume neutrino detectors are presented in chapter 2.

In the following, neutrinos emerging from the Sun, the atmosphere, or the astrophysical neutrino sources of main interest in this thesis: supernovae, are introduced.

### 1.4.1 Solar Neutrinos

Energy production in the Sun's core relies on the release of binding during the fusion of hydrogen to helium. In principle, the Coulomb forces between protons hinder the fusion of charged nuclei. However, the quantum mechanical tunnel effect allows the fusion process even at the relatively low Sun's core temperature ( $\sim 10^7$  K) [73]. In the 1930s, two different fusion mechanisms have been discovered, that transform four protons to  ${}^4\text{He}$ , resulting in both cases in the net reaction [74]



The dominant reaction chain, the so-called pp-chain, fuses hydrogen to helium in several steps and accounts for  $\sim 99\%$  of the solar energy production [73]. The sub-reactions of the pp-chain are shown in Fig. 1.7. The second fusion chain, the sub-dominant CNO cycle, contributes only  $\sim 1\%$  to the Sun's energy production and is depicted in Fig. 1.8 [73, 74]. The CNO cycle is divided into two reaction cycles using carbon, nitrogen, and oxygen as catalyzers [73]. In any case, independently of

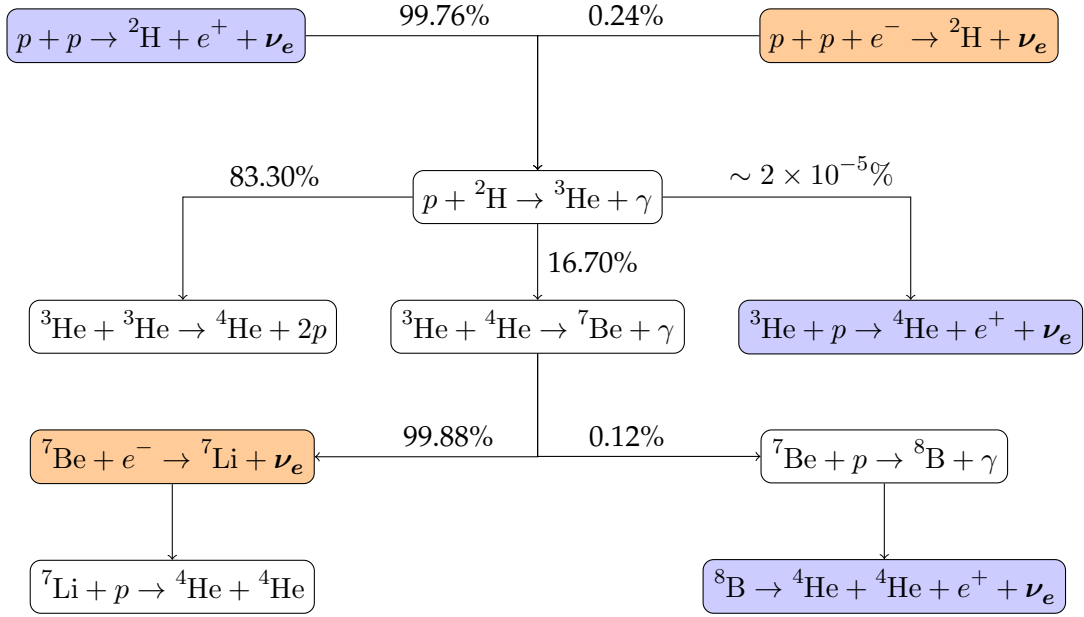


Figure 1.7: The sub-reactions of the solar pp-chain. The five generating neutrino reactions are highlighted. Neutrinos arising from the pp,  ${}^8\text{B}$ , and hep reactions have continuous energy spectra (blue), while the neutrinos from the  ${}^7\text{Be}$  and pep reactions are mono-energetic (orange). The sub-ratios of the different branches are taken from [73].

the sub-branch, two  $\nu_e$ 's are produced in every fusion to  ${}^4\text{He}$ . The radio-chemical Homestake experiment was in the late 1960s the first experiment that measured solar neutrinos [22].

Five reactions in the pp-chain produce neutrinos, which are commonly labeled by their essential step in the fusion chain: pp, pep,  ${}^7\text{Be}$ ,  ${}^8\text{B}$ , and hep neutrinos. The neutrino energy is strongly dependent on the originating nuclear reaction. While pp-neutrinos are of rather low energy ( $\lesssim 0.42$  MeV), the maximum energy of hep-neutrinos goes up to 18.8 MeV. The pp,  ${}^8\text{B}$ , and hep neutrinos have continuous energy spectra, while the  ${}^7\text{Be}$  and pep neutrinos are mono-energetic. The calculated solar neutrino spectra are shown in Fig. 1.9. The dominant neutrino source is the pp-reaction, as it stands at the beginning of the pp-chain. Therefore, the pp-neutrino flux is directly connected to the Sun's luminosity. As the branching ratio of the pp- and pep-reactions are precisely known, this leads to accurate theoretical predictions on fluxes produced in these reactions. In contrast, the incomplete knowledge of the other fusion reaction cross-sections, as well as element abundances in the Sun, giving high theoretical flux uncertainties [75].



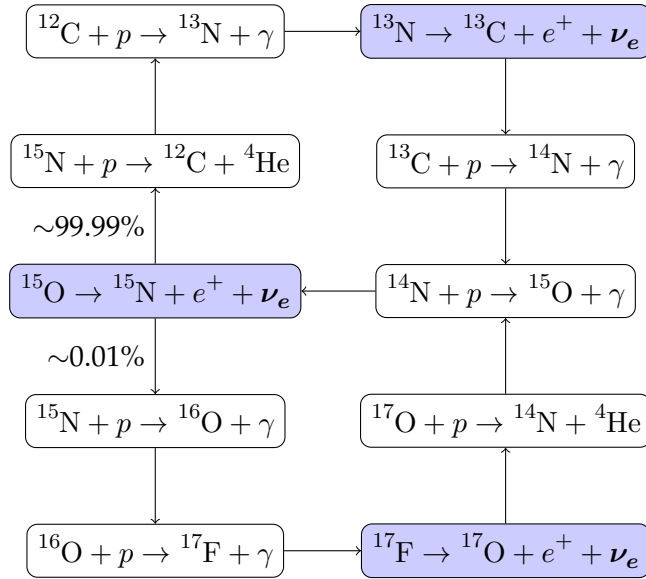


Figure 1.8: The hydrogen fusion by the CNO cycle occurs within two sub-cycles. There are three neutrino producing reactions that result in continuous neutrino energy spectra.

The in the CNO cycle generated neutrinos, labeled  $^{13}\text{N}$ ,  $^{15}\text{O}$ , and  $^{17}\text{F}$  neutrinos feature all continuous energy spectra, as can be seen in Fig. 1.9. Due to the higher Coulomb barrier, the CNO cycle is more sensitive to the core temperature of stars. As star core temperature scales with the mass of the stars, the CNO cycle becomes dominating in more massive stars. Presently, the solar core temperature is too low to allow for a substantial energy contribution of the CNO cycle, leading to a small CNO neutrino flux. For this reason, only upper limits for the CNO flux exist [79]. However, the CNO flux strongly depends on the Sun's metallicity<sup>8</sup>, and precise measurement of it could rule out one of the two different solar metallicity models [80, 81].<sup>9</sup>

<sup>8</sup> Here, metals include all elements heavier than helium.

<sup>9</sup> Besides the CNO flux, the  $^7\text{Be}$ ,  $^8\text{B}$  neutrino fluxes are also sensitive to the Sun's metallicity [82-84]. But due to high theoretical uncertainties on the neutrino fluxes, discrimination between the two solar models is not possible so far.

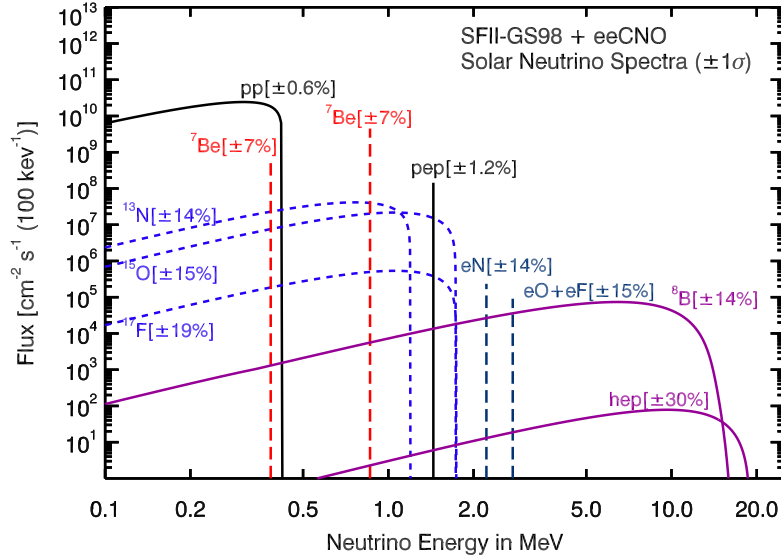


Figure 1.9: Solar neutrino energy spectra predicted by the Standard Solar Model including the neutrino fluxes from the  $pp$ -chain and the CNO cycle [76,77]. The neutrino fluxes with continuous energy spectra are given in units of  $\text{cm}^{-2}\text{s}^{-1}\text{MeV}^{-1}$ , while the discrete energy fluxes ( $pep$  and  ${}^7\text{Be}$ ) are given in  $\text{cm}^{-2}\text{s}^{-1}$ . The  ${}^7\text{Be}$  neutrinos are generated at two separate mono-energetic lines (red dashed), as in  $\sim 10\%$   ${}^7\text{Li}$  is formed in an excited state. The numbers associated with the neutrino sources give the theoretical  $\pm 1\sigma$  flux uncertainties. Figure from [78].

### 1.4.2 Atmospheric Neutrinos

Atmospheric neutrinos are produced in the Earth's atmosphere as a result of cosmic ray interactions and the weak decays of secondary mesons, in particular pions and kaons. Primary cosmic radiation constitutes 90% of protons, 9% of  $\alpha$ -particles, and 1% of heavier nuclei, and hits the atmosphere of the Earth with a rate of  $\sim 10^3 / (\text{m}^2 \text{s})$  [85]. The lower-energetic radiation originates mainly from solar processes, while processes outside the galaxy generate the high energy tail of the distribution. A broken power law can describe the energy spectrum of primary cosmic rays

$$\frac{dN}{dE} \propto E^{-\alpha}, \quad (1.25)$$

quite well, with the energy-dependent exponent  $\alpha$ . For energies below  $\sim 10^{15}$  eV,  $\alpha$  is found to be  $\simeq 2.7$  [85]. Between  $\sim 10^{15}$ - $10^{18}$  eV, a so-called knee is registered in the spectrum where it steepens with  $\alpha \simeq 2.3$  [86]. Above  $\sim 10^{18}$  eV,  $\alpha$  decreases again at

the so-called ankle [87]. A sharp cut off in the spectrum is observed around  $10^{20}$  eV, which is consistent with the expectations based on the Greisen-Zatsepin-Kuz'min effect, explaining the probability for high energy particles to be scattered on the blue-shifted cosmic microwave background radiation [88,89].

When the primary cosmic radiation impinges on the atoms of the atmosphere, hadronic showers, consist to a large extent of unstable mesons, are produced. The generated charged pions and kaons decay into muons and the corresponding neutrinos via

$$\pi^\pm \longrightarrow \mu^\pm + \nu_\mu^{(-)} \quad (1.26)$$

and

$$K^\pm \longrightarrow \mu^\pm + \nu_\mu^{(-)}. \quad (1.27)$$

Up to an energy of  $\sim 1$  GeV, these muons are expected to further decay on their way to surface of the Earth via

$$\begin{aligned} \mu^+ &\longrightarrow e^+ + \nu_e + \bar{\nu}_\mu \\ \mu^- &\longrightarrow e^- + \bar{\nu}_e + \nu_\mu. \end{aligned} \quad (1.28)$$

Below  $\sim 1$  GeV, all parent particles in the decay chain decay at equal probability, corresponding to an expected flux ratio of muon-type neutrinos to electron-type neutrinos of

$$R_{\mu/e} = \frac{\phi_{\nu_\mu} + \phi_{\bar{\nu}_\mu}}{\phi_{\nu_e} + \phi_{\bar{\nu}_e}} \sim 2. \quad (1.29)$$

Due to time dilation, the decay length of the muons becomes larger at higher energies, and muons are less likely to decay before hitting the ground, increasing the ratio of muon-type neutrinos to electron-type neutrinos. The neutrino energy spectrum initially follows the primary cosmic ray spectrum  $\propto E^{-2.7}$  and becomes steeper at higher energy reflecting the decreasing decay probability of the parent particles. The spectral shape of atmospheric neutrinos closely resembles the one of the primary cosmic radiation [90].

Furthermore, the propagation of a primary cosmic ray nucleus is strongly affected by the Earth's geomagnetic field. Thus, low energetic primary particles at low geomagnetic latitudes cannot reach the atmosphere due to their magnetic rigidity. This effect results in an angular distribution due to latitude dependence of the atmospheric neutrino flux at the Earth's surface with an increased flux towards the horizon [91,92]. The difference of flux among between polar and equator region manifests through the factor  $\sim 3$  at the low energy end [92].

When cosmic rays above a few 100 MeV enter the solar sphere, they are pushed back by the solar wind. As this effect is more pronounced for lower energy cosmic rays, their energy spectrum also varies with the strength of the solar wind, or with the solar activity. However, this modulation is expected to be around 5% at 10 GeV, and becomes even smaller above [93].

However, the air density profile is the most crucial quantity in the calculation of atmospheric neutrino fluxes. In the mid-latitude and tropical region, the seasonal differences are small, but fluxes are higher in summer. This may be understood by the fact that the air density at higher altitudes is higher in the summer, changing the relative probability of pions to decay or to interact with air nuclei. Moreover, there is a seasonal variation of the electron (anti-)neutrino fluxes above 10 GeV. When the air shrinks down, muons are created at lower altitudes, and the probability of muons to hit the ground before decaying increases. When the muons hit the earth material, they lose their energy quickly, producing neutrinos with very low energies. Besides, there is another seasonal mechanism with substantial effect on the low energy neutrino spectra. When the atmosphere shrinks lower, the muons travel in denser air and lose more energy before the decay, causing a shift in the neutrino energy spectra. As the energy spectra of atmospheric neutrinos are steeply decreasing at the energies  $\gtrsim 0.1$  GeV, the fluxes decrease in the denser air at those energies. Therefore, this mechanism is effecting the seasonal variation of the neutrino flux, when most muons decay in the air, and for the neutrinos with energies below a few GeV [92].

Through charged current interactions, the water Cherenkov detector Super-Kamiokande (cf. section 2.1.1) was able to compare the observed ratio of atmospheric muon and electron-type neutrinos, defined in Eq. (1.29) to a Monte-Carlo prediction and obtained a result of

$$R_{\mu/e} = 0.60_{-0.06}^{+0.07}(\text{stat.}) \pm 0.05(\text{syst.}), \quad (1.30)$$

formulating first the so-called *atmospheric neutrino problem* [94]. With the observation of zenith angle-dependent distribution of muon and electron type events in the detector, the deficit in the ratio was caused by events coming from below the horizon. Neutrino oscillations could unambiguously explain this deficit with the two flavor oscillation hypothesis of  $\nu_{\mu} \rightarrow \nu_{\tau}$  transitions mediated by the mixing angle  $\theta_{23}$ . Furthermore, these results allow inferring the oscillation mixing angle  $\theta_{23}$  and the squared mass difference  $\Delta m_{23}^2$  (cf. section 1.2.1).

Therefore, by revealing the existence of neutrino oscillations in the atmospheric sector, and determination of oscillation parameters, a significant contribution to the understanding of the neutrino and its properties could be accomplished through atmospheric neutrino observations.

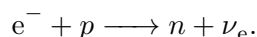
### 1.4.3 Supernova Neutrinos

Core-collapse supernovae (CCSNe) are the spectacular outcomes of the violent deaths of massive stars at the end of their burning cycles. The iron core, which gets gravitationally unstable, collapses and forms a neutron star (NS) or a black hole (BH) [95].

The fusion reactions proceed in stages that depend on temperature, defining the potential of successively overcoming the Coulomb barriers for the formation of heavier elements. While the Sun is not massive enough to produce energy in the subsequent steps after the helium-burning, more massive stars continue energy release through the fusion of heavier elements. At the end of iron burning, a star with more mass than  $8 M_{\odot}$  becomes unstable against gravity, because no further energy can be released in fusion processes when the binding energy reaches its maximum, and the radiation pressure declines [96].<sup>10</sup>

If a star is more massive than this limit, it can become hot and dense enough in the core to burn carbon and oxygen to iron and to develop an iron core at the end of its life [97]. The Fermi-pressure of electrons in the innermost iron core fails to balance the gravitational pressure, and the core collapses to a proto-neutron star (PNS). This collapse comes to a sudden end when the core reaches nuclear density ( $\sim 3 \times 10^{14} \text{ g cm}^{-3}$ ), where the core cannot be compressed further, and the repulsive nuclear forces stop the collapse. This inner core of the iron core forms the PNS and further in-falling material bounces off the core and forms an outward propagating shock front.

A successful CCSN explosion<sup>11</sup> can be divided into three typical phases, while the whole signal will last for  $\sim 10$  s. While the shock front propagates through the outer core, nuclei are dissociated into free nucleons, and the conversion of protons into neutrons releases a large number of  $\nu_e$ 's via the electron capture process,



When the shock front approaches the so-called neutrino-sphere, the region where neutrinos decouple from matter, neutrinos start propagating ahead of the shock in the so-called neutronization burst. Although the peak luminosity of this neutronization burst exceeds  $10^{53} \text{ erg s}^{-1}$ , the energy-release during this phase is only of the order of  $10^{51} \text{ erg}$  due to the short duration ( $\sim 20 \text{ ms}$ ) [100].

<sup>10</sup> Stars below  $\sim (8-9) M_{\odot}$  end in a white dwarf. A thermonuclear explosion could occur, named supernova (SN) type Ia, if they accrete matter or merge with another star.

<sup>11</sup> For convenience, the common name *core-collapse supernovae* for SNe of Types II, Type Ib and Ic is used. For observational classifications of SNe, see [99].

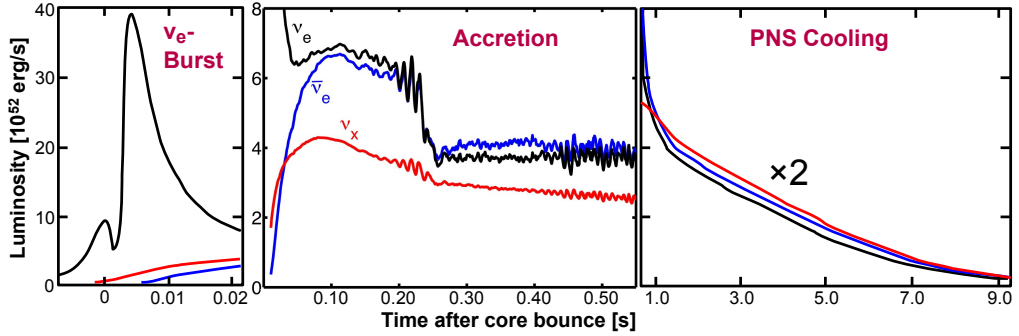


Figure 1.10: Neutrino luminosities of the different neutrino flavors during a **CCSN** as a function of time. Here:  $\nu_e$  is shown in black,  $\bar{\nu}_e$  depicted in blue, and  $\nu_x$  as one species of  $\nu_\mu, \bar{\nu}_\mu, \nu_\tau, \bar{\nu}_\tau$  in red. The left panel shows the prompt burst of electron neutrinos, while the middle panel corresponds to the post-bounce accretion phase. The right panel displays the decay of the neutrino luminosities over several seconds in the neutrino-cooling phase of the newly formed neutron star. Figure is taken from [98].

After the neutronization burst, the so-called accretion phase follows, during which the stellar matter of the surrounding shells continuously falls through the shock and settles onto an inflated accretion mantle around the **PNS**. During the mass accretion, the temperature of the accretion mantle increases. However, this ultra-dense core cools down by the emission of  $\nu\bar{\nu}$  pairs of all flavors.

Finally, with the cooling of the **PNS**, the neutrino luminosity declines. The **PNS** star deleptonizes and ends up as a **NS**. During this phase, it mainly cools through the emission of thermally produced neutrinos of all flavors for a duration of  $\sim 10$  s [100]. If the explosion is not successful, the accretion phase continues until a still unknown mass limit for **BH** formation. At this point, the neutrino release will stop abruptly. Fig. 1.10 shows the neutrino flux for the different neutrino flavors as a function of time after core bounce.

The neutrinos emerge the neutrino-sphere when they decouple from matter, and their energy distribution is determined by the temperature at which they decouple. The energy spectra of each neutrino species depend on the differential neutrino number spectrum from the time-dependent luminosity  $L_\nu(t)$  and mean energy  $\langle E_\nu(t) \rangle$  of each neutrino species:

$$\frac{dN_\nu}{dE_\nu} = \frac{L_\nu(t)}{\langle E_\nu \rangle} \frac{f_\alpha(E_\nu)}{\int_0^\infty f_\alpha(E_\nu) dE_\nu}. \quad (1.31)$$

Model	Progenitor Mass [ $M_\odot$ ]	$\langle E_{\nu_e} \rangle$ [MeV]	$\langle E_{\bar{\nu}_e} \rangle$ [MeV]	$\langle E_{\nu_x} \rangle$ [MeV]	$\alpha_{\bar{\nu}_e}$	$\alpha_{\nu_x}$
TBP [102]	11	10.0	11.4	14.1	3.7	2.2
	15	10.0	11.4	14.1	3.7	2.2
	20	10.0	11.9	14.4	3.6	2.2
KRJ [101]	-	13.0	15.4	15.7	4.2	2.5

Table 1.2: Monte-Carlo simulations of a CCSN from two different groups for three different progenitor masses. They predict different shapes for the emitted neutrino spectra: mean energies  $\langle E \rangle$  and pinching factors  $\alpha$ . The parameterization (cf. Eq. (1.32)) and fit values were taken from [105].

As low-energetic neutrinos may be emitted at higher densities, the corresponding neutrino-spheres have smaller radii than high-energetic neutrinos. This effect leads to pinched energy distribution with an assumed spectral shape parameter [100,101]:

$$f_\alpha = \left( \frac{E}{\langle E \rangle} \right)^\alpha \exp \left( -\frac{(\alpha + 1)E}{\langle E \rangle} \right). \quad (1.32)$$

The pinching factor  $\alpha$  accounts for a different shape of the neutrino energy spectra compared to the Fermi-Dirac assumption due to the finite width of the neutrino-sphere of a particular flavor.<sup>12</sup>

The spectral shape parameters for  $\nu_e$  and  $\nu_x$  obtained by two exemplary Monte-Carlo simulations are shown in Tab. 1.2 [101,102]. Indirect constraints from the chemical abundances of light elements produced through neutrino-nucleus reactions in SN environment predict  $\langle E \rangle = 12\text{--}21$  MeV [103]. Numerical SN simulations also predict  $\langle E_{\bar{\nu}_e} \rangle$  in the same energy range and agree with the measured neutrino spectrum from SN1987A [101,102,104]. While the thermalized  $\nu_\mu$  and  $\nu_\tau$  only interact via neutral current reactions with ordinary matter,  $\nu_e$ 's and  $\bar{\nu}_e$ 's are also affected by charged current reactions. Due to the high neutron density in and around the PNS, the surrounding matter is more permeable for  $\nu_\mu$  and  $\nu_\tau$ , explaining the temperature hierarchy  $\langle E_{\nu_e} \rangle < \langle E_{\nu_x} \rangle$ .

Since the flavor neutrinos are not mass eigenstates, they mix with other flavor neutrinos during their propagation (cf. section 1.2). To estimate the SN neutrino

<sup>12</sup> Parameter  $\alpha \approx 2.3$  corresponds to a Fermi-Dirac distribution with vanishing degeneracy parameter,  $\alpha > 2.3$  to a pinched, and  $\alpha < 2.3$  to an anti-pinched spectrum, where  $\alpha = 2.0$  gives the Maxwell-Boltzmann distribution.

spectrum in a terrestrial detector, the mixing and the impact of the matter potential caused by the core and the surrounding progenitor star on oscillation probabilities, has to be considered [100]. As the neutrinos pass from the core through the stellar matter to vacuum, the change of the mixing parameters in the PMNS matrix leads to the flavor conversion of  $\nu_x \leftrightarrow \nu_e/\bar{\nu}_e$ . The behavior of matter-induced flavor conversion<sup>13</sup> inside the SN envelope is well understood, because the relevant mixing angles and mass squared differences are well determined by recent solar, atmospheric, and reactor neutrino experiments [29, 108–110].

In 1987, the first observation of neutrinos emitted by a SN explosion in the Large Magellanic Cloud - named SN1987A - was performed by terrestrial neutrino detectors. At a distance of 50 kpc, two large-volume water Cherenkov detectors, the Irvine-Michigan-Brookhaven, and the Kamiokande experiment observed in total 19  $\bar{\nu}_e$  events [2, 111]. The next opportunity to detect SN neutrinos could be offered by the burst from a future galactic SN. With a predicted SN rate in the Milky Way of about 1–3 per century, a detector with a lifetime of 30 years would have an excellent chance to observe  $\nu$ 's from at least one galactic SN [100, 112]. Nowadays, many experiments (cf. chapter 2) are waiting for such a rare event, that would yield revolutionary neutrino data sets. Moreover, many experiments that can observe a neutrino signal from a SN are part of the SuperNova Early Warning System such that, in the case of a nearby SN, astronomers are prepared.

In summary, the coincidence neutrino burst signals could give information about the SN position and could provide a reliable test of SN explosion models. Furthermore, neutrinos are unique messengers of late stellar evolution in the central regions of core-collapse events. They can give information about nuclear and particle physics at the extreme conditions near the collapsing core.

However, despite looking for the occurrence of a supernova in the Milky Way, another approach is to look for the cumulative emission from all past CCSNe, called the diffuse supernova neutrino background.

---

<sup>13</sup> The effect of self-induced flavor conversions is subdominant ( $\mathcal{O}(10\%)$ ) compared to the MSW-effect (cf. section 1.2.2) and is therefore not considered in this thesis [106, 107].



#### 1.4.4 Diffuse Supernova Neutrino Background

There are about  $10^{20}$  stars in the universe, with  $\sim 0.3\%$  more massive than  $8M_{\odot}$ , leading to an estimate of  $10^{17}$  occurred **SN** explosions over the entire history of the universe [113]. In such a **CCSN**, a vast amount of gravitational binding energy is released. Neutrinos carry about  $\sim 99\%$  of the released energy and only less than 1% is emitted as optical light. On average, one **SN** explosion has been occurring every second somewhere in the universe, releasing a copious amount of  $\sim 10^{58}$  neutrinos [114].

Instead of waiting for the next galactic **SN** explosion, a different, complementary approach is to search for the diffuse supernova neutrino background (**DSNB**). As there is a vast amount of CCSNe, each releasing a huge amount of neutrinos, the cumulative neutrino emission of CCSNe must fill the present universe with an estimated flux in the order of a few tens/cm<sup>2</sup>/s [113]. So, the **DSNB** is the combined flux of neutrinos and antineutrinos emitted by all past CCSNe in the whole observable universe [115]. As this flux appears isotropic and stationary in time, it is a guaranteed steady source of **SN** neutrinos. Due to the low flux, progress towards its observation is essentially technologically driven, as it requires a large target mass and a good background suppression.

Up to now, the **DSNB** was not measured by present neutrino detectors. The Super-Kamiokande (**SuperK**) experiment (cf. section 2.1.1) sets the current best limit, imposing an upper limit<sup>14</sup> (90% C.L.) on the  $\bar{\nu}_e$  flux of  $(2.8-3.1)/\text{cm}^2/\text{s}$  above 17.3 MeV [3]. Current upper limits on the **DSNB** are close to the theoretically exciting region of the parameter space, leading to the hope that detection might be achieved at the next generation of neutrino observatories and motivating ongoing efforts.

Future experiments like **JUNO** and the gadolinium-enhanced **SuperK** experiment will offer sufficiently large target masses to achieve the first observation of **DSNB** neutrinos possibly [4, 117]. With the expectation of a few detectable events per year, the detection of neutrinos from the **DSNB** in the following  $\sim 10-15$  years seems achievable for **JUNO** and **SuperK**. However, both experiments will have to overcome notable experimental challenges.

As Earth is transparent to neutrinos, detectors see a total (over  $4\pi$  angle-integrated) diffuse differential number flux from the full sky. The predicted **DSNB** flux spectrum at Earth is computed as the line-of-sight integral of the initial mass func-

<sup>14</sup> The more stringent limit of  $\bar{\nu}_e$  flux of  $1.2/(\text{cm}^2\text{s})$  above 19.3 MeV was reported by **SuperK** collaboration in 2003 [116]. The result in 2012 includes updated uncertainty models, resulting in larger exclusion limits.

tion (IMF)-weighted average number spectrum of neutrinos emitted by one past SN explosion, multiplied by the evolving CCSN rate  $R_{SN}(z)$  as a function of redshift  $z$  over cosmic history

$$\frac{d\Phi_\nu}{dE_\nu} = c \int_0^\infty \frac{dN(E'_\nu)}{dE'_\nu} \times \frac{dE'_\nu}{dE_\nu} \times R_{SN}(z) \times \left| \frac{dt}{dz} \right| dz, \quad (1.33)$$

where  $c$  is the speed of light [105, 115]. The first term represents the neutrino emission spectrum, where  $E'_\nu$  denotes the energy at the time of emission from the corresponding SN sources at redshift  $z$ . Thus,  $E_\nu$ , as the received neutrino energy has to be redshift corrected via  $E'_\nu = (1+z)E_\nu$ , as it was emitted at higher energy. The detectable DSNB neutrino flux mainly originates from SNe occurring at redshifts  $z \lesssim 1-2$ . One reason is that the energies of neutrinos produced in farther SNe are too far red-shifted to contribute to the signal significantly [118, 119]. The SN neutrino spectrum can be derived from SN simulations [101, 102, 120-123]. As progenitors with different masses are not the same abundant, e.g., low mass progenitors are more frequent than heavier ones; the time-integrated neutrino spectra per core-collapse need to be weighted by a (constant in time) IMF [124]:

$$\psi(M) = \frac{dN}{dM} = M^{-\zeta}, \begin{cases} \zeta = 2.35, & M \geq 0.5 M_\odot \\ \zeta = 1.50, & 0.1 M_\odot \leq M < 0.5 M_\odot. \end{cases} \quad (1.34)$$

The IMF falls steeply with progenitor mass  $M$ , resulting in less relevant contributions from lower mass progenitors.

The last term in Eq. (1.33), accounts for the assumed cosmological model, which relates  $z$  to the cosmic time  $t$ . The Friedmann equation gives the differential distance through the expansion history of the Universe by

$$\left( \frac{dt}{dz} \right)^{-1} = -H_0(1+z) \sqrt{\Omega_\Lambda + \Omega_m(1+z)^3}. \quad (1.35)$$

Throughout, standard  $\Lambda$ CDM<sup>15</sup> cosmology is assumed, with  $\Omega_m = 0.3$ ,  $\Omega_\Lambda = 0.7$  as today's fractions of the cosmic energy density in matter and dark energy, respectively, and the Hubble constant  $H_0 = 70$  km/(s Mpc). By combining Eq. (1.33) with

---

<sup>15</sup> Standard cosmological model with cold dark matter (CDM) and a cosmological constant ( $\Lambda$ ).

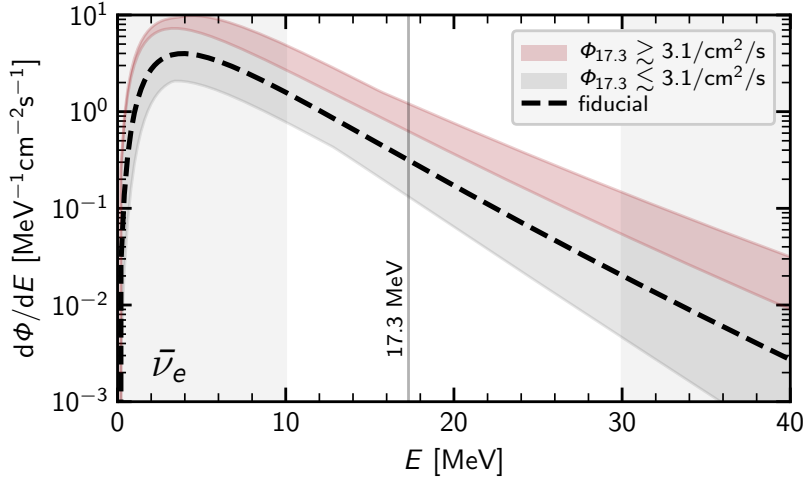


Figure 1.11: Comparison of the **DSNB** flux range together with the upper **SuperK** flux limits [3]. The shaded bands show the spread among the flux spectra of  $\bar{\nu}_e$ 's resulting from various combinations of the source parameters. The different input source parameters are explained in more detail in chapter 4. The fiducial model is marked by the dashed line. Figure is taken from [125].

Eq. (1.35), the estimated **DSNB** flux spectrum is transformed into

$$\frac{d\Phi_\nu}{dE_\nu} = \frac{c}{H_0} \int_0^{z_{max}} \frac{dN(E'_\nu)}{dE'_\nu} \times \frac{R_{SN}(z)}{\sqrt{\Omega_\Lambda + \Omega_m(1+z)^3}} dz. \quad (1.36)$$

The **CCSN** rate  $R_{SN}(z)$  can be determined by combining optical information on the star formation rate  $R_{SF}(z)$  and the **IMF** of the forming stars and will be discussed more detailed in section 4.2 [105]. Fig. 1.11 shows the obtained range of possible  $\bar{\nu}_e$  **DSNB** flux spectra, including uncertainties of the **CCSN** rate, and the **SN** neutrino source spectra that reaches a neutrino detector at Earth [125].

As the possible flux range is quite broad, a measurement of the spectrum of the **DSNB** neutrinos will be a probe of various neutrino physics [126]. It could probe the entire stellar population, in its diversity and cosmological evolution. As it describes the average, red-shifted **SN** neutrino emission spectrum, it carries imprints of the neutrino production processes and the equation of state of nuclear matter as well as the mass accretion rate onto the **PNS** [127]. Therefore, the **DSNB** provides an immediate opportunity to study the average emission of MeV-thermal neutri-

nos from CCSNe and possibly the explosion mechanism [123,127,128]. The DSNB also serves as a test whether an individual event, such as SN1987A, the only CCSN with neutrino detection to date, is typical in its neutrino signal [129,130]. Since the DSNB represents the average neutrino emission from all past core collapses, it is sensitive to subpopulations with potentially systematically different neutrino emission properties. So far, most predictions for the DSNB have considered only the most common scenario: the collapse into a NS. However, not all SNe terminate in the formation of a NS, but a fraction of  $\mathcal{O}(10\%)$  is thought to collapse further into a BH, especially for extremely massive progenitors [131]. Such so-called failed SNe are optically dark since no explosion occurs and, thus, contribute to the uncertainty of the measured SN rate. Additionally, it has been shown that in the case of collapse to a BH, neutrinos with significantly higher energies can be emitted compared to cases of successful explosions [127]. Therefore, the flux from stellar collapses with direct BH formation is expected to be more energetic than that from successful SNe. An observation of these neutrinos could answer many fundamental questions ranging from the nuclear equation of state of nuclear matter of SN progenitor to the existence of new particles and interactions [123,127,128]. Furthermore, a non-detection would aim for new stellar or neutrino physics, like invisible neutrino decays or the presence of hypothetical new particles [132,133]. The possibility to study the birth of BHs using neutrinos opens interesting interdisciplinary connections with the studies of general relativity and with the new frontier of gravitational wave detection from BH mergers [134]. The effect and the importance of the amount of failed SNe are discussed in more detail in section 4.1.

## Chapter 2

# Large Volume Neutrino Detectors

Neutrinos have very small interaction cross-sections. The first detector that was able to detect an interaction with a neutrino used an interaction target of approximately 1 t. The large target, with its many interaction opportunities, compensates for the small cross-section. Modern detectors use targets of up to several kilo tonnes in an attempt to increase the rate of neutrino interactions. Nevertheless, when looking for neutrinos from weak sources, such as the diffuse supernova neutrino background, exposure times of several years are necessary to acquire enough events for analysis. Moreover, a stable and reliable detector behavior over the time scale of several years is required.

The present chapter will introduce the primary methods of neutrino detection and present currently existing large volume neutrino detectors. Neutrino detectors can be divided into two types: Those that use the Cherenkov effect to detect the secondary particles (section 2.1), and those that use a scintillating material for detection (section 2.2). Future detectors, such as Theia (section 11.1), may use a combination of these two approaches. This chapter focuses on existing detector technologies.

Independent of the technique used to detect the scattered or secondary particles, all flavors of neutrinos and antineutrinos can be detected via elastic scattering (ES) reactions

$$\nu_x + e^- \longrightarrow \nu_x + e^- . \quad (2.1)$$

The quasielastic reaction of the inverse  $\beta$ -decay (IBD), where electron antineutrinos ( $\bar{\nu}_e$ 's) are detected by the reaction on free protons<sup>1</sup>

$$\bar{\nu}_e + p \longrightarrow e^+ + n, \quad (2.2)$$

producing a positron and a neutron. The scattered electron or produced positron can be detected in a water Cherenkov detector if its kinetic energy is at least the Cherenkov threshold of  $\sim 800$  keV.

<sup>1</sup> Here, free protons mean hydrogen nuclei in contrast to the bound protons in heavier nuclei, for which nuclear binding effects suppress interactions at low energies.

The most commonly used process in liquid scintillator (LS) detectors to detect MeV- $\bar{\nu}_e$  is the IBD, as the two resulting particles provide two time-separated signals. The positron deposits its kinetic energy immediately ( $\sim 100$  ps [135]), and, once thus, thermalized, creates a prompt signal through annihilation or the formation of positronium (Ps) [136].<sup>2</sup> When the resulting neutron from Eq. (2.2) is thermalized, an additional signal is present through the later capture by a nuclear core, giving a supplementary delayed gamma signal



A commonly used scintillator material is linear alkylbenzene, where 99% of the neutrons are captured by free protons<sup>3</sup>, releasing a characteristic 2.22 MeV  $\gamma$ -signal with a delay of  $\sim 206 \mu\text{s}$  [139, 140]. Contrary, a gamma of such low energy is difficult to detect in a large water Cherenkov detector (WCD). The minimum neutrino energy needed to initiate the IBD reaction is

$$E_\nu > Q \approx m_e + m_n - m_p = 1.806 \text{ MeV}. \quad (2.4)$$

As the neutron is much heavier than the positron, the kinetic energy of the resulting positron is strongly correlated with the incoming  $\bar{\nu}_e$  energy. If the neutron recoil can be neglected, the positron gets almost all the energy of the  $\bar{\nu}_e$  but reduced by the  $Q$ -value of the reaction. In contrast to the ES channel, Eq. (2.1), the kinetic energy of the incident neutrino can be determined on an event by event basis from the energy of the detected positron signal,

$$E(\bar{\nu}_e) = E_{\text{vis}} + (m_n - m_p) - m_e \approx E_{\text{vis}} + 0.78 \text{ MeV}, \quad (2.5)$$

allowing for neutrino spectroscopy. The delayed coincidence of prompt and delayed signals provides a distinctive event signature. Furthermore, the cross-section of the IBD reaction is relatively large in comparison to the ES cross-section [141].

A short summary of the within this chapter introduced neutrino detectors is given in Tab. 2.1

<sup>2</sup> The bound state Ps consisting of a positron and an electron occur in two spin states: the singlet state, parapositronium (p-Ps), which constitutes  $\sim 25\%$  of the formed Ps and the longer-lived triplet state, orthopositronium (o-Ps), that has a lifetime of about 3 ns in organic LS [137]. While p-Ps dominantly decays immediately ( $\mathcal{O}(\text{ps})$ ) via the diametrical emission of two 511 keV gammas, for the dominant decay channel of o-Ps in vacuum three gammas are emitted [138].

<sup>3</sup> The cross-section for the neutron capture on  ${}^{12}\text{C}$  is  $\sim 1\%$  of the cross-section for capture on protons [139]. Therefore, in only  $\sim 1\%$  of the cases, in hydrocarbons, neutrons are captured on  ${}^{12}\text{C}$ , releasing  $\gamma$ -rays of the combined energy of 4.9 MeV [140].

Water Cherenkov Detectors				
	Super-Kamiokande (+Gd)		IceCube	
Location	Japan		South Pole	
Overburden [km.w.e]	2.7		-	
Target Mass	50 kt		10 <sup>6</sup> kt	
Target Composition	water (+Gd)		ice	
PMTs	11k 20"		5k DOMs	
Liquid Scintillator Detectors				
	Borexino	SNO+	KamLAND	JUNO
Location	Italy	Canada	Japan	China
Overburden [km.w.e]	3.8	6	2.7	1.9
Target Mass	300 t	780 t	1 kt	20 kt
Target Composition	PC	LAB	dodecane + PC	LAB
Wavelength Shifter	PPO	PPO	PPO	PPO, bis-MSB
Light yield [p.e./MeV]	500	400	250	1200
PMTs	2200 8"	9300 8"	1320 17" 554 20"	17k 20" 25k 3"
Optical coverage	34%	73%	34%	77%
Energy resolution	5%	5%	6%	3%

Table 2.1: Comparison of technical parameters of **JUNO** to current **LS** experiments: Borexino, SNO+, and KamLAND [4, [142]-145]. The energy resolution is given at 1 MeV visible energy. The two large volume **WCDs** **SuperK** and IceCube are compared [146, 147]. The listed neutrino detectors are introduced separately in the following sections.

## 2.1 Water Cherenkov Detectors

The first real-time neutrino detectors were Cherenkov detectors, which mainly use water as the primary target and benefit from the possibility of building immensely large target volumes at a low cost.

If the secondary charged particle has enough energy, it will emit light by traversing the water, which is registered by light detectors, such as photomultiplier tubes (PMTs). So if, e.g., a scattered electron is energetic enough to move faster than the phase speed of light, e.g., in water, it emits so-called Cherenkov light [148]. This radiation is emitted along the charged particle's track and is mostly emitted in the ultraviolet and blue part of the visible spectrum with a usual light yield of  $\sim 200$  photons per MeV [149]. Through the constructive interference of spherical light waves, the radiation appears as a conical light front with the shape of a spherical cone, which is illustrated in Fig. 2.1. The light cone opening angle  $\alpha$  depends on the refractive index  $n$  of the material through which the particle is passing,

$$\sin \alpha = \frac{1}{\beta n}, \quad (2.6)$$

with  $\beta = \frac{v}{c}$  as the particles' velocity [148].

Usually, Cherenkov radiation is registered by PMTs distributed on the embedding of the detector. The detected radiation is characterized commonly by the angle  $\alpha_C$  at which the radiation impinges on a surface perpendicular to the particle track.

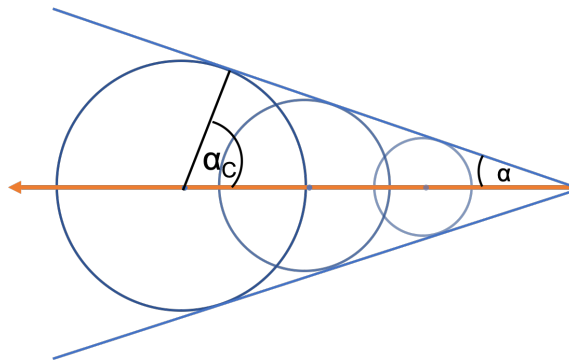


Figure 2.1: Illustration of the Cherenkov radiation created by an ultra-relativistic charged particle with  $\beta \sim 1$  passing through a medium with a refractive index  $n > 1$  [148]. Along the particle's track (orange), spherical light waves (blue) are emitted. Their interference manifest in a conical shape. The opening angle  $\alpha$  depends on the refractive index  $n$  of the material and the particle velocity.



The relation between the photon production angle compared to the charged particle's direction is given by  $\alpha_C = 90^\circ - \alpha$ . Thus, **WCDs** offer the possibility to use the orientation and the characteristic shape of the Cherenkov cone to determine the direction of the charged particle. Unfortunately, the neutrino does not radiate Cherenkov light itself, but for neutrino-electron elastic scattering (cf. Eq. (2.1)), forward scattering becomes more probable for high energy neutrinos and the direction of the electron and the neutrino nearly matches for higher energies.

However, a minimum energy of the charged particle is required to produce Cherenkov radiation, since the particle has to move faster than the phase speed of light of the material. Therefore, its velocity must be at least  $\beta \geq 1$ , implying threshold energy of

$$E_{\text{thr}} = \gamma m_0 = \frac{1}{\sqrt{1 - \frac{m_0^2}{n^2}}}, \quad (2.7)$$

with  $\gamma = 1/\sqrt{1 - \beta^2}$  and  $m_0$  the rest mass of the charged particle. For the refractive index of water  $n_W = 1.33$ , the corresponding threshold energy becomes  $E_{\text{thr}} = 1.52 m_0$ . Thus, a particle needs to possess at least a kinetic energy of half its rest mass to generate Cherenkov radiation in water. As the scattered neutrino cannot be detected directly, the neutrino energy cannot be reconstructed from the electron on an event by event basis. However, this becomes possible through a statistical analysis of several events. So, based on the number of photons registered by the **PMTs** and their respective arrival time, **WCDs** allow to explore the neutrinos energy spectra in real-time and offer the possibility to reconstruct roughly the direction of the incoming neutrino as well as their interaction position. Further, due to a differing distortion of the ring as which the Cherenkov cone arrives at the **PMTs**, the distinction between charged muons and electron-like events ( $e^\pm/\gamma$ ) is possible [113].

A disadvantage of **WCDs** and the neutrino-electron scattering detection channel is the indistinguishable background from **IBD** reactions (cf. Eq. (2.2)). Nevertheless, the forward-peaked nature of neutrino-electron scattering allows an angular cut that should contain the majority of scattering events. However, even in a narrow cone, near-isotropic **IBD** events contribute as background [112]. Neutron tagging can be utilized to overcome this disadvantage. For this, elements that feature a large neutron capture cross-section, like gadolinium, can be added to the detector target, in order to identify **IBD** events via radiative neutron capture on gadolinium (cf. Eq. (2.3)) [112]. The addition of such elements strongly enhances the **IBD** event signature.

Moreover, neutrinos created in solar or supernova processes are of rather low energies (100 keV–50 MeV), and the detection thresholds of neutrino Cherenkov telescopes are far too high in energy to be sensitive to these type of neutrinos. Therefore experiments dedicated to low-energy neutrino search are usually liquid scintillator detectors, which are lower in volume and, at the same time, more densely instrumented with light detectors that are explained in the section [2.2](#).

The focus in the following is on currently existing large volume [WCDs](#) that offer at least 1 kt of the target material. Therefore, Super-Kamiokande (section [2.1.1](#)), and IceCube (section [2.1.2](#)), are shortly introduced within the next sections. As the heavy [WCD](#) Sudbury Neutrino Observatory finished data taking 2006, it is not considered here, and the reader is referred to [\[150\]](#).

### 2.1.1 Super-Kamiokande

Super-Kamiokande ([SuperK](#)) is an imaging [WCD](#) located at the Kamioka Observatory in Japan [\[27, 146, 151\]](#). With 50 kt of ultra-pure water in a cylindrical tank with 39.3 m diameter and 41.4 m height, it is the world's largest low-energy neutrino detector. [SuperK](#) can detect neutrinos from the Sun, Earth's atmosphere, and the K2K long-baseline neutrino beam with high efficiency. The scientific goals of the [SuperK](#) experiment include searches for proton decays, and studies of neutrinos from various sources: the Sun, atmosphere, supernovae, gamma-ray bursters, and other astrophysical sources, as well as artificial neutrino beams [\[146\]](#).

To reduce cosmic-ray backgrounds, [SuperK](#) is covered by more than 1 km overburden corresponding to a residual muon rate in the detector of about 2 Hz [\[27\]](#). The fiducial volume of the detector, defined as the inside region with 2 m distance from the inner detector wall, contains  $\sim 22.5$  kt water.

Via the [ES](#) reaction of neutrinos off atomic electrons (cf. Eq. [\(2.1\)](#)), [SuperK](#) detects mainly solar low energy neutrinos. The scattered relativistic charged recoil electron loses energy and is detected by the cones of optical Cherenkov light. The Cherenkov process is only a small component of the energy loss rate but is the only one that [SuperK](#) detects directly. The emitted Cherenkov light travels through the water to the  $\sim 11.000$  inward-facing 20-inch [PMTs](#) on the walls, which watch the homogenous volume of transparent water. Even though the Cherenkov light yield amounts to about 200 photons per MeV [\[149\]](#), the PMT quantum efficiency of 21% (at 360–400 nm) and the optical coverage of  $\sim 40\%$  limit the number of detected photons [\[146\]](#). Furthermore, [PMT](#) dark noise limit the current detector threshold for electrons to  $E_{\text{kin}} = 4.0$  MeV.<sup>4</sup>

---

<sup>4</sup> Due to changes in the electronics and number of active [PMTs](#), the detector threshold varied from 4.0 MeV to 6.5 MeV over the lifetime of the experiment [\[146\]](#).

Significant SuperK results include the first unambiguous evidence of neutrino oscillation in atmospheric neutrinos [152]. Moreover, it was possible to confirm the solar neutrino flux deficit with realtime observations [153]. A first measurement of the solar neutrino energy spectrum above 5 MeV was achieved, and the world's best limits on partial lifetimes for nucleon decay modes were obtained [154-156].

The even larger SuperK-Gd is the approved gadolinium-based upgrade of the SuperK detector, which is limited by backgrounds [117]. The gamma-ray that is emitted following neutron capture in the IBD reaction has an energy of 2.2 MeV and cannot be reliably detected in SuperK [157]. Gadolinium, added to the water at a concentration of 0.2%, will capture the thermalized neutrons [117]. The subsequent de-excitation of the gadolinium nuclei leads to gamma rays with a total energy of about 8 MeV, which is easily detectable in SuperK [117]. The time correlation between the positron signal and the Gd( $n, \gamma$ 's)Gd cascade signals, combined with the vertex correlation, are reliable indicators for a real IBD event. In May 2018, SuperK stopped taking physics data to start the work toward SuperK-Gd [158]. The proposed upgrade could reduce the background substantially and justifies the ongoing research and development effort [159].

### 2.1.2 IceCube

IceCube is the first ever built gigaton neutrino detector and consists of a cubic kilometer of ice instrumented with PMTs, and was completed in 2011. The neutrino detector is sensitive to atmospheric neutrinos and high energy neutrinos from astrophysical sources [160]. IceCube uses strings with PMTs deployed in the ice at the South Pole, and detect the Cherenkov light emitted by charged particles after a neutrino interaction in this naturally abundant target material. The South Pole glacial ice is 2.8 km thick and extremely clear, making neutrino telescopes of unprecedented scale and sensitivity possible [161]. The age of the ice at 2.5 km depth is  $\simeq 10^6$  y, and radioactive contaminants in the deep ice are in the range of  $\sim 10^{-12}$  g(U/Th)/g and  $\sim 10^{-9}$  g(K)/g [162].

With a Cherenkov photon yield of  $\mathcal{O}(10^5)$  visible photons per GeV of secondary particle shower energy, the long optical attenuation length of South Pole ice, and large-area PMTs, it is possible to instrument cubic kilometers of ice with a rather sparse spacing of detectors. In order to detect the Cherenkov photons emitted by charged particles traversing the ice, 5160 optical sensors are deployed between 1450 m and 2450 m depth distributed on 86 vertical strings. The primary in-ice array consists of 78 strings with a vertical separation of 17 m between the optical modules, instrumenting a total volume of one cubic kilometer of ice. This design was chosen in order to meet the primary science requirement of detecting astrophysical neutrinos in the energy range of  $\mathcal{O}(\text{TeV})$ - $\mathcal{O}(\text{PeV})$ .

Two event topologies form the standard signatures of neutrinos in IceCube. First, track-like events originate from a charged current interaction of a high energy muon neutrino with a nucleus, producing a hadronic shower at the vertex and an outgoing muon that emits Cherenkov light in a cone along its track. The second class, the cascade-like events, arise from electromagnetic or hadronic showers from interactions of all neutrino flavors, resulting in a more spherical light generation in the detector.

IceCube detected the first very high energy astrophysical neutrino flux [163]. In 2018, Ice Cube detected the first likely source of high energy neutrinos, a blazar, that was also observed with gamma rays telescopes and lower energy photons and constitute the first-ever identification of a likely source of extragalactic neutrinos and high energy cosmic rays [164].

The future IceCube Upgrade consists of seven new additional strings of photosensors, each densely instrumented with approximately 700 optical sensors, and embedded near the bottom center of the existing cubic-kilometer-scale IceCube Neutrino Observatory allowing for an improved atmospheric neutrino event selection and reconstruction at a few GeV [165]. The Upgrade will provide leading sensitivity to neutrino oscillations through the reduction of statistical uncertainties in neutrino oscillation analyses. Furthermore, it will enable IceCube to take unique measurements of tau neutrino appearance with high precision and will be the world's most stringent test on the unitarity of the PMNS matrix [165]. Furthermore, IceCube results will contribute to the determination of the neutrino mass ordering (NMO), the fundamental parameter of neutrino physics. The combination of the atmospheric oscillations using IceCube results with complementary measurements of, e.g., the reactor neutrino oscillation data from the JUNO experiment, the NMO will be precisely determined soon (see section 3.4). Finally, the Upgrade represents the first stage in the development of the future IceCube-Gen2, and is planned to be constructed in 2022/23 [165,166].

## 2.2 Liquid Scintillator Detectors

Liquid scintillators (LSs) are good targets for neutrino detection because both, the positron and the neutron produced in the interaction (cf. Eq. (2.2)) can be detected. This specific double-coincidence signature allows for robust background suppression. Some LS materials are also cheap enough to build large detectors at a reasonable cost.

When an ionizing particle travels through a substance containing aromatic compounds, like LSs, it loses energy by exciting and ionizing the molecules forming the compounds. In this process, the  $\pi$ -electrons of the aromatic compounds get excited [167].<sup>5</sup> Upon de-excitation of the excited state, a luminescence photon can be emitted, which can be detected by light detectors. The energy states of the  $\pi$ -electrons can be schematically shown in a Jablonski diagram, as depicted in Fig. 2.2 [167].  $S_0$  is the ground state, while  $S_1$ ,  $S_2$ , and  $S_3$  are the excited singlet spin-states and  $T_1$ ,  $T_2$ , and  $T_3$ , the excited triplet spin-states. Dashed lines represent the vibrational sub-levels ( $S_{00}$ ,  $S_{01}$ ,...). If the de-excitation process proceeds from a singlet or triplet state to the ground state, fluorescence or phosphorescence photons are emitted, shown respectively in green or violet in Fig. 2.2. The  $T_1 \rightarrow S_0$  transition is suppressed by the selection rules for state transitions and has, therefore, a relatively long lifetime of the order of  $\mu s$ . Thus, energy is generally dissipated by faster processes. For triplet states  $T_i$ , reverse intersystem crossing from triplet into singlet states is also possible, resulting in delayed fluorescence light. As each particle type may create a different ratio of singlet and triplet states, the characteristic scintillation pulse shapes vary with the incident particle type. This allows for pulse shape discrimination, which is explained in chapter 8 for the JUNO scintillator.

The light yield (LY) of a scintillator is typically not linear with deposited energy. The term *quenching* is used for processes that dissipate energy without photon emission. Several effects contribute to quenching in a LS and can be described with the help of the Jablonski diagram, shown in Fig. 2.2.

First, the transition responsible for the emission of fluorescence light is from the lowest excited singlet state  $S_1$  to the ground state  $S_0$ . Contrary to that is the direct excitation of the first states,  $S_1$  or  $T_1$ , suppressed by symmetry and spin arguments, respectively [168]. Therefore, the molecules are mainly excited into the higher electronic states  $S_n$  and  $T_n$  by direct excitation and ion recombination, respectively [168]. The higher excited singlets  $S_n$  degrade rapidly by internal con-

<sup>5</sup> Detailed information about the chemical structure of the LS material of the JUNO detector can be found in section 3.2

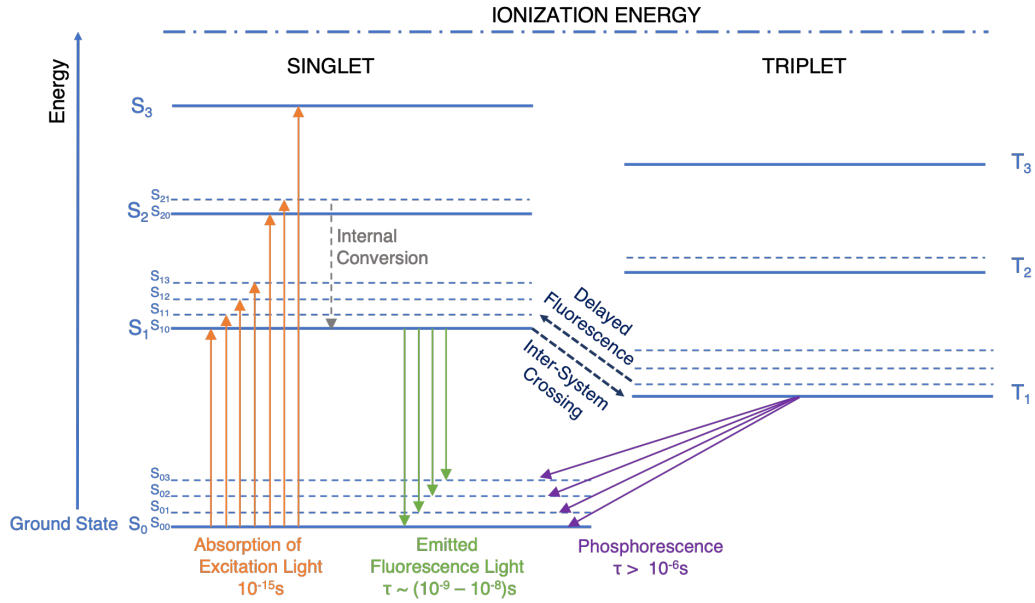


Figure 2.2: The Jablonski diagram is showing the energy levels of the  $\pi$ -electrons in an organic scintillator molecule [167].  $S_0$  is the ground state, while  $S_1$ ,  $S_2$ , and  $S_3$  are excited singlet spin-states (left) and  $T_1$ ,  $T_2$ , and  $T_3$  are the excited triplet spin-states (right). Dashed lines represent the vibrational sub-levels. Fluorescence photons are emitted by radiative de-excitation of the singlet state  $S_1$  to vibrational sub-levels of the ground state. Phosphorescence photons are emitted from the triplet state  $T_1$ .

version processes, and after several picoseconds, most excited singlets are in the  $S_1$  state [167]. Consequently, all energy that excites a scintillator molecule to an electronic or vibrational level above ( $S_{11}$ ,  $S_{12}, \dots$ ), dissipates first non-radiatively and very quickly to the lowest state via thermalization and is, therefore, undetectable [167, 169]. Hence, the maximal energy of the emitted photon is equal to the energy difference between the states  $S_{10}$  or  $T_{10}$  and  $S_{00}$  [169].

Secondly, an effect called *ionization quenching* contributes also to nonlinear behavior of the light output. This effect comes into play when the incident particle ionizes many molecules in a small region of the scintillator. These excited molecules interact with each other such that one of them reaches the ground state, leaving only one molecule to de-excite by photon emission [167]. This type of quenching is intrinsic to any scintillator.

The loss due to ionization quenching can be expressed as a function of the ionization density with a semi-empirical model described by Birks' formula [170]

$$\frac{dL}{dx} = \frac{L_0 \frac{dE}{dx}}{1 + kB \frac{dE}{dx}}, \quad (2.8)$$

with the number of photons emitted per unit path length  $\frac{dL}{dx}$ . The specific energy loss or stopping power of given scintillator material and with respect to the particle type is given by  $\frac{dE}{dx}$ , while  $L_0$  defines the absolute scintillation efficiency. The material-specific and empirically determined Birks factor  $kB$  links  $\frac{dL}{dx}$  to the differential energy deposition per unit path length  $\frac{dE}{dx}$ . The scintillator and particle type dependent Birks factor needs to be determined through measurements.<sup>6</sup> In general, the larger the energy deposition per unit path length, the higher is the ionization density, and thus, the quenching effect [173]. The absolute LY for a given deposited energy  $E_0$  is determined by [167]

$$LY(E_0) \equiv E_{\text{vis}}(E_0) = \int_0^{E_0} \frac{dL}{dx} \times \frac{dx}{dE} dE = \int_0^{E_0} \frac{L_0}{1 + kB \frac{dE}{dx}} dE, \quad (2.9)$$

where  $E_{\text{vis}}$  is the visible energy in the scintillator. Eq. (2.9) shows that for small values of  $kB$ , quenching effects can be neglected, and the relation between the deposited energy and the LY is almost linear. For heavy charged particles,  $\frac{dE}{dx}$  can be described in general with the energy-dependent Bethe-Bloch formula [174]. However, for electrons, additional effects like Bremsstrahlung and different scattering kinematics due to the small electron mass have to be considered and the Berger-Seltzer-formula accounts for these effects [174, 175]. All in all, the quenching effect has to be considered seriously in order to interpret the experimental outcome correctly. How an unknown quenching effect could influence the experimental results is exemplarily explained for the question of neutrino mass ordering in section 3.4.1.

The technology of LS detectors has been used in several experiments, e.g., in KamLAND [145], Borexino [143], Chooz [176], RENO [177] and Daya Bay [178]. An overview of their main technical parameters is given in Tab. 2.1. In the following, existing large volume LS detectors, Borexino (section 2.2.1), SNO+ [144] (section 2.2.2), and KamLAND (section 2.2.3), will be introduced separately.

<sup>6</sup> The  $kB$  value was measured to  $98 \mu\text{m}/\text{MeV}$  and  $127 \mu\text{m}/\text{MeV}$  for the JUNO scintillator and a JUNO-like LS material, respectively [171, 172].



### 2.2.1 Borexino

The Borexino experiment is built mainly to perform real-time spectroscopy of solar neutrinos. The detector is situated in the Laboratori Nazionali del Gran Sasso, an underground laboratory under the Gran Sasso mountain massif. The overburden, corresponding to  $\sim 3.8$  km.w.e., shields the laboratory effectively from cosmic radiation. The inner detector with a diameter of  $\sim 13.6$  m is encompassed by a steel dome of 18 m diameter and 16.9 m height filled with ultrapure water that acts as a **WCD** to veto muons. The transparent nylon vessel ( $\varnothing = 8.5$  m) as the detector core contains  $\sim 280$  t **LS** target and is surrounded by the buffer liquid. The **LS** is a mixture of pseudocumene and the wavelength shifter PPO. Circa 2000 **PMTs** are mounted on the inner surface of the stainless steel sphere of the inner detector to detect the light emitted by neutrino interactions in the **LS** target. To identify the cosmic muons passing through the detector,  $\sim 200$  additional **PMTs** are mounted on the outer surface and the floor to detect the emitted Cherenkov light produced in the outer **WCD**.

The primary goal of the first real-time measurement of the solar  ${}^7\text{Be}$  neutrinos was achieved in 2007, followed by a precision measurement of the solar  ${}^7\text{Be}$  neutrino flux [82,179].<sup>7</sup> A first measurement of the solar  ${}^8\text{B}$  neutrinos with 3 MeV threshold, as well as the first evidence of the solar pep neutrinos accompanied by the currently best limit on the CNO neutrino flux, was obtained [79,84]. After a purification campaign in 2010 and 2011, the reduction of the intrinsic background level allowed to accomplish the first real-time measurement of pp neutrinos generated in the low-energetic branch of the solar pp-chain [180]. Moreover, the first simultaneous spectroscopic measurement of the solar pp, pep, and  ${}^7\text{Be}$  neutrinos was performed [64]. In the future, the main effort will be centered around the CNO neutrino flux with the goal of a more stringent limit or even the first observation, which would constitute the final capstone of Borexino's rich solar neutrino program.

### 2.2.2 SNO+

The upgrade of the Sudbury Neutrino Observatory (**SNO**) experiment, the **SNO+** experiment, will have the main goal to search for the neutrinoless double  $\beta$ -decay ( $0\nu\beta\beta$ -decay) and reuses the infrastructure of the **SNO** experiment [181]. It is located in the Creighton mine near Sudbury, at SNOLAB, Canada,  $\sim 2$  km below the surface (corresponding to  $\sim 6$  km.w.e) [181]. The strategy will be to load more than a kiloton of the known double- $\beta$  isotope tellurium in a large volume **LS** detector, with a low background level, and high optical coverage. **SNO+** is sensitive also to other low energy physics and is an observatory for solar, geo, and supernova neutrinos. Detector commissioning is planned in a three-phase approach, in which the

---

<sup>7</sup> An overview of solar neutrinos can be found in section 1.4.1.



active medium is changed from water to ultra-pure scintillator, before loading the **LS** with 0.5% natural Tellurium, allowing for different physics goals. The experimental hall is filled with pure water for shielding with  $\sim 9300$  **PMTs** viewing the liquid medium, housed in a transparent spherical acrylic vessel that held 1 kt of heavy water in **SNO** and will hold 780 t of **LS** in SNO+.

The first phase began in May 2017, as a pure water Cherenkov detector allows for the characterization of the optical properties of the outer water and **PMT** response [182]. The main physics goal defined for the SNO+ water phase was the search for invisible nucleon decay of  $^{16}\text{O}$  and a measurement of the  $^8\text{B}$  solar neutrino flux [182-184].

The subsequent scintillator phase started in November 2018, where a pure **LS** detector allows to characterize the optical properties and backgrounds of the scintillator. The **LS** consists of **LAB**, as a solvent, and PPO in a concentration of 2 g/l. New measurements of lower energy signals, other solar neutrinos, or geo anti-neutrinos will become possible.

In the last, the tellurium phase, the **LS** is loaded with tellurium, and the two neutrino double  $\beta$ -decay ( $2\nu\beta\beta$ -decay) becomes the primary signal, dedicated to the  $0\nu\beta\beta$ -decay search. Tellurium was chosen due to the high natural abundance of the  $^{130}\text{Te}$  isotope ( $\sim 34\%$ ), which has a known low rate of the  $2\nu\beta\beta$ -decay ( $T_{1/2} = 8.2 \times 10^{20}$  yrs) with high endpoint energy ( $Q = 2.53$  MeV) [185]. A load of 0.5% by mass in 780 t of **LS** provides circa 1.33 t of the  $^{130}\text{Te}$  and has been shown to keep a high light yield, good transparency, and fast decay, allowing for pulse shape analysis for background discrimination [186]. This phase was planned to start at the end of 2019, and five-year data taking campaign is planned [182, 187].

### 2.2.3 KamLAND

The Kamioka Liquid-Scintillator Antineutrino Detector (**KamLAND**) has been collecting data since 2002 and was the first homogeneous large volume **LS** detector. It is located in the Kamioka mine  $\sim 1$  km under the peak of Ikenoyama mountain, providing a vertical rock overburden corresponding to  $\sim 2.7$  km.w.e [188]. 18 Japanese commercial power-stations surround the Kamioka mine and generate in total  $\sim 70$  GW power, which corresponds to  $\sim 12\%$  of the world's nuclear power-generation [145]. **KamLAND** consists of an active detector region of 1 kt of **LS** contained in a 13 m-diameter spherical balloon made of transparent nylon and supported by a network of Kevlar ropes. An array of  $\sim 1900$  **PMTs** are mounted on the inner surface of the outer containment vessel, providing 34% photocathode coverage. A 3.2 kt **WCD** instrumented with additional 225 **PMTs**, surrounds the inner **LS** detector. This outer detector absorbs  $\gamma$ -rays and neutrons from the surrounding rock and allows for muon tagging.

The primary physics goal of KamLAND is the search for the oscillation of  $\bar{\nu}_e$ 's emitted from the nearby nuclear power plants. The long-baseline of  $\sim 180$  km, enables KamLAND to address the oscillation solution of the solar neutrino problem with  $\bar{\nu}_e$ 's. KamLAND detected fewer reactor  $\bar{\nu}_e$  events than standard assumptions predicted, allows for the exclusion of all solutions to the solar neutrino problem, except for the large mixing angle region [29]. Furthermore, KamLAND gave the first evidence of the spectrum distortion in reactor neutrinos at long baselines for the first time with  $3\sigma$  confidence level [18]. Moreover, KamLAND performed the first experimental study of antineutrinos from the Earth's interior, so-called geoneutrinos, which are emitted by primordial U and Th and their daughter products [189].

# **THE JUNO DETECTOR**



## Chapter 3

# Jiangmen Underground Neutrino Observatory

The Jiangmen Underground Neutrino Observatory (JUNO) is a multipurpose neutrino oscillation experiment, currently under construction in southern China. Due to its large target mass of 20 kt liquid scintillator (LS) material, JUNO is capable of performing high statistics measurements of reactor neutrinos from the nearby nuclear power plants Taishan and Yangjiang [4]. With an unprecedented energy resolution of 3% at a visible energy of 1 MeV, it can precisely measure the energy-dependent survival probability of reactor electron antineutrinos [4].

Due to the excellent expected energy resolution and an adequate distance of the reactor complexes to the detector, JUNO is designed to determine the neutrino mass ordering (NMO) [4]. Besides, the observation of potential supernova neutrinos, the detection of the diffuse supernova neutrino background, as well as studies of atmospheric, solar, and geo-neutrinos are planned to be accomplished with this detector. Furthermore, JUNO can precisely measure neutrino oscillation parameters and is going to improve the precision on  $\Delta m_{21}^2$ ,  $\Delta m_{32}^2$ , and  $\sin^2 \theta_{12}$  [4]. The detector concept, as well as the LS characteristics, are described in section 3.1 and section 3.2, respectively. A short overview of the detector simulation can be found in section 3.3. Besides, a detailed summary of the physics program is given in section 3.4.

### 3.1 Detector Concept

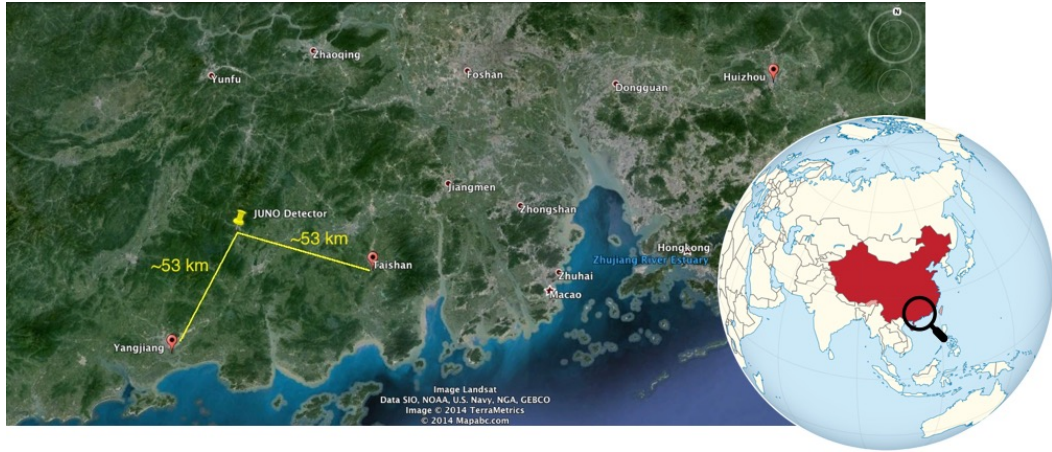


Figure 3.1: Experimental site of the **JUNO** experiment [190], located in southern China, west of Hongkong. The yellow pin represents the position of the detector, while the red pins represent the reactor complexes Yangjian and Taishan.

The **JUNO** experiment is located in Jiangmen, Kaiping, Guangdong province, in southern China, as shown in Fig. 3.1. It is positioned at a distance of  $\sim 53$  km from the two nuclear power plants (**NPPs**), Yangjian and Taishan. The Yangjian **NPP** is the largest nuclear power station in China, including six reactor cores, with 2.9 GW thermal power each [4]. The Taishan **NPP** is planned to have four reactor cores, each providing thermal power of 4.6 GW.<sup>1</sup> There is no other **NPP** within 200 km. The Daya Bay **NPP**, with 17.4 GW of total power, is  $\sim 215$  km away from the **JUNO** site and is expected to contribute  $\sim 3\%$  to the reactor electron antineutrino ( $\bar{\nu}_e$ ) events [4]. Further, the **NPPs** Huizhou and the proposed Lufeng, do not play a disturbing role, with a distance of 265 km and more than 300 km from the detector, respectively [4].

To suppress muon-induced backgrounds, the detector will be located deep underground, and a 270 m high granite mountain provides proper shielding of cosmic muons, a primary background source. With a total overburden of 650 m, the expected muon rate is reduced to  $\sim 3.5$  Hz for the central detector [192].<sup>2</sup>

<sup>1</sup> It is possible that two of the Taishan cores are not yet operational at the time when **JUNO** will start data taking [191]. This would reduce the total thermal power by  $\sim 25\%$ .

<sup>2</sup> In [4], the expected muon rate was quoted with  $\sim 3.0$  Hz. However, a change in location of the experimental hall results in a  $\sim 30$  m higher position with  $\sim 50$  m less overburden, and therefore in an enhanced muon flux.

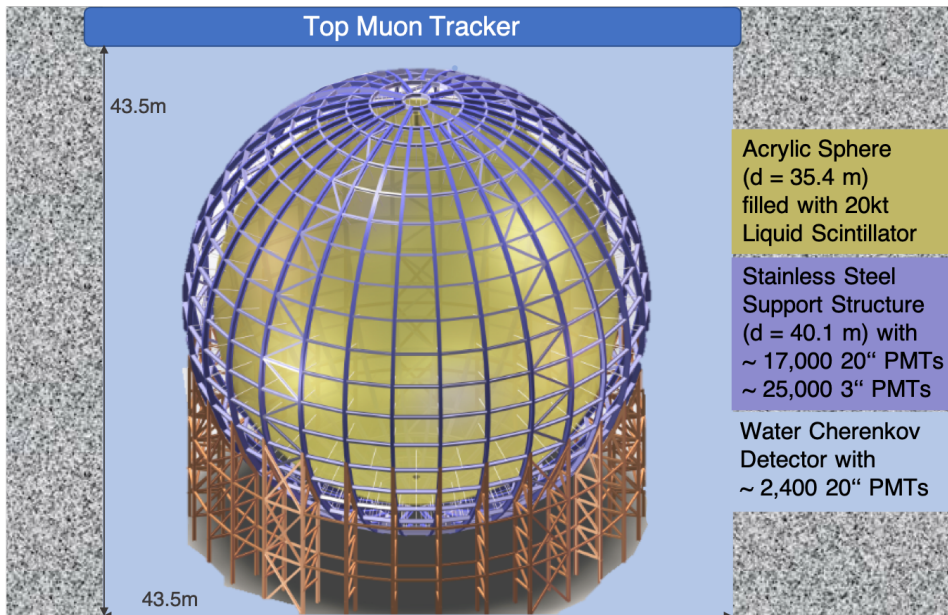


Figure 3.2: The proposed detector concept of **JUNO**, built underground within rock shielding. The **LAB**-based **LS** is in the acrylic sphere (yellow), which is fixed with struts in a stainless steel truss (violet), where the **PMTs** are mounted. Outside the acrylic sphere is a cylindrical water pool (light blue) as well as a top muon tracker (dark blue) placed above the central detector and the outer **WCD**.

The central detector concept, which is depicted in Fig. 3.2, consists of a spherical tank submerged in a water pool. The inner acrylic sphere, with a diameter of 35.4 m, is filled with 20 kt linear alkylbenzene (**LAB**)-based **LS** and is positioned in a stainless steel supporting structure, with a diameter of 40.1 m, where additionally the photomultiplier tubes (**PMTs**) are mounted. Therefore, the radial distance between the detector center and the photocathode of the **PMTs** is  $\sim 19.3$  m. About 17,000 20" **PMTs** are used to achieve an optical coverage of at least 75%, composed of  $\sim 12,000$  micro-channel plate **PMTs** and  $\sim 5,000$  Hamamatsu R12860 **PMTs** [193]. Additionally, about 25,000 3" **PMTs** are planned to be used alongside the large ones, in order to serve as a second calorimetric system [194]. Furthermore, technological advances allow the quantum efficiency of the photocathode to reach  $\sim 35\%$  [193]. The outer cylindrical water tank protects the central detector from radioactive background from the surrounding rock. After being equipped with additional 2400 20" **PMTs**, the water Cherenkov detector serves as an efficient muon veto.

Supplementary, there is a second muon tracking detector, composed of plastic scintillator strips from the decommissioned OPERA experiment [195]. The top tracker with an area of  $\sim 20 \times 47 \text{ m}^2$  is placed above the central detector and outer WCD. It covers 60% of the water pool top area to enhance muon identification efficiency and provide precise muon tracking to reach the expected muon detection efficiency of 99.8% [4, 196].

The experiment construction is scheduled to be completed in 2021, including also a tunnel, an underground experiment hall, a water pool, and some ancillary facilities. The detector construction and final cleaning will be completed end of 2021, and the start of data taking is scheduled for 2022.

The advantage of the JUNO experiment is the combination of a vast target mass with an excellent energy resolution of  $\sim 3\%$  at a visible energy deposition of 1 MeV. As the PMTs collect the light from particle interactions, the energy is in first order proportional to the number of collected photoelectrons. The photoelectron statistics dominate the error  $\sigma$  of a scintillator detector, hence

$$\frac{\sigma}{E_{\text{vis}}} \propto \frac{1}{\sqrt{n_{pe}}}. \quad (3.1)$$

As  $3\%/\sqrt{\text{MeV}}$  energy resolution is a mandatory requirement to answer the question of the neutrino mass ordering (NMO) (see section 3.4), the design goal for the photoelectron yield is  $\gtrsim 1100 \text{ p.e./MeV}$ , which represents a significant improvement compared to the state of the art detectors (compare Tab. 2.1 [142]). To reach this unrivaled energy resolution, high optical coverage ( $\sim 75\%$ ), highly efficient PMTs ( $\sim 35\%$ ), and a highly transparent LS with a long attenuation length ( $> 20 \text{ m}$ ) are required. The reduction of photons that reach the PMTs can be approximated by the factor  $\exp(-R/L)$ , with the detector radius  $R$  and  $L$  as the attenuation length. With a light yield of LAB of  $\sim 10400 \gamma/\text{MeV}$ , the photoelectron yield can be approximated by

$$10400 \gamma/\text{MeV} \times 0.75 \times 0.35 \text{ p.e./}\gamma \times \exp\left(-\frac{17.7 \text{ m}}{20 \text{ m}}\right) \simeq 1100 \text{ p.e./MeV}, \quad (3.2)$$

where 17.7 m is the radius of the LS vessel [4]. This short calculation motivates the above-mentioned detector characteristics, that were chosen in order to fulfill the NMO energy resolution condition.



### 3.2 Liquid Scintillator

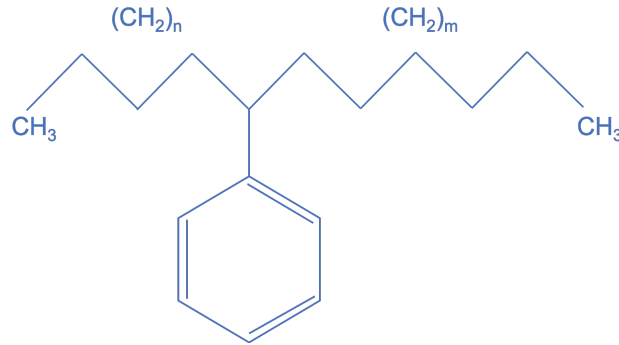


Figure 3.3: Chemical structure of linear alkylbenzene. A benzene ring is attached to a linear alkyl chain.

The liquid scintillator (LS) solvent linear alkylbenzene (LAB) will serve as the detector target in JUNO. It is chosen due to its good transparency, high flash point, low chemical reactivity, and excellent light yield. The solvent LAB refers to several scintillator compounds, that generally share the same structure formula, but vary in the length of the carbon chain. It is a mixture of hydrocarbons, consisting of a linear alkyl chain of 10–13 carbon atoms, attached to a benzene ring. The chemical formula can be written as

$$\text{C}_9\text{H}_{12}(\text{CH}_2)_{n+m}, \quad (3.3)$$

with  $n + m$  between 7 and 10 and is schematically shown in Fig. 3.3 [197]. The mass weighted composition of JUNO's LS is listed in Tab. 3.1, with the number of atoms and protons per kiloton of scintillating material. LAB is liquid at room temperature having a density of  $\rho = 0.856 \text{ g/cm}^3$  and a refractive index of  $n = 1.54$  [4]. Particles, which deposit their energy by interaction in the LS volume, excite the LAB molecules (compare section 2.2). The following emission of light at a wavelength of 283 nm is very close to the LAB's absorption maximum at 260 nm [197]. Hence, scintillation light from pure LAB would be strongly affected by self-absorption. Therefore, two solutes will be added to the scintillator in order to improve the transmittance. The two wavelength shifters, PPO<sup>3</sup> and bis-MSB<sup>4</sup>, will transform the emitted light to a wavelength of  $\sim 420 \text{ nm}$ , with a contribution of 3 g/l and 15 mg/l, respectively [4, 197]. As this wavelength is subject to less reabsorption, the light can traverse the detector volume.

<sup>3</sup> 2,5-diphenyloxazole

<sup>4</sup> p-bis-(o-methylstyryl)-benzene

	mass fraction [%]	atoms [kt <sup>-1</sup> ]	protons [kt <sup>-1</sup> ]
<sup>1</sup> H	12.010	$7.16 \times 10^{31}$	$7.16 \times 10^{31}$
<sup>12</sup> C	87.924	$4.41 \times 10^{31}$	$2.65 \times 10^{32}$
<sup>14</sup> N	0.027	$1.16 \times 10^{28}$	$1.62 \times 10^{29}$
<sup>16</sup> O	0.034	$1.28 \times 10^{28}$	$2.05 \times 10^{29}$
<sup>32</sup> S	0.005	$9.36 \times 10^{26}$	$3.00 \times 10^{28}$

Table 3.1: The number of target atoms and protons for the **JUNO** scintillator [4]. Note that protons from hydrogen are "free" protons, whereas protons from the other nuclei are bound protons.

To ensure that enough produced light can reach the **PMTs**, a high optical transparency of the scintillator material is crucial. If light traverses through a medium, it is attenuated by scattering and absorption processes. For the case that multiple scattering is negligible, the intensity of a light beam traveling a distance  $x$  through a medium is attenuated exponentially, with [198]

$$I(x) = I_0 \exp\left(-\frac{x}{\Lambda}\right). \quad (3.4)$$

The attenuation length  $\Lambda$  is quantified as the distance over which the light intensity is reduced to a fraction of  $1/e$  [199]. The attenuation is due to two kinds of processes: light absorption on organic impurities, in which case the photon can either be fully absorbed and potentially re-emitted, and light scattering of the solvent molecules [200]

$$\frac{1}{\Lambda} = \frac{1}{\Lambda_{\text{absorption}}} + \frac{1}{\Lambda_{\text{scattering}}}. \quad (3.5)$$

The attenuation length has to be at least of the order of the detector radius. For a **LS** medium, absorption processes convert the scintillation light into heat or re-emitted photons, whereas scattering changes the direction of the produced photons within the medium. This leads to the fact that absorption processes have to be suppressed, and the **LS** material has to be cleaned in several steps to improve the optical transparency of the scintillator solvent. Besides aluminum oxide column purification, distillation, water extraction, and nitrogen stripping purification techniques are proposed [193].<sup>5</sup> The Rayleigh scattering length was measured with  $(27.0 \pm 2.3)$  m [200]. Based on the measured attenuation length of  $\sim 20$  m [201], an

<sup>5</sup> Different purification techniques are explained in more detail in [201].

absorption length of  $\sim 77$  m is obtained, which warrants excellent detector performance and allows for a rich physics program for the **JUNO** detector within the next years [201].

### 3.3 Detector Simulation

In the present thesis, the potential for JUNO to detect the diffuse supernova neutrino background is studied using a detector simulation. Therefore a short introduction into the simulation framework of JUNO is given. The signal and background events were simulated with the JUNO full detector Monte-Carlo simulation based on Geant4 (Version 9.4.p4), in the following called JUNO's Offline Simulation Framework (JOSF) [202-205].

The JOSF is a serial simulation framework, based on SNIPEr (Software for Non-collider Physics Experiment) and composes a full chain of data processing, visualized in Fig. 3.4 [206,207]. JOSF is composed of SNIPEr plugin components, with dependencies on external packages. First, the physics generators produce kinematic information of the primary particles. In the subsequent step, the detector simulation algorithm starts tracking of these particles.<sup>6</sup> Here, the hits of the photons on the PMT photocathode, containing charge and time information, are generated. Within the simulation, also quantum efficiencies of the PMTs are considered. After that, the electronics simulation algorithm performs the digitization, containing waveforms information. These waveforms are processed by the PMT calibration algorithm to calibrate charge and time for each PMT. Afterward, reconstruction algorithms are used to perform event reconstruction. Lastly, physics analysis becomes possible, and the reliable Monte-Carlo simulation software plays an essential role in detector parameter optimization and physics studies [207].

In the present thesis, the signal, as well as the background sources, are simulated within the JOSF version J18v1r1.

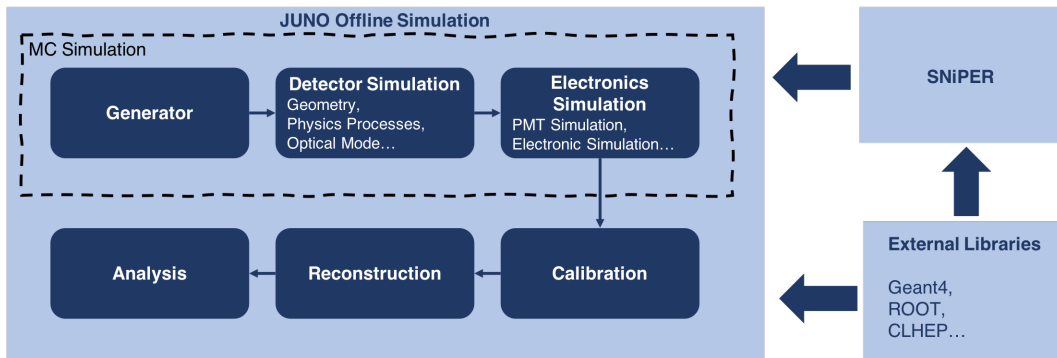


Figure 3.4: The serial simulation framework implemented to perform physics analysis for the JUNO detector [207].

<sup>6</sup> The absorption and Rayleigh scattering length was set to 77 m and 27 m, respectively, to obtain an attenuation length of 20 m, as discussed in previous section.

## 3.4 Physics Potential

With the future JUNO experiment, a broad physics program is achievable within the next years. Besides the primary goal of determine the neutrino mass ordering (section 3.4.1), solar (section 3.4.3), supernova (section 3.4.4), and geo-neutrino (section 3.4.5) measurements are discussed in the next sections. Furthermore, neutrino measurements within JUNO will allow to constrain some of the neutrino oscillation parameters further (section 3.4.2). Moreover, also the possibility to study the presence of sterile neutrinos (section 3.4.6), proton decay (section 3.4.7), and dark matter (section 3.4.8) will be part of the following sections. As the central part of this thesis is a feasibility study of observing the diffuse supernova neutrino background (DSNB), the DSNB signal in JUNO will be explained separately in chapter 4.

### 3.4.1 Neutrino Mass Ordering

The oscillated reactor  $\bar{\nu}_e$  event spectrum measured by the JUNO detector is the product of the initial  $\bar{\nu}_e$  flux spectrum, the inverse  $\beta$ -decay (IBD) cross-section and the oscillation probability  $P(E_\nu, L)$ :

$$\frac{dN_\nu}{dE_\nu} = \frac{d\Phi_\nu}{dE_\nu} \times \sigma_\nu(E_\nu) \times P_{\bar{\nu}_e \rightarrow \bar{\nu}_e}(E_\nu, L) \times N_p, \quad (3.6)$$

with the number of protons in the target volume  $N_p$ , following Tab. 3.1 [141]. The oscillation probability is given in section 1.2.1. The measured reactor  $\bar{\nu}_e$  spectrum for JUNO calculated with the oscillation parameters presented in Tab. 1.1 is shown as a function of the neutrino energy in Fig. 3.5. Both possibilities for the neutrino mass ordering (NMO) are compared: the normal ordering (NO) (blue) and the inverted ordering (IO) (orange). Please note that no detector response function, e.g., detector resolution, is inserted. The ability to resolve the position of the minima and maxima will provide the NMO determination within JUNO [4]. JUNO's goal is the identification of the NMO at a confidence level of 3–4  $\sigma$  after six years of data taking [193].

Three main types of systematics could influence this measurement. First, the uncertainty on the large mass differences  $\Delta m_{31}^2$  and  $\Delta m_{32}^2$  strongly affect the survival probability, as it will influence the primary oscillation frequency and hence, the ability to resolve the effect of the NMO.<sup>7</sup>

Second, an (unknown) uncertainty in the detector energy response would influence the interpretation of the experiment, as, e.g., a shift of the energy scale has

<sup>7</sup> The actual uncertainty on  $|\Delta m_{32}^2|$  is  $\sim 2\%$ . The reader is referred to the next section 3.4.2 for discussion of this topic.

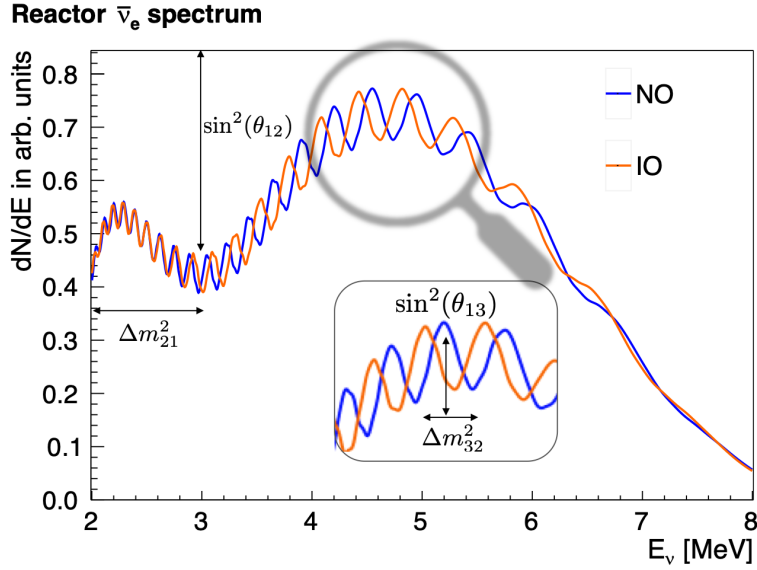


Figure 3.5: Reactor neutrino spectrum for **JUNO** without detector resolution for normal (blue) and inverted (orange) ordering. The aim of **JUNO** is to resolve the position of the maxima and minima, which actually are determined by the **NMO**

the same effect as a change in  $\Delta m_{31}^2$ . This shift could stem from quenching effects (introduced in section 2.2). An illustration of this effect is given in Fig. 3.6, where the reactor  $\bar{\nu}_e$  spectrum is plotted for two values that characterize the strength of the quenching effect, the  $kB$  parameter (compare Eq. (2.8)). The  $kB$  parameter was set to  $kB = (0.980 \pm 0.078) \times 10^{-7}$  m/MeV and  $kB = 2.00 \times 10^{-7}$  m/MeV. While a measurement motivates the first value for  $kB$ , the second value was chosen large enough to demonstrate the impact of an uncertainty of this parameter [171]. Furthermore, both orderings: the **NO** and **IO** are compared. Fig. 3.6 illustrates how an unknown non-linearity could significantly influence the interpretation of the spectral measurement in connection with the **NMO** determination. At  $\sim 5$  MeV, an overlay of the solid blue curve with the red dashed curve is present, which represents different orderings and could lead to a misinterpretation if the non-linearity is not precisely known. Therefore, several measurements are ongoing to investigate the non-linearity of the **LS** [171, 208].

Lastly, an unprecise knowledge on the reactor  $\bar{\nu}_e$  flux spectrum will influence the **NMO** measurement as well. Since one is searching for frequencies in the Fourier spectrum, any unknown high-frequency components in the flux can lead to misinterpretations. Neutrino reactor fluxes have a microstructure at the 50 keV level, which is similar to the **NMO** signal in **JUNO** [209]. This uncertainty arises, as

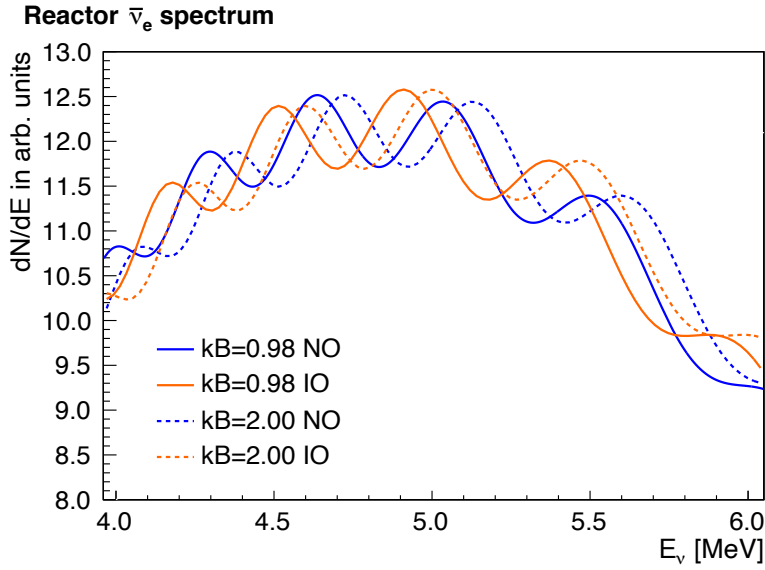


Figure 3.6: Reactor neutrino spectrum for two different  $kB$  parameters:  $kB = 0.98 \times 10^{-7} \text{ m/MeV}$  (solid) and  $kB = 2.00 \times 10^{-7} \text{ m/MeV}$  (dashed) and normal ordering (blue) and inverted ordering (orange) in the most sensitive energy region. An energy resolution of 3% is also included.

antineutrinos from reactors are produced in the  $\beta$ -decays of neutron-rich fission products. There are  $\sim 100$  isotopes with  $\sim 100$  individual  $\beta$ -decay branches, which would have to be known with reasonable accuracy to compute the antineutrino flux with percent level precision. Therefore measurements of the total  $\beta$ -decay spectrum from fission fragments are used to reconstruct the antineutrino spectrum [210–212]. A priori calculations account for about 80–90% of all  $\beta$ -decays and, thus, reproduce the total  $\beta$ -spectrum as measured to about the same degree [213]. This problem can be resolved entirely by using a second reference reactor  $\bar{\nu}_e$  spectrum measured with at least similar energy resolution. The sensitivity may improve beyond the original one since all flux uncertainties are eliminated [214].

The proposed Taishan Antineutrino Observatory (TAO) detector is planned to be a 2.6 t (1 t fiducial) volume Gd-loaded LS detector placed  $\sim 30$  m from a 4.6 GW Taishan reactor core, which ensures  $\sim 30$  times the JUNO event rate [214, 215]. With the desired energy resolution of  $\sim 1.5\%$  at 1 MeV, the reference detector TAO should be able to look for fine structures in the reactor energy spectrum.

Besides the existing systematics of this measurement, background events, that are mimicking the **IBD** coincidence signature arise and should be considered for the determination of the **NMO**. These are mainly accidental coincidences, cosmogenically produced  $^8\text{He}$  and  $^9\text{Li}$  (described in section 7.1), fast neutrons (described in section 7.2),  $^{13}\text{C}(\alpha,n)^{16}\text{O}$  reactions, and geoneutrinos. In order to suppress background, the temporal and spatial cuts between the prompt  $\bar{\nu}_e$  signal and a delayed signal neutron capture must be tuned. The detector volume around a muon track should be vetoed for several lifetimes of the neutron unstable cosmogenic radioisotopes. After the application of such cuts,  $\sim 60$  **IBD** events per day, of which  $\sim 4$  are caused by backgrounds, are expected in **JUNO** [4].

Due to the broad range of neutrino experiments, some neutrino oscillation parameters can be determined by several measurements. Therefore, combined analyses can give access to the full information on neutrino oscillation parameters. In the case of the **NMO**, there is the possibility of combining **JUNO** with the atmospheric neutrino oscillation experiment IceCube (cf. section 2.1.2). Especially through the combination of complementary measurements the **NMO** will be precisely determined even sooner [216]. While **JUNO** aims for a careful investigation of the energy spectrum of oscillated  $\bar{\nu}_e$  produced by nuclear reactor cores, the IceCube array will observe large numbers of atmospheric neutrinos that have undergone oscillations impacted by Earth matter effects. Their neutrino source, reactor vs. atmospheric neutrinos, as well as their energy range, MeV vs. GeV, differ. Moreover, the oscillation effects are entirely complementary, sub-dominant vacuum oscillations vs. matter-induced differences in the oscillation patterns, for **JUNO** and IceCube, respectively. The different  $\Delta m_{31}^2$  dependencies of the **NMO** measurements by **JUNO** and IceCube constitute the most pronounced synergy effect of their combined analysis. Due to the different positions of the minimum  $\chi^2$ -values in the oscillation parameter space within the wrong ordering, the combined analysis achieves a better sensitivity than the purely statistical combination of the sensitivity from the two experiments, as depicted in Fig. 3.7 [217].

Depending on the detector configurations, the combined analysis will reach a median **NMO** sensitivity of  $5\sigma$  within less than two years of joint lifetime [217]. Even if **JUNO** has no more than eight (instead of the ten nominally expected) reactor cores available and the less instrumented IceCube Upgrade is assumed, the resulting combined analysis exceeds a significance of  $5\sigma$  in 3–5 years of the lifetime of both detectors [217].



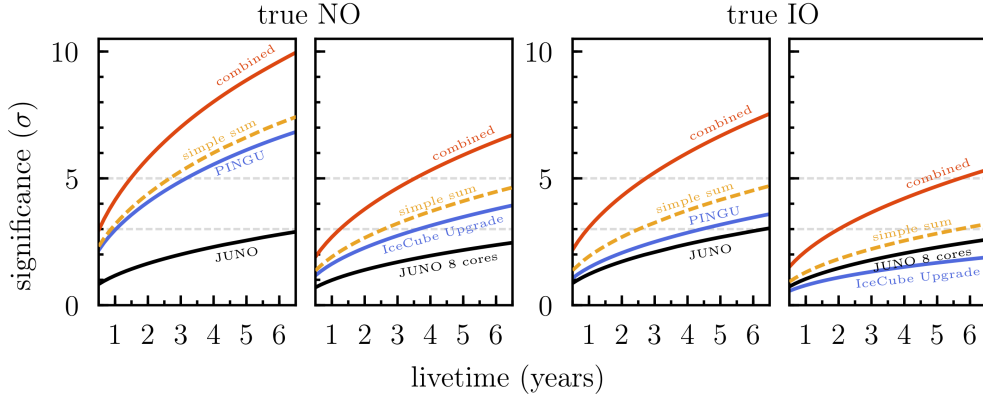


Figure 3.7: Lifetime evolution of the **NMO** sensitivity of the individual experiments and their (statistical and full) combination, assuming the parallel start of data taking. The results from the stand-alone (blue and black line) are compared to the simple (quadratic) sum (yellow dashed), and the combinational result (red). Results for the PINGU and nominal JUNO configuration are shown with the IceCube Upgrade and the 8-reactor-core **JUNO** configuration. The left panels assume true **NO**, while the right panels corresponding to assumed true **IO**. Figure from [217].

### 3.4.2 Determination of Oscillation Parameters

Additionally, the excellent energy resolution of the **JUNO** detector allows to improve the precision of some neutrino mixing parameters significantly. The observed energy spectrum allows access to the three oscillations parameters:  $\theta_{12}$ ,  $\Delta m_{21}^2$ , and  $|\Delta m_{32}^2|$  to a sub-percent level (cf. Fig. 3.5) [193]. The expected precisions of mixing

Parameter	Experiment	Individual $1\sigma$	Global $1\sigma$	JUNO
$\Delta m_{21}^2$	KamLAND [50]	$\sim 2.5\%$	$\sim 2.4\%$	$\sim 0.6\%$
$ \Delta m_{32}^2 $	Daya Bay [218]	$\sim 2.8\%$	$\sim 2\%$	$\sim 0.5\%$ and sign
$\sin^2(\theta_{12})$	SK [49]	$\sim 8\%$	$\sim 4.2\%$	$\sim 0.7\%$
$\sin^2(\theta_{23})$	T2K [219]	$\sim 6.8\%$	$\sim 5\%$	N/A
$\sin^2(\theta_{13})$	Daya Bay [218]	$\sim 3.5\%$	$\sim 3.2\%$	$\sim 15\%$

Table 3.2: Expected precision of mixing parameters achieved by **JUNO** in comparison to the current precision, including systematic and statistical uncertainties [10, 142, 220]. The experiments with the main contribution to the individual parameters are listed.

parameters for JUNO are listed in Tab. 3.2<sup>8</sup>. The accuracy of the JUNO detector will not be competitive regarding  $\theta_{13}$ , as it will not improve the Daya Bay achieved precision [51, 193]. Together with the expected Daya Bay experiment results on  $\theta_{13}$  (better than  $\sim 4\%$ ), the unitarity of the neutrino mixing matrix can be tested at the 1% level [220]. Any deviation from unitarity is considered to be a hint towards new physics, such as the existence of more than three light neutrinos [221]. Even in the framework of only three light neutrinos, extensions of the Standard Model, that are postulated in order to generate the observed small neutrino masses, typically produce a leptonic mixing matrix that is non-unitary [221].

### 3.4.3 Solar Neutrinos

The JUNO detector may also study neutrinos originating from the Sun (cf. section 1.4.1). With its large target mass, JUNO could provide a high statistics measurement of the solar higher energetic  $^8\text{B}$  neutrinos via the elastic scattering channel. However, a successful measurement, especially of lower-energetic solar neutrinos, strongly depends on the actual intrinsic background level [4]. Furthermore, the relatively high rate of cosmic muons of  $\sim 3.5\text{ Hz}$  worsens the solar neutrino measurements [192]. Based on the same purity as reached in the KamLAND experiment [188], a signal to background ratio of  $\sim 3 : 1$  is expected for JUNO, allowing only for a  $^7\text{Be}$  neutrino measurement at lower energies [4]. Fig. 3.8 shows the expected solar neutrino spectra for  $^7\text{Be}$ , pep, and pp neutrinos (red) and  $^{13}\text{N}$ ,  $^{15}\text{O}$ , and  $^{17}\text{F}$  neutrino spectra (grey). Besides, radioactive and cosmogenic background sources are shown.

Although, a  $^7\text{Be}$  neutrino measurement is still challenging since especially the  $^{210}\text{Bi}$  background (pink) needs to be determined precisely. Also, the radioactive decay decays of  $^{85}\text{Kr}$  (yellow),  $^{238}\text{U}$  (violet), and  $^{40}\text{K}$  (dark blue) contribute non-negligibly in the energy range between 0.2 MeV and 0.7 MeV. Despite the comparably high rate of cosmic muons, cosmogenic  $^{11}\text{C}$  (turquoise) does not affect the measurement since the minimum energy deposition is 1.022 MeV that can be well separated from the  $^7\text{Be}$  neutrinos with a maximum visible energy of 665 keV. If JUNO could reach a purity level similar to that of Borexino phase I, also pp neutrinos could potentially be observed [4, 222].<sup>9</sup> In this case, the  $^{210}\text{Bi}$  background would be small enough that the pp neutrino flux dominates the energy spectrum between  $\sim 160\text{ keV}$  and 230 keV. The separation from the overwhelming  $^{14}\text{C}$  background that goes up to  $\sim 156\text{ keV}$  is only possible due to the excellent resolution of the JUNO detector. Nevertheless, a good pulse shape discrimination of highly quenched  $\alpha$ -particles,

<sup>8</sup> Current values of oscillation parameters can be found in Tab. 1.1.

<sup>9</sup> Solar neutrino spectra with radioactive background for this scenario can be found in the appendix in Fig. A.1.

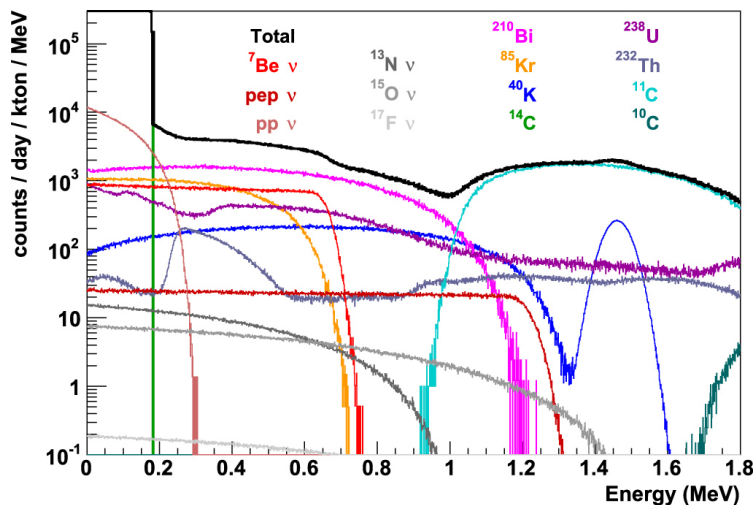


Figure 3.8: The expected solar neutrino spectra in [JUNO](#) with radio-purity assumption from the [KamLAND](#) experiment [\[188\]](#). Even if the  ${}^7\text{Be}$  neutrino flux is below the  ${}^{210}\text{Bi}$  background level, the  ${}^7\text{Be}$  shoulder is still visible in the spectrum at 665 keV. Figure from [\[4\]](#).

clean removal of pile-up events, and a good understanding of low-energetic noise are still mandatory but challenging. The observations of solar pep and CNO neutrinos are supposed to be extremely difficult with the [JUNO](#) detector since the  ${}^{210}\text{Bi}$  decays at low energies and the cosmogenic  ${}^{11}\text{C}$  decays at high energies are expected to overwhelm these neutrino signals entirely [\[4\]](#).

Besides the mentioned prospects for low-energetic solar neutrinos, [JUNO](#) will be able to measure the higher energetic  ${}^8\text{B}$  neutrino flux with unprecedented energy resolution and even with a lower energy threshold compared to previous measurements [\[4\]](#). For the high-energy  ${}^8\text{B}$  neutrinos, with an endpoint at  $\sim 15$  MeV, the decay of  ${}^{208}\text{Tl}$  with a Q-value of 5 MeV causes the main component of the intrinsic background for this measurement. While this background can, in principle, be estimated via the coincidence of  ${}^{212}\text{Bi}$ - ${}^{212}\text{Po}$  decays, it is still mandatory to keep the internal  ${}^{232}\text{Th}$  contamination at a level below  $10^{-17}$  g/g to enable an analysis threshold significantly smaller than 5 MeV. The dominant external background will arise from the 2.6 MeV  $\gamma$ -rays of  ${}^{208}\text{Tl}$  decays in the photomultiplier tubes. However, this background may be efficiently reduced by applying a fiducial volume cut. Above 5 MeV, the most relevant background sources are cosmogenic radioisotopes such as  ${}^8\text{Li}$ ,  ${}^{16}\text{N}$ , and  ${}^{11}\text{Be}$  [\[4\]](#). If muon identification and tracking will be possible, the shorter-lived isotopes may be suppressed by vetoing a specific volume

around a muon track. Contrary, the spectra, and rates of the longer-lived isotopes have to be measured accurately and subtracted from the accumulated data. Besides the elastic scattering channel, also the  $\nu_e + {}^{13}\text{C} \rightarrow e^- + {}^{13}\text{N}$  reaction with a threshold of 2.2 MeV may be used to study the solar  ${}^8\text{B}$  neutrino flux [142]. With a high statistics  ${}^8\text{B}$  neutrino measurement, the JUNO experiment could explore the transition region between the vacuum and matter-dominated oscillation regimes and probe the MSW-LMA solution. As mentioned in section 1.2.2, probing the survival probability in this energy region allows investigating many potential hints of new physics.

### 3.4.4 Supernova Burst Neutrinos

As introduced in section 1.4.3, an immense burst of (anti-)neutrinos of all three flavors accompanies the core collapse of massive stars. These neutrinos carry valuable information on the environment in which they have been produced and allow to approach many characteristic properties of these particles themselves. With its large target mass, JUNO may acquire a high statistics measurement of neutrinos originating from a near supernova (SN).

Tab. 3.3 lists the expected number of SN neutrino interactions dependent on the detection channels, for a hypothetical "typical" core-collapse supernova at a distance of 10 kpc and assuming a mean neutrino energy of  $\langle E_\nu \rangle = 14 \text{ MeV}$  [4]. Within 10 s, approximately 5000  $\bar{\nu}_e$  events are expected to be detected via IBD, which serves as the primary detection channel. Neutral current (NC) neutrino-proton elastic scattering (ES) will contribute to additional  $\sim 1200$  events. More than 300 events are expected to be caused by ES on electrons, which represents the most potent channel for extracting the direction of a potential SN [4]. Contrary, the separation between

Detection Channel	Events
$\bar{\nu}_e + p \longrightarrow e^+ + n$	$\sim 5000$
$\nu_x + p \longrightarrow \nu_x + p$	$\sim 1200$
$\nu_x + e^- \longrightarrow \nu_x + e^-$	$\sim 360$
$\nu_x + {}^{12}\text{C} \longrightarrow \nu_x + {}^{12}\text{C}$	$\sim 320$
$\bar{\nu}_e + {}^{12}\text{C} \longrightarrow e^+ + {}^{12}\text{B}$	$\sim 110$
$\nu_e + {}^{12}\text{C} \longrightarrow e^- + {}^{12}\text{N}$	$\sim 90$

Table 3.3: Expected neutrino signal in JUNO, for the main detection channels of neutrinos produced by a core-collapse supernova at a distance of 10 kpc. A mean neutrino energy of  $\langle E_\nu \rangle = 14 \text{ MeV}$  is assumed [4].

the prompt and the delayed signal of the 5000 [IBD](#) reactions allows only for the statistical determination of the direction of the incoming neutrinos, reaching an accuracy of  $\sim 9^\circ$  [\[4\]](#). Additionally,  $\sim 500$  events caused by neutrinos interacting with  $^{12}\text{C}$  in the scintillator are possible [\[4\]](#).

By measuring the time evolution of the neutrino signal, the energy spectrum, and the flavor composition, the neutrino-driven explosion mechanism, described in section [1.4.3](#), may be probed. Also, a possible correlation between the [SN](#) neutrino signal and a gravitational wave signal may be investigated and could be used to combine the complementary information of both signals. Further, information on the [SN](#) nucleosynthesis may be gained by extracting the time-averaged spectra of different neutrino emission channels through the detection and identification of significant numbers of neutrinos of different flavors. Besides these astrophysical implications, the detection of [SN](#) neutrinos would give significant insights into the properties of the neutrino as a particle itself. Thus, the time delay between arriving neutrinos may be used to extract a bound on the absolute neutrino mass scale, and the estimated statistics are, in principle, sufficient to investigate the neutrino mass ordering through the shape of the  $\bar{\nu}_e$  spectrum [\[4\]](#).

### 3.4.5 Geoneutrinos

An interdisciplinary topic of interest for geology is the study of geoneutrinos. They are produced by  $\beta$ -decays of radioactive isotopes of the  $^{238}\text{U}$ ,  $^{232}\text{Th}$  chains and  $^{40}\text{K}$  naturally abundant in the Earth. A fraction of antineutrinos from  $^{232}\text{Th}$  decay chain with end-points energies of 2.1 MeV ( $^{228}\text{Ac}$ ) and 2.3 MeV ( $^{212}\text{Bi}$ ) and those from  $^{238}\text{U}$  with end-points 1.9, 2.7, and 3.3 MeV ( $^{214}\text{Bi}$ ) and 2.2 MeV ( $^{234}\text{Pa}^m$ ) will be detectable via the [IBD](#) in [JUNO](#) [\[223\]](#).<sup>10</sup> The geoneutrino flux and the radiogenic heat, released during radioactive decays, are given in a well-fixed ratio [\[223\]](#). Hence, the observation of these  $\bar{\nu}_e$ 's and the determination of the contribution of radioactive heat to the total thermal power of the Earth allows to extract information on the Earth's composition [\[224\]](#). Therefore, discrimination between different geo-dynamical models that give an insight into the structure of the mantle and the nature of mantle convection becomes possible [\[223\]](#). So far, geoneutrinos were first observed in 2005 by the [KamLAND](#) and later also by the Borexino experiment [\[189, 225\]](#). Due to its enormous target mass, the [JUNO](#) detector should detect  $\sim 400$  events caused by geoneutrinos only during the first year of data taking. Even though the reactor  $\bar{\nu}_e$  flux immensely overpowers the geoneutrino signal in [JUNO](#), an observation is expected to be feasible through precise knowledge of the reactor neutrino spectrum. Thus, after approximately six months, [JUNO](#) would match the present world sample of recorded geoneutrino interactions [\[4\]](#).

<sup>10</sup> The geoneutrinos produced in the  $^{40}\text{K}$  decays cannot be detected, as the end-point ( $\sim 1.3$  MeV) of their energy spectrum is below the threshold of the [IBD](#) reaction ( $\sim 1.8$  MeV).

### 3.4.6 Sterile Neutrinos

Results from the Large Electron-Positron Collider on the decay width of the  $Z^0$ -boson show that there are only three species of light neutrinos coupling to the  $Z^0$  [37]. Therefore, a hypothesized fourth neutrino flavor must be a sterile neutrino without direct coupling to standard model gauge bosons. As gauge singlets of the Standard Model, they do not participate in standard weak interactions. Though, sterile neutrinos with mass would couple to the active neutrinos through non-zero mixing between active and sterile flavors [10].

The not proven existence of sterile neutrinos allows for a wide hypothetical sterile neutrino mass range. Heavy sterile neutrinos featuring masses near the Grand Unified Theory scale can explain the smallness of the three active neutrino masses via the traditional type-I seesaw mechanism, and play a crucial role in the leptogenesis explanation of the cosmological matter-antimatter asymmetry [226-230]. On the other hand, light sterile neutrinos at the eV or sub-eV scale can play an influential role in particle physics, astrophysics and cosmology, and are well motivated by data of several experiments [231-236]. Short-baseline reactor neutrino experiments observed a rate deficit, known as the *reactor neutrino anomaly* [236,237]. Short-baseline oscillations could describe the anomalies via a mass splitting  $\Delta m^2$  of sterile and active neutrino mass eigenstates of around  $1 \text{ eV}^2$ . Contrary, several measurements contradict the interpretation of a sterile neutrino state with a mass of  $\sim 1 \text{ eV}$  [238-242]. Therefore, an unambiguous confirmation or refusal of the existence of light sterile neutrinos by dedicated short-baseline oscillation experiments is an urgent requirement.

JUNO offers the potential to search for sterile neutrino oscillation in the eV and sub-eV range, with  $\Delta m^2$  values on the scale of  $\text{eV}^2$  and  $\mathcal{O}(10^{-5}) \text{ eV}^2$ . The  $\text{eV}^2$  range could be tested if a radioactive (anti-)neutrino source is placed inside or near the detector, and oscillations (with  $L_{\text{osc}} \sim 1 \text{ m}$ ) can be observed. There are two possible source options under discussion.<sup>11</sup> A monochromatic electron neutrino ( $\bar{\nu}_e$ ) emitter and an  $\bar{\nu}_e$  emitter with a continuous  $\beta$ -spectrum are potential candidates. As  $\bar{\nu}_e$  can scatter elastically off electrons in the liquid scintillator target, the event signature cannot be distinguished from many background sources, like  $\beta$ -decays, Compton scattering of gamma-rays, or elastic scattering of solar neutrinos. Especially if the source would be placed outside of the detector target, a very high source activity is required to overcome these backgrounds.

<sup>11</sup> There is the perspective of using a cyclotron-produced neutrino beam to directly test the short baseline anomalies at  $\sim 5 \text{ m}$  distance [243].

As  $\bar{\nu}_e$  can be detected via the  $\overline{\text{IBD}}$ , efficient rejection power for the backgrounds mentioned above is provided, and favor this approach. Nevertheless, a suitable  $\bar{\nu}_e$  source must feature a Q-value larger than the  $\overline{\text{IBD}}$  threshold of  $\sim 1.8$  MeV, and a sufficiently long lifetime, to allow for source production and transportation. Nevertheless, placing a 50 to 100 kCi  $^{144}\text{Ce}$  source inside or outside the central detector gives sensitivity to the entire global analysis region for electron-flavor disappearance at more than  $3\sigma$  confidence level after 1.5 years of data taking [4].

Moreover, super-light sterile neutrinos on a  $\Delta m^2$  scale of  $\mathcal{O}(10^{-5}) \text{ eV}^2$ , near the solar mass-squared difference, could be discovered through a precise study of the reactor antineutrino oscillations [244,245]. With six years of running at full reactor power, a total of  $\sim 10^5$  reactor  $\bar{\nu}_e$  events will be collected. If super-light sterile neutrinos exist, additional distortion could be observed in the reactor neutrino spectrum, with the most sensitive region between  $10^{-5}$  and  $10^{-2} \text{ eV}^2$  [4].

### 3.4.7 Proton Decay

Baryon number violation is one of the three prerequisites needed to explain the observed matter-antimatter asymmetry of the universe [246].<sup>12</sup> However, there has been, up to now, no experimental evidence for baryon number violation. In many Grand Unified Theories (GUTs) that unify strong and weak interactions, baryon number conservation is only an approximate symmetry, e.g., a slightly broken symmetry. The gauge coupling unification scale of such  $\overline{\text{GUT}}$  models is typical of the order of  $10^{16}$  GeV, which cannot be reached with particle accelerators even in the future. Fortunately, an indirect experimental test of some GUTs is possible through observation of one of the unique predictions of GUTs: the proton decay. The predicted decay of the proton in the GUTs leads to a non-conservation of the baryon and lepton numbers. Therefore, a measurement of such a decay could be a probe of those theories and give further evidence for new physics beyond the Standard Model.

The two decay modes which have often been searched for are

$$\begin{aligned} p &\longrightarrow \pi^0 + e^+ \quad \text{and} \\ p &\longrightarrow K^+ + \bar{\nu}_x. \end{aligned} \tag{3.7}$$

The Super-Kamiokande ( $\overline{\text{SuperK}}$ ) collaboration has set the current lower limit on the dominant decay mode into positron and pion with a lifetime of  $\tau > 1.6 \times 10^{34} \text{ yr}$  (90%  $\overline{\text{C.L.}}$ ) [247]. The search for the second listed mode is hindered by the decay kinematics for  $\overline{\text{WCDs}}$ , as the kinetic energy of the resulting kaon

<sup>12</sup> Besides violation of C- and CP-symmetry, and interactions out of thermal equilibrium [246].



is below the Cherenkov threshold ( $\sim 253$  MeV) and therefore invisible. However, this mode opens the window for JUNO to improve existing limits on this channel. Today's best limit is  $\tau > 5.9 \times 10^{33}$  yr (90% C.L.) reported by the SuperK collaboration [248]. For most other decay modes, the liquid scintillator technique does not provide any immediate advantages over WCDs in the aspects of the signal efficiency and background. Consequently, only the target mass determines the detection capability. Therefore, the signal characteristic of this mentioned decay mode is shortly discussed in the following.

If the decaying proton originates from hydrogen<sup>13</sup>, it will decay at rest, and the kaon and the neutrino receive fixed kinetic energies of 105 MeV and 339 MeV, respectively. The kaon will cause a prompt mono-energetic signal, while the neutrino escapes without producing any detectable signal. Afterward, the  $K^+$  meson decays with a lifetime of  $\tau \simeq 12.4$  ns in one of the following main channels:

$$K^+ \rightarrow \mu^+ + \nu_\mu \quad (63.4\%)$$

$$K^+ \rightarrow \pi^+ + \pi^0 \quad (21.1\%)$$

$$K^+ \rightarrow \pi^+ + \pi^+ + \pi^- \quad (5.6\%)$$

$$K^+ \rightarrow \pi^0 + e^+ + \nu_e \quad (4.9\%)$$

$$K^+ \rightarrow \pi^+ + \pi^0 + \pi^0 \quad (1.7\%)$$

Hence, a second delayed mono-energetic signal arises, if the  $K^+$  meson decays into the most probable branch with a corresponding fixed kinetic muon energy of 152 MeV. After  $\sim 2.2 \mu\text{s}$ , the muon also decays via  $\mu^+ \rightarrow e^+ + \nu_e + \bar{\nu}_\mu$  leading to the third long-delayed signal [4].

If the kaon decays into pions (second most probable channel), the  $\pi^+$  deposits its 108 MeV kinetic energy, whereas the  $\pi^0$  instantaneously ( $\tau \sim 9.4 \times 10^{-8}$  ns) decays into two  $\gamma$ -rays with the sum of the energies equal to the total energy of  $E(\pi^0) = 246$  MeV. Afterward, the  $\pi^+$  decays ( $\tau \sim 26$  ns) primarily to muon:  $\pi^+ \rightarrow \mu^+ + \nu_\mu$ . The muon itself has low kinetic energy ( $\sim 4.1$  MeV), but it decays as in the other case about  $2.2 \mu\text{s}$  later, yielding the third long-delayed decay positron signal.

---

<sup>13</sup> If a proton decays in a carbon nucleus, nuclear effects have to be taken into account. In particular, the effective mass of the proton is reduced by the binding energy, and the Fermi motion modifies the decaying proton's momentum, leading to a change of the kinematics of the decay process. These effects are discussed in [249][250].



In both cases, a clear signature of a three-fold coincidence arises

$$p \rightarrow K^+ \xrightarrow{12\text{ ns}} \mu^+ \xrightarrow{2.2\ \mu\text{s}} e^+, \quad (3.8)$$

that allows to search for that possible channel of proton decay. Both the prompt and the delayed signal will have well-defined energies. Additionally, with the third long-delayed signal, a powerful tool to reject backgrounds is provided. As the decay time of 12 ns the kaon is very short, the signal pulses from  $K^+$  and its daughter particles ( $\mu^+$ ) will typically be in fast sequence or even mixed. Therefore, a good time resolution is necessary in order to resolve prompt and delayed pulses. Although the three-fold coincidence provides good background suppression, neutral particles, produced by muons outside the veto system can penetrate the scintillator before being tagged. These neutral particles with energies ranging from few MeV to a few GeV could serve as a background source [251]. Through the passive shielding from JUNO's water pool and the possibility of particle identification using pulse shape discrimination techniques, additional background suppression can be expected. A detailed discussion about background sources and their discrimination strategy is given in [4]. After ten years of measurement and no event observation, a sensitivity on the proton lifetime of  $\tau > 1.9 \times 10^{34}$  yr (90% C.L.) can be reached, which improves today's best limit of SuperK by a factor of three [4].

### 3.4.8 Dark Matter

The existence of non-baryonic dark matter (DM) in the Universe is, by now, well established by astronomical observations [252]. For most spiral galaxies, the rotation curve of stars or gas far from the galactic center does not decline with increasing distance but instead stays above expectations, indicating the existence of a massive dark halo that envelops the galactic disk and extends well beyond the size of the visible part of the galaxy [253]. The currently most accurate, if somewhat indirect, determination of the DM energy density comes from global fits of cosmological parameters to a variety of observations. Thus, the current cosmological observations have helped to establish the concordance cosmological model where the present Universe consists of about 69% dark energy, 26% dark matter, and 5% baryonic matter [254]. Understanding the nature of DM is an open problem in astroparticle physics and cosmology.

DM candidates must be stable on the cosmological time scale and might only interact weakly with ordinary matter and electromagnetic radiation. Within the Standard Model (SM) of particle physics, only the neutrinos are electromagnetically neutral and carry no strong interaction charge. However, the relic density of the neutrinos is too low today to explain the DM effects. Therefore, DM hints at

physics beyond the SM. A widely studied class of DM candidates are the weakly interacting massive particles (WIMPs). The masses of WIMPs are in the range of GeV to TeV, and their interaction strengths with SM particles are in the range of the weak interaction scale.

DM might be detected either directly, through observation of a nuclear recoil, or indirectly, by detecting the final-state particles resulting from DM annihilation or decays in the galactic halo. Direct detection could be possible because the DM particles continuously bombard the Earth as the Earth sweeps through the local DM halo.

The possible DM detection in JUNO will focus on the neutrino signal of all flavors that are produced from DM annihilation in the Sun. When the Sun sweeps through the DM halo, a WIMP could elastically scatter with a nucleus in the Sun. If the WIMP loses most of its energy, and the speed becomes less than its escape velocity, it can be captured by the Sun's gravitational force [252]. The DM particles will be accumulated in the core of the Sun due to repeated scattering and the Sun's gravity potential, and DM particles can begin to annihilate into the SM particles at an appreciable rate. In general, DM inside the Sun might annihilate into leptons, quarks, and gauge bosons. However, only the neutrino, as annihilation products, can escape from the Sun and reach the Earth, where they could be detected. Hence, the Sun's neutrino flux would be enhanced due to the decays of such final-state particles.

A possibility is the detection of the muon neutrino ( $\nu_\mu$ )/muon antineutrino ( $\bar{\nu}_\mu$ ) flux from the annihilation channels. The charged current (CC) interactions of  $\nu_\mu/\bar{\nu}_\mu$  result in detectable and reconstructable single muon tracks, for muon neutrinos with at least  $\sim 1$  GeV energy. [4].<sup>14</sup> Moreover, the possibility to explore the  $\nu_e/\bar{\nu}_e$  signals in JUNO from the light ( $\sim 4$ – $20$  GeV) DM annihilation was studied [255]. In that case,  $\nu_e/\bar{\nu}_e$  CC events with visible energy above 1 GeV can be identified and reconstructed well with an assumed angular resolution of  $10^\circ$ .

Overall, as shown in the right plot of Fig. 3.9, JUNO can reach a much better sensitivity on spin-dependent DM-nucleon scattering cross-section than the current direct detection constraints. The expected sensitivities for JUNO to a cross-section from  $\nu\bar{\nu}$  (solid line) and  $\tau^+\tau^-$  channels (dash-dotted) are much better than current experimental limits [255]. In the case of spin-independent cross-sections (left plot), JUNO is only competitive with direct detection experiments for DM masses below 7 GeV [4].

---

<sup>14</sup> It is assumed that an angular resolution better than  $1^\circ$  is feasible if the muon track is longer than 5 m and intrinsic PMT timing resolution better than 4 ns [4].

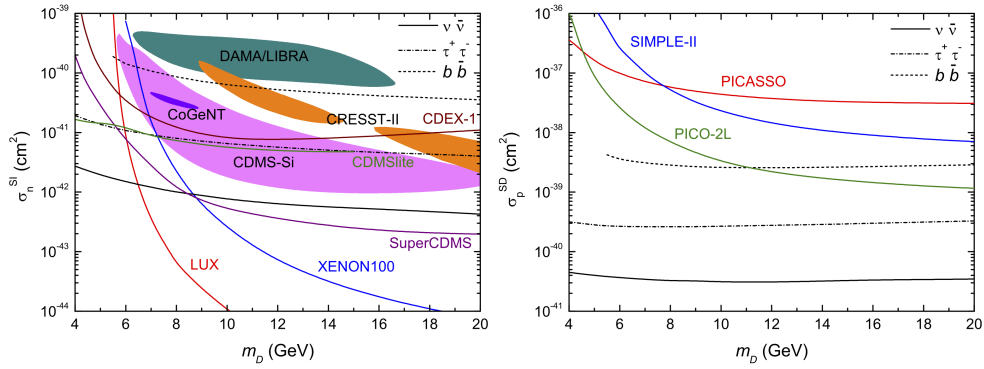


Figure 3.9: The expected sensitivities for **JUNKO** after ten years to spin-independent (left) and spin-dependent (right) **DM**-nucleon cross-section as a function of **DM** mass  $m_D$ . The three possible **DM** annihilation channels into  $\nu\bar{\nu}$  (solid line),  $\tau^+\tau^-$  (dash-dotted line), and  $b\bar{b}$  (dashed line) are compared to current limits from experiments. Figure from [255].



# **THE DSNB SIGNAL**



## Chapter 4

# Diffuse Supernova Neutrino Signal

As the current limit on the diffuse supernova neutrino background (DSNB) flux is already close to theoretical predictions, future experiments, like the Jiangmen Underground Neutrino Observatory (JUNO) (chapter 3) or the Gd-upgrade of the Super-Kamiokande detector (section 2.1.1), will have a substantial chance to observe the DSNB within the next decade.<sup>1</sup>

The focus of this chapter will be the description and discussion of the main input parameters, that control the DSNB flux spectrum, and their influence on the predicted spectra (compare Eq. (1.33)). Besides, the cosmology part, that was shortly discussed in section 1.4.4, the supernova neutrino physics that determines the neutrino source spectrum, as well as the astrophysics part, defining the rate of supernovae, will be discussed. Differences in the neutrino outcome from successful and failed supernovae are presented in section 4.1. The impact of the cosmic core-collapse supernovae rate on the DSNB spectrum is the topic of section 4.2. Section 4.3 presents the possible allowed range of the DSNB flux and discusses the variety of the signal rate in the JUNO detector. Lastly, a description of the simulation and event selection procedure for the JUNO detector follows in section 4.4.

---

<sup>1</sup> Later, longer-term projects like the Hyper-Kamiokande experiment (section 12.2), the water-based liquid scintillator detector Theia (chapter 11), or the Argon-based Deep Underground Neutrino Experiment (section 12.3) could follow.

## 4.1 Neutrino Signals from Successful and Failed Core-Collapse Supernovae

Due to the limited amount of near distanced supernova (SN) events, SN physics can be probed with the help of simulations, while waiting for future SN observations to validate the simulation data. Neutrino signals from core-collapse supernovae (CC-SNe) can, in principle, be computed with the help of detailed SN simulations (e.g., [256]). However, it is challenging to simulate SN neutrino emission in its full complexity within three-dimensional explosion models over time scales longer than some hundred milliseconds. Further depends the outcome of CCSN strongly on the progenitor structure, making simulations over wide ranges of SN progenitors necessary. Thus, most diffuse supernova neutrino background (DSNB) studies were based only on exemplary progenitor models.

The following discussion and analysis are based on the work done in [125], where DSNB predictions were computed from large sets of parametrized SN simulations. A "calibrated neutrino engine" was placed into the center of all pre-SN models to explore the outcome of stellar core collapse over a wide range of progenitor masses [257].<sup>2</sup> Thereby, reliable neutrino signals for a broad set of individual stars, unevenly distributed over the ZAMS (zero-age main sequence) masses 9–120  $M_{\odot}$ , were obtained [125]. The neutrino engine placed into the centers of all progenitors was calibrated to yield explosions in agreement with the well-studied cases of SN1987A and the Crab-SN [261, 264]. Depending on the calibration model, the simulation resulted in more or less successful explosions, as can be seen in Fig. 4.1. From top to bottom, the initial mass function-weighted fraction of successful explosions (red) ranges from 81.9% (top) to 57.6% (bottom). One could note that there is no characteristic mass, separating successful and failed SNe (at low or high masses, respectively) [265, 266]. Contrary, as Fig. 4.1 illustrates, there is a non-monotonic pattern of explodability instead, arising from a strongly varying progenitor structure [267–269]. The intermediate engine model is used in the following as the reference case, which has a fraction of successful and failed SNe of 72.7% and 27.3%, respectively.

Successful SNe were simulated in [125] up to a post-bounce time of 15 s when the neutrino luminosities from proto-neutron star (PNS) cooling have already declined to an insignificant level. In the case of failed explosions, the continued infall of the surrounding mass shells is adding energy to the PNS, leading to an ongoing accretion component of the neutrino luminosities. The signals from failed explosions

---

<sup>2</sup> In detail, a set of 200 non-rotating single star solar-metallicity progenitor models is used [258–260].



#### 4.1 Neutrino Signals from Successful and Failed Core-Collapse Supernovae

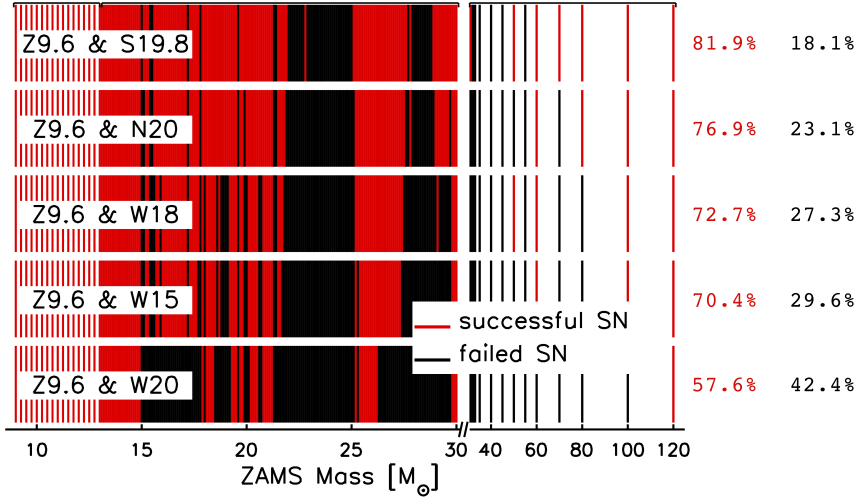


Figure 4.1: Explodability of five different engine models employed in [125]. Successful SNe explosions are depicted in red, while the formation of a black hole (failed SN) is shown in black. The numbers at the right correspond to the initial mass function-weighted fractions of successful versus failed SNe. Figure from [125].

truncate when the PNS reaches the (uncertain) limit for black hole (BH) formation. Either way, time-dependent neutrino luminosities and mean energies of each neutrino species were obtained for every single progenitor [125]. For successful SNe, a mean value  $\langle E_\nu \rangle \simeq 15$  MeV was obtained from the simulations, while the mean energies from failed explosions vary considerably among the progenitors and depend strongly on the threshold mass [125]. The total neutrino energies radiated from failed explosions lie between  $5.2 \times 10^{53}$  erg and  $6.7 \times 10^{53}$  erg [125].

The fiducial DSNB electron antineutrino ( $\bar{\nu}_e$ ) flux spectrum is shown in Fig. 4.2 [125]. The figure further illustrates how the various sources add to the total flux spectrum, and shows the individual contributions from successful iron-core SNe (red), and BH-forming failed SNe (dark red). In this fiducial model, conventional iron-core SNe and failed SNe contribute with comparable fluxes, with  $18.6 / (\text{cm}^2 \text{ s})$  and  $14.3 / (\text{cm}^2 \text{ s})$ , respectively, but with distinctly different spectral shapes [125]. Below  $\sim 15$  MeV, the contribution from successful explosions predominates, while failed explosions dominate the flux at high energies. Even between 20 MeV and 30 MeV, failed SNe make up 57% of the total flux [125]. Hence, it might be possible to probe the fraction of invisible events by measuring the spectral shape of the DSNB.

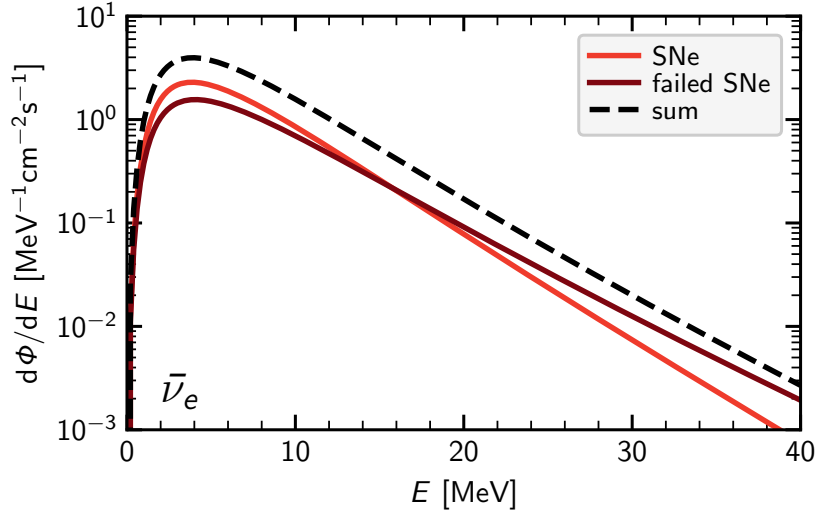


Figure 4.2: Components of the differential DSNB flux of  $\bar{\nu}_e$ 's arriving on Earth with energy  $E$  assuming the reference model. The total flux is depicted as the dashed black line, while the solid lines represent the contributions from successful iron-core SNe (red), and failed SNe (dark red). Figure from [125].

Besides the unknown fraction of failed SNe, the critical mass, above which a neutron star (NS) turns into a BH and neutrino signal breaks down, is also still uncertain. Therefore, four different values of the maximum baryonic NS mass, ranging from  $2.3 M_\odot$  to  $3.5 M_\odot$  were considered in [125] as a mass threshold. The lowest assumed baryonic NS mass of  $2.3 M_\odot$  corresponds to a gravitating mass<sup>3</sup> of  $\sim 1.95 M_\odot$  and is compatible with the largest currently measured pulsar masses of  $\sim 2 M_\odot$  [270–272]. The baryonic mass of  $2.7 M_\odot$  is motivated through the first gravitational wave observation of a binary NS merger (GW170817 [134]) and its electromagnetic counterparts, setting this value to the reference threshold [273,274]. Nevertheless, there are still uncertainties, motivating the two more extreme values of  $3.1 M_\odot$  and  $3.5 M_\odot$ . Eventually, further pulsar timing measurements, as well as an increased number of observed binary NS mergers should be able to shed more light on the mass threshold [270–272]. Fig. 4.3 shows the DSNB flux spectra for the four various choices of mass limits [125]. Raising the mass limit from  $2.3 M_\odot$  to  $3.5 M_\odot$ , the DSNB flux drastically enhances towards higher energies.

<sup>3</sup> The baryonic mass is the sum of all particles that comprise the mass and is theoretically relevant as it is directly connected to the mass of the iron core, which is conserved in merging neutron stars. The mass measured through observations is the gravitational mass. For neutron stars, gravitational mass is smaller due to the binding energy.

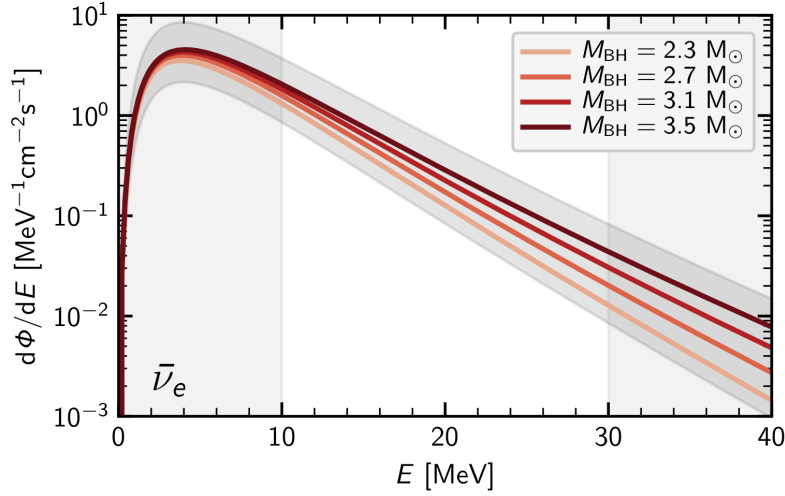


Figure 4.3: Parameter dependence of the [DSNB](#) flux spectrum on the black hole mass threshold. A gray shaded band indicates the uncertainty arising from the cosmic [CCSN](#) rate (corresponding to the  $\pm 1\sigma$  upper and lower limits to the star formation history rate [\[122\]](#)), that is explained in more detail in the following section. The approximate detection window is indicated by shaded vertical bands. Figure from [\[125\]](#).

The reason is that a higher threshold mass corresponds to a longer accretion phase, leading to enhanced time-integrated neutrino luminosities and generally hotter spectra. Nevertheless, the most considerable uncertainty arises from the cosmic [CCSN](#) rate, shown as the grey band in Fig. [4.3](#), which will be discussed within the following section.

## 4.2 Cosmic Core-Collapse Supernova Rate

One of the crucial inputs for calculating the **DSNB** flux is the cosmic rate of core-collapse supernovae (CCSNe). As nuclear burning proceeds fast in massive stars, the progenitors of CCSNe and failed SNe are short-lived ( $< 10^8$  years) compared to cosmological time scales [275]. Therefore, one could assume that the CCSNe rate density  $R_{SN}(z)$  as a function of redshift equals the birth rate density of massive stars [114, 122]:

$$R_{SN}(z) = R_{SFH}(z) \frac{\int_{8.7 M_{\odot}}^{125 M_{\odot}} \psi(M) dM}{\int_{0.1 M_{\odot}}^{\infty} M \psi(M) dM}. \quad (4.1)$$

Although the CCSNe rate is denoted in the following work as  $R_{SN}$ , it should be noted, that this rate also includes the cases of failed SNe. The star formation history  $R_{SFH}(z)$  is defined as the mass that forms stars per comoving volume per unit time at redshift  $z$ . The upper integral in Eq. (4.1) corresponds to the number of stars that lead to core collapse, while the lower integral represents the total mass of stars. The initial mass function  $\psi(M)$ , describes the progenitor mass distribution of stars at birth (cf. section 1.4.4). For the choice of the integration limit in the numerator, one needs to know the mass range of stars leading to a core-collapse. In general, it is difficult to predict accurately from theory, because stellar properties change rapidly in the lower mass range ( $\sim 6-10 M_{\odot}$ ). In principle, the mass can be determined from direct identifications of progenitor stars from pre-explosion imaging, where the luminosity of the star determines its mass, leading to a minimum mass of  $(8.5 \pm 1.5) M_{\odot}$  [276]. This certainly high uncertainty would translate to an uncertainty of about ten percent in  $R_{SN}(z)$  [114].

The star formation history (**SFH**) is most often derived from measurements of living massive stars [277-279]. The measured luminosities, together with knowledge of their masses and lifetimes, results in their birth rates. Since the most massive stars have the shortest lifetimes, they provide a measure of the most recent star formation activity, and the cosmic **SFH** is relatively well-known out to  $z \sim 1$ . The red-shift dependent **SFH**, gained from observations in different wavelength bands, is shown in Fig. 4.4. The red lines correspond to the fit function of the **SFH** and the  $\pm 1\sigma$  upper and lower limits [122]. From the present epoch to  $z \sim 1$ , the cosmic **SFH** increases by an order of magnitude. From  $z = 1$  to at least  $z \sim 4-5$ , the **SFH** is nearly flat, while at higher redshifts, the rate becomes less certain. However, only sources at low redshifts  $z \lesssim 1-2$  noticeably add to the high-energy part of the **DSNB** [105, 119, 121-123]. Concretely, in the energy range of interest, more than 70% of the flux arises from SNe explosions at  $z < 1$  [125]. The reason is that the energy of neutrinos that were emitted from a **SN** at redshift  $z$  is reduced

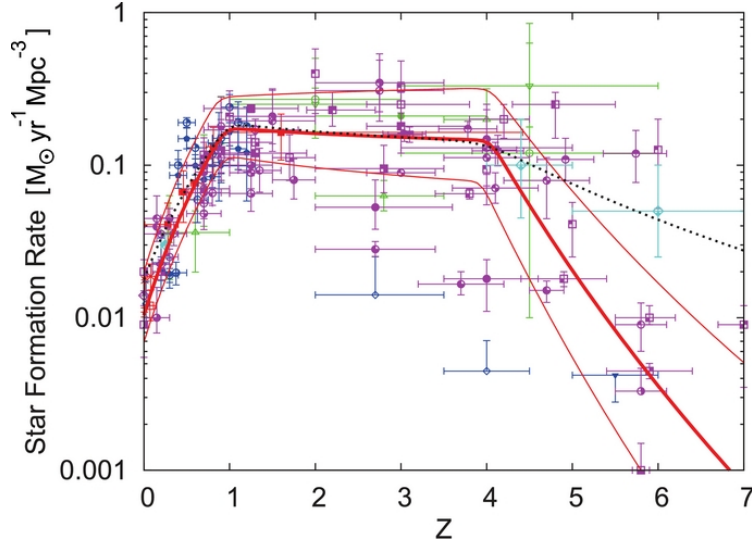


Figure 4.4: The red-shift dependent star formation rate function. Observed data in infrared (red), optical (blue), ultraviolet (magenta), X-ray (light blue) and radio band (green) are shown. Red lines show the star formation rate as a function of redshift  $z$  deduced from fitting, along with the  $\pm 1\sigma$  upper and lower limits [122]. The black dotted line represents the SFH based upon the data set used in [280]. Figure from [122].

by a factor of  $(1+z)^{-1}$  reflecting the expansion of the universe. Hence, neutrinos from high redshifts are almost entirely shifted to energies below 10 MeV, where background sources dominate the flux. Fig. 4.5 shows the contribution by SN neutrinos emitted from different redshift ranges, where low redshifts corresponding to light color and high values of  $z$  to dark color. At energies above  $\sim 20$  MeV, the flux is mainly originating from sources below redshift  $z \leq 1$ . Recent estimates using multi-wavelength proxies for the SFH rate indicate  $\pm 20\%$  uncertainty at  $z = 0$  and a larger uncertainty at higher redshift, producing an average of  $\pm 40\%$  uncertainty on the total DSNB detection rate [114].

In [125], the parametrization for the SFH [122] function was applied, which is represented as the black dotted line in Fig. 4.4. In order to allow for a range of possible normalizations of  $R_{SN}(z)$ , the  $\pm 1\sigma$  upper and lower limits to the SFH are employed additionally, such that

$$R_{SN}(0) = 1.04_{-0.35}^{+0.96} \times 10^{-4} / (\text{Mpc}^3 \text{ yr}) \quad (4.2)$$

for the local universe is obtained [122, 125].

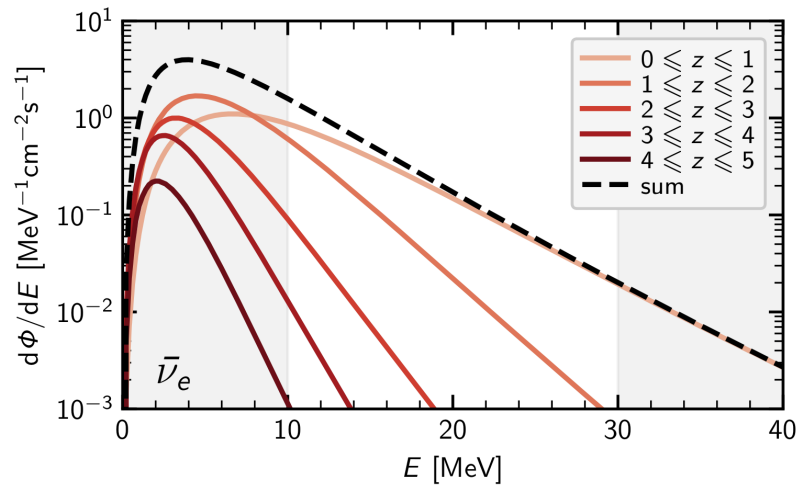


Figure 4.5: Contributions to the differential  $\bar{\nu}_e$ 's DSNB flux from various redshift regions. The approximate detection window is indicated by shaded vertical bands. Figure from [125].

### 4.3 Signal Expectation in JUNO

The variation of astrophysical parameters, like the explodability of a progenitor, the maximum baryonic neutron star mass, and the cosmic **CCSN** rate, spans a range of possible **DSNB** fluxes. The impact of single source properties on the **DSNB** flux was discussed in previous sections. It will be discussed within this section how the variety of fluxes will translate to differences in observable signals in the **JUNO** detector.

Therefore, three exemplary **DSNB** flux models, defined in Tab. 4.1, are compared. The *fiducial* flux model has the reference parameters described in the previous sections. Beside the fiducial model, two "extreme" cases, called *low* and *high* flux model, are defined as well.

The corresponding  $\bar{\nu}_e$  **DSNB** fluxes for the three flux models are plotted in the left panel of Fig. 4.6. Besides, the most stringent  $\bar{\nu}_e$  limit set by the Super-Kamiokande (**SuperK**) experiment,  $\Phi(E > 17.3 \text{ MeV}) \lesssim (2.8-3.1)/(\text{cm}^2 \text{ s})$ , is shown as a red line [3].<sup>4</sup> The various combinations of the considered parameters lead to an extensive spread within **DSNB** flux. At high energies, individual models can differ by over an order of magnitude, with the most extreme cases yielding an integrated flux which exceeds the **SuperK** limit. Unfortunately, it is not possible to restrict single parameter spaces using the current **SuperK** limit, as the high flux model is a combination of several parameters. Hence, it is only possible to exclude parameter combinations.

flux model	parameter			events [/(100 kt yr)]	
	$R_{SN}(z)$	failed SNe	$M_{BH}$	< 40 MeV	11–30 MeV
low	$-1\sigma$ [122]	18.1%	$2.3 M_{\odot}$	18.3	10.6
fiducial	[122]	27.3%	$2.7 M_{\odot}$	37.7	22.6
high	$+1\sigma$ [122]	42.4%	$3.5 M_{\odot}$	133.4	86.8

Table 4.1: Defining three **DSNB** flux models, with their corresponding parameters. The last column shows the expected number of **DSNB** events for neutrino energies between (0–40) MeV and (11–30) MeV.

<sup>4</sup> The flux shape of the fiducial flux is applied, when plotting the current **DSNB** flux limit. Here, the integral between 17.3 MeV and 50 MeV corresponds to a flux of  $2.9 \text{ cm}^{-2} \text{ s}^{-1}$ .

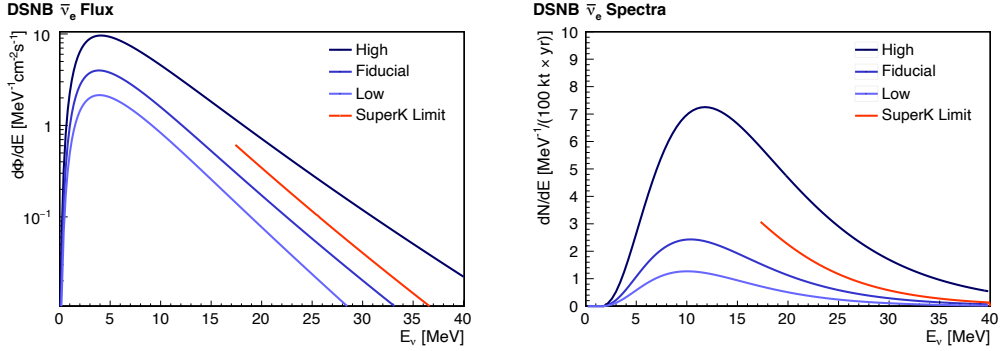


Figure 4.6: Left: Differential  $\bar{\nu}_e$  DSNB flux arriving at Earth with neutrino energy  $E_\nu$  for the fiducial model (blue), laying between the low (light blue) and high flux model (dark blue) [125]. Besides, the SuperK upper-flux limit is given in red [3]. The right plot shows corresponding DSNB  $\bar{\nu}_e$  spectra for exposure of 100 kt yr.

The expected DSNB energy spectrum in a neutrino detector is given by

$$\frac{dN_\nu}{dE_\nu} = \frac{d\Phi_\nu}{dE_\nu} \times \sigma_\nu(E_\nu) \times N_p, \quad (4.3)$$

with the differential DSNB flux  $\frac{d\Phi_\nu}{dE_\nu}$ , the inverse  $\beta$ -decay cross-section  $\sigma_\nu(E_\nu)$ , and the number of protons in the target volume  $N_p$  [141].<sup>5</sup> The number of target protons can be taken from Tab. 3.1. The right panel of Fig. 4.6 gives the resulting DSNB spectrum for JUNO for exposure of 100 kt yr. The number of expected events is calculated by integration of Eq. (4.3) and listed in the last two columns of Tab. 4.1. The strong variation within the different DSNB flux models leads to possible signal rates between  $\sim 18$  and 130 events for 100 kt yr exposure. Approximately half of them are falling in the relevant energy window  $\sim (11-30)$  MeV. Therefore, JUNO will have a substantial chance to observe DSNB events within the next decade, but the signal rates strongly depend on the astrophysical (unknown) parameters. The two-dimensional rate expectation is plotted in Fig. 4.7, where the amount of failed SNe is fixed, while the color represents the DSNB events in dependence of the CCSN rate and on the BH mass threshold.

<sup>5</sup> It is concentrated on the detection of  $\bar{\nu}_e$ 's via the inverse  $\beta$ -decay, as the coincidence signal provides excellent background suppression properties, as explained in chapter 2.



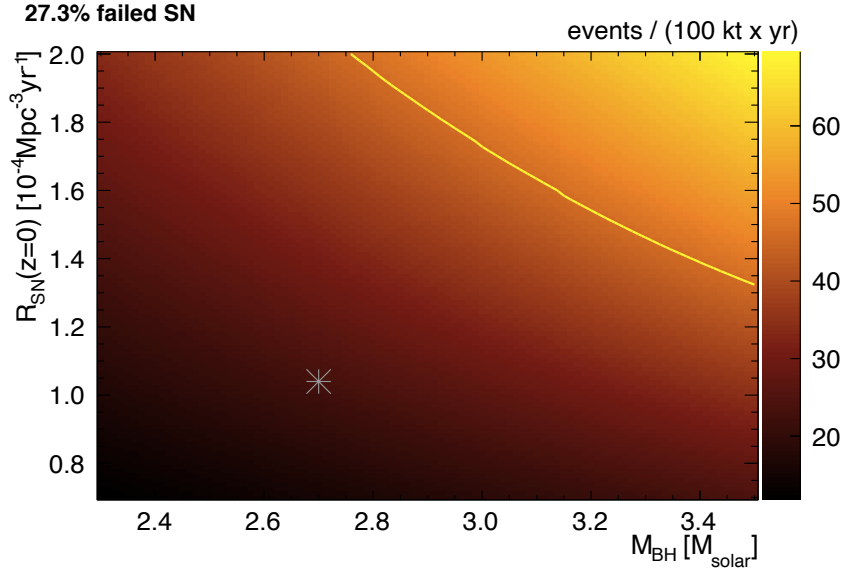


Figure 4.7: Expected **DSNB** signal rates for a **LAB** filled scintillator detector, between 11–30 MeV. The number of events is displayed with a color scheme, where light colors represents more events than dark colors. The amount of failed SNe is fixed to 27.3%, and the CCSNe rate  $R_{SN}$  and the minimum mass for **BH** formation are varied. The grey star represents the fiducial flux model and the yellow line, the current **SuperK** upper limit [3].

As the range of possible signal rates is quite broad, a measurement of the spectrum of the **DSNB** neutrinos will be a probe of stellar physics and cosmological evolution. The neutrino signals carrying imprints of the neutrino production processes and the equation of state of nuclear matter [127]. Therefore, the **DSNB** provides a great opportunity to study the average neutrino emission to fully understand the explosion mechanism [123, 127, 128]. So far, most predictions considered only the collapse into a **NS**, a fraction terminate into **BH**s. These optically dark explosions can be accessed through their released neutrino signals.

To evaluate the amount of detectable **DSNB** events within **JUNO** including detector performance, the detector simulation, which was introduced in section 3.3, is used to simulate the signal events, and is explained in the next section.

## 4.4 Simulation and Event Selection

In order to estimate the sensitivity of **DSNB** measurements in **JUNO**, a detector simulation is performed. The signal events were simulated with the **JUNO** full detector Monte-Carlo simulation, in the following called JUNO's Offline Simulation Framework (**JOSF**) and introduced in section 3.3. The **DSNB** generator produces positron - neutron pairs, where the energy distribution is sampled from the forecasted **DSNB** spectrum. An isotropic flux of incoming neutrinos is assumed. Therefore, the direction of the incoming neutrinos is homogeneously distributed. As the inverse  $\beta$ -decay (**IBD**) cross-section depends on neutrino energy  $E_\nu$  and scattering angle  $\theta$  the two parameters are sampled from the two-dimensional function

$$f(E_\nu, \theta) = \frac{d\Phi(E_\nu)}{dE_\nu} \times \frac{d\sigma(\theta, E_\nu)}{d\cos\theta}, \quad (4.4)$$

with the incoming **DSNB** neutrino flux  $\Phi(E_\nu)$ , and the differential cross-section  $\sigma(\theta, E_\nu)$  [281]. The energy-dependent cross-section divided by energy  $\sigma/E_\nu$  is plotted for different angles in Fig. 4.8, where  $\theta$  is the angle between the incoming neutrino and the outgoing positron direction. The resulting positron and neutron energies, as well as momenta, were calculated using energy and momentum conservation and inserted into the detector simulation **JOSF**.

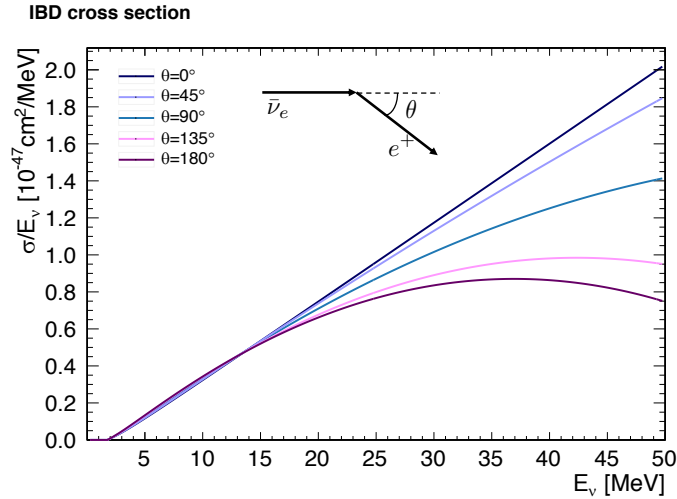


Figure 4.8: The differential cross-section for the inverse  $\beta$ -decay reaction in dependency of the neutrino energy for different fixed angles  $\theta$  [281].

After simulating the **DSNB** events, several defined criteria prove the **IBD** event signature.<sup>6,7</sup> Four main **IBD** cut criteria are defined:

1. **Fiducial Volume Cut.** In order to avoid background events, penetrating from outside into the detector volume, only events within a certain radius  $R < 16$  m are accepted.
2. **Time Difference Cut.** The difference in time  $\delta t$  between the prompt and delayed pulse must lay in the defined time interval:  $600 \text{ ns} < \delta t < 1 \text{ ms}$ . For a neutron capture time of  $\sim 200 \mu\text{s}$  [139], this time window is long enough to ensure that delayed pulse will be included.
3. **Multiplicity Cut.** To avoid background events, only events with exactly two pulses within a time window of 1 ms are allowed, as illustrated schematically in Fig. 4.9. The signal of the first (prompt) pulse opens the 1 ms time window. If there are more than two pulses within the window, the multiplicity cut is applied.
4. **Delayed Energy Cut.** To ensure that the second pulse originates from the 2.2 MeV neutron capture, the number of delayed registered photoelectrons should correspond to this energy.<sup>8</sup> Therefore,  $10^3$   $\gamma$ -events with 2.2 MeV were simulated randomly distributed in the detector volume. The distribution of photoelectrons per event is shown in the appendix in Fig. A.2 with a mean of  $\simeq 3250$  p.e. and  $\sigma = 160$  p.e. Hence, it is defined that the number of delayed photoelectrons has to be between 2750 and 3750.

In total,  $2 \times 10^4$  **DSNB** events, assuming the fiducial flux model, were simulated homogeneously distributed within the liquid scintillator detector volume, and  $\sim 98\%$  of them surviving the above-described **IBD** cuts. The prompt energy spectrum is depicted in Fig. 4.10.

Unfortunately, a **DSNB** measurement will not be background free, as there exist various background sources. Their origin, and their impact will be the main topic of the next chapters.

<sup>6</sup> These criteria are applied in the same way to the simulated background signals, described in the next chapters.

<sup>7</sup> The characteristic of the **IBD** event signature is discussed and explained in chapter 2.

<sup>8</sup> The detector concept of **JUNO** is introduced in section 3.1, explaining the connection between deposited energy and number of detected photoelectrons.

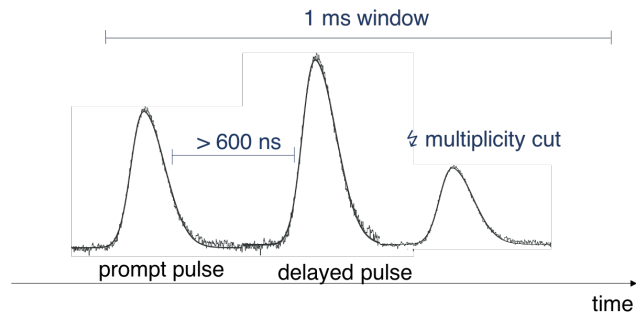


Figure 4.9: This sketch illustrates the time difference cut and the multiplicity cut. Within the 1 ms time window, there have to be precisely two pulses, where the minimal time difference between these two is 600 ns. As more than two pulses are vetoed, this is called the multiplicity cut.

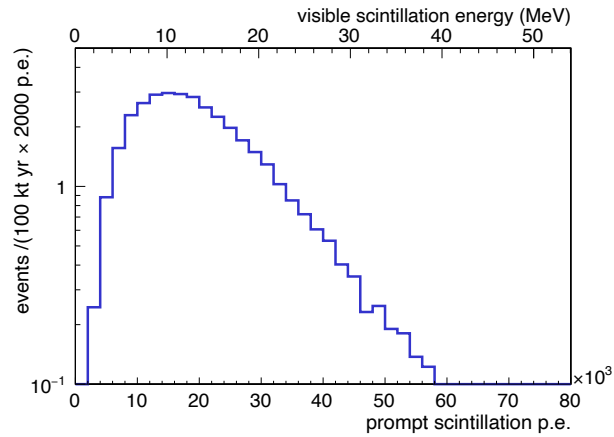


Figure 4.10: Prompt energy spectrum obtained from simulation of DSNB events in JOSE. The event spectrum follows the calculated theoretical spectrum, explained in section 4.3.

# **THE BACKGROUND SOURCES**



## Chapter 5

### Reactor Neutrino Background

The nuclear reactor complexes Taishan and Yangjian produce an enormous amount of electron antineutrinos ( $\bar{\nu}_e$ 's), which will be detected by the Jiangmen Underground Neutrino Observatory (JUNO) via the inverse  $\beta$ -decay (IBD). Hence, reactor neutrinos provide a source of background for the diffuse supernova neutrino background (DSNB) signal. In conventional nuclear power plants (NPPs),  $\bar{\nu}_e$ 's are created in the fission processes of the four fuel components  $^{235}\text{U}$ ,  $^{238}\text{U}$ ,  $^{239}\text{Pu}$ , and  $^{241}\text{Pu}$ .

The differential reactor  $\bar{\nu}_e$  rate detected in the JUNO detector per reactor core is the product of the initial differential reactor  $\bar{\nu}_e$  flux, the energy-dependent IBD cross-section  $\sigma(E_\nu)$  and the oscillation survival probability  $P_{\bar{\nu}_e \rightarrow \bar{\nu}_e}(E_\nu, L)$ :

$$\frac{dR_{\text{reactor}}}{dE_\nu} = \frac{d\Phi_{\text{reactor}}}{dE_\nu} \times \sigma(E_\nu) \times P_{\bar{\nu}_e \rightarrow \bar{\nu}_e}(E_\nu, L). \quad (5.1)$$

Eq. (1.11) in section 1.2 gives the energy-dependent probability for an  $\bar{\nu}_e$  to be detected as an  $\bar{\nu}_e$  after having traveled the distance  $L$ .

Knowledge on the resulting  $\bar{\nu}_e$  spectrum can be directly derived from neutrino experiments by inversion of the measured spectra or by calculation of the superposition of thousands of  $\beta$ -decays of the fission fragments with nuclear database [209–212, 236, 282, 283]. However, a first-principle calculation is challenging even with modern nuclear databases. In general, the uncertainty is  $\sim 10\%$ , while the alternative method of measuring, carries an uncertainty of  $\sim 3\%$  [31, 283]. Using the method of determining the reactor neutrino flux by measuring the spectra and decay schemes of the individual fission products, the  $\bar{\nu}_e$  flux for a single reactor may be calculated as:

$$\frac{d\Phi_{\text{reactor}}}{dE_\nu} = \frac{W_{th}}{\sum_k \alpha_k e_k} \times \sum_k \alpha_k S_k(E_\nu), \quad (5.2)$$

where the index  $k$  considers the fission isotopes  $^{235}\text{U}$ ,  $^{238}\text{U}$ ,  $^{239}\text{Pu}$ , and  $^{241}\text{Pu}$  [4].

Fission Isotope	$\alpha_k$	$e_k$ [MeV]
$^{235}\text{U}$	0.577 (0.60)	$201.92 \pm 0.46$
$^{238}\text{U}$	0.076 (0.05)	$205.52 \pm 0.96$
$^{239}\text{Pu}$	0.295 (0.30)	$209.99 \pm 0.60$
$^{241}\text{Pu}$	0.052 (0.05)	$213.60 \pm 0.65$

Table 5.1: The contributions  $\alpha_k$  of the four main fissile isotopes  $^{235}\text{U}$ ,  $^{238}\text{U}$ ,  $^{239}\text{Pu}$ , and  $^{241}\text{Pu}$  in the reactor fuel and the energy release per fission  $e_k$  in MeV [284]. The power fractions are adopted to be equal to the averaged values of the Daya Bay nuclear cores [4]. The brackets are the values used in JUNO's Offline Simulation Framework (cf. section 3.3).

The first term of Eq. (5.2) represents the number of fissions per isotope occurring in the reactor with total thermal power  $W_{th}$ . In total, the two NPPs next to the location of JUNO will have  $W_{th} \sim 36 \text{ GW}$  [4].<sup>1</sup> The energy-release per fission  $e_k$  of each isotope and the contributions  $\alpha_k$  of the four main fissile isotopes are given in Tab. 5.1

The second term of Eq. (5.2) gives the corresponding neutrino flux per fission, where  $S_k(E_\nu)$  is the  $\bar{\nu}_e$  spectrum of the corresponding isotope. A possible parametrization for  $S_k(E_\nu)$  is given in [282]. The quotas  $\alpha_k$  of the isotopes to the total fission rate averaged over a nuclear burning cycle are also listed in Tab. 5.1.

The power fractions are adopted to be equal to the averaged values of the Daya Bay nuclear cores [4]. As the normalized reactor  $\bar{\nu}_e$  spectrum is approximated as a superposition of the  $^{235}\text{U}$ ,  $^{238}\text{U}$ ,  $^{239}\text{Pu}$ , and  $^{241}\text{Pu}$   $\bar{\nu}_e$  spectra, the reactor  $\bar{\nu}_e$  spectrum is very sensitive to the contributions of different isotopes  $\alpha_k$ . Above 10 MeV, 50% more events are expected when taking the Daya Bay values instead of the values used in the JUNO's Offline Simulation Framework (JOSF) simulation (cf. section 3.3), given as the values in brackets in Tab. 5.1. In order not to underestimate the reactor flux background, the Daya Bay values are assumed. In principle, the neutrino output of any reactor changes over time as the proportions of the four main fissile isotopes varies throughout the fuel cycle. However, time-independent average contributions  $\alpha_k$  of the isotopes in the reactor fuel are assumed in the following. In order to consider possible reactor shutdowns during the experimental lifetime, 300 working days per year are assumed for the NPPs.

<sup>1</sup> It is possible that two of the Taishan cores will not be operating when JUNO starts taking data, resulting in a lower total thermal power of 27 GW [191].



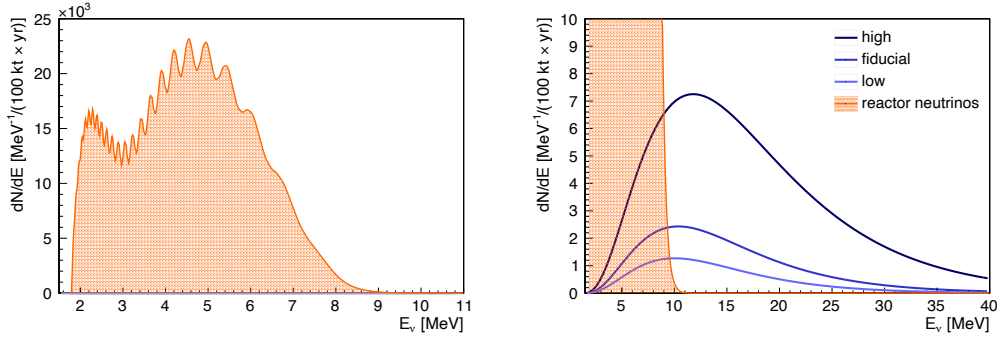


Figure 5.1: The exponential decreasing reactor  $\bar{\nu}_e$  background spectrum (orange) for normal ordering with the DSNB spectra for the fiducial case (medium blue) and the two cases of high and low flux model (light and dark blue), introduced in chapter 4. The reactor neutrino background is calculated with flux approximation given in [282] and IBD cross-section from [141]. As the reactor background is overwhelming the DSNB signal by orders of magnitude, this background sets a lower limit on the DSNB detection window at  $\sim 10$  MeV.

With the approximation for the reactor neutrino flux given in Eq. (5.2), the reactor neutrino spectrum, without any detector response function, is depicted in orange for normal ordering<sup>2</sup> in Fig. 5.1. The right panel corresponds to a zoom-in with the three defined models for the DSNB flux (compare section 4.3) shown in blue. In the energy regime below  $\sim 9$  MeV, the background of nuclear reactor  $\bar{\nu}_e$  dominates the DSNB signal by several orders of magnitude, making detection of the DSNB in the energy region of the reactor neutrinos impossible. Above 6 MeV, the reactor neutrino spectrum decreases almost exponentially and drops below the DSNB signal at  $\sim 9$  MeV.<sup>3</sup> The reactor neutrinos high-energetic tail above 8 MeV is nevertheless relevant as it determines the lower energy limit on the DSNB detection window. By restricting the DSNB detection window to  $E_\nu > 10$  MeV, the reactor  $\bar{\nu}_e$ 's background is reduced by approximately four orders of magnitude, reducing background already below the DSNB signal. As this energy cut also reduces the DSNB signal, by almost 30%, it is mandatory to optimize the lower energy threshold. A summary of signal and background rate depending on the lower neutrino energy threshold is visible in Fig. 5.2<sup>4</sup>

<sup>2</sup> A comparison of the reactor spectrum dependent on neutrino mass ordering is given in section 3.4.1

<sup>3</sup> This threshold is independent of neutrino mass ordering, as the differences are negligible in the higher energy range (compare section 3.4.1).

<sup>4</sup> The corresponding signal and background rates for different lower energy cut thresholds can be found in the appendix in Tab. A.1

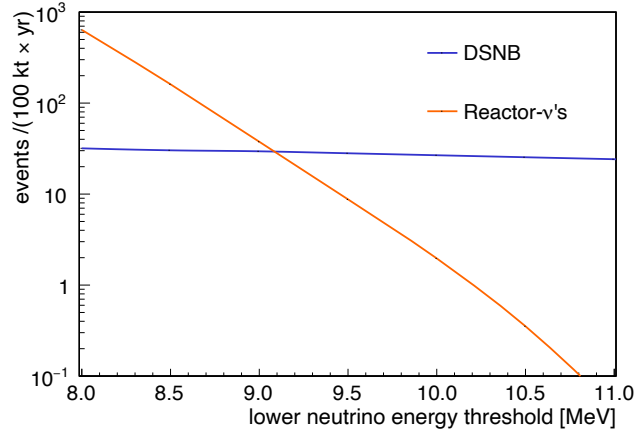


Figure 5.2: The exponential decreasing reactor neutrino background rate (orange) with the [DSNB](#) rate for the fiducial flux. The integration is performed to neutrino energies  $E_\nu \leq 40$  MeV, where the lower energy threshold is varied. Note that no detector response function is considered. As the reactor background is overwhelming the [DSNB](#) signal by orders of magnitude, this background sets a lower limit on the [DSNB](#) detection window. Above  $\sim 9$  MeV, the reactor background drops below the [DSNB](#) signal rate.

Within [IOSF](#), the ILL+Vogel reactor flux model is inserted [\[210-212, 283\]](#). An updated flux model is proposed in [\[236, 282\]](#), showing a 3.5% increase in total flux and a small excess<sup>5</sup> in the high energy part of the spectra compared to the ILL+Vogel model [\[4\]](#). As for [DSNB](#) detection, the high energy part of the reactor spectrum is of relevance, a 5% uncertainty on the rate calculation given in Tab. [A.1](#) is assumed. Using [IOSF](#),  $6 \times 10^3$  reactor  $\bar{\nu}_e$  events, corresponding to  $\sim 1.6 \times 10^4$  kt yr, were simulated homogeneously distributed over the detector volume. Due to the exponential decreasing energy spectrum, the simulation was performed with an initial reactor  $\bar{\nu}_e$  energy threshold of 9 MeV. Fig. [5.3](#) shows the resulting simulated reactor  $\bar{\nu}_e$  spectrum (orange) in comparison with the fiducial [DSNB](#) spectrum (blue).

<sup>5</sup> The bump that has been observed by several experiments in the reactor neutrino spectrum around 5 MeV is not considered here, as it is present in an energy regime that does not play a critical role for [DSNB](#) detection [\[237\]](#).

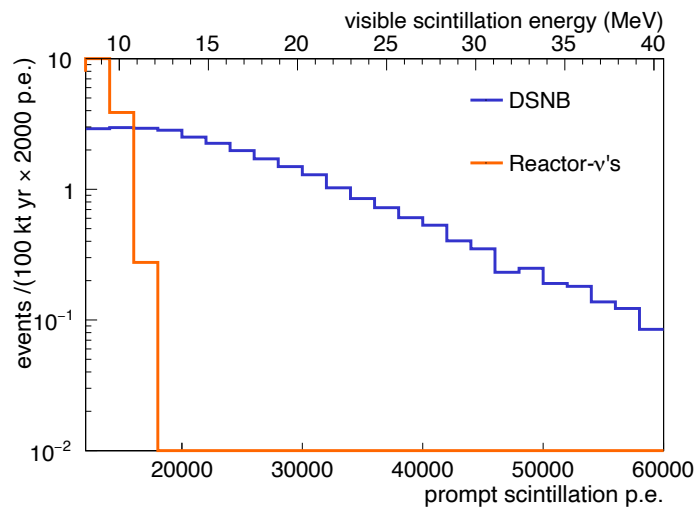


Figure 5.3: The simulated reactor neutrino spectrum (orange) with the fiducial DSNB spectrum (blue).



## Chapter 6

# Atmospheric Neutrino Background

Atmospheric neutrinos are produced when primary cosmic radiation impinges on the atoms of the Earth's atmosphere. The resulting hadronic showers consist to a large extent of unstable mesons. If the generated secondary mesons, in particular, charged pions and kaons, decay into muons, and as these muons are expected to decay further, neutrinos are produced.<sup>1</sup>

As atmospheric neutrinos originate from cosmic radiation and the propagation of primary cosmic rays is affected by the Earth's geomagnetic field, the neutrino flux at Earth is location-dependent. Accordingly, the atmospheric neutrino flux for the location of the Jiangmen Underground Neutrino Observatory is presented in section 6.1. The following discussion on how atmospheric neutrino interactions appear as background sources for diffuse supernova neutrino background detections is divided in the atmospherically charged current and neutral current reactions, in section 6.2 and section 6.3, respectively. The subsequent section explains the simulation procedure of the atmospheric neutrino reactions.

---

<sup>1</sup> Section 1.4.2 introduces atmospheric neutrino production in more detail.

## 6.1 Atmospheric Neutrino Flux

Atmospheric neutrino fluxes for the location of the Jiangmen Underground Neutrino Observatory (JUNO) above 100 MeV up to an energy of  $10^4$  GeV are given in [92]. As solar activity influences the primary cosmic radiation, activity is inversely proportional to atmospheric neutrino flux (cf. section 1.4.2). Hence, in order not to underestimate the flux, minimal solar activity is assumed.<sup>2</sup> The flavor dependent atmospheric neutrino fluxes above 100 MeV are shown in the right panel of Fig. 6.1. Atmospheric neutrino fluxes from electron and muon (anti-)neutrinos are shown in red and blue, respectively, while solid and dashed lines correspond to neutrinos and antineutrinos. The sum is shown in black. The fluxes are higher for muon neutrinos, as the decay of kaons and pions with their subsequent muon decay, provide more muon neutrinos than electron neutrinos (cf. section 1.4.2). The total error is given to be a little lower than 10% in the energy region 1–10 GeV [92].

For even lower neutrino energies, atmospheric neutrino fluxes were obtained from FLUKA simulations, as HKKM fluxes does not include information for  $E_\nu < 100$  MeV [285]. Their simulations provide low energy atmospheric neutrino fluxes between 13 MeV and 944 MeV for the location of Kamioka mine (latitude  $\simeq 36.6^\circ$ N).

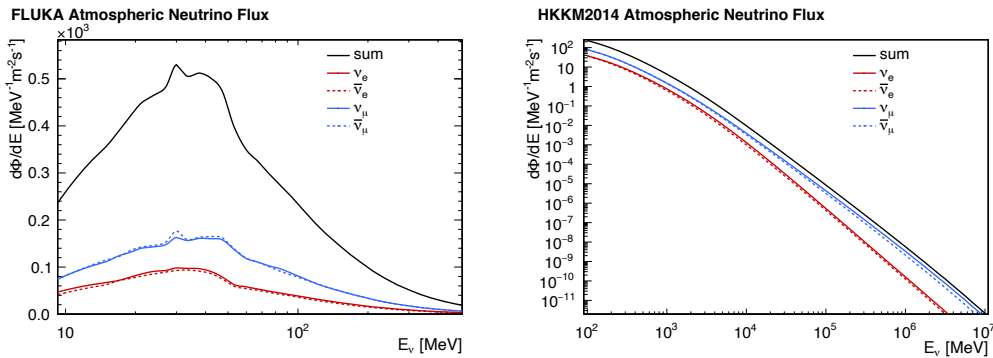


Figure 6.1: Atmospheric neutrino flux is given for the JUNO location for  $\nu_e$ ,  $\bar{\nu}_e$ ,  $\nu_\mu$ , and  $\bar{\nu}_\mu$  as well as their sum (black). The flux for electron neutrinos is shown in red and for muon neutrinos in blue. The dotted lines represent the antineutrino fluxes. The right panel shows the HKKM fluxes for minimum solar activity and neutrino energies above 100 MeV [92]. FLUKA atmospheric neutrino fluxes below 100 MeV for Kamioka location were scaled by a factor of 0.9 and shown in the left panel [285].

<sup>2</sup> The difference manifests mainly at smaller neutrino energies and is  $\sim 6\%$  for 100 MeV neutrino energy [92].

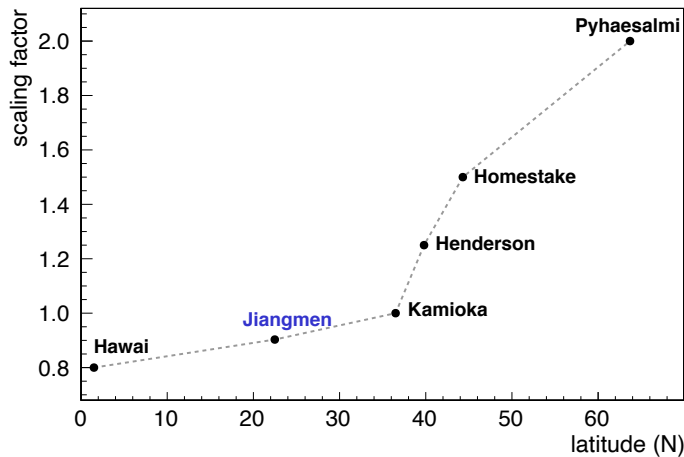


Figure 6.2: Dependence of the total atmospheric neutrino flux below 60 MeV on the detector location. The scaling factor compares atmospheric neutrino fluxes to the one at the Kamioka site [286].

As the neutrino flux depends on geographic latitude, a scaling factor, introduced in [286] and normalized to Kamioka location, that scales atmospheric neutrino flux below 60 MeV, is shown in Fig. 6.2. If one assumes a linear dependency below a latitude of  $\sim 35^\circ\text{N}$ , the scaling factor for the location of JUNO with a geographical latitude of  $22.6^\circ\text{N}$  [4] is approximately 0.9. Therefore, the atmospheric neutrino fluxes below 100 MeV were obtained by taking the simulated fluxes for Kamioka location and scaling them by a factor of 0.9 [285]. The obtained low energy neutrino spectrum is plotted in the left panel of Fig. 6.1.

The uncertainties in the prediction of the atmospheric neutrino flux in the very low energy region are related to the knowledge of the primary spectrum and, in part, to the hadronic interaction models. The overall uncertainty on the absolute value of these fluxes is estimated to be below 25% and dominated by the uncertainty on the primary spectrum [285]. Comparisons of the event rates using the atmospheric flux in [116, 287], show that previous calculations underestimated the atmospheric neutrino background by up to 40% for  $E \lesssim 30$  MeV compared to what is predicted by [285].

To merge the two flux models, it is assumed, that they should be almost the same in the energy range above 100 MeV. The difference between the two flux models is always less than 3% between 100 MeV and 200 MeV. It is assumed that HKKM fluxes are more precise. Therefore, FLUKA fluxes are scaled to fit the HKKM expectation.

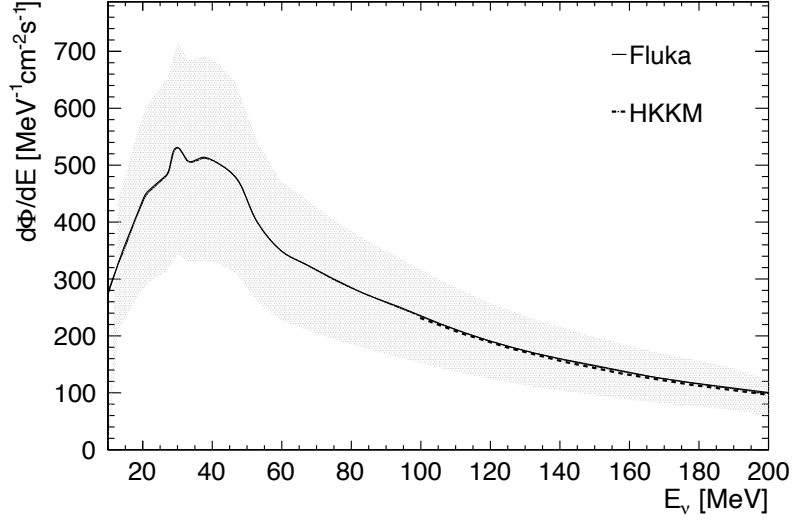


Figure 6.3: Atmospheric neutrino flux (sum of all flavors) for **JUNO** location derived from FLUKA (solid) and HKKM (dashed) simulations [92,285]. For energies below 100 MeV, the FLUKA flux is taken, while for higher energies, the HKKM flux is used. A 35% uncertainty in the lower energetic region is assumed, shown as a grey band.

The atmospheric neutrino flux for **JUNO** location above 10 MeV up to 10 TeV can be expressed as

$$\Phi_{\text{JUNO}}(E_\nu) = \begin{cases} 1.03 \times 0.9 \times \Phi_{\text{Kamioka}}(\text{FLUKA}) & E_\nu < 100 \text{ MeV} \\ \Phi_{\text{JUNO}}(\text{HKKM, solar min}) & E_\nu \geq 100 \text{ MeV}. \end{cases} \quad (6.1)$$

Both fluxes in the low energy range are shown in Fig. 6.3. The grey band represents the assumed uncertainty of 35%, which is motivated in the following.

Besides the neutrino production in the atmosphere, the effect of neutrino production in the Earth through atmospheric produced muons is mentioned. A large number of atmospheric muons are produced, and some of them can penetrate the rock and seawater of Earth's surface to significant depths. These muons will finally stop in the Earth and then produce low energy neutrinos ( $E_\nu \leq 53 \text{ MeV}$ ) through their decay [288]. Unlike  $\mu^+$ , a stopped  $\mu^-$  cannot only decay but can be captured, in  $\sim 40\%$  of the cases<sup>3</sup>, by the nucleus and produce a  $\nu_\mu$  with energy less than the

<sup>3</sup> The value of  $\sim 40\%$  corresponds to the capture probability in rock. In water, the nuclear capture probability is  $\sim 18\%$  [289].



muon mass. For neutrino fluxes of  $\bar{\nu}_e$ ,  $\nu_\mu$ , and  $\bar{\nu}_\mu$  the differences between a stopped muon in rock and water are tiny [289]. Except, the  $\bar{\nu}_e$  flux is larger in the water than in the rock case due to a higher muon decay probability in water. Therefore, the  $\bar{\nu}_e$  flux from stopped muons depends on the local rock and water distributions for a given detector. For neutrino energies below 53 MeV, the  $\bar{\nu}_e$ ,  $\nu_e$ ,  $\nu_\mu$ , and  $\bar{\nu}_\mu$  fluxes are on average 10.8%, 6.3%, 3.7%, and 6.2% of the corresponding atmospheric neutrino fluxes at the location of Super-Kamiokande [285, 289]. Therefore, the uncertainty of 25% is enhanced by 10% in the lower energetic part, including the uncertainty of the primary spectrum and the enhanced flux due to stopped muons [285].

## 6.2 Charged Current Reactions

The most relevant backgrounds for the diffuse supernova neutrino background (DSNB) detection are other  $\bar{\nu}_e$  sources appearing in the same energy range as the DSNB signal. Unfortunately, these background events are indistinguishable from the DSNB signal and can only be suppressed by an energy cut, which also limits the detection window.

A list of possible charged current (CC) reactions of atmospheric neutrinos on  $^1\text{H}$  and  $^{12}\text{C}$  in the scintillator is given in Tab. 6.1

CC Reaction	Veto Strategy
$\bar{\nu}_e + ^1\text{H} \longrightarrow \text{n} + \text{e}^+$	-
$\bar{\nu}_\mu + ^1\text{H} \longrightarrow \text{n} + \mu^+$	muon veto
$\nu_e + ^{12}\text{C} \longrightarrow ^{12}\text{N} + \text{e}^-$	no neutron
$\bar{\nu}_e + ^{12}\text{C} \longrightarrow ^{12}\text{B} + \text{e}^+$	no neutron
$\nu_\mu + ^{12}\text{C} \longrightarrow ^{12}\text{N} + \mu^-$	no neutron & muon veto
$\bar{\nu}_\mu + ^{12}\text{C} \longrightarrow ^{12}\text{B} + \mu^+$	no neutron & muon veto

Table 6.1: The possible atmospheric charged current reactions in the scintillator are listed. Besides the irreducible  $\bar{\nu}_e + ^1\text{H}$  reaction, one could veto this background through the missing delayed neutron signal or the assumption that the resulting muon will be detected.

First, there is the reaction of  $\bar{\nu}_e$  on protons, that serves as an irreducible background. Most of the other reactions do not provide a neutron, that is necessary for fulfilling the inverse  $\beta$ -decay (IBD) coincidence condition. Additionally, it is assumed, that resulting muons will be visible in the detector and that these events can be vetoed sufficiently. Hence, in the following, we will focus on the  $\bar{\nu}_e + ^1\text{H}$  CC reaction.<sup>4</sup>

The expected background rate of atmospheric  $\bar{\nu}_e$  CC reactions is then given through

$$\frac{dR_{CC}}{dE_\nu} = \frac{d\Phi_{\text{Atm}}}{dE_\nu} \times \sigma_{\text{IBD}}(E_\nu) \times N_p. \quad (6.2)$$

A simple approximation of the fully relativistic result of the energy-dependent IBD cross-section  $\sigma_{\text{IBD}}$ , that agrees within a few permille for neutrino energies less than 300 MeV, is given in [141]. The atmospheric neutrino flux  $\frac{d\Phi_{\text{Atm}}}{dE_\nu}$  was given in

<sup>4</sup> There is the possibility that the decay of  $^{12}\text{B}$  and  $^{12}\text{N}$  would provide a delayed signal. That the amount is negligible is shown in the appendix.

Eq. (11.3) and the number of protons  $N_p$  in the liquid scintillator can be taken from Tab. 3.1. Through the integration of Eq. (6.2), an expected atmospheric CC background rate of

$$R_{CC} = (0.2 \pm 0.07)/(\text{kt yr}), \quad (6.3)$$

is obtained for neutrino energies below 100 MeV and with the estimated uncertainty in the lower energetic flux regime of 35%. The corresponding calculated atmospheric CC event spectrum is plotted in Fig. 6.4

The atmospheric CC background, depicted in green, overwhelms the DSNB spectrum above  $\sim 30$  MeV, shown in blue for three different DSNB flux models introduced in section 4.3. As this background is indistinguishable from the signal, it defines the high energy limit on the DSNB detection window. The precise limit strongly depends on the DSNB flux and the lower energetic atmospheric neutrino flux. As both fluxes provide high uncertainties, the higher energy limit is difficult to estimate but would settle between  $\sim 30$  MeV and 40 MeV.

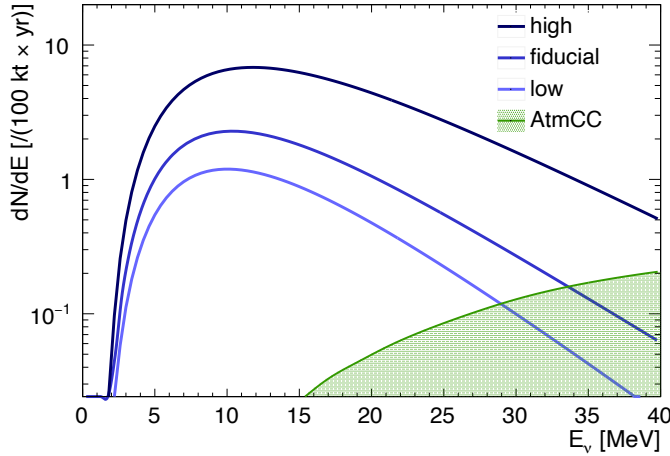
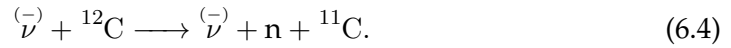


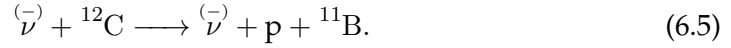
Figure 6.4: The increasing atmospheric CC reaction spectrum of  $\bar{\nu}_e$ 's on protons is shown in green. For comparison, the DSNB spectra for the fiducial case (medium blue) and the two cases of high and low flux models (light and dark blue), introduced in chapter 4 are also shown. The atmospheric CC background overwhelms the DSNB signal in the higher energy part and defines the upper limit on the DSNB detection window.

### 6.3 Neutral Current Reactions

Besides the indistinguishable **CC** reactions of atmospheric  $\bar{\nu}_e$ , also the neutral current **NC** reactions of atmospheric neutrinos and antineutrinos of all flavors pose a possible background for the **DSNB** detection. This background was first discovered in 2012 by the Kamioka Liquid-Scintillator Antineutrino Detector experiment [290]. There is a variety of possible reactions that contribute to the atmospheric **NC** background. In the reaction with the largest branching ratio, an atmospheric (anti-)neutrino knocks out a neutron of a  $^{12}\text{C}$  nucleus in the target volume:



Neutrinos can also produce protons by interacting with carbon nuclei by so-called proton knockouts:



In contrast to the neutron knockout, proton knockout events do not mimic the **IBD** event signature, due to the missing neutron. Enclosed to this, the following focus will be on **NC** reactions on  $^{12}\text{C}$ , as the reaction on  $^1\text{H}$  also provides no neutron in the end state.<sup>5</sup>

The atmospheric **NC** spectrum can be calculated via:

$$\frac{dR_{NC}}{dE_\nu} = \left( \frac{d\Phi_\nu}{dE_\nu} \times \sigma_\nu(E_\nu) + \frac{d\Phi_{\bar{\nu}}}{dE_{\bar{\nu}}} \times \sigma_{\bar{\nu}}(E_{\bar{\nu}}) \right) \times N_t, \quad (6.6)$$

with  $N_t$  as the number of target atoms in the scintillator and

$$\sigma_{(\bar{\nu})} = \sigma_{(\bar{\nu})}^p + \sigma_{(\bar{\nu})}^n \quad (6.7)$$

as the neutrino flavor independent quasielastic cross-section on protons and neutrons, respectively. The atmospheric neutrino flux in Eq. (6.6) represents the sum of the (anti-)neutrino flavors. Fig. 6.5 shows the flavor dependent atmospheric **NC** neutrino interaction spectrum on  $^{12}\text{C}$ .

---

<sup>5</sup> Heavier nuclei targets in the liquid scintillator are also not considered, as they contribute with less than 1% (compare Tab. 3.1).

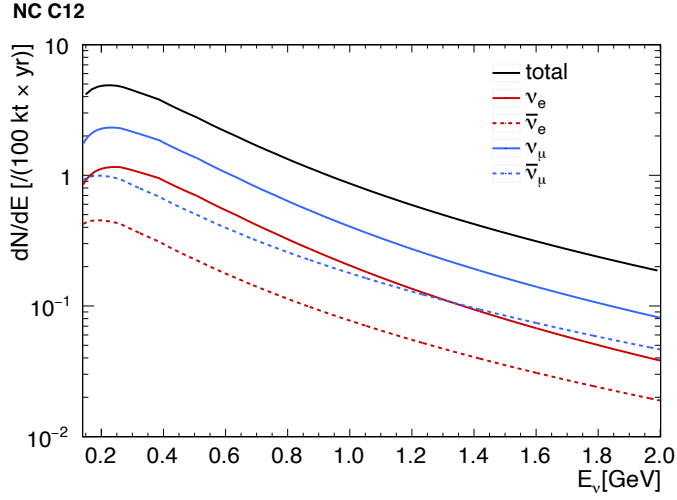


Figure 6.5: The atmospheric  $\overline{\text{NC}}$  spectrum of quasielastic reactions on  $^{12}\text{C}$  for different neutrino flavors. The sum is shown in black.

The expected  $\overline{\text{NC}}$  event rate between 100 MeV and 10 GeV is

$$R_{NC} = (30.8 \pm 0.31)/(\text{kt yr}), \quad (6.8)$$

with the in section 6.1 motivated uncertainty due to atmospheric flux uncertainty of 10% [92].

### Deexcitation of Resulting Nuclei

When an atmospheric neutrino interacts with a  $^{12}\text{C}$  nucleus, there is the possibility of knocking out nucleons. Therefore, the remaining nucleus is often left in an excited state, giving additional particles from the de-excitation. In the simple nuclear shell-model, the  $^{12}\text{C}$  ground state is described as a closed-shell nucleus. For both protons and neutrons, the lowest-lying  $P_{3/2}$  and  $S_{1/2}$  shells are filled, while all higher (sub-)shells are empty. A sketch of the shell model with excited  $^{12}\text{C}$  nucleus is pictured in Fig. 6.6.

In the ground state, there are two neutrons in the  $S_{1/2}$  shell and four neutrons in the  $P_{3/2}$  shell. The situation for protons is basically the same, with 2.7 MeV upwards shifted energy levels due to the Coulomb repulsion. If, in the simple shell-model picture, a neutron disappears from the  $P_{3/2}$  shell, the residual  $^{11}\text{C}$  nucleus is always left in the ground state. As the energy of an atmospheric neutrino is usually large compared to the binding energies of the nucleons, it is assumed that the probability of interacting with an atmospheric neutrino is the same for each nucleon. After the

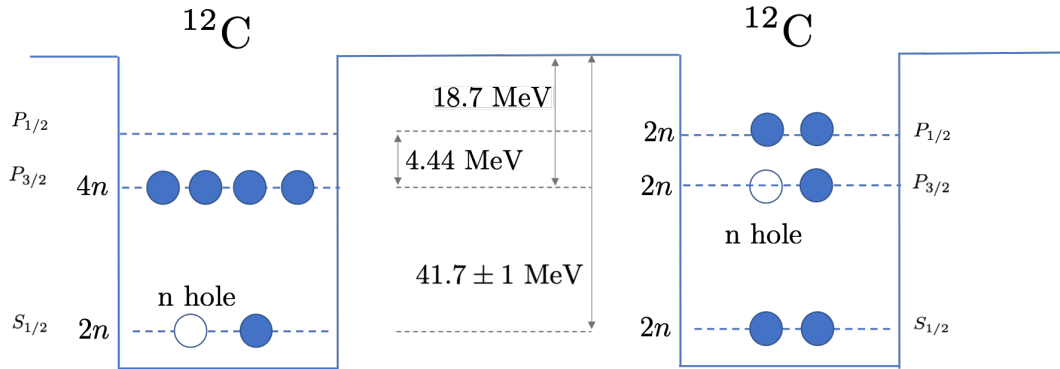


Figure 6.6: The sketch shows the occupation of energy levels by neutrons for the  $^{12}\text{C}$  ground state in a simple shell model picture. In the left part, the closed-shell model is shown, while the right part considers the partially filled shell model of the nucleus. One neutron has been knocked out from the  $S_{1/2}$  level in the left sketch, whereas the neutron hole is in the  $P_{3/2}$  level in the right part.

neutrino has interacted with a nucleon, the nucleon can scatter with other nucleons before it leaves the nucleus. Due to these so-called intranuclear scattering reactions, further nucleons can be emitted. If one assumes that only nucleons from the  $P_{3/2}$  shell are released in these reactions, there is a  $2/6$  chance that the residual nucleus has a hole in the  $S_{1/2}$  neutron or proton shell, depicted in the left part of Fig. 6.6.

In more sophisticated shell-model calculations, it has been shown that the simple closed-shell picture of the  $^{12}\text{C}$  ground state has to be remedied. Due to correlations, especially pairing effects, the  $P_{1/2}$  shell is also partially filled with nucleons from the  $P_{3/2}$  level lying just 4.44 MeV below [291]. Various shell-model calculations give partial occupation numbers of the  $P_{1/2}$  shell of  $\sim 0.8$ , which can be interpreted as by saying that approximately 60% of the time, the  $P_{3/2}$  shell is filled, while in 40% of the cases two neutrons are in the  $P_{1/2}$  shell [292, 293]. This scenario is shown in the right part of Fig. 6.6, which introduced a finite probability that a neutron disappearing from the  $P_{3/2}$  state will leave the residual  $^{11}\text{C}$  nucleus in an excited state. As the de-excitation energy of this scenario is below the knockout scenario with a hole in the  $S_{1/2}$  shell, this will lead to less energy release. Moreover, a comparison showed that including the scenario with the partially filled  $P$ -shell nucleons, will not affect the atmospheric neutrino spectrum significantly [294]. Therefore, only the de-excitations with an empty  $P_{1/2}$  shell are considered in the following.

The excitation energy of the residual  $^{11}\text{C}$  in the case of a hole in the  $S_{1/2}$  shell can be calculated by the difference between the binding energy of the  $S_{1/2}$  neutron level and the neutron separation energy:

$$E^* = 41.7 \text{ MeV} - 18.72 \text{ MeV} \simeq 23 \text{ MeV}. \quad (6.9)$$

This is high enough to exceed the separation energy for protons, neutrons, and  $\alpha$ -particles in  $^{11}\text{C}$ , making them the primary emission products of the highly excited nucleus. Qualitatively, the emission of a proton should be more frequent than the emission of a neutron since  $^{11}\text{C}$  is a proton-rich nucleus. Assuming equality is not underestimating the resulting background, as the neutron emission is needed to ensure coincidence.

## 6.4 Simulation Setup

The simulation of atmospheric neutrino events is performed in two stages. First, an event generator models the interactions of atmospheric neutrinos in the liquid scintillator (LS) of JUNO. Final-state particles resulting from these interactions are then tracked in a Geant4-simulation of the detector response.

First, for the simulation of neutrino interactions inside the LS target volume, the GENIE Neutrino Monte-Carlo Generator (Version 2.12.4) is used [70, 295]. For the atmospheric neutrino flux input, the HKKM flux is inserted [92]. The upper neutrino energy threshold for simulation was set to 10 GeV and the LS composition given in Tab. 3.1 was adopted. In total,  $2 \times 10^6$  atmospheric neutrino interactions were simulated in GENIE, corresponding to an exposure of  $\sim 1.1 \times 10^4 / (\text{kt yr})$ . The left column of Tab. 6.2 list the quasielastic (QEL) NC interactions, obtained from the GENIE simulation.

Afterward, the GENIE output was read into the Geant4 JUNO's Offline Simulation Framework (JOSF). For the CC background,  $1.5 \times 10^4$  atmospheric neutrino events of  $\bar{\nu}_e$  on  $^1\text{H}$  with  $E_\nu < 100 \text{ MeV}$ , were simulated. In addition, for the NC reactions,  $1.17 \times 10^5$  atmospheric QEL neutrino events of all flavors on  $^{12}\text{C}$  with  $E_\nu < 10 \text{ GeV}$  were simulated. The de-excitation branches were simulated in [296] using the nuclear reaction program TALYS (Version 1.4) with an excitation energy of  $E^* = 23 \text{ MeV}$  [297]. Within the Geant4 simulation, one-third of the reactions are assumed to de-excite. In these cases, a de-excitation channel is chosen based on the TALYS output and added to the particles that go into the detector simulation.

After simulating atmospheric reactions in JUNO with JOSF, including de-excitation modes, the event selection algorithm, presented in section 4.4, was applied. A summary of the most probable atmospheric neutrino NC interactions is provided in the right column of Tab. 6.2. The upper energy limit on the prompt energy deposition was set to  $1 \times 10^5$  photoelectrons, corresponding to  $\sim 68 \text{ MeV}$ . The prompt energy spectra of the simulated atmospheric neutrino background are shown in Fig. 6.7. Even though only a part of all atmospheric NC events passes the IBD event selection criteria, this background still overwhelms the DSNB signal by at least one order of magnitude. In order to make the DSNB detection still feasible, excellent background identification methods have to be applied and will be discussed within the next chapter.



$\nu_x + {}^{12}\text{C} \longrightarrow \nu_x +$			
NC interactions in LS	[%]	after event selection	[%]
p + ${}^{11}\text{B}$	29.1	n + ${}^{11}\text{C}$	33.1
n + ${}^{11}\text{C}$	25.0	n + p + ${}^{10}\text{B}$	22.8
n + p + ${}^{10}\text{B}$	18.2	n + 2p + ${}^{10}\text{Be}$	9.3
2p + ${}^{10}\text{Be}$	4.2	n + p + ${}^2\text{H} + {}^8\text{Be}$	7.1
2n + ${}^{10}\text{C}$	4.0	n + p + ${}^4\text{He} + {}^6\text{Li}$	6.5
n + 2p + ${}^9\text{Be}$	1.1	2n + ${}^{10}\text{C}$	5.1
2n + p + ${}^9\text{B}$	1.1	2n + 2p + ${}^8\text{Be}$	2.8
2n + 2p + ${}^8\text{Be}$	1.0	2n + p + ${}^9\text{B}$	2.7
3n + 3p + ${}^6\text{Li}$	0.9	n + 3p + ${}^8\text{Li}$	2.0
other channels	15.4	other channels	8.6
30.8 / (kt yr)		7.8 / (kt yr)	

Table 6.2: Reaction channels of atmospheric **QEL NC** reactions on  ${}^{12}\text{C}$ , sorted by their prevalence. The left column lists the **NC** interactions obtained from the GENIE simulation. The right column lists the reactions taking into account the de-excitation products and the event selection described in section 4.4.

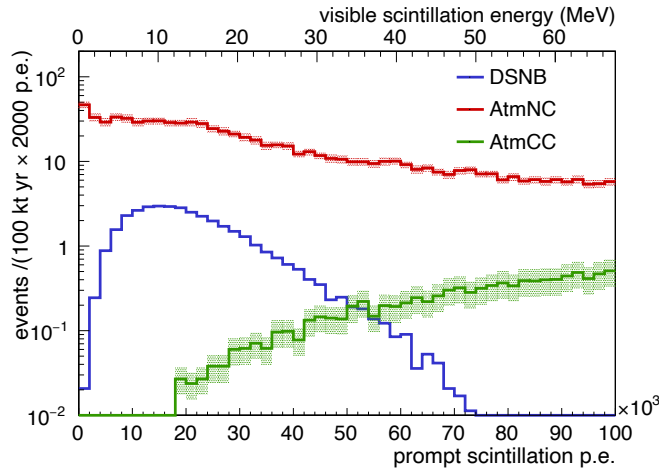


Figure 6.7: The prompt energy spectrum of the simulated atmospheric neutrino background and the fiducial **DSNB** spectrum (blue). The plot shows in green the atmospheric **CC** reactions, while the atmospheric **NC** spectrum corresponds to the red line.



## Chapter 7

# Muon-Induced Background

Muons, generated in air showers in the atmosphere, penetrate deep underground and could produce particles in the rock surrounding the detector hall or in the detector material itself. Hence, cosmic-ray muons and their spallation products are potential sources of background for neutrino detectors. In the present chapter, muon-induced backgrounds include events created by muons appearing close to the detector. The effect of neutrino production through muons in the whole Earth material is treated in chapter 6. To shield the detector against cosmic muons, a 270 m high granite mountain provides shielding for the Jiangmen Underground Neutrino Observatory (JUNO) experiment. To further suppress muon-induced backgrounds, the detector will be located underground with a total overburden of 650 m rock, corresponding to 1.9 km.w.e [4, 192]. Nevertheless, a non-neglectable number of cosmic ray muons can still reach the detector with an expected muon rate in the central detector of  $\sim 3.5$  Hz and mean muon energy of 215 GeV [4, 192].

When muons travel through matter, their energy loss leads to nuclear breakup processes. Hence, at sufficiently high muon energies, many subsequent particles can be produced by muon-induced electromagnetic or hadronic processes, like cosmogenic radioactive isotopes, neutrons, protons, pions, and gamma rays. Understanding the background produced by muon-initiated spallation processes is essential for the interpretation of the data. Two cosmogenic muon-produced background scenarios are discussed in this chapter. First of all, the background generated by muons that transverse the inner detector volume and secondly, muon-induced neutrons that could enter the detector from the surrounding experimental hall, are considered.

Nonetheless, in JUNO, cosmic-ray muons will be identified either by a large amount of scintillation and Cherenkov light detected by the photomultiplier tubes (PMTs) watching the detector volume or by the Cherenkov light detected by the outer PMTs, observing the water buffer (see section 3.1). Supplementary, the second muon tracking detector placed on top of the water pool enhances muon identification efficiency. Moreover, the muon tracks can be reconstructed from

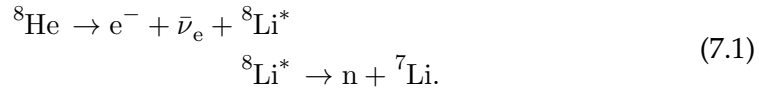
arrival times of the first-arriving Cherenkov or scintillation photons at the **PMTs**. Thus, it is easy to veto the muons themselves. Unfortunately, cosmogenic muons can produce relatively long-lived radioactive isotopes. The delayed decays of unstable daughter nuclei are a relevant background source for the diffuse supernova neutrino background search. The cosmogenic isotope production and their meaning as a background source are discussed in section **7.1**.

Contrary to muons that traverse the detector, muons can pass the water Cherenkov veto volume or the rock outside the detector volume. In interactions with the rock material, high-energetic particles can be produced, like neutrons. Some of these outside produced neutrons can enter the detector volume without being tagged and provide an additional background source. This so-called *fast neutron background* is explained and discussed in section **7.2**.

## 7.1 In-Situ Produced Cosmogenic Isotopes

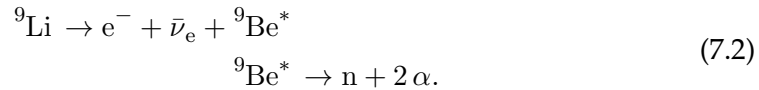
A cosmic muon, which traverses the target volume, can interact with the carbon nuclei in the liquid scintillator (LS) and produce cosmogenic (unstable) radioisotopes inside the target volume by muon-induced spallation reactions. It is quite efficient to veto the muons themselves, through the produced Cherenkov light in the inner or outer detector, but the decay of relatively long-lived radioactive isotopes can produce background signals. As the majority of these decaying radioisotopes events will not provide a delayed neutron signal, they are no background events for the inverse  $\beta$ -decay (IBD) channel. However, e.g.,  $^8\text{He}$  and  $^9\text{Li}$  are  $\beta$ -unstable radioisotopes and can decay into an excited state, which leads indeed to the emission of a neutron. Hence, these two isotopes can mimic the IBD event signature and constitute a possible background in the diffuse supernova neutrino background (DSNB) search.

The radioisotope  $^8\text{He}$  decays ( $Q = 10.6 \text{ MeV}$ ,  $\tau = 172 \text{ ms}$ ) with a 16% branching ratio into an unstable state of  $^8\text{Li}^*$ , leading to the subsequent instantaneous emission of a neutron [298]:



The neutron separation energy of  $^8\text{Li}$  is 2.0 MeV, reducing the Q-Value to  $\sim 8.6 \text{ MeV}$ , corresponding to  $\sim 9.4 \text{ MeV}$  reconstructed neutrino energy [299].<sup>1</sup> For DSNB analysis, it is only necessary to consider the background that falls into the observation window above  $\sim 10 \text{ MeV}$ , defined by the overwhelming reactor neutrino background fluxes below this energy threshold (compare chapter 5). Consequently, the background produced by the decay of  $^8\text{He}$  is not relevant in the case of DSNB detection.

On the contrary, the decay of  $^9\text{Li}$  features a large enough Q-value to remain as a background candidate.  $^9\text{Li}$  decays ( $Q = 13.6 \text{ MeV}$ ,  $\tau = 257 \text{ ms}$ ) with 50.8% branching ratio into an excited state of  $^9\text{Be}$ , which leads to a followed emission of a neutron and two  $\alpha$ -particles [298]:



<sup>1</sup> Furthermore, the light output from neutron scattering reactions is strongly quenched, which also reduces the reconstructed prompt energy.

The electron would provide the prompt signal, and with the delayed neutron capture signal, the coincidence condition for an [IBD](#) event would be fulfilled. As just the decays from an excited state lead to a neutron, the maximum kinetic energy of the emitted electron is the Q-value, reduced by the energy of the excited state. Therefore, the maximum energy of the electron corresponds to the first excited state and is

$$Q - 2.43 \text{ MeV} \simeq 11.2 \text{ MeV}, \quad (7.3)$$

correlated to  $\sim 12 \text{ MeV}$  reconstructed neutrino energy. This is well above the lower energy threshold of  $10 \text{ MeV}$ , and so  ${}^9\text{Li}$  could provide a background source in the low energetic part of [DSNB](#).

For the expected  ${}^9\text{Li}$  background rate in [JUNO](#), the Borexino result for the  ${}^9\text{Li}$ -production yield is considered, which is  $\sim 30\%$  higher than the yield determined by Kamioka Liquid-Scintillator Antineutrino Detector ([KamLAND](#)) [[300](#),[301](#)]. The cosmogenic production yields are summarized in [Tab. 7.1](#). The muon-initiated spallation production yields depend on the number of carbon atoms per weight and the muon energy spectrum. As [KamLAND](#) has 5% less carbon nuclei per ton of [LS](#) and the mean residual muon energies differ between the two experimental sites, this explains the difference in the observed production yields. Moreover, it was found that there is a factor two of discrepancies between the calculated and the measured production yields, mainly resulting from hadronic uncertainties [[302](#)]. As the calculated yields for both experiments have a lower value than the measured ones, the measured yield of Borexino is adopted. As the production cross-section of cosmogenic isotopes scales with the muon energy  $\sigma \propto E_\mu^{0.75}$ , the production yield for [JUNO](#) is reduced by a factor of  $\sim 0.8$  [[303](#)]. Moreover, [JUNO](#) has fewer carbon atoms per ton [LS](#), reducing the production yield by an additional small amount of 3%.

	Borexino	KamLAND	JUNO
number of carbon atoms [ $10^{28} / \text{t}$ ]	4.52	4.3	4.41
$\langle E_\mu \rangle$ [GeV]	283	260	215
$Y_{9\text{Li}}$ [ $10^{-7} (\mu\text{g}/\text{cm}^2)^{-1}$ ]	$(2.9 \pm 0.3)$	$(2.2 \pm 0.2)$	-

Table 7.1: The measured cosmogenic  ${}^9\text{Li}$  production yield of Borexino and [KamLAND](#) [[300](#),[301](#)].

Overall, a  ${}^9\text{Li}$  production rate of

$$\begin{aligned} R({}^9\text{Li}) &= 0.8 \times 0.97 \times Y_{9\text{Li}} \times R_{\mu} \\ &\simeq (2580 \pm 260) / (\text{kt yr}) \end{aligned} \quad (7.4)$$

is expected with  $R_{\mu}$  as the muon rate in the **LS** target. In line with measurements, an uncertainty of 10% is assumed [300, 301]. As in only 50.8% of the cases,  ${}^9\text{Li}$  decays into an excited state, the rate is reduced to  $\sim (1310 \pm 130) / (\text{kt yr})$ . Nevertheless, the possible background due to  ${}^9\text{Li}$  production overwhelms the **DSNB** signal by orders of magnitude. Hence, veto strategies are urgently needed.

Luckily, there are spatial and temporal correlations between spallation events and the parent muons. As the  ${}^9\text{Li}$  production is close to the traversing muon track, this offers the possibility to veto these events by using a volume cut around the reconstructed muon tracks. Once isotopes are produced, they do not move far before they decay. It was found that 99% of isotopes decay within 3 m [302]. Through precise muon tracking, muon detection efficiency is expected to reach 99.8% [4]. For muons that either deposit a large amount of energy or cannot be tracked, one could apply an additional time veto of the full detector [4]. The possibility of vetoing a cylinder with a radius  $r_{\text{veto}}$  around the reconstructed muon track for a particular time  $t_{\text{veto}}$  is schematically shown in Fig. 7.1.

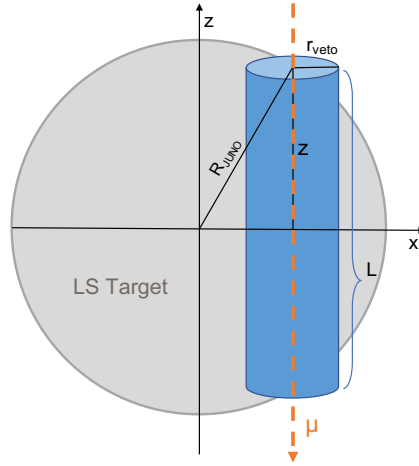


Figure 7.1: Sketch of the fiducial volume cut to reduce cosmogenic produced  ${}^9\text{Li}$  background in the **LS** target (grey) of the **JUNO** detector. A cylinder (blue) with radius  $r_{\text{veto}}$  is vetoed for a certain time  $t_{\text{veto}}$  after each reconstructed muon track (orange) that traversed the detector volume.

The baseline veto strategy suggests a cut with  $r_{\text{veto}} = 3$  m and  $t_{\text{veto}} = 1.2$  s after each muon along its track through the central detector. This veto can reduce the cosmogenic background by 98%, which reduces the  ${}^9\text{Li}$  background to  $(26.2 \pm 2.6) / (\text{kt yr})$  [4].

The dead time caused by the cylindrical veto cut, with a mean muon track length of  $\langle L_{\mu} \rangle = 23$  m, is in total  $\sim 12\%$  [4]. Additionally, it is assumed that for tagged and non-trackable muons (1% of all muons), the whole LS volume is vetoed for 1.2 s, resulting in a signal loss due to this fiducial volume cut of  $\sim 16\%$ .

A simulation of the  ${}^9\text{Li}$  decay is performed within JUNO's Offline Simulation Framework. The implemented decay scheme is presented in the appendix in Fig. A.3. Only the decays into excited states were simulated, as the ground state does not provide neutrons for the delayed neutron signal. In total,  $1.5 \times 10^4$   $\beta$ -decays into the excited states are simulated, and the prompt energy distribution is visible in turquoise in Fig. 7.2 with the predicted DSNB signal given in blue. The  ${}^9\text{Li}$  signal sets, besides the reactor neutrinos, an additional lower energy limit on the DSNB detectable energy window. Please note that the maximum prompt energy deposition of  ${}^9\text{Li}$  goes beyond the maximum energy of the released electron, as the scattering reactions of neutrons and  $\alpha$ -particles also contribute to the prompt signal. The  ${}^9\text{Li}$  background rates in comparison with the DSNB signal rates are plotted in the right panel of Fig. 7.2

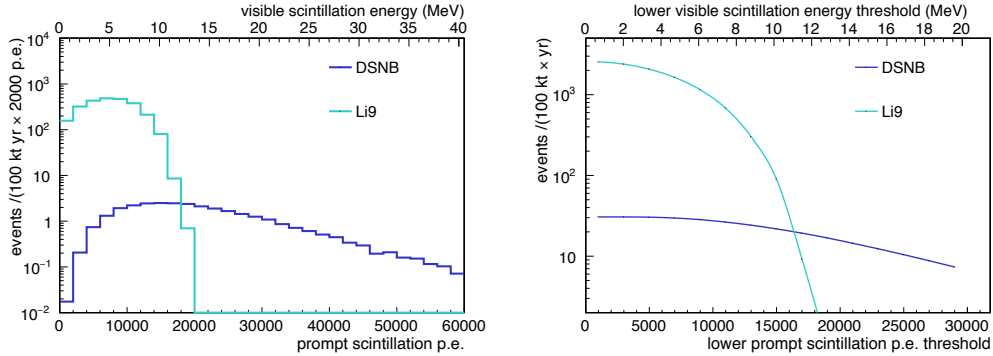


Figure 7.2: The prompt energy spectrum of the simulated cosmogenic  ${}^9\text{Li}$  decay (turquoise) and the fiducial DSNB spectrum (blue) is given in the left panel. The cylindrical fiducial volume cut is applied. The right panel shows the total expected event rates for exposure of 100 kt y of in-situ produced cosmogenic  ${}^9\text{Li}$  and the fiducial DSNB flux model as a function of the lower energy threshold.



## 7.2 Fast Neutrons

If a muon enters the detector, neutron signals can be efficiently suppressed with a time-interval veto of  $\sim 1$  s following the muon. A further source of background is arising from highly energetic neutrons, produced by a cosmic-ray muon outside the detector in the surrounding rocks. Since the primary muon is not penetrating the detector or muon veto, they are invisible and cannot be used for discrimination purposes. In nuclear cascades, high energy neutrons can be produced up to GeV energies, and above.<sup>2</sup> Therefore, a fraction of neutrons is energetic enough that they can reach the scintillator volume before they are moderated and absorbed. Neutrons that are reaching the scintillator volume can scatter and create a recoil proton. After thermalization, the neutrons are captured by hydrogen atoms, which can produce a fake event for the electron antineutrino ( $\bar{\nu}_e$ ) search. The elastic scattering reactions of high energy neutrons, which produce nuclear recoils, can fall into the expected energy range of **DSNB** interactions. Summing up, the recoil protons provide the prompt signal, and the neutron once thermalized and captured, produces the delayed event.

The intensities of the residual muons and the muon-induced neutrons depend strongly on the depth of the underground detector. Due to the relatively low depths of the **JUNO** detector cavern, neutrons created by cosmic muons passing through the rock close by the detector are relatively frequent and constitute a relevant source of background. The deposited prompt energy distribution is assumed to be flat **[304]**.<sup>3</sup> It should be noted that an a priori knowledge of the precise shape is not necessary, as the spectral shape could be studied during measurement. Because of the finite mean free path of the neutrons, most of the events are concentrated on the verge of the scintillator volume. Hence, fast neutron background events show a radial dependency. The study of this background, matching online measurements with simulations, will help to understand this kind of background very well and allows for statistical subtraction.<sup>4</sup>

<sup>2</sup> The vast majority of neutrons are produced by natural radioactivity in the rock. U/Th emit  $\alpha$ -particles, which may then interact with light nuclei ( $Z < 30$ ) to produce neutrons. Neutrons from the spontaneous fission of heavy elements (mainly  $^{238}\text{U}$ ) are restricted to a few MeV, allowing for shielding from rock neutrons using H-rich material, which moderate and capture them. Hence, they are not discussed here.

<sup>3</sup> This was mainly verified in **[305]**. Nevertheless, the energy spectra show a slight decrease at higher energies. Contrary to **[296]**, where a small increase is noted.

<sup>4</sup> Furthermore, the application of pulse shape discrimination method will further reduce this kind of background, which is discussed in chapter **8**

The expected rate of fast neutron background events for the **LS** volume was determined to 3.4 events per year between 11 MeV and 30 MeV of deposited energy [304]. This value is enhanced by  $\sim 16\%$  due to the updated higher muon flux for JUNO arising from less overburden [304]. The local dependency was fitted with an exponential function.

The obtained expected background rate is plotted in dependency of the maximum radius of the fiducial volume cut in the left panel of Fig. 7.3. Within a radius of 16.8 m the **DSNB** signal surpasses the fast neutron background. The amount of expected events is added with flat energy distribution to the data, visible in the right panel of Fig. 7.3 for a fiducial radius of 16 m. The assumed uncertainty rate of 20% is visible as the shaded band.

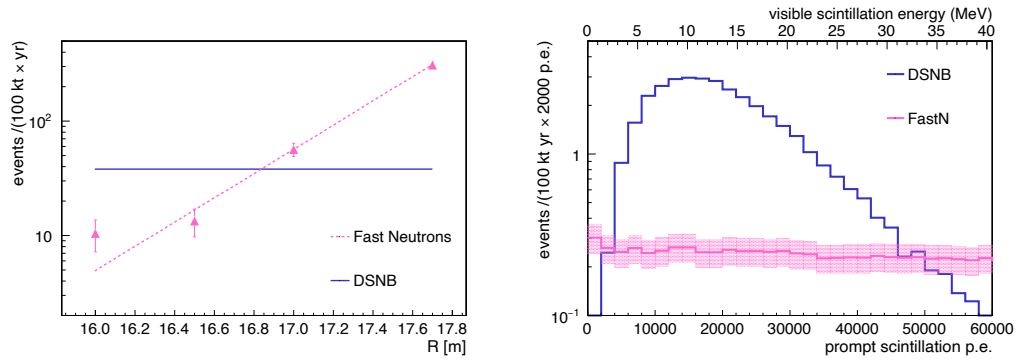


Figure 7.3: Event rate in the **LS** volume from muon-induced fast neutrons per 100 kt yr below 40 MeV and assuming flat energy distribution [304].

Left panel: The fast neutron background (pink) is showing a radial dependency, while the **DSNB** signal (blue) is homogeneously distributed in the central detector volume. The exponential fit function is plotted as the dotted line, where the data points, including their statistical error, are also given. Within a radius of 16.8 m, the **DSNB** signal surpasses the fast neutron background.

Right panel: Flat fast neutron background (pink) for  $R < 16$  m with simulated **DSNB** signal (blue). The assumed 20% uncertainty is plotted as the shaded area.

# **BACKGROUND IDENTIFICATION**



## Chapter 8

# Pulse Shape Discrimination

To overcome the enormous amount of background reactions, mainly arising from atmospheric neutral current (NC) reactions (cf. section 6.3), background identification methods are necessary to allow for a diffuse supernova neutrino background (DSNB) measurement with the Jiangmen Underground Neutrino Observatory (JUNO). A powerful tool is the so-called pulse shape discrimination (PSD), which will be explained in this chapter. It is based on the fact that positrons create the prompt pulses of DSNB events, while the atmospheric NC events arise mainly from much heavier protons and neutrons. Hence their pulse shapes differ due to different fractions of singlet and triplet excitations in the scintillator, which is explained in section 2.2, making background reduction possible.

The photon emission process in a liquid scintillator (LS), can be described with the exponential decays of several components. The sum of the functions can express the probability density function  $F(t)$ :

$$F(t) = \sum_i \frac{N_i}{\tau_i} e^{-\frac{t}{\tau_i}}. \quad (8.1)$$

Here,  $\tau_i$  is the time constant of the  $i$ th component, and  $N_i$  is the mean fraction of photons that are emitted with the time constant  $\tau_i$ , such that  $\sum_i N_i = 1$ . The number of exponential functions is adjustable, and the values of  $N_i$  and  $\tau_i$  are particle dependent.

In the JUNO's Offline Simulation Framework (introduced in section 3.3), the LS light emission is modeled by three fluorescence components with the default parameters of the optical model summarized in Tab. 8.1. The amplitudes of the time constants depend on the particle's energy deposition per unit path length [197]. More massive particles deposit more energy per unit path length and thus emit a larger fraction of photons by the slower components because a higher density of ionized and excited molecules increases the possibility for intermolecular interactions [197]. The light emission parameters for  $e^-$ ,  $e^+$ , and  $\gamma$  particles were adopted

	$e^-, e^+, \gamma$	$\alpha$	n/p
Fast fraction $N_1$	79.9%	65.0%	65.0%
Medium fraction $N_2$	17.1%	22.75%	23.1%
Slow fraction $N_3$	3.0%	12.25%	11.9%
Emission time $\tau_1$	4.93 ns	1 ns	1 ns
Emission time $\tau_2$	20.6 ns	35.0 ns	34.0 ns
Emission time $\tau_3$	190 ns	220 ns	220 ns

Table 8.1: The **LS** photon emission default parameters of JUNO's Offline Simulation Framework [4]. Fast, medium and slow components describe the fluorescence light emission.

from measurements, while parameters for neutrons, protons, and  $\alpha$ -particles were obtained from Monte-Carlo tuning in Daya Bay [306, 307].<sup>1</sup> The normalized photon emission distributions from Eq. (8.1) using the parameters given in Tab. 8.1 are plotted exemplary for neutrons and electrons in Fig. 8.1. The pulse levels off much slower for neutrons than for electrons, mainly due to the more strongly populated third fluorescence time component. Hence, this behavior can be used to distinguish between different particle types by analyzing their observed pulse shape.

As the power of particle identification through **PSD** strongly depends on the parameters describing the time profile of the light output, one has to determine them carefully. Typically, these parameters will be obtained through a scintillator calibration with neutrons or  $\alpha$ -particles with energies below  $\sim 8$  MeV. Through quenching effects (compare section 2.2), the amount of deposited energy will be further reduced, so, unfortunately, no knowledge at higher particle energies on the emission timing can be gained. However, to estimate the pulse form of the prompt **DSNB** or atmospheric neutrino interaction events in the energy window  $\gtrsim 11$  MeV, this knowledge is necessary. Nevertheless, Borexino first showed that pulse shape based particle identification allows identifying atmospheric **NC** neutrino events even with higher deposited energies (7.6 MeV–29 MeV) [308]. By adopting knowledge on pulse shapes at low energies to the higher energetic region, the **PSD** algorithm was able to separate between different particle interactions [308]. With

<sup>1</sup> Note, that there is no difference implemented between electrons and positrons. Positrons may form a bound state with an electron, so-called positronium, shortly discussed in chapter 2. As the longer-lived spin state orthopositronium has a lifetime of  $\sim 3$  ns in **LS**, its formation changes the time distribution of photon emission [137]. Hence the pulse shapes of electrons and positrons in principle differ, but as the lifetime of positronium is small compared to the slower emission times on which the particle identification is most sensitive, this should not affect the present discrimination results.

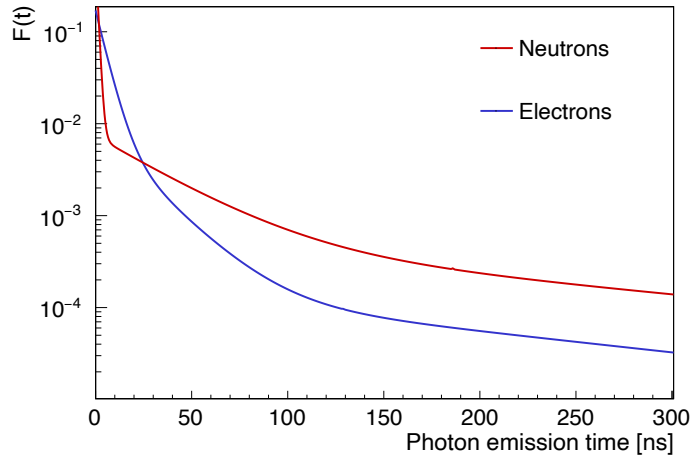


Figure 8.1: The probability density function  $F(t)$  from Eq. (8.1) describes the photon emission process in a LS. The time-dependent light emission is shown for neutrons (red) and electrons (blue) with the parameters from Tab. 8.1.

this proof of principle, it was shown that PSD techniques constitute a promising tool to suppress the overwhelming background from atmospheric neutrino NC interactions. As Borexino uses a different scintillator material (pseudocumene), it is not possible to unequivocally conclude that this will be feasible for JUNO's LS to the same extent. Nonetheless, this motivates the following discussion, where the particle dependent parameters, presented in Tab. 8.1, are assumed to be energy independent and that one can apply the information measured at low energies without restrictions to the high energy regime. It is crucial to emphasize that the subsequent considerations strongly depend on this assumption.

The simulation process, which is implemented to study the PSD efficiency, is described in section 8.1. Afterward, the simple but powerful method to distinguish pulse shapes, the tail-to-total ratio method, is introduced in section 8.2. Applying this method, the discrimination power to distinguish atmospheric NC events from DSNB events is evaluated subsequently.

## 8.1 Obtaining Pulse Shapes within the Simulation Process

JUNO's Offline Simulation Framework was introduced in section 3.3 and includes four steps of data handling. In the first step of the detector simulation, the physics simulation, including photon propagation up to the photosensors, is performed, resulting in Monte-Carlo (MC) truth data. This step was accomplished for signal and background sources described before (see, e.g., section 6.4). The second step includes the electronics simulation, which translates the MC truth information into FADC (Flash Analog to Digital Converter) waveforms. The waveform reconstruction follows as the third step, to receive the charge and hit time information from the waveform. Lastly, the event is reconstructed, based on charge and timing information.

In order to have more flexibility, the pulse shape analysis is mainly based on MC truth data directly obtained from the first step of detector simulation. The main effects appearing by performing steps 2–4 are added manually.<sup>2</sup> The pulse - meaning the timing information of detected photoelectrons - is not equal to the timing distribution of the light-emission process in the scintillator. This is mainly due to a time shift due to the photomultiplier tube (PMT) performance and to scintillator optics, such as scattering<sup>3</sup>, absorption, and the varying time of flight (TOF) to the photodetector surface. It follows a description of the data handling process to add such effects manually.

For JUNO, the pulse shape is measured with a set of PMTs, and the pulse is defined by the time distribution of light emission (LE), which can be reconstructed from the photon hit time at the PMT  $t_{\text{hit}}$  and the reconstructed TOF  $t_{\text{TOF}}$ :

$$t_{\text{LE}} = t_{\text{hit}} - t_{\text{TOF}}. \quad (8.2)$$

Due to the geometry of a PMT, there is a marked time delay between the hit time of the photon on the photocathode and the creation of the electrical pulse, which is registered. This delay is characterized by the transit time and results directly from the process of amplifying photoelectrons and collecting the cascade of secondary electrons on the anode. As this is a statistical process and various systematic effects can affect the transit time (TT), the TT varies, characterized by the transit time spread (TTS), given in full width at half maximum (FWHM).<sup>4</sup> Fig. 8.2 illustrates the described time shifts.

<sup>2</sup> Moreover, this procedure was motivated by [309], where it was shown that there is no relevant difference in performing full detector simulation compared to the manual approach.

<sup>3</sup> It is assumed that the Rayleigh scattering length will not be noticeably smaller than the 27 m, assumed in the detector simulation, as this would influence the timing information.

<sup>4</sup> The transit time of the Hamamatsu R12860 PMTs is  $\sim 95$  ns [310].



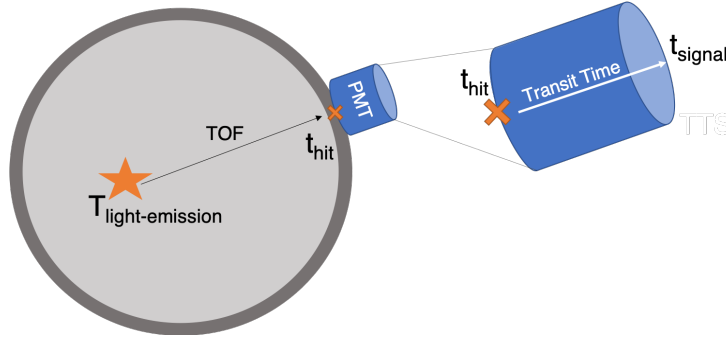


Figure 8.2: The light emission time of a photon can be reconstructed from the detected time  $t_{\text{signal}}$ , the  $\text{TOF}$  and the transit time of the  $\text{PMT}$ . The  $\text{LS}$  volume (grey) is surrounded by the  $\text{PMTs}$  (blue).

In the current analysis, only 20-inch  $\text{PMTs}$  are considered, and the  $\text{TTS}$  distribution of the sensors is shown in Fig. 8.3. The majority of the  $\text{PMTs}$  are micro-channel plate  $\text{PMTs}$  with a  $\text{TTS}$  of  $\sim 12$  ns, while the  $\sim 5000$  Hamamatsu R12860  $\text{PMTs}$  have a much shorter  $\text{TTS}$  of  $\sim 3$  ns [311]. The delay due to  $\text{TTS}$  is added to the  $\text{PMT}$  hit time for each  $\text{PMT}$  with the corresponding random draw  $\text{TTS}$  values from Gaussian with  $\sigma = \text{TTS}/2.35$ , so that Eq. (8.2) transfers to

$$t_{\text{LE}} = t_{\text{hit}} + t_{\text{TTS}} - t_{\text{TOF}}. \quad (8.3)$$

The measurable value of  $t_{\text{TT}}$  represents a constant time offset. Therefore, for simplicity,  $t_{\text{TT}} = t_{\text{TTS}}$ , as the "unknown"  $\text{TTS}$  will influence the pulse reconstruction.

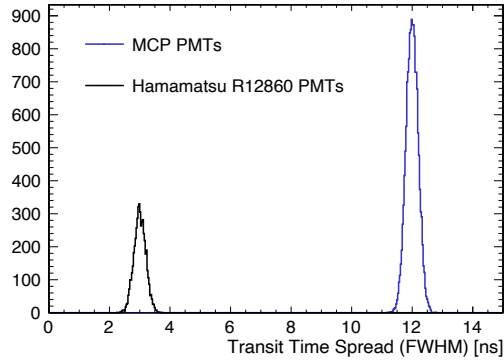
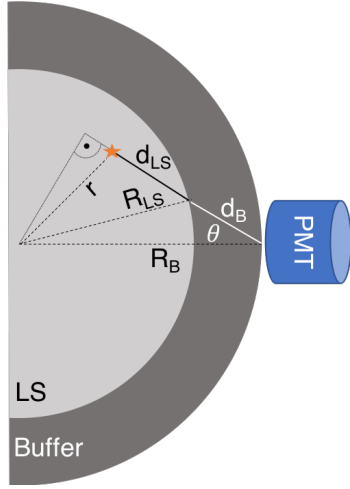


Figure 8.3: Distribution of  $\text{TTS}$  (FWHM) for Hamamatsu R12860  $\text{PMTs}$  (black) and micro-channel plate (MCP)  $\text{PMTs}$  (blue).

$$\begin{aligned}
 t_{\text{TOF}} &= \frac{d_{\text{LS}}}{v_{\text{LS}}} + \frac{d_{\text{B}}}{v_{\text{B}}} \\
 d &= |\vec{x}_{\text{vertex}} - \vec{x}_{\text{hit}}| = d_{\text{LS}} + d_{\text{B}} \\
 d_{\text{B}} &= R_{\text{B}} \cos \theta - \sqrt{R_{\text{LS}}^2 - (R_{\text{B}} \sin \theta)^2} \\
 \cos \theta &= \frac{R_{\text{B}}^2 + d^2 - r^2}{2R_{\text{B}} \times d}
 \end{aligned}$$


The diagram shows a cross-section of a detector. It consists of an inner light grey semi-circle labeled 'LS' (Liquid Scintillator) and an outer dark grey semi-circle labeled 'Buffer'. A blue cylinder labeled 'PMT' is positioned to the right. A star represents a photon source within the LS volume. A dashed line of length  $r$  connects the center of the LS volume to the star. A dashed line of length  $R_{\text{LS}}$  connects the center to the PMT. A dashed line of length  $R_{\text{B}}$  connects the center to the PMT. The distance from the star to the PMT is  $d$ , which is the sum of  $d_{\text{LS}}$  (distance from star to the LS-Buffer interface) and  $d_{\text{B}}$  (distance from the interface to the PMT). The angle between the  $R_{\text{B}}$  line and the  $d_{\text{B}}$  line is  $\theta$ .

Figure 8.4: Not to scale sketch of the acrylic sphere surrounding the **LS** volume (light grey). The buffer medium water (dark grey) is between the **PMTs** (blue) and the scintillator. If a photon is created within the **LS** volume, shown here with the star, the **TOF** can be separated in the **TOF** in the **LS** and the buffer volume, with the effective light speed  $v_{\text{LS}}$  and  $v_{\text{B}}$ , respectively.

Note that the background effect due to the dark noise of the **PMTs** is not considered in this work. If one assumes a dark count rate of 50 kHz per **PMT**, one expects less than  $10^3$  photoelectrons due to dark noise during a time window of  $1 \mu\text{s}$ , which is well below the signal. As they should be uniformly distributed in time and independent of **PMT** location, it is assumed that they will not change the pulse shape noticeably. Moreover, due to the uniform distribution in space, a fraction of them could be vetoed with specific clustering algorithms [296].

Furthermore, it is assumed that the uncertainty of the time offset due to electronics is small in comparison to the **TTS**, resulting in a negligible effect on the pulse shape. Moreover, it is assumed that the waveform reconstruction will not affect the pulse form, as the waveform reconstruction can be optimized for different energy regions such that time-dependent effects on the signal can be neglected [312].

The **TOF** can be obtained from the **PMT** position and the reconstructed event vertex  $\vec{x}_{\text{vertex}}$ . The approximated calculation of **TOF** is shown in the illustration in Fig. 8.4. Note, that no refraction is inserted, which underestimated the actual **TOF**. The differences by including refraction effects was evaluated to be less than 1.6 ns, and even smaller ( $< 0.2$  ns) in the inner detector volume with  $R < 16$  m [313].

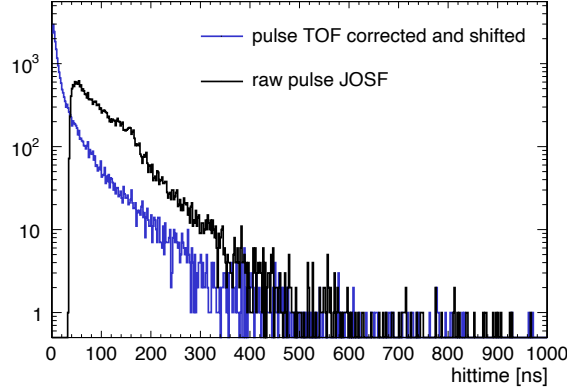


Figure 8.5: An arbitrarily chosen pulse of a simulated **DSNB** event. The "raw" pulse corresponds to the time distribution of the photons, reaching the photocathode of the **PMTs** (black). The effect of the **TOF** correction and pulse shifting is illustrated with the blue distribution.

The event vertex  $\vec{x}_{\text{vertex}}$  is extracted from the **MC** detector simulation, giving the actual event position, which is smeared afterward with a position independent vertex resolution. Starting from  $\sigma = 12 \text{ cm} / \sqrt{E(\text{MeV})}$ , the spatial resolution is set to a fixed value of  $\sigma = 3.8 \text{ cm}$ , assuming a minimum energy deposition of 10 MeV in the **DSNB** study [4]. After the previous described steps, including first the vertex smearing, followed by offset correction using Eq. (8.3), the light emission time distribution is shifted so that the beginning of a pulse, defined as where the amplitude reaches 10% of total pulse height, is at  $t = 0$ . The pulse handling, including the effect of **TOF** correction, is shown in Fig. 8.5 for an arbitrarily chosen pulse.

The above-described procedure is applied to all events that survive the inverse  $\beta$ -decay event selection cut, described in section 4.4. Fig. 8.6 illustrates the normalized sum of all prompt pulses from the simulated atmospheric **NC** and **DSNB** events.<sup>5</sup> The difference in pulse form, especially above 100 ns, is recognized and could verify that the pulse shapes follow the light emission time distribution plotted in Fig. 8.1. The obtained pulse shapes in Fig. 8.6 are less separated below  $\sim 30 \text{ ns}$  in comparison to Fig. 8.1 due to detector effects. The prompt pulses arising from atmospheric **NC** events decrease slower than **DSNB** events. This characteristic can be used to identify different particles in **LS** reactions.

<sup>5</sup> Information about the simulation procedure used to obtain signal and background events are given in section 4.4 and section 6.4 respectively.

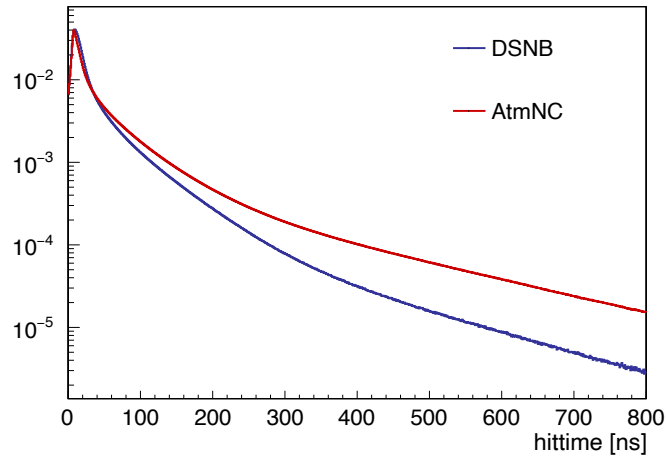


Figure 8.6: The normalized and averaged prompt pulse of atmospheric **NC** (red) and **DSNB** (blue) events.

Over the past decades, several methods have been developed to distinguish between different particles in a **LS** by analyzing pulse shapes. For the study of **PSD** in **JUNO**, the tail-to-total ratio method is investigated within this work, which will be presented and discussed in the next section. Since the main challenge in the field of **DSNB** detection is the suppression of the overwhelming atmospheric **NC** neutrino background, the following analysis on **PSD** analysis is based on these two event classes.

## 8.2 Discrimination Efficiency using the Tail-to-Total Method

With the tail-to-total ratio (TTR) method, the integrated photon emission signals  $p(t)$  are compared within a predefined time interval. The so-called *tail interval* includes only the last part of the signal, where the difference between  $\alpha$ - and  $\beta$ -pulses is most significant (cf. Fig. 8.6), while the *total interval* is used as a normalization factor. Subsequently, the ratio between the tail and the total interval, TTR, is given as:

$$\text{TTR} = \frac{\int_{\text{tail}}^{\infty} p(t) dt}{\int_0^{\infty} p(t) dt} = \frac{\sum_{i=\text{tail}}^{1250 \text{ ns}} p_i}{\sum_{i=0}^{1250 \text{ ns}} p_i}, \quad (8.4)$$

with the entries in the pulse histogram  $p_i$ .

An advantage of the TTR method is its straightforward implementation. Furthermore, no knowledge of average pulse shapes is required. A disadvantage is that only integrated information is used. Thus, the TTR method is often not as powerful as other, more sophisticated methods.<sup>6</sup>

As neutron and proton signals have a more substantial fraction of the slow components, these events have, on average, a higher TTR value than  $\beta$ -events. The optimal start value of the tail interval depends mainly on the probability density function of the photon emission process, described by Eq. (8.1). Consulting Tab. 8.1, after  $\sim 100$  ns, the majority of photons are emitted by the third, slow component. Hence, the fraction of photon hits in the tail interval is directly connected to the strength of the third component  $N_3$ , which differ for  $\alpha$ - and  $\beta$ -events.

First, the impact of the start value of the tail interval named *tail value* on the discrimination efficiency is studied. Therefore, the tail value is varied between 80 ns and 260 ns, and the resulting TTR distributions are shown for atmospheric NC and DSNB events in Fig. 8.7. In principle, the separation is enhanced by higher tail values, as the difference between the pulses is most visible for later times. However, the amount of photon entries is reduced. A value of 120 ns as the start for the tail value is chosen as a reasonable compromise to ensure that enough entries remain in the tail of the pulse.

Moreover, from Fig. 8.7 one can see that the distribution is not symmetric, which is caused by a slight position dependence of the pulse form, and visualized in Fig. 8.8. There are several reasons for a position-dependent pulse shape. First of all, the probability for a photon to be scattered before reaching the PMT depends on the event position. At the center of the detector,  $\sim 35\%$  of all detected photons

<sup>6</sup> Advanced methods, like the Gatti method or methods using neural networks, could provide better discrimination efficiencies [314, 315]. However, they are not discussed within this work, as the present work aims to assess the potential of a PSD. It is not assumed that the obtained background identification efficiencies are already maximized for DSNB detection purposes.

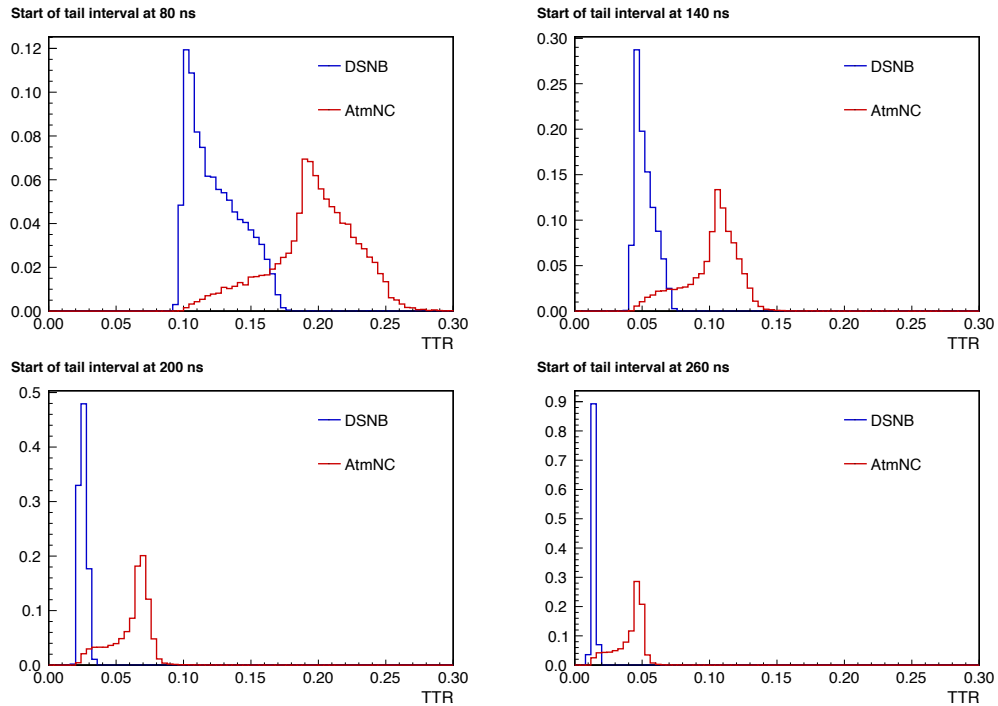


Figure 8.7: The normalized  $TTR$  distribution of simulated atmospheric  $NC$  (red) and  $DSNB$  (blue) events is shown. The integration starting point of the tail interval - tail value - following Eq. (8.4) is varied between 80 ns and 260 ns from top left to bottom right. A higher tail value shifts the  $TTR$  distribution to lower values, while the separation improves.

were scattered while at the edge only  $\sim 23\%$  undergo scattering. Hence, the statistical fluctuation of the photon detection time is increased due to the scattering effect, as scattered photons are detected later than un-scattered ones. The  $TOF$  of a scattered photon is longer than the one assumed in pulse reconstruction. Thus, the  $TOF$  corrected emission time of a scattered photon is delayed, and therefore the  $TTR$  rises with the number of scattered photons, which deteriorates the discrimination efficiency. This effect of position dependence explains the shape of the distribution of  $DSNB$  events in, e.g., the left upper panel of Fig. 8.7, which is the sum of Gaussian distributions. As more events in the outer shells show lower  $TTR$  values, this explains the right-skewed distribution. Contrary the flat amount of atmospheric  $NC$  events cannot be explained through this. That are mainly events with de-excitation  $\gamma$ 's (cf. section 6.3), which are "positron" like events due to the same fluorescence timing parameters (Tab. 8.1) and reach therefore into the  $TTR$  distribution of  $DSNB$  events.

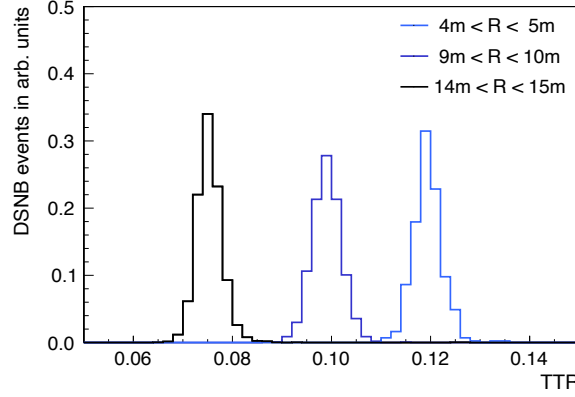


Figure 8.8: The normalized  $TTR$  distribution of  $DSNB$  events dependent on the event position in the detector is plotted. The plot shows the distribution for events within three exemplary detector shells of 1 m width. The  $TTR$  value decreases for events occurring near the detector edge.

Furthermore, the pulse form could change due to the enhanced probability for total reflection at the edge of the scintillator volume. As the scintillator and the buffer medium have different refraction indices, a certain number of photons will not be detected directly at the photocathode, if the angle of photons impinging on the sphere is large enough. The critical angle for total internal reflection is

$$\theta_C = \arcsin\left(\frac{n_{\text{Buffer}}}{n_{\text{LS}}}\right) = \arcsin\left(\frac{1.33}{1.54}\right) \sim 60^\circ. \quad (8.5)$$

The angle  $\alpha$  under that photons impinging (cf. Fig. 8.4)

$$\cos \alpha = \frac{R_{LS}^2 + d_{LS}^2 - r^2}{2R_{LS} \times d_{LS}}, \quad (8.6)$$

can be determined through the law of cosine and maximizes for  $d_{LS} = \sqrt{R_{LS}^2 - r^2}$  with

$$\hat{\alpha} = \arccos\left(\frac{\sqrt{R^2 - r^2}}{R}\right) \sim 65^\circ, \quad (8.7)$$

for  $r = 16$  m and  $R_{LS} = 17.7$  m. Therefore, the simulation was performed within the inner 16 m detector volume, to get rid of most effects due to reflection, appearing at the detector edge.

In order to consider the position-dependent pulse form and to avoid pulse shape corrections, a radius dependent  $TTR$  cut value is chosen to increase separation efficiency.

All in all, for each simulated event, the  $TTR$  was calculated based on the obtained pulse gained from the pulse simulation process explained in section 8.1. The ratio of the detected photons in the time intervals [120 ns, 1250 ns] and [0 ns, 1250 ns] was saved. As a loss in signal mostly accompanies the usage of background identification methods, eight different cut modi were defined by their minimum amount of surviving  $DSNB$  signal events, meaning that the  $TTR$  cut values were chosen to meet the requirements for the signal efficiency, which were varied between 40% and 98%. A  $DSNB$  signal rate of 37.7/(100 kt yr) (cf. Tab. 4.1 from chapter 4), and an atmospheric  $NC$  background rate of 780/(100 kt yr) (cf. Tab. 6.2 in chapter 6) was used. Fig. 8.9 shows the resulting signal and background rates in the dependence of the  $TTR$  cut modus. Linear interpolation between the cut modi is visible as the solid black line. Besides, background rejection efficiency can be taken from the upper x-axis.

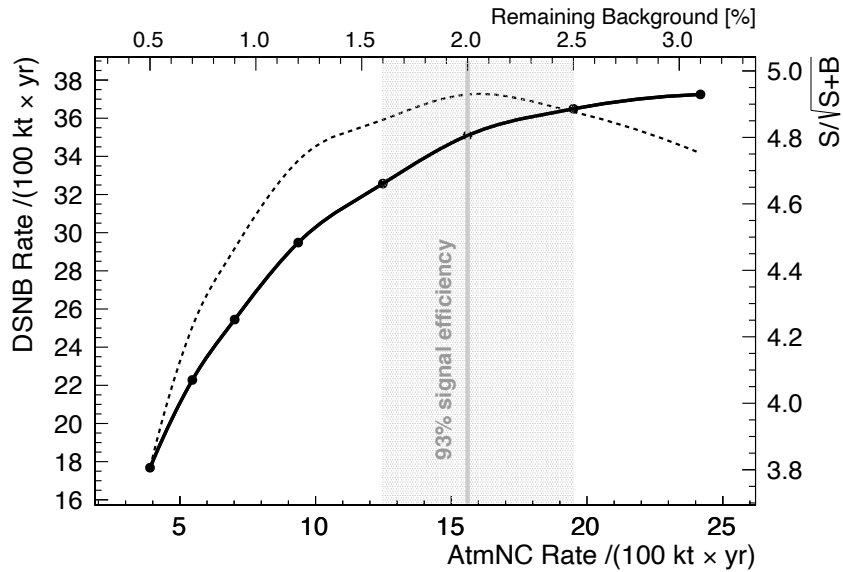


Figure 8.9: The solid black line shows the amount of  $DSNB$  signal events compared to the remaining atmospheric  $NC$  event rate and dependent on the  $TTR$  cut setting. The dashed line corresponds to the right y-axis and shows the significance, defined in Eq. (8.8), with  $S$  and  $B$  the amount of signal and background events, respectively. The cut that maximizes the significance is marked with the grey line, corresponding to a signal efficiency of  $\sim 93\%$ .



Moreover, the "significance", defined as

$$\frac{S}{\sqrt{S+B}}, \quad (8.8)$$

with  $S$  and  $B$  the amount of signal and background events, respectively, is given by the dashed line, corresponding to the right y-axis. This simple significance-like expression is used for optimization purposes. As the imposed maximization could be overestimated, in the following, the focus will be on all cut strategies shown as the shaded area in Fig. 8.9, with signal efficiencies between 86% and 97% [316].

In addition, the PSD efficiency for the background induced by fast neutrons, which was introduced in section 7.2 was studied. For this purpose  $10^5$  neutrons with a flat energy distribution up to 50 MeV were simulated in the central detector volume. If neutrons with flat energy distribution not necessarily show a flat distribution of deposited energy, an energy-dependent correction factor was introduced. The resulting TTR distribution of the simulated neutrons with flat energy distribution was afterward weighted with this correction factor. Based on the TTR cut strategy favored in Fig. 8.9, the fast neutron background is reduced to  $\sim 4\%$ .<sup>7</sup>

It is assumed that other background sources, like reactor neutrinos, atmospheric charged current reactions, and cosmogenic  ${}^9\text{Li}$  background, will have the same signal loss due to PSD as obtained for the DSNB signal.

All in all, Fig. 8.10 shows the potential of a PSD cut. The prompt energy spectra shown for the simulated data from the signal (section 4.4) and the background events (chapters 5, 7, and 6). The upper plot shows the spectra of the IBD-like events, where the muon veto cut, described in section 7.1, is applied. The PSD method with a signal efficiency of  $\sim 93\%$  is applied, visible in the lower plot, mainly reducing the amount of atmospheric NC events and fast neutron background.

The PSD represents a promising tool in LS detectors to suppress the background below the aimed for DSNB signal. Nevertheless, a second background identification method in order to further suppress the atmospheric NC events is discussed within the next chapter.

<sup>7</sup> An overview of all cut efficiencies can be found in the appendix in Tab. A.2

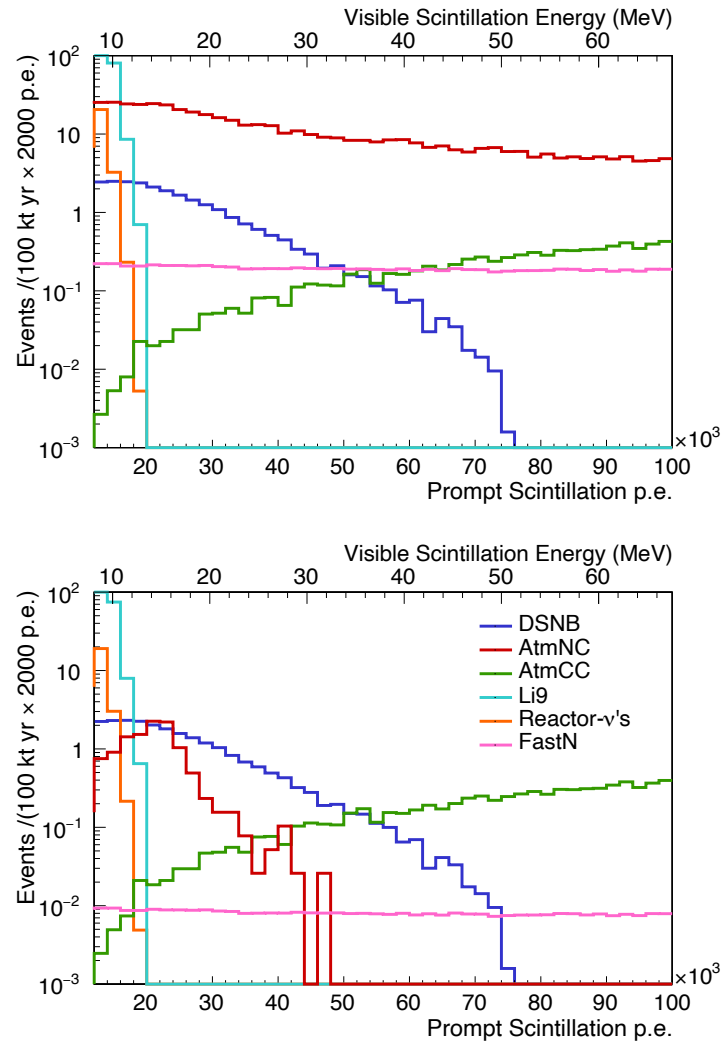


Figure 8.10: The visible energy spectrum expected for the **DSNB** signal (blue) and its ample backgrounds, including reactor neutrinos (orange), cosmogenic  ${}^9\text{Li}$  (turquoise), fast neutrons (pink) as well as atmospheric neutrino **CC** (green) and **NC** (red) interaction rates. The upper plot is before application of discrimination techniques. The lower plot shows the potential of application of **PSD**, with the **TTR** cut ensuring 93% signal efficiency, greatly reducing the atmospheric **NC** background, as well as background events from fast neutrons.

## Chapter 9

# Delayed Decay Triple Coincidence

As the atmospheric neutral current (NC) background overwhelms the diffuse supernova neutrino background (DSNB) signal by orders of magnitude (cf. chapter 6), it is necessary to develop powerful veto strategies in order to reduce the background. A possible proposed background suppression method, beside pulse shape discrimination, is to search for the coincidence of atmospheric NC events with the subsequent decay of any within the NC reaction produced radioactive isotope. In atmospheric NC events, nucleons are knocked out of the  $^{12}\text{C}$  nucleus, where the thermalization of final particles provides the prompt signal, and the neutron capture the delayed signal. As some of the resulting final nuclei of atmospheric NC reactions (cf. Tab. 6.2) are not stable, they will decay afterward. Depending on the isotope, they will decay immediately or after several microseconds up to days. If there is a third time-resolvable signal arising from a delayed decay after a prompt-delayed inverse  $\beta$ -decay (IBD)-like candidate, this offers an additional veto strategy.<sup>1</sup> The possibility of a three-fold coincidence to tag the decay events on a one-by-one basis is depicted schematically in Fig. 9.1. After the IBD coincidence signal, the event is tagged if there is a third signal within a proposed veto time  $t_V$ . This veto procedure is discussed in the present chapter.

Outgoing from the resulting nuclei given in Tab. 6.2 in chapter 6, such a cut can be applied to tag  $^{11}\text{C}$ ,  $^{10}\text{C}$ , and  $^8\text{Li}$ . All other listed isotopes are either stable ( $^{11}\text{B}$ ,  $^{10}\text{B}$ ,  $^9\text{Be}$ ,  $^6\text{Li}$ ), or decay almost instantly ( $^9\text{B}$ ,  $^8\text{Be}$ )<sup>2,3</sup>. Therefore, the following discussion concentrates on the possibility of tagging the delayed decays of  $^{11}\text{C}$ ,  $^{10}\text{C}$ , and  $^8\text{Li}$ .<sup>4</sup> As the promising channels of atmospheric NC reactions with  $^{11}\text{C}$ ,  $^{10}\text{C}$ , and  $^8\text{Li}$  in

<sup>1</sup> This procedure is adapted from the three-fold coincidence after a muon track to look for  $^{11}\text{C}$  production [317].

<sup>2</sup> As  $^9\text{B}$ ,  $^8\text{Be}$  will decay instantly into two  $\alpha$ -particles, these reactions should be possible to veto through PSD described in chapter 8. As the decaying particles are not included in JUNO's Offline Simulation Framework, the observed PSD potential is slightly underestimated.

<sup>3</sup> Tab. A.3 in the appendix lists the radioactive decays of the final state nuclei from atmospheric NC reactions on  $^{12}\text{C}$ .

<sup>4</sup> Their decay schemes are shown in the appendix in Fig. A.4

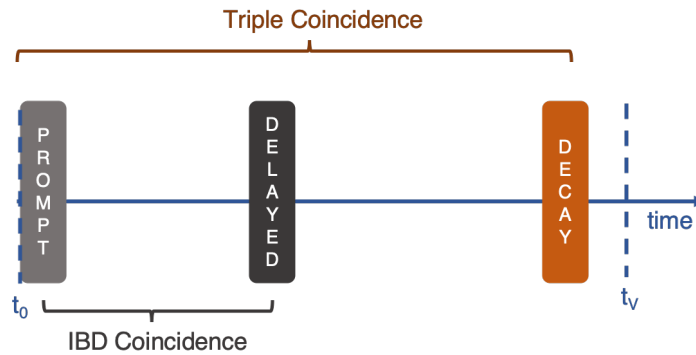


Figure 9.1: The basic idea of the proposed triple coincidence veto. After each **IBD**-candidate, consisting of the prompt and delayed signal, one can probably tag one-by-one events from atmospheric **NC** reactions. If there is a third signal arising from radioactive decay of the unstable nuclei, this allows distinguishing between **DSNB** events and atmospheric **NC** background.

the end state sum up to  $\sim 40\%$  of all background events, it is encouraging to study the possibility of a triple coincidence veto.

$^{11}\text{C}$  is a positron emitter with an endpoint at 0.96 MeV, and therefore, the total deposited positron energy in the scintillator after annihilation is between 1.02 MeV and 1.98 MeV. The energy deposition of the released positron of the  $^{10}\text{C}$  decay is between 1.02 MeV and 2.93 MeV, accompanied by one (718 keV) or two (1.022 keV)  $\gamma$ -lines so that the total amount of deposited energy will be between 1.74 MeV and 3.65 MeV. The maximum energy of the released electron from  $^8\text{Li}$  decay is 12.97 MeV, released with one 3.03 MeV- $\gamma$ , summing up to a deposited energy up to  $\sim 16$  MeV. As the energy depositions, as well as the decay times, differ, a more advanced veto strategy compared to Fig. 9.1 is proposed and presented in Fig. 9.2. The total veto time  $t_V$  is separated into three veto time windows, with different vetoed energy regions, to account for different energy depositions and half-life times of  $^{11}\text{C}$ ,  $^{10}\text{C}$  and  $^8\text{Li}$ . The veto time  $t_V^i$  should be set to a few times the lifetime  $\tau$  of the isotopes. The energy ranges consider energy resolution effect and is chosen large enough ( $3\sigma$ ) to ensure that the energy deposition will be within the vetoed window.

Once the position of the prompt signal and/or the closeby delayed neutron capture is known, one needs to apply a cut in space and time around each **IBD**-candidate and veto events with the corresponding energy deposition. This is sketched in Fig. 9.3 where the grey shaded area represents the vetoed volume with radius  $R_V$ . As the reconstructed position of the neutron capture or the prompt signal does not

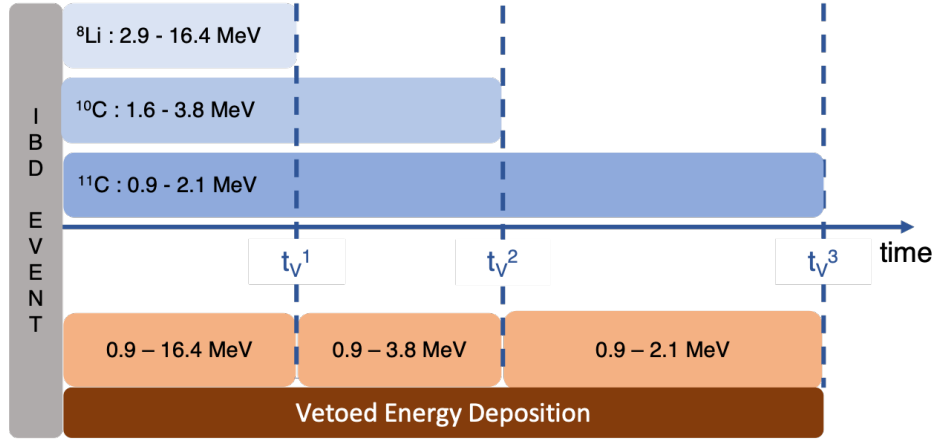


Figure 9.2: The advanced triple coincidence veto strategy. After an **IBD** event candidate, for a specific time  $t_V^1$ , any event with an energy deposition between 0.9 MeV and 16.4 MeV will be vetoed, to tag  $^{11}\text{C}$ ,  $^{10}\text{C}$ , and  $^8\text{Li}$ . To consider the longer half-lives of  $^{10}\text{C}$  and  $^{11}\text{C}$ , even smaller energy windows are vetoed for  $t_V^2$ , and  $t_V^3$ , respectively.

tell us about the position of the isotopes birthplace, compare Fig. 9.4, it is crucial to set the radius of the spherical cut large enough to ensure that the decay could happen inside the defined volume.

Hence, if events occur during the defined vetoed time  $t_V$  from the **IBD** coincidence and inside a sphere of radius  $R_V$  from the event point, they are rejected, and the probability  $P_{\text{veto}}$  to veto such a delayed decay is given through

$$P_{\text{veto}} = \left(1 - \exp\left(-\frac{t_V}{\tau}\right)\right) \times P_{R_V}. \quad (9.1)$$

Here,  $P_{R_V}$  is the probability that the decay will happen inside the defined veto sphere with radius  $R_V$ . The displacement of the third signal arising from a decay of the residual nucleus from the prompt and delayed signal, that determines the probability to be within the vetoed sphere will be discussed in the next section. As large veto volume, as well as long veto times, are accompanied by higher signal losses, this aspect is the topic of section 9.2

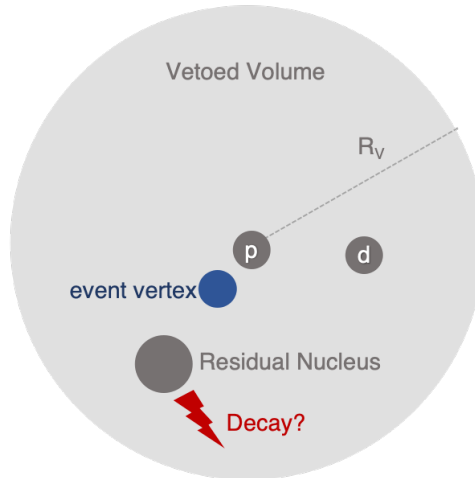


Figure 9.3: After each **IBD**-candidate, consisting of a prompt ( $p$ ) and delayed ( $d$ ) event, a volume is vetoed with radius  $R_V$  around the event point. Here the position of the prompt event is chosen as the midpoint. The decay of the residual nucleus does not have to take place at the prompt signal position. Therefore, the chosen vetoed volume has to be large enough to ensure that the third signal of the triple coincidence will be within the volume.

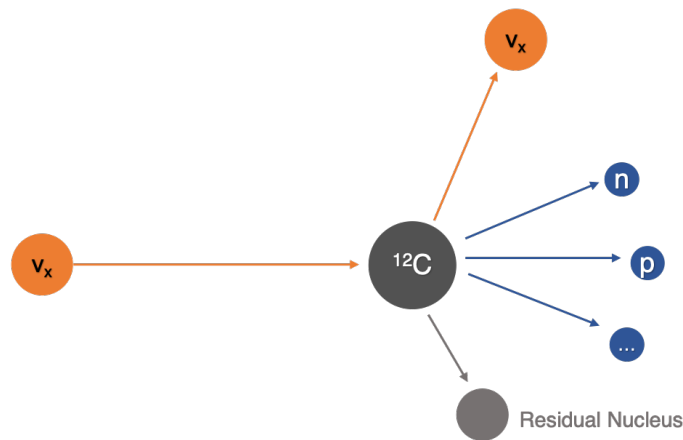


Figure 9.4: Sketch of an atmospheric **NC** event. The neutrino hits a  $^{12}\text{C}$  nucleus and is scattered, while neutrons, protons, etc. can be created. The residual nucleus could also drift from the point of reaction if it gets some kinetic energy. The prompt event results from scattering reactions of the neutrons and protons, and the delayed neutron capture happens where the neutron is thermalized. Hence, there is less information about the position of the residual nucleus obtained from observation of the prompt and delayed event.

## 9.1 Size of the Vetoed Volume

If the residual nuclei have less momentum energy, compared to the knocked out nucleons, they will rest close to the point of creation. Hence, the chosen veto volume should consider, besides the detector vertex resolution effect, also the length that the resulting decay products (electrons, positrons,  $\gamma$ 's) need to deposit their energy. Moreover, it is often possible to localize, at least crudely, the point where the positron annihilates and where the neutron is captured. Even though the neutron is captured only after many elastic scatterings until it reaches thermal energy, its final position maintains some memory of its initial direction. In the following, the displacement between the prompt and the delayed neutron signal from the event vertex will be studied in order to choose an appropriate vetoed volume.

The true event vertex is obtained from JUNO's Offline Simulation Framework and the Monte-Carlo (MC) truth information. Therefore, the energy deposition of a Geant4 particle track is divided into steps, that contain delta-information of the track, like the energy loss per step. The reconstructed event position  $\vec{r}$  can be approximated through:

$$\vec{r} = \frac{1}{E} \sum_{\text{steps}} E_{\text{step}} \vec{r}_{\text{step}}, \begin{cases} \text{prompt:} & 0 < t_{\text{step}} < 2 \mu\text{s} \\ \text{delayed:} & 2 \mu\text{s} < t_{\text{step}} < 1 \text{ ms}, \end{cases} \quad (9.2)$$

with  $E$  as total deposited energy  $E = \sum E_{\text{step}}$ . Note that the following discussion is based on the MC truth data without any reconstruction or vertex resolution effect.

Within the simulation of the DSNB signal events (cf. section 4) and the atmospheric NC events (cf. section 6), the event positions of the prompt and delayed signals were obtained using Eq. (9.2). The distribution of distances for simulated DSNB and atmospheric NC events is shown in the left and right plot of Fig. 9.5, respectively. The plot shows the difference in positions between the prompt signal (red) and delayed signal (green) to the point where the particles were created in the simulation. The black line represents the distribution of the difference between prompt and delayed signals.

First, for both event classes, the prompt signal (red) is closer to the point of particle creation than the delayed signal (green). Furthermore, the prompt DSNB signal is closer to the point of creation compared to the prompt signals of the atmospheric NC events. In first order, this is because, the positron from the DSNB signal annihilates immediately, while the prompt signal of atmospheric NC events is a combination of the longer-lasting thermalization processes of the resulting particles.

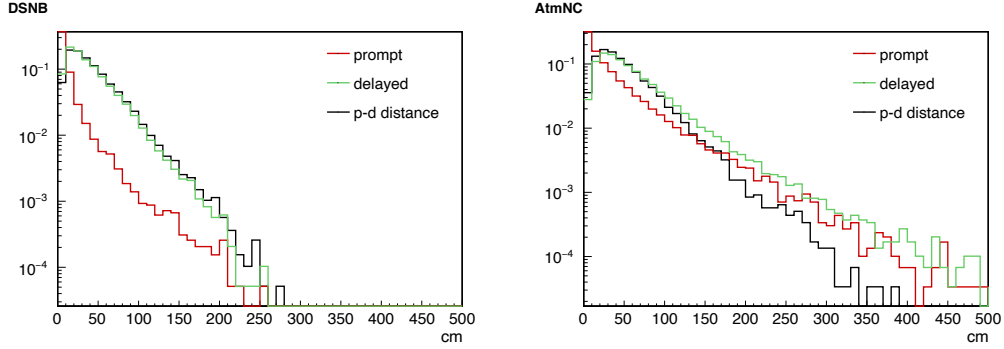


Figure 9.5: Distribution of position displacement for **DSNB** (left plot) and simulated atmospheric **NC** events (right plot). The difference between the prompt signal position and the point of particle creation (red) is compared to the difference of the delayed signal position to the point of initial event vertex (green). The black line represents the distribution of the difference between prompt and delayed signals.

Moreover, the delayed signal is further away from the point of creation for atmospheric than for **DSNB** events. This is because the energy transfer to the neutron is negligible for the relatively "low energy" **DSNB** neutrinos, compared to the energy transferred to the positron. Contrary to atmospheric neutrinos, which can have several GeV energy, and the energy transfer to the neutron cannot be neglected anymore.<sup>5</sup> As the kinetic energy of the resulting neutron is much smaller than the kinetic energy of the released positron in a **DSNB** reaction, the position of the prompt signal is mainly determined by the kinetic energy deposition of the positron. The two 511 keV gammas from positron annihilation are sent in the opposite direction so that there is in first-order no effect on position due to the annihilation gammas. Contrary, the prompt signal of the atmospheric neutrino events is mainly caused by the same particle, neutron, as the delayed signal. This gives a directional correlation between prompt and delayed signals and manifests in the fact that the prompt-delayed distance (black) is smaller than the distance of the delayed signal to the point of creation (green), which can be seen in the right plot of Fig. 9.5.

That is the difference in comparison to **DSNB** events, where the prompt-delayed distance is slightly larger than the delayed-creation distance. To explain this behavior, the angle

$$\theta = \arccos \left( \frac{\vec{p}_e \cdot \vec{p}_n}{|\vec{p}_e| + |\vec{p}_n|} \right), \quad (9.3)$$

between the direction of positrons and neutrons from **DSNB** events, with infor-

<sup>5</sup> The kinetic energy distribution of neutrons from **DSNB** and atmospheric **NC** events is given in the appendix in Fig. A.5



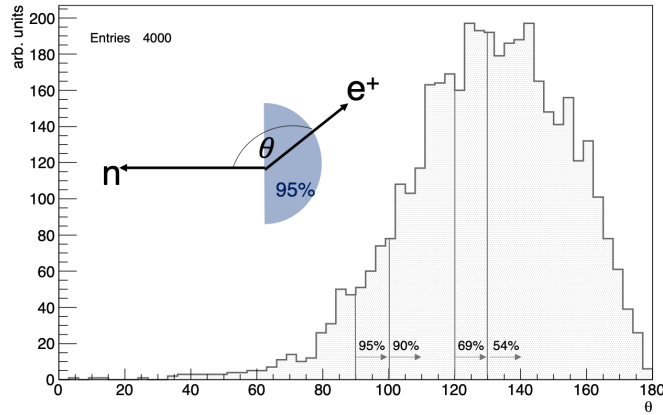


Figure 9.6: The angular directional distribution between positron and neutron of **DSNB** events, obtained using Eq. (9.3) with momentum information from **MC** simulation. Approximately 95% of the values are between  $90^\circ$  and  $180^\circ$ , which means the majority of resulting particles are sent in the nearly opposite direction.

mation from **MC** truth on the initial momenta  $\vec{p}_e$  and  $\vec{p}_n$ , was determined. The  $\theta$ -distribution is plotted in Fig. 9.6 and shows that  $\sim 95\%$  of the particles are sent in the nearly opposite direction. Hence, the prompt-delayed separation is enhanced for **DSNB** events through this effect. The discussion is summarized in Fig. 9.7, where the yellow boxes represent the reconstructed prompt and delayed vertices of an exemplary **DSNB** (left) and atmospheric **NC** background event (right).



Figure 9.7: Sketch of an exemplary **DSNB** and atmospheric **NC** event. The prompt (**P**) and delayed (**D**) vertex position are closer to the reaction vertex for **DSNB** events than for atmospheric **NC** events. Since the prompt and delayed events of atmospheric **NC** events are caused by mainly the same neutron particle, the distance between prompt and delayed signal vertices is reduced. As the neutron and positron from the **DSNB** event, are in first-order emitted in opposite directions, the prompt-delayed distance is enhanced.

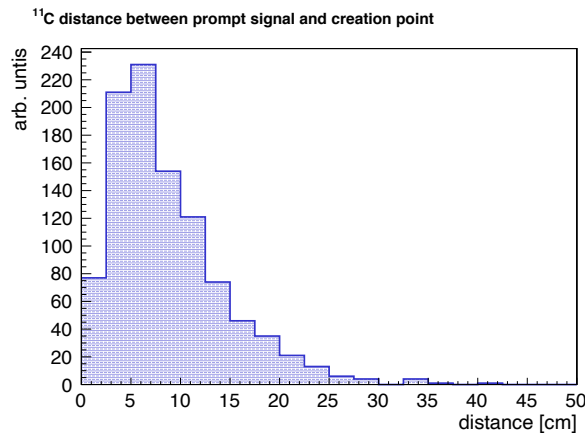


Figure 9.8: Displacement between the  $^{11}\text{C}$  decay vertex and the event position of the deposited positron energy.

Finally, one has to consider the displacement between the point of creation and the energy deposition of the decaying unstable isotope. This was studied exemplary by simulating positrons from the decay of  $^{11}\text{C}$ . Fig. 9.8 shows that the displacement between the production point of the positron from the  $^{11}\text{C}$  decay and the energy deposition place is less than 0.5 m and negligible in comparison to the displacement of the prompt and delayed signal described above.

The discussion is concluded as follows. First, it is assumed that the residual nucleus is getting a small amount of energy so that the decay will happen approximately at the reaction vertex. For that, the convective motion of the liquid scintillator has to be sufficiently slow [317].<sup>6</sup> Therefore, the assumption that the  $^{11}\text{C}$  nuclides displacement over their  $\sim 30$  min lifetime can be kept small in comparison to the neutrons range seems entirely justified.

Secondly, it is proposed to veto a volume around the reconstructed prompt event position, which is closer to the event vertex, where the resulting nuclei are expected to decay. The efficiency factor  $P_{RV}$ , introduced in Eq. (9.1), accounts for the probability that the radioactive decay will be within the vetoed sphere, and is approximated as follows.  $P_{RV}$  is estimated as the amount of atmospheric  $^{14}\text{C}$  events with the prompt-creation distance shorter than radius  $R_V$  (compare red distribution in Fig. 9.5). The efficiency depends on the chosen value of  $R_V$  and can be seen in Fig. 9.9. For a sphere with  $R_V = 0.5$  m the probability is estimated to be  $\sim 79\%$

<sup>6</sup> KamLAND data showed that the measured average displacement of the diffusive  $^{222}\text{Rn}$  over its 5.5 days mean life is less than 1 m [318].

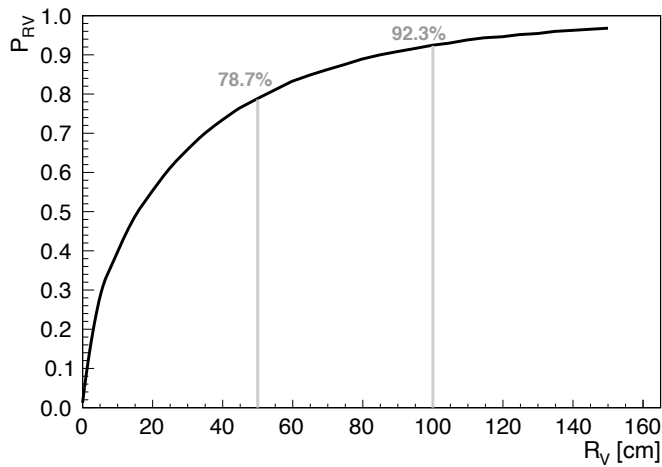


Figure 9.9: The estimated probability  $P_{RV}$  for a delayed decay of an atmospheric  $\overline{NC}$  event to be within a sphere with radius  $R_V$ . Approximately 79% or 92% will be within the sphere for  $R_V = 0.5$  m and  $R_V = 1$  m, respectively, considering no effect of vertex resolution due to detector effects as well as no convection.

and increases for even larger radii to  $\sim 92\%$  for  $R_V = 1$  m.<sup>7</sup> A larger veto volume will lead to an increased signal loss due to larger dead times and will be discussed in the next section.

<sup>7</sup> Please note, that no detector effect on the spatial resolution is considered here, which would minor decrease the efficiency as well.

## 9.2 Signal Efficiency

The usage of the proposed triple coincidence cut enables the possibility that **DSNB** signal events are accidentally vetoed. This could happen if signal events fall into the vetoed volume during the vetoed time, called dead time. Moreover, there is the possibility of accidentally arising third delayed signals after a DSNB signal, which would lead to a veto, which is not wanted. Hence, the reduction of the DSNB signal due to the proposed veto strategy is the topic of the following discussion.

The cumulative dead time  $T_{\text{dead}}$  corresponding to the triple coincidence cut can be approximated through the amount of nuclei, resulting from atmospheric **NC** reactions multiplied with the corresponding veto time  $t_V^i$ :

$$T_{\text{dead}} = \sum_i T_{\text{dead}}^i \simeq \left( \frac{R_V}{16 \text{ m}} \right)^3 \times R_{\text{NC}} \times \sum_i BR_i \times t_V^i, \quad (9.4)$$

with the branching ratio  $BR_i$  of the corresponding reaction from Tab. 6.2 and the atmospheric **NC** background rate of  $R_{\text{NC}} = 7.8 / (\text{kt yr})$ . The dead time  $T_{\text{dead}}^i$  corresponding to isotope  $i$  is plotted in Fig. 9.10 in dependency of veto time. For simplicity, the dead time is overestimated due to  $t_V = t_V^3$  and  $R_V = 2 \text{ m}$ . As can be seen in Fig. 9.10, the signal loss due to atmospheric events is not considered in the following, as it is well below 0.01%.

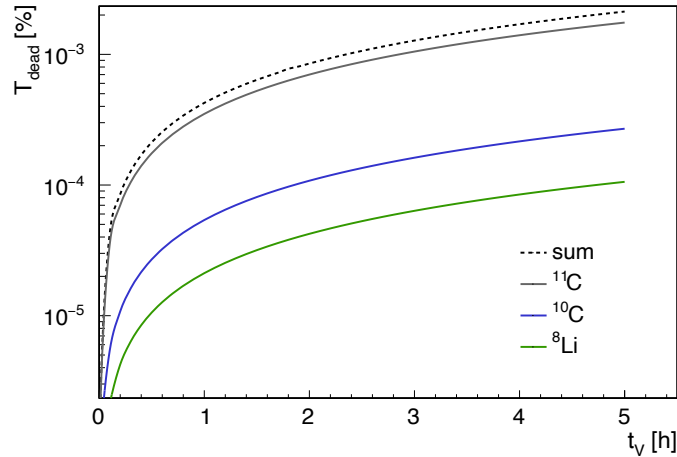


Figure 9.10: Dead time for  $R_V = 2 \text{ m}$ .

Even though the delayed decay search offers a great opportunity to veto atmospheric  $\overline{\text{NC}}$  reactions, there is the possibility of vetoing signal events in the detector, followed by an accidental third signal. These could arise from natural radioactivity or decays of cosmogenic produced isotopes and will be considered in the following.

Muons traveling through the scintillator will also produce cosmogenic isotopes, like  $^{11}\text{C}$ . As the expected muon rate in the central detector is quite high ( $\sim 3.5$  Hz), the majority of, e.g.,  $^{11}\text{C}$  in the liquid scintillator (LS) will be produced through muons instead of atmospheric neutrino reactions [192]. To estimate the influence of the cosmogenic isotope production on the proposed strategy, the possibility to veto a  $\overline{\text{DSNB}}$  signal with a random coincidence of a cosmogenic signal is calculated. The cosmogenic isotope production yields  $Y$  of  $^{11}\text{C}$ ,  $^{10}\text{C}$ , and  $^8\text{Li}$  are scaled from KamLAND measurements and summarized in Tab. 9.1 [301]. As the production yields depend on the experimental location due to the different muon rates and average muon energies, they were scaled to fit for JUNO. At JUNO's site, the mean muon energy is smaller than for KamLAND (compare Tab. 7.1 in chapter 7), the spallation production is therefore about 0.8 times lower for JUNO, expecting a cosmogenic production rate  $R_{\text{cosm}}$ , which can be taken from Tab. 9.1.

Besides cosmogenic radioisotope production, there is the possibility of having an accidental event from radioactive decays, following an  $\overline{\text{IBD}}$  signal event. Based on the radioactivity level assumptions given in [4], an overview of the different spectra of decays in the LS due to radioactivity is given in Fig. 9.11. Tab. 9.1 lists the amount of radioactive signals, expected in the proposed vetoed energy windows.

	Cosmogenic Isotopes		Radioactivity	
	$Y_{\text{KamLAND}}$ [ $10^{-7} \mu^{-1} \text{g}^{-1} \text{cm}^2$ ]	$R_{\text{cosm}}$ [/(kt h)]	vetoed energy window	$R_{\text{radio}}$ [/(kt h)]
$^{11}\text{C}$	$866 \pm 153$	$93.5 \pm 16.5$	(0.9 - 16.4) MeV	0.96
$^{10}\text{C}$	$16.5 \pm 1.9$	$1.8 \pm 0.2$	(0.9 - 3.8) MeV	0.94
$^8\text{Li}$	$12.2 \pm 2.6$	$1.3 \pm 0.3$	(0.9 - 2.1) MeV	0.90

Table 9.1: The table summarizes the cosmogenic production yields from KamLAND measurements and the expected cosmogenic production rates for JUNO for  $^{11}\text{C}$ ,  $^{10}\text{C}$ , and  $^8\text{Li}$  [301]. The right part gives the expected rate of events arising from radioactivity within the different energy regions.

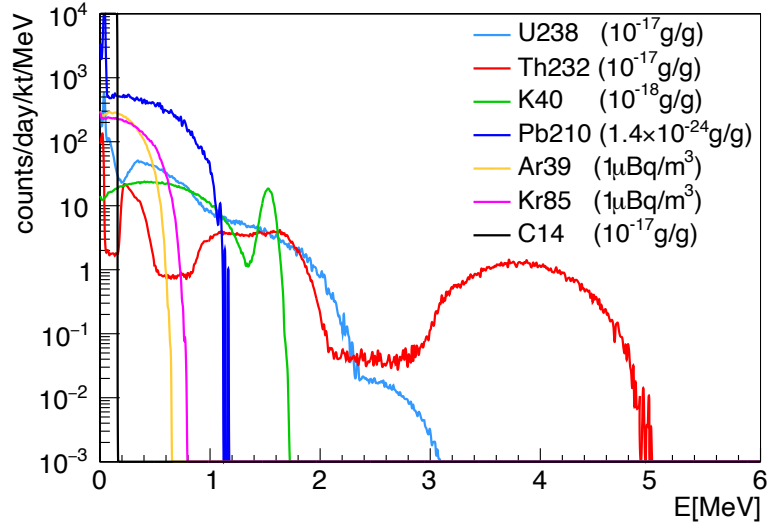


Figure 9.11: Radioactivity spectra from different radioactive isotopes marked with different colors. Figure from [319] with the radiopurity levels assumed in [4].

The Poisson possibility for zero accidental events, arising from cosmogenic isotope production or radioactivity, appearing during the vetoed time window  $t_V$  is given through

$$P = \exp[-M_V \times (R_{\text{cosm}} + R_{\text{radios}}) \times t_V], \quad (9.5)$$

for a vetoed detector mass  $M_V$ . As this represents the possibility for an event to be not vetoed through accidental events, it is assumed as the signal efficiency. Within the next section, the veto strategy is optimized in order to suppress the background by limiting the signal loss.

### 9.3 Atmospheric Background Reduction

To determine appropriate parameters for the triple coincidence cut, the gained knowledge from previous sections 9.1 and 9.2 will be merged within this section. The signal efficiency follows Eq. (9.5), while the background rejection is calculated using Eq. (9.1).

The left panel of Fig. 9.12 shows the background reduction factor dependent on the veto time  $t_V^1$  for  $R_V = 1$  m. The solid lines correspond to the three end states of atmospheric  $\text{NC}$  reactions with  $^8\text{Li}$  (green),  $^{10}\text{C}$  (blue), and  $^{11}\text{C}$  (grey). Due to the relatively short lifetime of  $^8\text{Li}$  compared to the other two isotopes, it is possible to veto nearly all of the reactions with  $^8\text{Li}$ , choosing  $t_V^1$  in the order of several seconds. The black dashed line corresponds to the right y-axis and represents the signal efficiency. If the vetoed time is short enough, the signal efficiency is nearly one. Therefore,  $t_V^1 = 8$  s is chosen, which is visualized through the vertical grey line in Fig. 9.12. After fixing  $t_V^1$ , the background rejection is shown dependent on the length of the second time interval  $t_V^2$  in the right panel of Fig. 9.12. It can be seen that it is necessary to set  $t_V^2$  to a few minutes, to reduce mainly the atmospheric  $\text{NC}$  background with  $^{10}\text{C}$ . However, this veto time is not long enough to reduce the  $^{11}\text{C}$  reactions noticeably. Again, the right y-axis shows the signal efficiency corresponding to the black dashed line. Therefore, the length of the second time interval  $t_V^2 = 3$  min is chosen, which is accompanied by a signal loss of  $\sim 2\%$ .

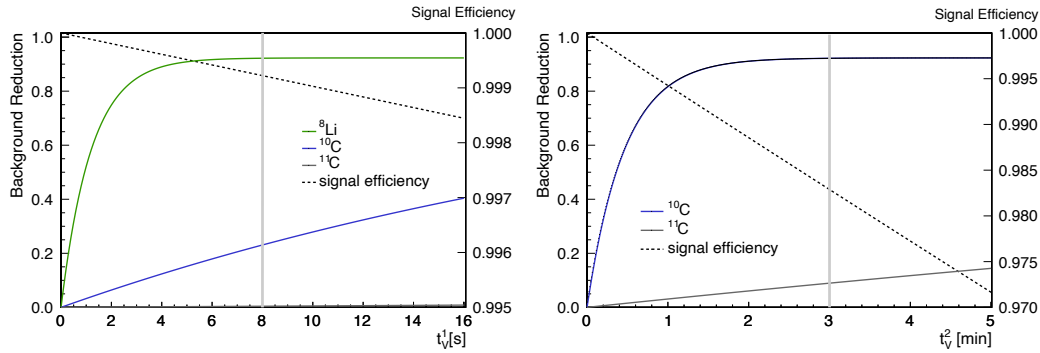


Figure 9.12: The background rejection factor is shown dependent on the length of the vetoed time intervals  $t_V^1$  (left panel) and  $t_V^2$  (right panel). The solid lines represent the background rejection of atmospheric  $\text{NC}$  events with  $^8\text{Li}$  (green),  $^{10}\text{C}$  (blue), and  $^{11}\text{C}$  (grey) in the end state. The signal efficiency is given as the dashed black line, corresponding to the right y-axis. For both plots, a vetoed volume with  $R_V = 1$  m is assumed. The length of the time intervals  $t_V^1$  and  $t_V^2$  are chosen to be 8 s and 3 min, respectively, which is visualized through the vertical grey line.

Lastly,  $t_V^3$  has to be determined to reduce the reactions with  $^{11}\text{C}$ , as this corresponds to the reaction with the highest branching ratio ( $\sim 33\%$ ). The  $^{11}\text{C}$  background reduction related to  $t_V^3$  is given in Fig. 9.13. The background rejections (solid lines) are given for two vetoed volumes with  $R_V = 0.5$  m (red) and  $R_V = 1.0$  m (grey). A larger vetoed volume enhances the background rejection. The signal efficiencies (dashed lines) are shown for comparison related to the right y-axis. Hence, a larger veto volume drastically reduces the signal efficiency.

To find a reasonable compromise, the signal and background rates are compared in Fig. 9.14. The atmospheric **NC** event rate is given for different values of  $t_V^3$  for the two proposed vetoed volumes with  $R_V = 0.5$  m (red) and  $R_V = 1.0$  m (grey). A **DSNB** signal rate of  $37.7 / (100 \text{ kt yr})$  (cf. Tab. 4.1 in chapter 4), and an atmospheric **NC** background rate of  $780 / (100 \text{ kt yr})$  (cf. Tab. 6.2 in chapter 6) was used. Within the first hour, the background rate decreases fast, while the slope mitigates after  $\sim 2$  h. Now, the right y-axis is related to the signal to background ratio  $S/\sqrt{S+B}$ , with the amount of signal events  $S$  and remaining background events  $B$ . The significance-like value is used to optimize the length of the veto time window  $t_V^3$  (dashed lines). As the larger veto volume would drastically decrease the signal efficiency (Fig. 9.13), this strongly affects the signal-to-background ratio. Therefore, the smaller veto volume with  $R_V = 0.5$  m and the length of the third veto time  $t_V^3 = 1.5$  h is chosen.

The **DSNB** signal efficiency, corresponding to the probability of zero cosmogenic and radioactive events during the vetoed time, is  $\sim 94\%$ . As the possibility to get a random event after an event candidate, is not depending on the type of background, we assume that all the other background rates are reduced as well by 6% by applying this proposed veto. The total amount of atmospheric **NC** reactions can be reduced by  $\sim 35\%$ . The effect on the different reaction channels can be taken from Tab. 9.2.



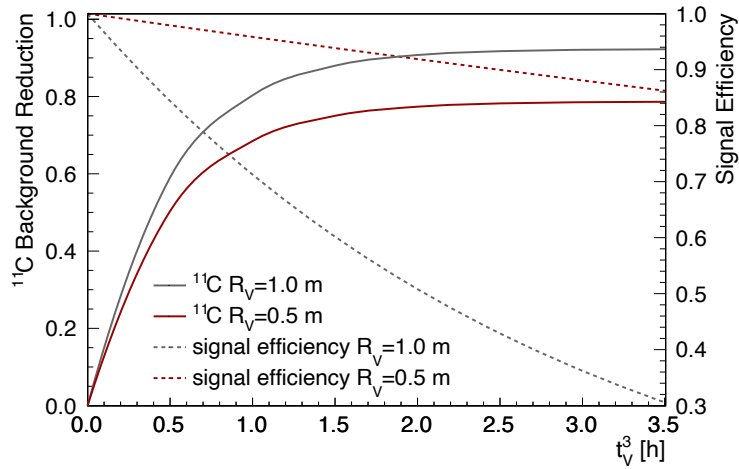


Figure 9.13: The  $^{11}\text{C}$  background rejection (solid lines) is given for two vetoed volumes with  $R_V = 0.5$  m (red) and  $R_V = 1.0$  m (grey). The signal efficiencies (dashed lines) are shown for comparison related to the right y-axis.

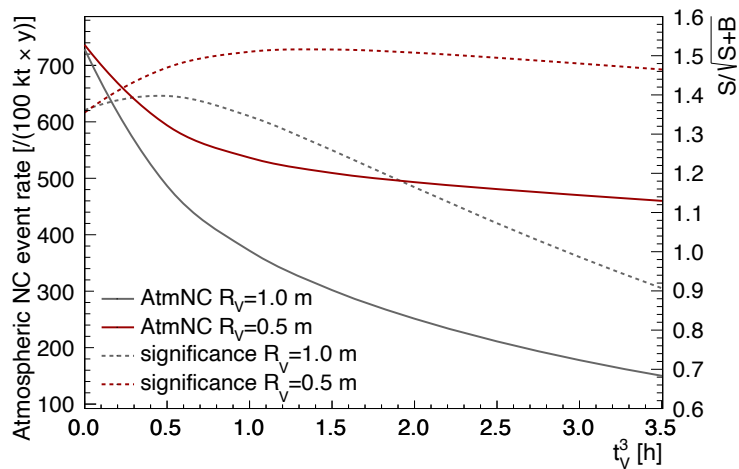


Figure 9.14: The remaining atmospheric  $\boxed{\text{NC}}$  event rate in relation to the length of the third veto time  $t_V^3$  for the two proposed vetoed volumes with  $R_V = 0.5$  m (red) and  $R_V = 1.0$  m (grey). The signal-to-background ratio  $S/\sqrt{S+B}$  is given with the dashed line and corresponds to the right y-axis. The length of the third veto time  $t_V^3 = 1.5$  h is chosen.

Atmospheric $\overline{\text{NC}}$ interactions [/(kt yr)]		
$\nu_x + {}^{12}\text{C} \longrightarrow \nu_x + \dots$		Triple Coincidence Veto
$n + {}^{11}\text{C}$	2.6	0.6
$n + p + {}^{10}\text{B}$	1.8	1.7
$n + 2p + {}^{10}\text{Be}$	0.7	0.7
$n + p + {}^2\text{H} + {}^8\text{Be}$	0.6	0.5
$n + p + {}^4\text{He} + {}^6\text{Li}$	0.5	0.5
$2n + {}^{10}\text{C}$	0.4	0.08
$2n + 2p + {}^8\text{Be}$	0.2	0.2
$2n + p + {}^9\text{B}$	0.2	0.2
$n + 3p + {}^8\text{Li}$	0.2	0.03
other channels	0.7	0.6
sum	7.8	5.1

Table 9.2: Reaction channels of atmospheric  $\overline{\text{QEL}} \overline{\text{NC}}$  reactions on  ${}^{12}\text{C}$ , sorted by their prevalence. The left column lists the  $\overline{\text{NC}}$  interactions after the event selection described in section 4.4. The right column shows the reduction after applying the triple coincidence veto with a vetoed volume of  $R_V = 0.5$  m. The reaction channels that are can be reduced through a tag of the third delayed decay signal are highlighted in grey.

# **DSNB DETECTION POTENTIAL**



## Chapter 10

### DSNB Detection Potential in JUNO

Besides the aimed-for diffuse supernova neutrino background (DSNB) signal, several background sources are present. The signal estimation for the Jiangmen Underground Neutrino Observatory (JUNO) detector is discussed in section 4.3.<sup>1</sup> The background arising from atmospheric neutrino interactions: the charged current reactions of atmospheric electron antineutrinos on  $^1\text{H}$ , and the quasielastic neutral current (NC) reactions of atmospheric events on  $^{12}\text{C}$  are the topic of chapter 6. The reactor neutrino background (cf. chapter 5), as well as muon-induced backgrounds from the decay of cosmogenic produced  $^9\text{Li}$  (cf. section 7.1) and from fast neutrons (cf. section 7.2), also contribute.

Apart from the background arising from fast neutron interactions, the signal and background sources were simulated within the JUNO's Offline Simulation Framework (OSF), which is introduced in section 3.3. After the event simulation, the inverse  $\beta$ -decay (IBD) event selection was performed, which is described in section 4.4. The obtained simulated event spectrum, including the signal and different background sources, is shown in Fig. 10.1. As the background events surpass the DSNB signal by orders of magnitude, there is a need for potent background identification methods, which are the topic of chapter 7–9.

First, the so-called muon veto cut (cf. section 7.1), allows reducing the cosmogenic  $^9\text{Li}$  background events by  $\sim 98\%$  by vetoing a cylinder around reconstructed muon tracks. However, this cut introduces dead-time and reduces signal efficiency by 16%. The simulated event spectra after applying the muon veto cut are shown in the left plot of Fig. 10.2. Furthermore, the powerful tool of pulse shape discrimination (PSD) (described in chapter 8) allows for noticeably background reduction of fast neutron and atmospheric NC background, which can be seen in the right plot of Fig. 10.2. Moreover, the possibility to reduce the atmospheric NC background with the so-called triple coincidence cut is studied in chapter 9. The option to identify atmospheric NC events through the delayed decay of produced unstable

---

<sup>1</sup> In the present chapter, the DSNB signal is referred to as the fiducial flux model unless otherwise stated.

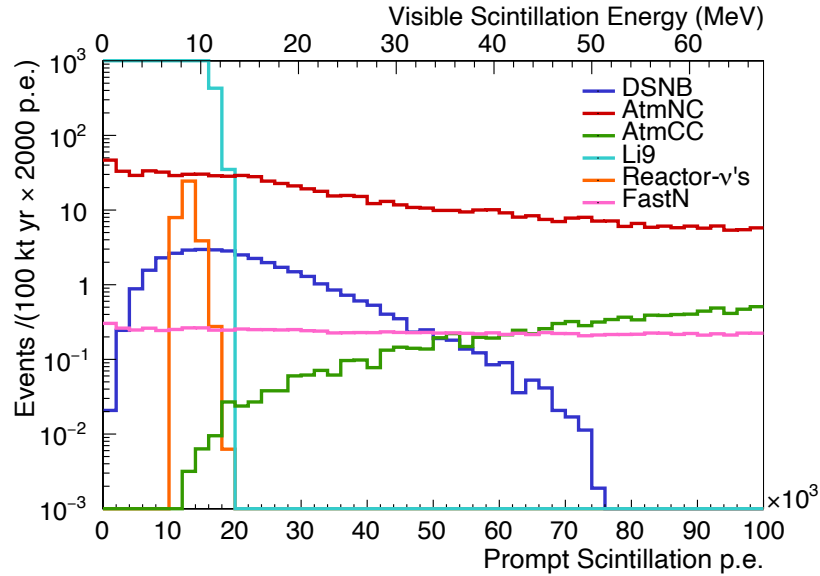


Figure 10.1: Prompt energy spectrum obtained from event simulation using [JOSF](#) and after [IBD](#) event selection. The visible energy deposition of the prompt event corresponding to the number of scintillation photoelectrons is given on the upper x-axis. The background events surpass the [DSNB](#) signal (dark blue) by orders of magnitude. Note that reactor neutrinos (orange) are simulated with a lower energy threshold of  $\sim 9$  MeV. The fast neutron rate corresponds to an inner detector volume with  $R < 16$  m.

isotopes introduces an additional dead-time of  $\sim 7\%$ , but could reduce the atmospheric [NC](#) background further by  $\sim 40\%$ . Therefore, evaluation, if this cut will even improve the signal-to-background ratio, is necessary. A summary of the event rates can be taken from Tab. [10.1](#).<sup>2</sup>

Within the present chapter, the detection potential of the [DSNB](#) in [JUNO](#) will be estimated and discussed. First, a proposal for the data processing procedure, called the detection strategy, is given in section [10.1](#), which is necessary to extract the signal from the overwhelming background. Assuming the feasibility of the described strategy, the sensitivity of successful detection is estimated in section [10.2](#). Finally, the possibility to extract information about astrophysical parameters out of the hopefully successful [DSNB](#) detection in the future is discussed in section [10.3](#).

<sup>2</sup> The table containing the corresponding cut efficiencies can be found in the appendix in Tab. [A.4](#)

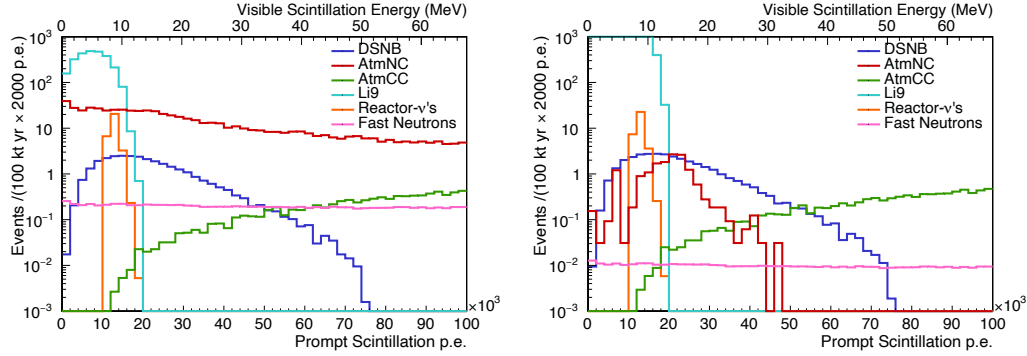


Figure 10.2: Prompt energy spectrum obtained from event simulation using **JOSF** and after **IBD** event selection. The muon veto cut was applied for the left plot, which drastically reduces the background events from the decay of cosmogenic produced  ${}^9\text{Li}$  but introduces  $\sim 16\%$  dead time. Additionally, **PSD** was used to distinguish  $\alpha$ - and  $\beta$ -like events, visible in the right plot. The **PSD** tool strongly reduces the background from atmospheric NC events (red) and fast neutrons (pink). The signal efficiency is reduced by  $\sim 3\%$ .

Cut	Remaining Event Rate [ /147 kt yr ]					
	DSNB	AtmNC	AtmCC	FastN	Li9	Reactor
IBD	53.6	1136	13.7	17.1	$1.9 \times 10^5$	53.7
Muon Veto	45.0	954	11.5	14.4	3750	45.2
<b>PSD</b>	49.7	22.5	12.7	0.72	$1.7 \times 10^5$	49.8
Triple Coincidence	50.3	696	12.9	16.0	$1.8 \times 10^5$	50.4

Table 10.1: The event rates for an exposure of  $147\text{kt yr}$ , corresponding to a 10-year measurement and the inner detector volume with  $R < 16\text{ m}$ . Different selection techniques are applied. The **IBD** selection criteria are described in section 4.4. The muon veto cut reduces mainly the cosmogenic  ${}^9\text{Li}$  background. The background rejection through **PSD** mainly affects the atmospheric **NC** and the fast neutron rate. Lastly, the effect of the triple coincidence cut is shown. Note that the background suppression methods are applied separately after the **IBD** cut and that the number of reactor neutrinos corresponds to a lower energy threshold of  $9\text{ MeV}$ . The maximum prompt energy deposition is  $\sim 68\text{ MeV}$ .

## 10.1 Proposal for Detection Strategy

In the present section, a proposal for a detection strategy is given, assuming that the backgrounds behave within their ranges of uncertainties, as described in the previous chapters. As the DSNB flux was not measured until now, minor additional background sources may occur, that are not considered at the moment. Furthermore, the fiducial DSNB flux model is assumed. The suggested steps of data analysis after 10-year data-taking in JUNO are enumerated and explained in the following in order to generate a positive signal to background ratio.<sup>3</sup>

1. Event candidates that fulfill the selection criteria defined for IBD events, described in section 4.4, are selected. Furthermore, it is necessary to veto a cylindrical volume around the reconstructed muon tracks, which is described in section 7.1. The resulting event spectrum is visible in Fig. 10.3. The lower energy threshold is set to 9 MeV, to avoid the enormous amount of reactor neutrino events, that will be present in the lower energetic part of the spectrum. The spectrum decreases steep, and the slope becomes weaker above  $\sim 12$  MeV of energy deposition.

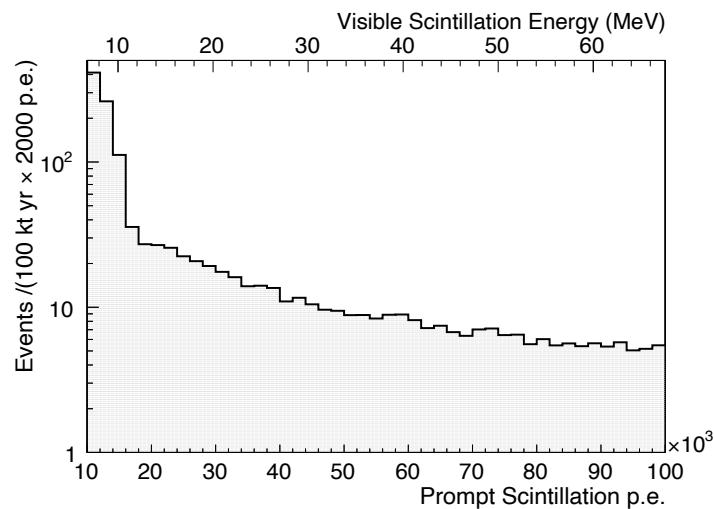


Figure 10.3: Prompt event spectrum of IBD-like events in JUNO after applying the muon veto cut.

<sup>3</sup> As the determination of the fast neutron rate and the atmospheric NC rate is quite complicated, the DSNB detection window should be blinded during the first years of data taking. During this time, the analysis procedure should be fixed by looking at the events that are outside the energy window of interest. After the detection window has been unblinded, the analysis procedures should be applied without any changes to avoid experimental bias. See, e.g. [320].

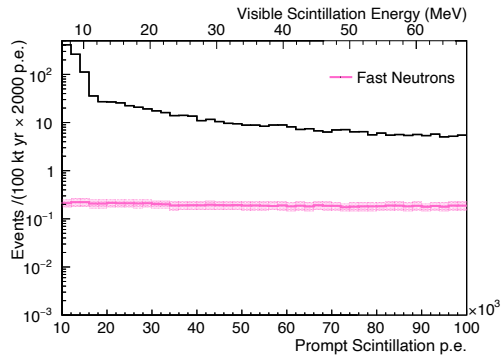


2. Consistent with section 7.2 the background arising from fast neutrons is the only background component that shows a radial dependency of events in the detector volume. As the fast neutrons enter the detector volume from outside, the rate decreases with the radius of the fiducial volume. Therefore, it is assumed that the number of fast neutron events can be determined by analyzing the dependence of the event rate on the radius of the reconstructed position. Hence, through a radial dependent study of events, knowledge about the rate and shape of the fast neutron background should be gained. The results should be corroborated with Monte-Carlo (MC) simulations that allow understanding of this background component. Furthermore, one can look for IBD-like events, that were detected in coincidence with a muon which crosses the muon veto. The top tracker placed above the central detector and outer water Cherenkov detector (WCD), covers 60% of the water pool top area [196]. Although the fast neutron rate cannot be calculated directly from these events, they can still be used to validate the MC simulation if the top tracker detects some muons that neither cross the central detector nor the WCD but produce fast neutrons in the surrounding rock. Subsequently, the expected fast neutron rate can be calculated by using the validated MC simulation. It is assumed that the determination of this background component is feasible with an uncertainty of 20%. The data spectrum with the fast neutron component and the assumed uncertainty is visible in Fig. 10.4a.
3. Subsequently, the method of PSD should be applied. Here, the discrimination strategy with the best significance obtained in section 8.2 is used, with a corresponding signal efficiency of 93%. Using PSD the background could be reduced significantly, which is visible in Fig. 10.4b. Due to the uncertainty of PSD efficiency, the uncertainty of the fast neutron background increases. How the uncertainty of PSD efficiency influences the detection potential is discussed in the following section 10.2.
4. Through the previous background evaluations, it is known that the atmospheric charged current (CC) interactions are the dominant background reactions above  $\sim 35$  MeV, as the fast neutron background is considerably suppressed through PSD. Hence, it is possible to study the atmospheric CC background in the higher energy region and transfer the knowledge into the low energy region. Therefore, above  $\sim 35$  MeV, the number of atmospheric CC events is the difference of the event spectrum and the tiny amount of fast neutron background events. It is assumed that the spectrum can be obtained with a 10% uncertainty above 40 MeV, resulting in an increased error-band of atmospheric CC events due to the error of the fast neutron rate. Below 40 MeV, the atmospheric CC spectrum is extrapolated into the lower ener-

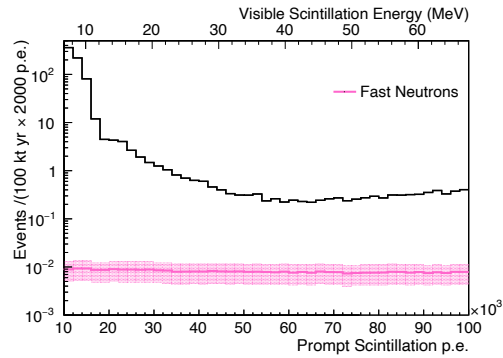
getic regime. The extrapolation is assumed to insert an additional uncertainty of 10%, visible in Fig. 10.4c. The 40 MeV-threshold, above which the CC background is studied, depends on the actual DSNB flux model, and the corresponding spectral plots are given in the appendix in Fig. A.6. For lower DSNB fluxes, the atmospheric flux will surpass the signal at even lower energies. Therefore the suggested threshold can be kept as a conservative choice. For even higher DSNB fluxes, the atmospheric flux overpass the DSNB signal at even higher energies (cf. Fig. 6.4 in section 6.2). As there are significant uncertainties on the atmospheric flux predictions at low energies ( $\leq 100$  MeV), the actual threshold is hard to predict. However, after PSD, the fast neutron background is entirely below atmospheric CC reactions. Hence, the knowledge that the DSNB signal is decreasing in energy while atmospheric neutrino flux is increasing, can be used to determine the point in the spectrum where the slope of the histogram will change the sign. This would be a quick cross-check to validate the energy threshold.

5. The strongly exponentially decreasing energy spectrum below  $\sim 12$  MeV is due to the decay of cosmogenic produced  ${}^9\text{Li}$  (cf. section 7.1) and reactor neutrino interactions (cf. chapter 5). Through analysis of the spectral shape, it is possible to define the lower energy threshold at the point where the exponential decrease mitigates, which is visible in Fig. 10.4d at  $\sim 12$  MeV. By combining knowledge about  ${}^9\text{Li}$  background and the reactor neutrino background, the number of events expected to reach into this window can be determined from measurements below 10 MeV.
6. Lastly, the amount of atmospheric NC reactions has to be determined. Contrary to the atmospheric CC reactions, the direct measurement of the atmospheric NC background is quite challenging. It is assumed that the atmospheric neutrino flux is known with 10% uncertainty. Hence, with the known efficiency of the applied PSD method, one can determine the remaining number of atmospheric NC events in the data set, shown in Fig. 10.4e. It is evident that the prediction of atmospheric NC background events strongly depends on the uncertainty of the PSD efficiency, which is discussed within the next section.
7. To further reduce background, there is the possibility for the triple coincidence veto, which is described in chapter 9. It could reduce the atmospheric NC background by additional  $\sim 40\%$ . However, the uncertainty on the triple coincidence cut efficiency further enhances the error, visible in Fig. 10.4f.

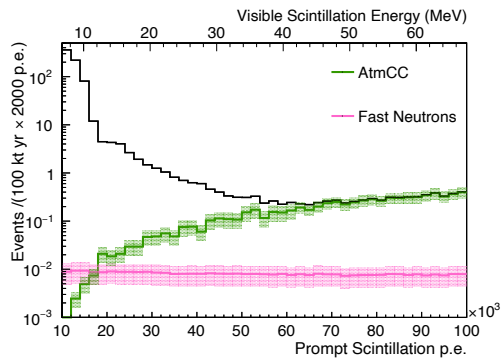
## 10.1 Proposal for Detection Strategy



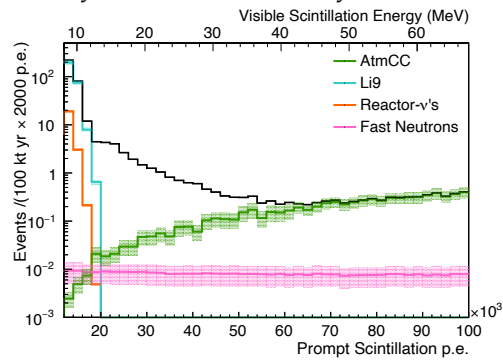
(a) Determination of the fast neutron background with 20% uncertainty.



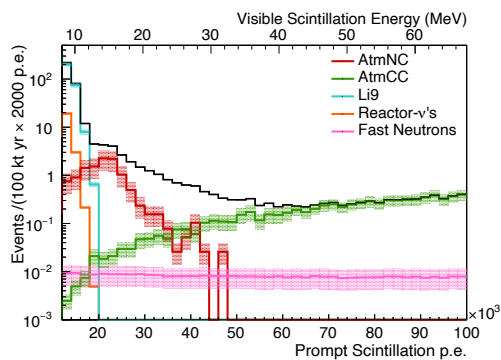
(b) PSD allows to reduce the background. The uncertainty on the fast neutron rate increases, due to the uncertainty on the PSD efficiency.



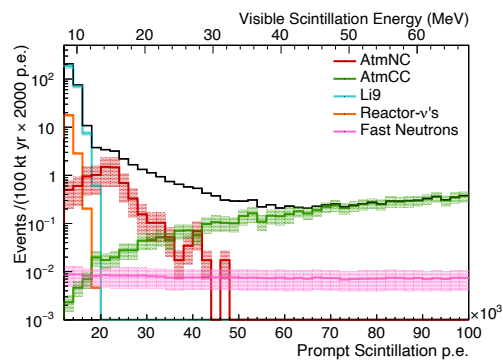
(c) Atmospheric CC interactions are measured above  $\sim 40$  MeV, while below the background estimation is extrapolated.



(d) The reactor neutrino background and background events arising from the decay of cosmogenic produced  ${}^9\text{Li}$  defining the lower energy threshold on the detection window.



(e) Estimation of remaining atmospheric NC background events with knowledge of PSD efficiency and atmospheric NC interactions.



(f) The triple coincidence cut further reduces atmospheric NC background, but enhances the uncertainty.

Figure 10.4: Illustration of the proposed steps of data handling.

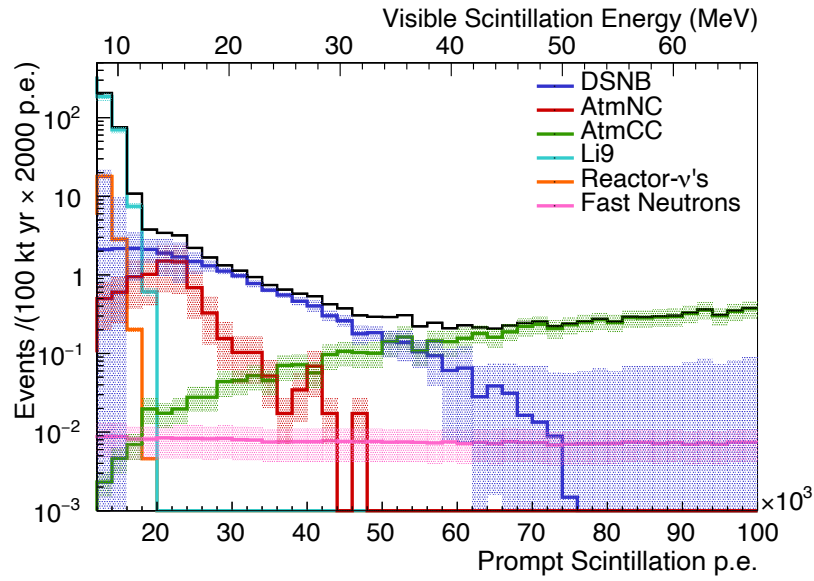


Figure 10.5: Prompt event spectrum of *IBD*-like events in *JUNO* performing the described steps of data analysis. A positive number of *DSNB* signal events can be extracted between 12 MeV and 35 MeV.

Finally, present *DSNB* events can be extracted by subtracting the number of expected background events from the data, visible in Fig. 10.5. Here, above 12 MeV and below 35 MeV, a definite amount *DSNB* signal can be extracted.

The assumptions of this section are transferred into the next one, where the sensitivity of a successful *DSNB* detection is calculated. Furthermore, the dependence of the sensitivity on the *DSNB* flux model, the cut strategy, and uncertainties will be discussed.

## 10.2 Detection Significance

From the expected number of detected signal and background events, the confidence interval can be calculated by using the Feldman-Cousins method [321]. By increasing the size of the confidence interval such that the lower limit is almost zero, the significance of the detection of the DSNB can be calculated. Within this section, an extension of the Feldman-Cousins method, which allows to include uncertainty on the expected amount of background events, is used to calculate the detection significance [322].

The optimal energy window of detection can be obtained as described in previous section. The energy where the steep exponential decreasing spectrum is decreasing in slope determines the lower energy threshold, and the upper limit is where the slope starts to rise again. For the fiducial DSNB flux model, the energy window is chosen to be  $(1.8-5.0) \times 10^4$  prompt photoelectrons, corresponding to a visible energy deposition between  $\sim 12$  MeV and  $\sim 34$  MeV. Tab. 10.2 provides a summary of the expected signal and background rates. Besides, the signal rates for the two extreme DSNB flux models are given, while the high DSNB flux model is limited to the actual Super-Kamiokande limit [3]. If the triple coincidence cut (cf. chapter 9) is applied, the background rate is further reduced, as the signal efficiency.

The significance of detection is calculated for the three different PSD cut strategies and results are plotted in the upper panel of Fig. 10.6, where darker colors refer to higher signal efficiencies. The detection significance by using the triple coincidence cut is plotted besides with dashed lines. From the upper panel of Fig. 10.6, one can conclude that the PSD cut strategy, corresponding to a signal efficiency of  $\sim 71\%$  (light grey), shows the highest significance. This choice for the cut modulus is independent of the decision for or against the triple coincidence cut. Therefore, this cut strategy is favored in the following. Moreover, as there is less difference in significance for triple coincidence cut, we will disfavor the option in the following.

The influence of uncertainty of the PSD efficiency on the significance will be discussed in the following. The favored PSD cut strategy reduces the atmospheric NC background to  $\sim 1.8\%$  in the considered energy window. A less known PSD efficiency  $\epsilon_{PSD} = 1.8\% \pm \delta_{PSD}$ , increases the total uncertainty of the background events. The relative PSD uncertainty is varied by up to 50%, and the effect on the signal significance can be taken from lower panel of Fig. 10.6. An unprecise knowledge on the PSD efficiency heavily reduces the detection sensitivity. If  $\delta_{PSD}$  is larger than  $\sim 30\%$  even after ten years of data taking, a  $3\sigma$  detection becomes nearly impossible assuming the fiducial DSNB flux model. There is the chance

that the actual flux will be higher than the predicted fiducial one, which would enhance significance. Nevertheless, with the same argument, the flux can be even lower, making precise knowledge of **PSD** efficiency even more important. Therefore, it is stated that  $\delta_{PSD}$  should be below 10%, which represents an ambitious goal and opens the question of how precise knowledge of **PSD** efficiency could be gained. For the detection of **DSNB** signals, the **PSD** has to be robust in the energy range above an energy deposition of  $\sim 10$  MeV. Due to quenching effects, it is not easily possible to calibrate the scintillator using neutron- or  $\alpha$ -sources at such high energies. Neutron beams would allow for higher particle energies, but due to the self-shielding, it is not possible to reach the inner detector volume from outside (cf. section 7.2). A possible approach would be to study background events from atmospheric interactions, above the DSNB signal energy. The results should be compared with **MC** simulations, and through **MC** tuning, there is hope that the **PSD** can be studied at higher energies. Nevertheless, the knowledge and the prognosis of the **MC** simulation have to be transferred to the DSNB signal energy region, and one has to rely on the **MC** simulations. Requiring a relative uncertainty of 10%, DSNB detection significance manifests at  $\sim 4\sigma$  for ten years of measurement.

Finally, the exposure is fixed to 147 kt yr, corresponding to ten years of **JUNO** data, and the detection significance is plotted in dependence of the two-dimensional astrophysical parameter space. Therefore, the amount of failed supernovae (SNe) is set to the fiducial value of 27.3%, while the **SN** rate and the minimal black hole mass are varied, visible in the upper panel of Fig. 10.7. As the actual values of the astrophysical parameters firmly influence the signal strength (cf. chapter 4), the significance also strongly depends on the parameter constellation. Hence, it is even possible to reach  $5\sigma$  after ten years with a parameter constellation that differs from the assumed fiducial one. Moreover, it is assumed that the mass threshold above a neutron star turns into a black hole will be determined more precisely within the next years (cf. section 4.1). Therefore, the mass threshold is fixed to its reference value of  $2.7 M_{\odot}$ , and the amount of failed SNe and the core-collapse supernova rate are varied in the lower panel of Fig. 10.7.

To summarize, a **DSNB** detection within **JUNO** seems feasible, provided that the method of **PSD** will be in reality as powerful as predictions from simulations. A  $3\sigma$  signal could be feasible after only five years if the fiducial flux predictions corresponds to reality. In the unfortunate case of lower fluxes, even longer measuring times are needed. Besides a successful detection, the following section will discuss the possibility of constraining the astrophysical parameter space through a **DSNB** measurement.

Pulse Shape Discrimination			
signal efficiency	71%	76%	78%
DSNB flux model	Signal Rate [/(147 kt yr)]		
low	9.0	9.7	9.9
fiducial	21.1	22.4	23.1
high (SK-limit)	46.3	49.2	50.6
Background Rate [/(147 kt yr)]			
atmospheric NC	$9.6 \pm 1.0$	$12.3 \pm 1.2$	$14.9 \pm 1.5$
atmospheric CC	$1.3 \pm 0.3$	$1.4 \pm 0.3$	$1.5 \pm 0.3$
cosmogenic ${}^9\text{Li}$	$0.9 \pm 0.09$	$1.0 \pm 0.1$	$1.0 \pm 0.1$
fast neutrons	$0.14 \pm 0.03$	$0.20 \pm 0.04$	$0.23 \pm 0.05$
sum	$11.9 \pm 1.3$	$14.9 \pm 1.7$	$17.7 \pm 1.9$
Pulse Shape Discrimination and Triple Coincidence Cut			
signal efficiency	67%	71%	73%
DSNB flux model	Signal Rate [/(147 kt yr)]		
low	8.5	9.1	9.3
fiducial	19.8	21.0	21.7
high (SK-limit)	43.5	46.1	47.4
Background Rate [/(147 kt yr)]			
atmospheric NC	$5.9 \pm 1.2$	$7.6 \pm 1.5$	$9.2 \pm 1.8$
atmospheric CC	$1.2 \pm 0.2$	$1.3 \pm 0.3$	$1.4 \pm 0.3$
cosmogenic ${}^9\text{Li}$	$0.8 \pm 0.08$	$0.9 \pm 0.1$	$1.0 \pm 0.1$
fast neutrons	$0.13 \pm 0.03$	$0.19 \pm 0.04$	$0.22 \pm 0.04$
sum	$8.1 \pm 1.5$	$10.0 \pm 1.9$	$11.7 \pm 2.3$

Table 10.2: Expected signal and background event rates per 147 kt yr, corresponding to a 10-year measurement and the inner detector volume with  $R < 16$  m. The tool of [PSD](#) is applied, and the triple coincidence cut is additionally applied in the lower table. The rates correspond to the energy window of  $(1.8-5.0) \times 10^4$  prompt photoelectrons. Three different [PSD](#) cut strategies, favored in section [8.2](#), are compared varying in signal and discrimination efficiency. The total signal efficiency includes the IBD-, [PSD](#)- and triple coincidence cut efficiencies, as well as the dead time due to the muon veto cut. The background components with their assumed uncertainties are also listed. Note that no uncertainty of the [PSD](#) efficiency is considered and the uncertainty on the triple coincidence cut is assumed to be 10%.



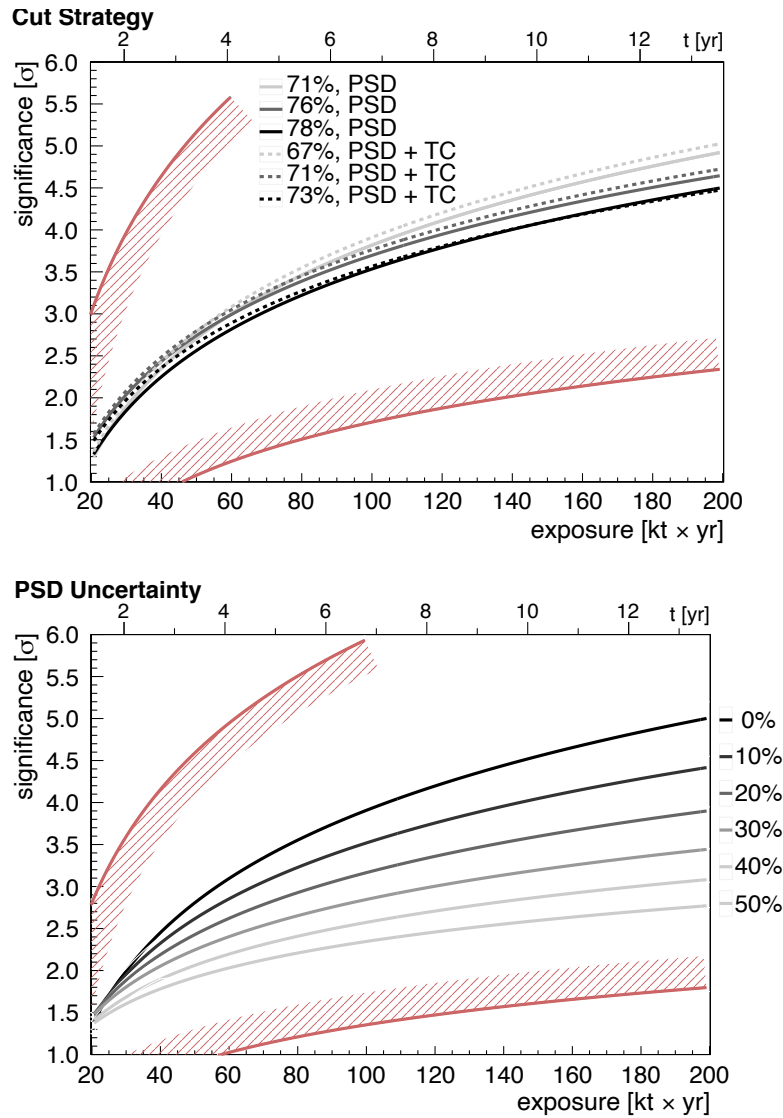


Figure 10.6: **DSNB** detection significance in dependence of exposure calculated according to [322]. The upper x-axis corresponds to the lifetime of **JUNO**, assuming a fiducial detector mass of 14.7kt, corresponding to the inner detector volume with  $R < 16$  m. The red lines correspond to the allowed range due to the uncertainty of the **DSNB** flux.

Upper panel: The three different **PSD** cut strategies were compared, where darker colors refer to higher signal efficiencies (compare Tab. 10.2). The **PSD** method was used to reduce the background (solid lines) with the triple coincidence cut (TC) as an additional option (dashed lines). No uncertainty of the **PSD** efficiency is considered.

Lower panel: the uncertainty of the **PSD** efficiency was varied by up to 50%. An unprecise knowledge of the **PSD** efficiency strongly reduces the detection sensitivity. The **PSD** cut strategy is fixed and corresponds to  $\sim 71\%$  signal efficiency, and no triple coincidence cut was applied.



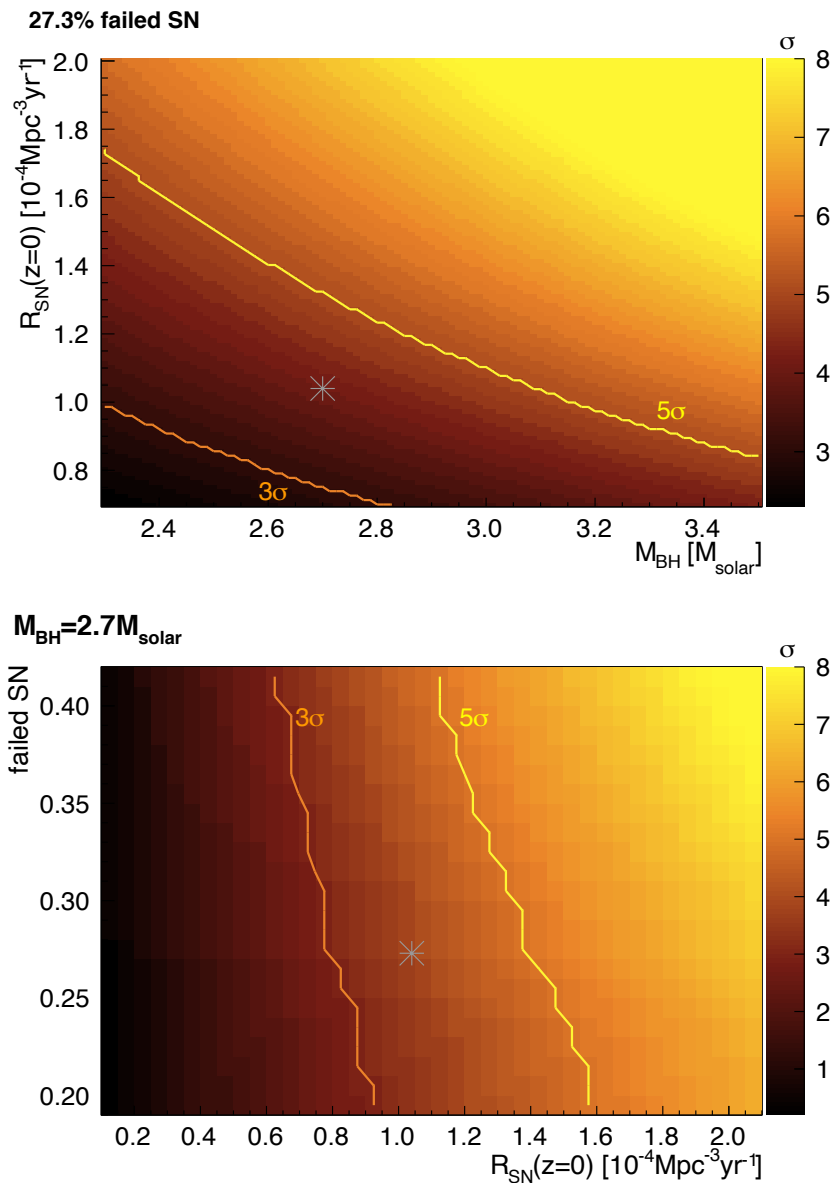


Figure 10.7: **DSNB** detection significance for exposure of 147 kt yr, corresponding to a 10-year measurement and the inner detector volume with  $R < 16$  m. The grey star corresponds to the fiducial flux model. The **PSD** cut strategy is fixed and corresponds to  $\sim 71\%$  signal efficiency with 10% uncertainty, and no triple coincidence cut was applied. The orange and yellow line correspond to  $3\sigma$  and  $5\sigma$ , respectively.

Upper plot: the amount of failed SNe is set to 27.3%, while the supernova rate and the minimal black hole mass are varied.

Lower plot: The minimum mass of the black hole is set to  $2.7 M_{\odot}$ , while the amount of failed supernovae and **CCSN** rate are varied.

### 10.3 Constraining the Astrophysical Parameter Space

Besides a first-time detection of the DSNB signal, the possibility to constrain astrophysical parameter(s) through a DSNB measurement is shortly discussed within this section. The three main parameters with the most substantial impact on the strength and shape of the DSNB flux were worked out in chapter 4.

First, the DSNB spectral shape is studied and visualized in Fig. 10.8. The DSNB spectra differ in the position of the maximum, and the exponential slope  $E_0$ , which is defined as

$$\frac{dN_\nu}{dE_\nu} \propto \exp\left(-\frac{E_\nu}{E_0}\right). \quad (10.1)$$

The exponential fit of the spectrum is performed between 15 MeV and 30 MeV. The impact of the astrophysical parameters on the position of the maximum and the slope was studied to resolve the impact of the individual parameters on the attributes separately. Therefore, each astrophysical parameter was varied within the uncertainty range (cf. section 4.3), while the other two parameters are fixed at the reference values. The impact on the spectral shape parameters can be taken from Tab. 10.3. The value  $\delta$  is defined as the difference between the values of the high and low model, normalized to the fiducial value. The parameter of the black hole

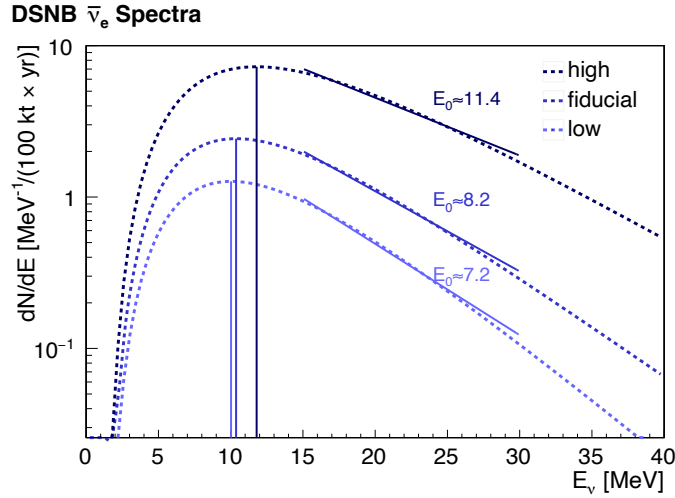


Figure 10.8: Differential  $\bar{\nu}_e$  DSNB spectra arriving at Earth with neutrino energy  $E_\nu$ , for the fiducial model, laying between the low and high flux model for 100 ktyr exposure. For the flux models, see section 4.3. The neutrino energy at the maximum and the exponential slope differ for the three flux models.

### 10.3 Constraining the Astrophysical Parameter Space

	Position of Maximum [MeV]				Slope $E_0$ [MeV]			
	low	fiducial	high	$\delta$ [%]	low	fiducial	high	$\delta$ [%]
$R_{SN}(z)$	10.5	10.4	10.5	0.6	8.3	8.2	8.4	1.3
$M_{BH}$	10.0	10.4	11.2	11.6	7.4	8.2	10.3	34.9
$f_{SN}$	10.1	10.4	10.7	6.1	7.6	8.2	8.8	14.9

Table 10.3: The table gives the neutrino energy of the spectral maximum and the slope, compare Eq. (10.1), of the exponential decreasing **DSNB** spectrum. The astrophysical parameters are varied separately while the others are kept constant at their reference values. Here,  $\delta$  is defined as  $\delta = (\text{high}-\text{low})/\text{fiducial}$ . The amount of failed SNe  $f_{SN}$  shows the second-highest impact on both parameters and is highlighted in grey.

mass threshold  $M_{BH}$  shows the highest impact on the position of the maximum and the slope. As even with the large neutrino detector **JUNO**, successful **DSNB** detection requires several years of data taking, it is assumed that the parameter of the neutron star mass threshold will be determined with sufficient accuracy within the next years. Hence, it is fixed in the following analysis to its reference value  $M_{BH} = 2.7 M_{\odot}$ . The amount of failed SNe shows the second-highest impact on both parameters and is, therefore, highlighted in grey in Tab. 10.3. Hence, it should be principally possible to gain knowledge on this parameter through a spectral **DSNB** analysis.

The sensitivity on the parameters is evaluated in the following through a  $\chi$ -analysis, performed between 13.0 MeV and 34.6 MeV. The fiducial **DSNB** flux is assumed as the true one, and the detector signal efficiency was set to 75%. The number of expected events is sampled from the Poisson distributed number of expected signal events. The **DSNB** spectrum hypothesis depends on astrophysical parameters, which are collectively denoted by  $\Theta$ .

The value of  $\chi_{\text{stat}}^2$  describes the deviation from the expected values of the outcome of a series of  $n$  independent measurements  $M_i$  of the normal distributions  $N(\mu_i, \sigma_i)$  [323]

$$\chi_{\text{stat}}^2 = \sum_{i=1}^n \left( \frac{M_i - \mu_i}{\sigma_i} \right)^2. \quad (10.2)$$

In order to determine the  $\chi^2$  for a given experimental event spectrum, the sum is calculated over  $n$  bins (instead of  $n$  measurements), to compare the theoretically expected entry  $T_i$  in each bin with the experimental measured data  $M_i$ :

$$\chi_{\text{stat}}^2(\Theta) = \sum_{\text{bin } i} \frac{(M_i - T_i(\Theta))^2}{M_i}. \quad (10.3)$$

The further the observations are away from the expected values, i.e., the more extreme the outcome, the larger is the  $\chi^2$ -value. If the mean values  $\mu_i$  depend on a set of parameters  $\Theta$  whose values have to be estimated from the data, one usually considers the minimum  $\chi^2$  with respect to the parameters

$$\chi^2(\hat{\Theta}) = \min_{\Theta} \chi^2(\Theta), \quad (10.4)$$

with  $\hat{\Theta}$  the set of parameters at the minimum  $\chi^2$ . The minimization is done with respect to the astrophysical parameters  $R_{SN}$  and the amount of failed SNe  $f_{SN}$ . As the supernova rate  $R_{SN}$  has less effect on the spectral shape, it is defined as a scaling factor, and  $T_i$  is transferred to

$$T_i = R_{SN} \times \Phi(E_\nu, M_{BH}, f_{SN}). \quad (10.5)$$

To allow for continuous variation of  $f_{SN}$ , the **DSNB** spectra were linearly approximated between the given spectra. Moreover, the parameters in the fit are not allowed to be completely free, because they are known to a particular precision, which has to be considered in the minimization process. Therefore, for each minimized parameter, a pull term is added to the static  $\chi_{\text{stat}}^2$  value,

$$\chi^2 = \chi_{\text{stat}}^2 + \sum_{\text{parameters}} \left( \frac{\theta_{\text{fit}} - \theta_0}{\sigma(\theta)} \right)^2, \quad (10.6)$$

where  $\theta_{\text{fit}}$  is the minimized fit parameter, and  $\theta_0$  the global best fit value. The corresponding uncertainty in the knowledge of the parameter is given by  $\sigma(\theta)$ . The parameters of the pull-terms can be taken from Tab. **10.4**. The number of pull parameters minimizes the degrees of freedom to  $n - 2$ . Finally, for a given assumed exposure,  $\Delta\chi^2$  is determined

$$\Delta\chi^2 = \chi^2(\Theta) - \chi^2(\hat{\Theta}), \quad (10.7)$$

as the difference between the  $\chi^2$  value and the value for the parameter set  $\hat{\Theta}$  that minimizes the  $\chi^2$ . The  $\Delta\chi^2$  shapes are close to parabolic<sup>4</sup>, indicating that the  $\chi^2$

<sup>4</sup> Compare Fig. **A.7** in the appendix.

fit parameter	$\theta_0$	$\sigma$
$R_{SN} [10^{-4}/(\text{Mpc}^3 \text{ yr})]$	1.04	$0.35, \theta_{fit} \leq \theta_0$ $0.96, \theta_{fit} > \theta_0$
$f_{SN} [\%]$	27.3	10

Table 10.4: The parameters for the pull-terms of the  $\chi^2$ -function for the fit parameters of **CCSN** rate  $R_{SN}$  and the amount of failed SNe  $f_{SN}$  [122, 125]. It is assumed that the mass threshold  $M_{BH}$  will be determined in the future, and therefore, this parameter is not minimized.

approximation for the distribution should hold to good accuracy. Therefore,  $\Delta\chi^2$  values given below can be converted into an approximate number of standard deviations by

$$\sigma = \sqrt{\Delta\chi^2}, \quad (10.8)$$

with the significance averaged over the amount of **MC** histograms.

The exclusion plots can be seen in Fig. 10.9, assuming the fiducial **DSNB** flux as the true one, represented by the grey star. The color code gives the needed detector exposure to be able to exclude a point in the two-dimensional parameter space with  $3\sigma$ . The exposure was maximized to 1000 kt yr. As can be taken from the plot, it is not possible to gain knowledge on the amount of failed SNe under the presence of large uncertainties on the CCSNe. Hence, it is only possible to exclude some areas in the two-dimensional parameter space, but also, therefore, high exposures are needed. However, the exclusion plot for a higher black hole mass threshold  $M_{BH} = 3.5 M_{\odot}$  can be found in the lower panel of Fig. 10.9 and allowing for a larger exclusion area. Note that the  $\chi^2$  analysis is not including background nor background uncertainties, which represents a very conservative approach. Nevertheless, it is capable of showing tendencies in the analysis.

In the future analysis a complex multivariate data analysis is recommendable, which includes all background sources within their allowed ranges of uncertainties, as well as the signal spectra with the at this time accessible knowledge.<sup>5</sup> Stand-alone experiments will not have enough statistics to allow for spectral analysis. An overview of recent and future large neutrino detector projects, which have a substantial chance to observe the **DSNB** successfully, can be found in chapter 12.

<sup>5</sup> See e.g., [64].

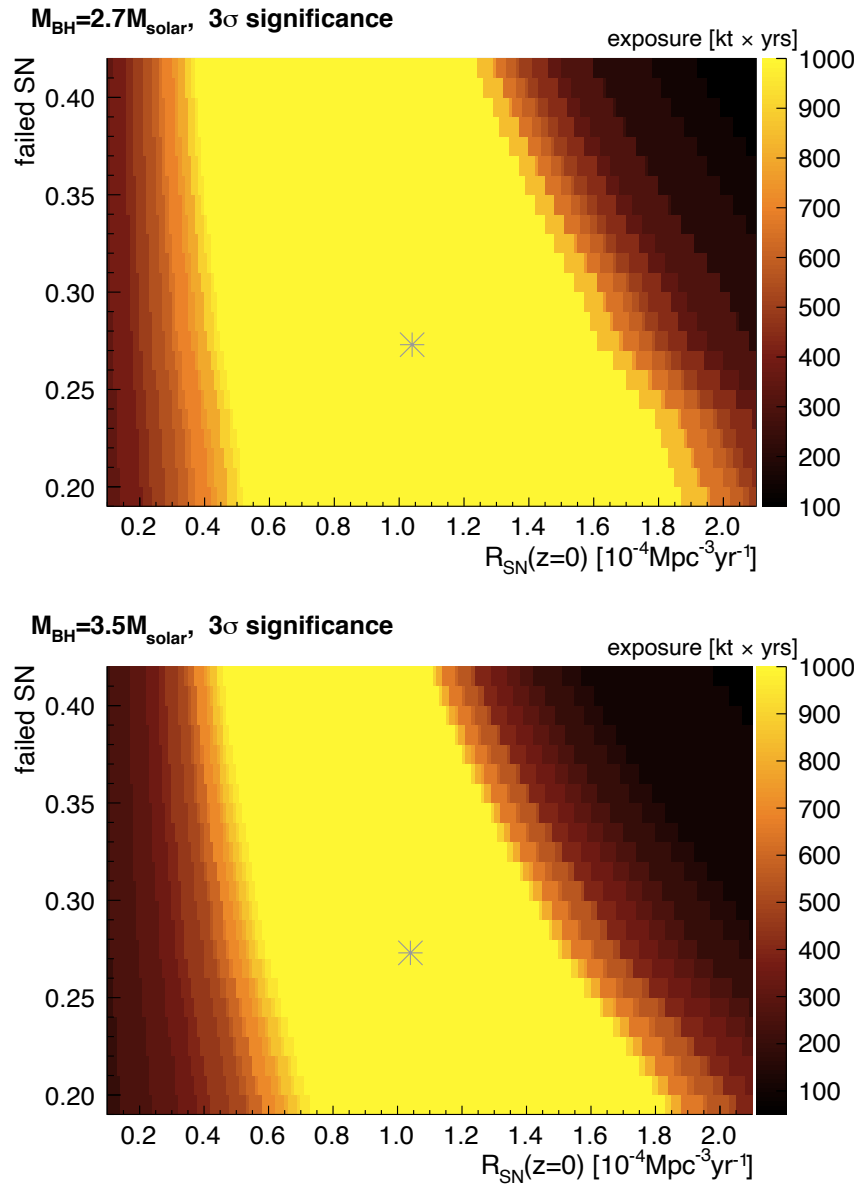


Figure 10.9: Exclusion plot from  $\chi^2$  analysis assuming the fiducial **DSNB** flux model as the true one, represented by the grey star. The color code gives the detector needed exposure to exclude a point in the two-dimensional parameter space with  $3\sigma$ . The yellow areas imply that more than 1000 kt yr of exposure are needed. The black hole mass threshold is set to  $M_{\text{BH}} = 2.7M_{\odot}$  and  $M_{\text{BH}} = 3.5M_{\odot}$ , in the upper and the lower plot, respectively.

## Chapter 11

# DSNB Detection in the Proposed Water-Based Liquid Scintillator Detector Theia

The future of neutrino detection technology lies in large-mass, high-precision, cost-effective, and multichannel detectors [324]. Currently, the choice of target material constrains experiment. The two main approaches of neutrino detection: water Cherenkov detectors (WCDs) and liquid scintillator (LS) detectors were introduced in section 2.1 and section 2.2, respectively. As in WCDs, the charged particle must overcome the Cherenkov threshold to be detected, these detectors are limited in the energy threshold. Moreover, due to lower light yield (LY), the technology is limited in energy resolution. Contrary, LS detectors have a much lower detection threshold but are limited in size by optical attenuation in the target itself. Furthermore, they are limited in directional event reconstruction due to the isotropic nature of scintillation light.

A technique that could combine the different features of WCDs and LS is highly desired, and a field of recent developments opens up the possibility for a new kind of large-scale detectors - the so-called water-based liquid scintillator (WbLS) detectors [325]. An overview of the (dis-)advantages of the different neutrino detector technologies can be found in Tab. 11.1 and will be shortly discussed in the following.

By introducing a small amount (typically 1%–10%) of LS into water, the LY can be adjusted to allow the detection of particles below the Cherenkov threshold, lowering the detector energy threshold. At the same time, through the detection of Cherenkov light, the directional capability is not sacrificed. The material cocktail offers a unique combination of different features by combining high LY and with long attenuation length. However, the purification of water is not possible to the same extent as it is feasible for liquid scintillators, and WCDs would reach higher internal radioactivity levels.

	WCD	LS detector	WbLS detector
energy threshold	×	✓	✓
light yield, energy resolution	×	✓	✓
size, attenuation length	✓	×	✓
directional resolution	✓	×	✓
radiopurity	×	✓	×

Table 11.1: (Dis-)advantages of the different detector technologies of water Cherenkov detectors, liquid scintillator detectors, and water-based liquid scintillator detectors.

If the excitation and de-excitation responsible for scintillation emission are slower than the Cherenkov light emission, it will be possible to measure these two types of lights separately. Types of LS material featuring a scintillation light emission time significantly longer than the Cherenkov light emission, so-called slow LSs, may thus help identify different particles and can be either water-like or oil-like [325–329]. New developments in LSs, highly-efficient fast photon detectors, and chromatic photon sorting have opened up the possibility for building a large-scale detector that can discriminate between Cherenkov and scintillation signals [329]. As the characteristic angular dependence of Cherenkov emission will cause a ring-shaped local enhancement in the detected light intensity on top of the isotropic scintillation signal, this additionally, characterizes the separation [330]. A wavelength-sensitive photosensor could be used to distinguish near-UV scintillation light from the blue-green lower end of the Cherenkov spectrum. Its far-UV component will have been absorbed and isotropically re-emitted by the organic compounds in the WbLS. There is an additional possibility to probe the particle type twice when particles with the same kinetic energy have different amounts of Cherenkov-light emission [327]. This feature is studied in section 11.3.2. All in all, this separation provides many key benefits, including the potential to perform ring-imaging as in a pure WCD, direction reconstruction using the prompt Cherenkov photons, and the detection of sub-Cherenkov threshold scintillation light. Such a low-threshold, directional neutrino detector could achieve outstanding background rejection.

The present chapter will estimate the possibility to observe the diffuse supernova neutrino background (DSNB) flux with the new proposed neutrino detector technology, exemplary for the proposed detector Theia, which is introduced in section 11.1. The estimation of the signal and background levels is the topic of section 11.2. Different methods to identify background are presented in section 11.3. Finally, the expected detection sensitivity is given in section 11.4.



## 11.1 Detector Concept

One realization of a future advanced large-volume **WbLS** detector concept is the proposed *Theia* detector, called after the Titaness of light, with the aim for neutrino and astrophysics measurements [327]. The proposed detector combines the use of a 25–100 kt **WbLS** target, high-efficiency ultra-fast timing photosensors located in a deep underground location [324, 327]. A potential site is at the SURF (Sanford Underground Research Facility) in South Dakota. *Theia* is planned to operate in an on-axis neutrino beam and has been proposed to be deployed in one of the four detector caverns that are currently prepared for the Deep Underground Neutrino Experiment (**DUNE**) project. Such a cavern can house a **WbLS** detector of 30 kt mass, of which maybe 20 kt can be used for low-energy antineutrino detection. In the following, two scenarios of the *Theia* detector are considered and visualized in Fig. 11.1. In the first option, *Theia25*, *Theia* would be placed in a cavern intended to be excavated for **DUNE**, and the lying cuboid contains  $\sim 25$  kt of detector material. In the second and larger option, *Theia100*, *Theia* would provide  $\sim 100$  kt of target material in a vertical cylinder.

The organic fraction foreseen for the scintillator is to be 1–10%, resulting in a relatively low scintillation signal comparable to the Cherenkov light emission. The **LY** of the resulting **WbLS** is roughly proportional to its organic fraction. For the studies presented here, the following reasonable assumptions for **WbLS** performance are made. First, the absorption and scattering are weighted averages of pure water and **LAB**-based **LS**. Secondly, 10% of **LS LY** can be achieved with satisfying stability and at reasonable costs. Therefore, the chosen detector configuration corresponds to a **WbLS** of 10% organic fraction and 70% photo-coverage, resulting in a photo-

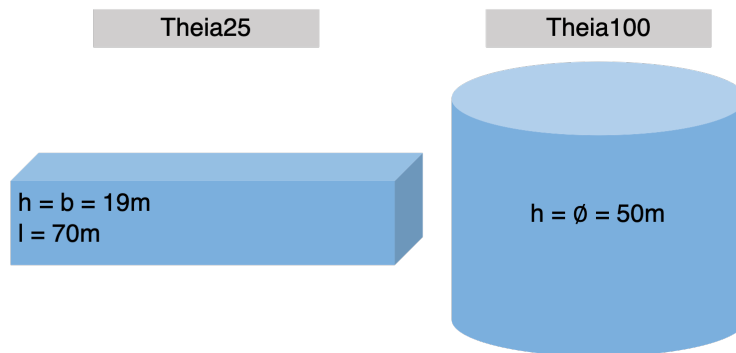


Figure 11.1: The full realization of *Theia* is a 100 kt right cylindrical volume (*Theia100*). A smaller 25 kt realization (*Theia25*) in one of the four **LBNE** caverns.

electron yield of 130 (80) for the scintillation (Cherenkov) component, where the LY for the Theia simulation is adjusted from the LY in the JUNO's Offline Simulation Framework. The simulation is performed with a coverage of 70%, while the smaller Theia25 detector configuration is assumed to have a photo-coverage of 25%. The effect of less coverage on the background rejection techniques will be discussed within the relevant sections.

To obtain a sufficiently detailed signal for a resolved detection of scintillation and Cherenkov light, the detector is to be instrumented with high quantum-efficiency photomultiplier tubes (PMTs), interspaced with Large Area Picosecond Photo-Detectors that provide ultra-fast timing allowing for Cherenkov/scintillation light separation.

Theia can achieve a broad range of physics and can be realized in phases to expand the physics program further. In an initial phase consisting of lightly-doped scintillator and very fast photosensors, Theia will have good sensitivity as a long-baseline neutrino beam to neutrino oscillation parameters [331]. Theia will also contribute to atmospheric neutrino measurements and searches for nucleon decay. A second phase with enhanced photon detection to enable a very low energy solar neutrino program could follow. Theia will also make a definitive measurement of the solar CNO neutrinos, and a high-statistics, low-threshold measurement of the shape of the  ${}^8\text{B}$  neutrinos. Geoneutrinos produced in the Earth's crust and mantle will be measured precisely with statistical uncertainty far exceeding all detectors to date [331]. Should a nearby supernova occur, a high-statistics and simultaneous detection of the electron antineutrino component, complementary to the detection of the electron neutrino flux in the DUNE liquid argon detectors, allows rich supernova astrophysics. The most ambitious goal, which would likely come in a future third phase, is a search for neutrinoless double  $\beta$ -decay, with a total isotopic mass of 10 t, and with decay lifetime sensitivity above  $10^{28}$  years [331]. More details on the physics program can be found in [331]. The ability to measure the DSNB will be discussed within the next sections.

## 11.2 Signal and Background Estimation

The expected number of **DSNB** events in Theia is calculated as described in section 4.3 using Eq. (4.3). With the number of protons,  $N_p = 6.73 \times 10^{31}$  /kt, corresponding to the number of hydrogen atoms per kiloton detector material, a signal rate of

$$R_{\text{DSNB}} = 35.4/(100 \text{ kt yr}) \quad (11.1)$$

for neutrino energies below 40 MeV and assuming the fiducial **DSNB** flux model is expected. For the low and high **DSNB** flux model, the rates are 17.2/(100 kt yr) and 125.3/(100 kt yr), respectively. As the high **DSNB** flux model already overcomes the current limit set by Super-Kamiokande, the **DSNB** flux is limited to 70.8/(100 kt yr) [3].

With a small expected signal rate of  $\sim 0.3$  per year per kiloton of detector material, overwhelming backgrounds have to be faced. A variety of backgrounds besets the **DSNB** signal, which can be divided into three categories: Indistinguishable backgrounds from other electron antineutrino ( $\bar{\nu}_e$ ) sources, muon-induced backgrounds, and the neutral current (**NC**) reactions of atmospheric neutrinos. The observation window is reduced by two irreducible  $\bar{\nu}_e$  backgrounds that induce inverse  $\beta$ -decays, that are explained in section 11.2.1. Within this window, several further backgrounds of cosmogenic origin contribute and have to be considered. These are radionuclides, like the  $\beta$ n-emitter  $^9\text{Li}$ , which are created by muon spallation on the oxygen (and carbon) nuclei of the target and fast neutrons, induced by muons passing the surrounding rock. Muon-induced backgrounds are the topic of section 11.2.2. Lastly, **NC** reactions provide the most dangerous background for a potential **DSNB** detection and are discussed in section 11.2.3.

### 11.2.1 Charged Current Background

Reactor neutrinos constitute an overwhelming background for terrestrial detectors and limit the detection in the energy range below  $\sim 10$  MeV. At higher energies, charged current (**CC**) interactions of atmospheric neutrinos start to dominate the **DSNB** rate from  $\sim 35$  MeV. These are intrinsically indistinguishable from **DSNB**  $\bar{\nu}_e$ 's and, therefore, independent of the type of detector used and defining the observation window. In the following, the rates of these two backgrounds are estimated for the Theia detector.

### Reactor $\bar{\nu}_e$

For energies below  $\sim 10$  MeV, the human-made background due to nuclear reactors defining a lower threshold for DSNB detection. The  $\beta^-$ -decays of neutron-rich fission products of  $^{235}\text{U}$ ,  $^{238}\text{U}$ ,  $^{239}\text{Pu}$ , and  $^{241}\text{Pu}$  generate  $\bar{\nu}_e$  (cf. chapter 5). The total rate of reactor neutrinos for the proposed Theia location is given in [332], resulting in an estimated background rate of

$$R_{\text{Reactor}} = (2240 \pm 112)/(100 \text{ kt yr}), \quad (11.2)$$

for  $E_\nu < 10$  MeV. The uncertainty is approximated with 5% [332]. As the reactor neutrino background overwhelms the expected signal rate, this background defines the energy threshold of the detection window.

### Atmospheric $\bar{\nu}_e$

The flux of atmospheric  $\bar{\nu}_e$  is increasing with their energy and starts to surpass the DSNB signal at energies around 30 MeV (cf. section 6.2). The total flux of atmospheric  $\bar{\nu}_e$  is dependent on the geographic (geomagnetic) latitude and will, therefore, depend on the detector site [287]. The atmospheric neutrino fluxes for Theia are obtained similarly to the description of obtaining atmospheric neutrino fluxes for JUNO, given in section 6.1. For energies above 100 MeV, HKKM atmospheric neutrino fluxes are given for a latitude of  $44.4^\circ$  up to an energy of  $10^4$  GeV [92]. For energies below 100 MeV, FLUKA fluxes calculated for Gran Sasso location ( $42.5^\circ$ ) are used [285]. The FLUKA fluxes are scaled in the same way as described in section 6.1 to be equal with HKKM flux between 100 MeV and 200 MeV, with an average scaling factor of  $\sim 1.5$ . Summarizing, the atmospheric neutrino flux for Theia is

$$\Phi_{\text{Theia}}(E_\nu) = \begin{cases} 1.5 \times \Phi_{\text{Gran Sasso}}(\text{FLUKA}) & E_\nu < 100 \text{ MeV} \\ \Phi_{\text{SURF}}(\text{HKKM}) & E_\nu \geq 100 \text{ MeV}. \end{cases} \quad (11.3)$$

The resulting low energy atmospheric neutrino flux is shown in Fig. 11.2. The reason for the significant difference between the two flux predictions is due to the steep dependence of the scaling factor on the latitude. Similar to section 6.1, 35% flux uncertainty in the lower energy region ( $< 100$  MeV) is assumed. Beside  $^1\text{H}$ , there is also the possibility for a CC reaction on  $^{12}\text{C}$  or  $^{16}\text{O}$ , and Tab. 11.2 extends the Tab. 6.1 in section 6.2 by the reactions on  $^{16}\text{O}$ . The necessary condition of neutron capture and the assumption that accompanying muons will be visible in the detector, only the  $\bar{\nu}_e$  reactions on protons are considered as dangerous CC background. Following Eq. (6.2), the atmospheric CC background rate for  $E_\nu < 100$  MeV is calculated to

$$R_{\text{CC}} = (48 \pm 17)/(100 \text{ kt yr}). \quad (11.4)$$

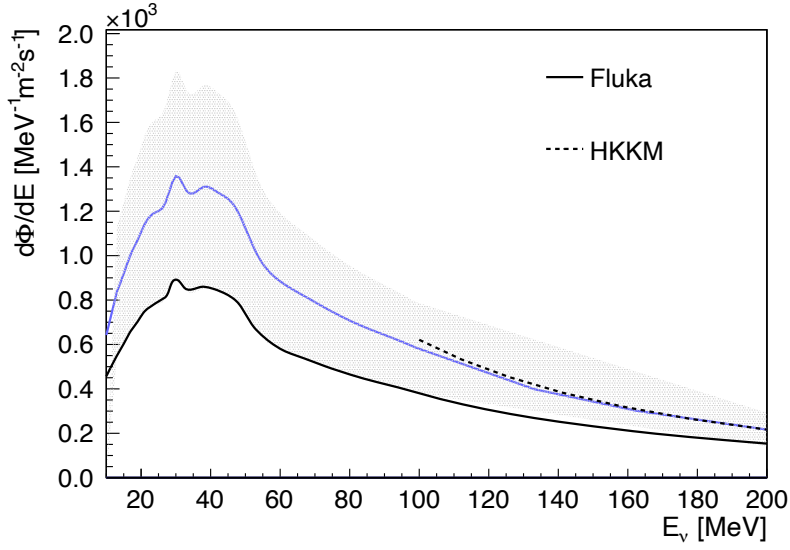


Figure 11.2: Atmospheric neutrino flux (sum of all flavors) for Theia location derived from Fluka (solid) and HKKM (dashed) flux predictions [92, 285]. The approximated flux for Theia is given as the blue line. A flux uncertainty of 35% is assumed and highlighted as the grey shaded area.

CC Reaction	Veto Strategy
$\nu_e + {}^{16}\text{O} \rightarrow {}^{16}\text{F} + e^-$	no neutron
$\bar{\nu}_e + {}^{16}\text{O} \rightarrow {}^{16}\text{N} + e^+$	no neutron
$\nu_\mu + {}^{16}\text{O} \rightarrow {}^{16}\text{F} + \mu^-$	no neutron & muon veto
$\bar{\nu}_\mu + {}^{16}\text{O} \rightarrow {}^{16}\text{N} + \mu^+$	no neutron & muon veto

Table 11.2: The atmospheric charged current reactions on  ${}^{16}\text{O}$  with the veto strategy for each reaction. Besides the irreducible **IBD** reaction of  $\bar{\nu}_e$  on  ${}^1\text{H}$ , one could veto the background through the missing delayed neutron signal or the assumption that the resulting muon will be detected.

## 11.2.2 Muon-Induced Background

The location preferred for Theia provides a depth of 4.3 km.w.e with a corresponding muon flux of  $4.2 \times 10^{-9} \text{ cm}^{-2} \text{ s}^{-1}$  and a mean muon energy of  $\langle E_\mu \rangle = 293 \text{ GeV}$  [333]. The muon-induced backgrounds for Theia are discussed in the following.

### Cosmogenic ${}^9\text{Li}$ In-situ production.

Cosmogenic  $\beta n$ -emitters are created by muon spallation on the oxygen (and carbon) nuclei of the target. The only isotope produced at a relevant cross-section and providing a  $\beta$ -signal of sufficiently high energy to reach into the DSNB observation window is  ${}^9\text{Li}$ , which can decay into excited states of  ${}^9\text{Be}$ , leading to the emission of a neutron (cf. section 7.1). The  $\beta$ -endpoint of  ${}^9\text{Li}$  is at 13.6 MeV and, therefore, will affect the DSNB detection only in the lower energy region of the observational window. Depending on the depth of the detector, this background can be efficiently suppressed by forming a time-coincidence veto with the parent muon. For a rough estimate of the expected event rate, the  ${}^9\text{Li}$ -yield in water, which is approximately a sixth of the yield in the scintillator, is adopted and summarized in Tab. 11.3. The production cross-section of cosmogenic isotopes scales with the muon energy  $\sigma \propto E_\mu^{0.75}$  [301, 303]. Therefore, the above-given yields are enhanced by 6% and 3% respectively for water (SuperK) and scintillator (Borexino), resulting in a  ${}^9\text{Li}$  production rate of

$$\begin{aligned} R_{\text{Li}9}^{\text{H2O}} &\simeq 7.2 / (\text{kt yr}) \\ R_{\text{Li}9}^{\text{LAB}} &\simeq 39.4 / (\text{kt yr}). \end{aligned} \quad (11.5)$$

For a 10% scintillator composition, the total  ${}^9\text{Li}$  background rate is calculated to 10.4/(kt yr). As the branching ratio of  ${}^9\text{Li}$  into an excited state is 50.8%, it is assumed that half of the produced  ${}^9\text{Li}$  will have a neutron in the end state, reducing the

	Borexino	Super-Kamiokande
$\langle E_\mu \rangle$ [GeV]	283	270
$Y_{9\text{Li}} [10^{-7} (\mu \text{g}/\text{cm}^2)^{-1}]$	$2.9 \pm 0.3$	$0.51 \pm 0.16$

Table 11.3: The cosmogenic production yield of  ${}^9\text{Li}$  from measurements of Borexino and Super-Kamiokande [300, 334, 335].

background rate due to cosmogenic  ${}^9\text{Li}$  to

$$R_{\text{Li}9} = (529 \pm 106)/(100 \text{ kt yr}). \quad (11.6)$$

In line with measurements, an uncertainty of 20% is assumed [300,334]. As already discussed in section 7.1 it is possible to veto such events if the cylinder vetoed around muon track is large and the veto time long enough. A veto time of 2 s is chosen and a cylinder radius of 5 m. With the typical muon track length of 50 m and 19 m, respectively, for the two geometries, the total dead time is below 1%. Therefore, such a conservative cut can reduce the background from  ${}^9\text{Li}$  decay to a negligible rate without a noticeable loss in exposure, and  ${}^9\text{Li}$  is not considered in the following.

### Fast Neutrons

Whereas muon tracks in the inner detector can be identified, neutrons that are induced by muons passing the rock surrounding the detector can, in principle, enter the detector unnoticed. The combination of a prompt signal created by elastic scattering (ES) off protons and the subsequent neutron capture can mimic the IBD event signature. Since these events enter the detector from outside, they can be effectively addressed by a fiducial volume cut.

For estimation of the fast neutron background rate, the simulation results, with mean cosmic muon energy of  $\langle E_\mu \rangle = 300 \text{ GeV}$  (at 4 km.w.e) and a muon flux of  $\Phi_\mu^L = 0.2 / \text{m}^2 / \text{h}$ , were adopted from a similar study for LENA [336]. The LENA simulation was performed in limestone rock ( $\text{CaCO}_3$ ,  $\rho = 2.74 \text{ g/cm}^3$ ), resulting in neutron yields of

$$Y_n = 5 \times 10^{-4} (\mu \text{ g/cm}^2)^{-1} \text{ and} \quad (11.7)$$

$$Y_n(E > 10 \text{ MeV}) = 2.8 \times 10^{-4} (\mu \text{ g/cm}^2)^{-1}.$$

It turned out that it is enough to simulate neutrons in a 4 m thick cylinder around the detector/muon veto [336]. Neutrons that were produced farther away do not need to be considered, as the mean free path length of these neutrons is below 1 m, and thus a vast majority of them will be absorbed in the rock [336,337]. Moreover, it is assumed that all muon tracks are vertical. Due to the large and homogenous overburden of the mine, this is a reasonable assumption.

Chapter 11 DSNB Detection in the Proposed Water-Based Liquid Scintillator Detector Theia

Fiducial Volume Radius Cut	Fast Neutron Events [/(100 kt yr)]		exposure loss [%]	
	Theia100	Theia25	Theia100	Theia25
	113.2	49.2	-	-
-0.5 m	41.9	18.2	4	7
-1.0 m	16.6	7.2	8	13
-1.5 m	7.6	<b>3.3</b>	12	<b>19</b>
-2.0 m	3.5	1.5	15	26
-2.5 m	<b>1.7</b>	0.7	<b>19</b>	32

Table 11.4: The fast neutron background rate for Theia, approximated from the LENA results [336]. The given rates correspond to an upper energy deposition of 40 MeV and for the two discussed geometries of Theia100 and Theia25. A fiducial volume cut will reduce this radial dependent background, but is accompanied by an exposure loss.

Assuming the detector geometry of Theia100, it is approximated that,  $9 \times 10^5$  muons traverse per year through the 4 m thick outer detector volume.<sup>1</sup> As the neutron production rate scales with the mean muon energy, one crossing muon produces on average

$$Y_n(E > 10 \text{ MeV}) \times \rho_{CaCO_3} \times 50 \text{ m} \times \left( \frac{293 \text{ GeV}}{300 \text{ GeV}} \right)^{0.75} = 3.8 \text{ n}/\mu. \quad (11.8)$$

Hence, approximately four neutrons above 10 MeV are produced in this volume along the traversing 50 m. In total, about  $3.4 \times 10^6$  n / yr are produced in the surrounding volume. This neutron production rate is only  $\sim 50\%$  of the LENA one, due to the lower muon flux and smaller detector size [336]. Therefore the LENA results were scaled by this factor, resulting in radius-dependent fast neutron background rates below 40 MeV given in Tab. 11.4.

For the second proposed geometry of Theia25, there are 15% more muons that traverse per year the 4 m thick space around the detector, but the path where neutrons can be produced is shorter. Therefore only,  $\sim 1.4$  neutrons are produced per muon, resulting in a total in neutron production of  $1.5 \times 10^6$  n / y, which is less than obtained for Theia100 geometry. It is assumed that a fiducial volume is reduced by the outer 2.5 m and 1.5 m, for the geometry of Theia100 and Theia25, respectively. Fig. 11.3 visualizes the fast neutron background rates compared to the DSNB signal rate.

<sup>1</sup> Please note that no buffer medium between fiducial volume and rock is assumed.



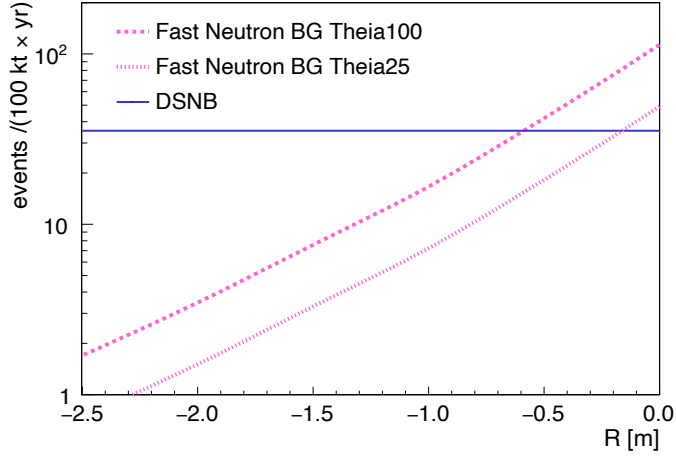
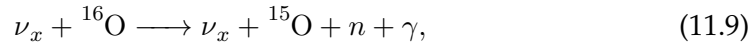


Figure 11.3: The fast neutron background rates (pink) are given for the two proposed geometries of Theia100 (dashed) and Theia25 (dotted). The event rates are given for different fiducial volume cuts and are compared to the [DSNB](#) signal rate (blue). For both geometries, reduction of the fiducial detector volume by  $\sim 0.7$  m, allows for signal-to-background-ratios larger one.

### 11.2.3 Neutral Current Atmospheric Background

Neutral current ([NC](#)) reactions of atmospheric neutrinos can resemble the [IBD](#) coincidence. A prompt signal is generated due to the recoils and possible de-excitation of the fragments of the target nucleus and a delayed signal in case a neutron is released from the nuclear break-up. First recognized by the [KamLAND](#) experiment, it dominates the [DSNB](#) signal by more than one order of magnitude in organic [LS](#) detectors [\[290\]](#). The quasielastic ([QEL](#)) [NC](#) interactions of atmospheric neutrinos on oxygen form, as well, one of the main backgrounds in the search for [DSNB](#) neutrinos with water-based Cherenkov detectors. The interaction processes can be written as



in which neutrinos knock out nucleons from oxygen. The total calculated rate of [QEL](#) atmospheric [NC](#) reactions dependent on target are listed in [Tab. 11.5](#). The atmospheric neutrino interactions in the water-based scintillator were simulated with GENIE (Version 2.12.4) [\[70, 295\]](#) with an upper neutrino energy threshold of 10 GeV and the cross-sections (*gxspl-FNALsmall.xml*) based on [\[338-340\]](#). The [NC](#) reactions on  ${}^{16}\text{O}$  with their branching ratios are listed in [Tab. 11.6](#).

	Atoms [/ <i>kt</i> ]	Rate [/( <i>kt yr</i> )]
$^1\text{H}$	$6.73 \times 10^{31}$	12.4
$^{12}\text{C}$	$4.41 \times 10^{30}$	5.6
$^{16}\text{O}$	$3.01 \times 10^{31}$	69.0

Table 11.5: **QEL NC** interactions of atmospheric neutrinos on hydrogen, carbon, and oxygen per kiloton of target nuclei and year.

The visible signals of **QEL** atmospheric **NC** reactions on oxygen were simulated within JUNO's Offline Simulation Framework, where the light yield was adjusted to reflect **WbLS** properties. Reactions on hydrogen and  $^{12}\text{C}$  were not simulated, as **NC** reactions on hydrogen, will not release a neutron at all, and the **NC** reactions on  $^{12}\text{C}$  contribute only  $\sim 8\%$  to the total number of interactions due to the mass fraction. Moreover, only reactions with a maximum of one neutron in the final state were simulated to fulfill the **IBD** coincidence condition, which was valid for  $\sim 79\%$  of the reactions. Instead, the atmospheric **NC** background rate was enhanced by 10% to account for the missing carbon in simulation, assuming that the spectral shape for the **NC** background on carbon does not differ from the one on oxygen.

As discussed in section **6.3**, when a neutron disappears from the nucleus, the residual nucleus can be left in an excited state. In the  $^{16}\text{O}$  nucleus, two neutrons occupy the lowest  $S_{1/2}$  level, four neutrons fill the next  $P_{3/2}$  shell, and the remaining two neutrons populate the highest  $P_{1/2}$  state **[291]**. If a nucleon is knocked out, the interacting nucleus is left with a hole in the  $P_{1/2}$ ,  $P_{3/2}$ , or  $S_{1/2}$  state in the simple shell model. The de-excitation gamma energy (and corresponding branching ratio) for a knockout from the  $P_{3/2}$  state is 6.32 MeV (86.9%) or 9.93 MeV (4.9%) in the case of a proton knockout, and 6.18 MeV (86.9%) in the case of a neutron knockout **[341]**. A nucleon hole in the  $S_{1/2}$  shell, allows for further nucleon emission, as the excitation energy exceeds the separation energy for protons and neutrons in  $^{15}\text{O}$ . In this case, de-excitation proceeds mainly by the emission of a proton, neutron,  $\alpha$ -particle, and, to a smaller extent, by the emission of  $\gamma$ 's **[291]**. The probability for a nucleon knockout from the  $S_{1/2}$  shell in the simple shell model is  $2/8=0.25$  **[342]**.

In the following, the simulated **NC** background events are subjected to the analysis cuts commonly used to identify **IBD** candidates. In **IBDs**, the number of neutrons has to be precisely one, which is valid for only  $\sim 27\%$  of the atmospheric **NC** background reactions. To get rid of the highly energetic **NC** reactions, the prompt number of photoelectrons is limited to  $10^4$ , which corresponds to  $\sim 80$  MeV.

## 11.2 Signal and Background Estimation

$\nu_x + {}^{16}\text{O} \longrightarrow \nu_x +$	[%]
p + ${}^{15}\text{N}$	28.1
n + ${}^{15}\text{O}$	24.1
n + p + ${}^{14}\text{N}$	18.8
2p + ${}^{14}\text{C}$	4.5
2n + ${}^{14}\text{O}$	4.3
n + 2p + ${}^{13}\text{C}$	1.0
2n + p + ${}^{13}\text{N}$	0.9
2n + 2p + ${}^{12}\text{C}$	0.9
2n + 3p + ${}^{11}\text{B}$	0.7
other reaction channels	16.6
$R_{NC} \simeq 75/(\text{kt yr})$	

Table 11.6: Reaction channels of atmospheric **QEL** **NC** reactions on  ${}^{16}\text{O}$ , sorted by their prevalence. The left column lists the **NC** interactions obtained from the *GENIE* simulation.

$\nu_x + {}^{16}\text{O} \longrightarrow \nu_x +$	[%]
n + ${}^{15}\text{O}$	45.9
n + p + ${}^{14}\text{N}$	19.7
n + 2p + ${}^{13}\text{C}$	14.7
n + p + d + ${}^{12}\text{C}$	9.1
n + p + d + $\alpha$ + ${}^8\text{Be}$	2.0
n + 3p + ${}^{12}\text{B}$	1.8
n + $\alpha$ + ${}^3\text{He}$ + ${}^8\text{Be}$	1.6
n + p + $\alpha$ + ${}^{10}\text{B}$	1.4
n + 2p + $\alpha$ + ${}^9\text{Be}$	1.2
other reaction channels	2.6
$R_{NC} \simeq 15/(\text{kt yr})$	

Table 11.7: Atmospheric **NC** reactions after the neutron counting, including the de-excitation channels.

The final number of **NC** events mimicking **IBD** reactions can be taken from Tab. 11.7. The atmospheric **NC** background overwhelms the **DSNB** signal by at least one order of magnitude within the detection window. Therefore, background identification methods are needed to reduce the background.

### 11.3 Background Identification

The left plot of Fig. 11.4 shows the expected signal and background spectra of IBD like events in Theia. Nearly all background sources surpass the DSNB signal. The proposed cylindrical veto cut around muon tracks and a radial fiducial volume cut, allow the reduction of the cosmogenic  ${}^9\text{Li}$  background and the fast neutron background, respectively. This is visualized in the right panel of Fig. 11.4, and the signal and background rates can be taken from Tab. 11.8.

The irreducible  $\bar{\nu}_e$  background produced in reactors or the atmosphere define the lower and upper edges of the DSNB detection window, respectively. However, the atmospheric NC background overwhelms the DSNB signal by at least one order of magnitude within the detection window.<sup>2</sup> Therefore, powerful background identification methods are needed to reduce the atmospheric NC background to a level making a DSNB measurement possible, and are presented within this section.

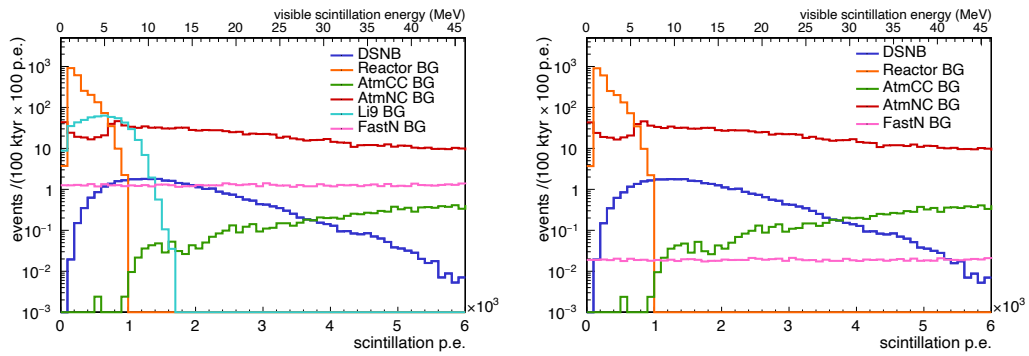


Figure 11.4: The visible scintillation energy spectrum expected for the DSNB signal (blue) and its ample backgrounds. The presented spectra include reactor neutrinos (orange), cosmogenic- ${}^9\text{Li}$  (turquoise), fast neutrons (pink) as well as atmospheric neutrino CC (green) and NC (red) interaction rates. The left plot corresponds to the spectra after proven of the IBD event selection. The right plot is after the application of discrimination techniques: it assumes a 2.5 m fiducial volume cut or presence of corresponding active shielding surrounding the target volume. The  ${}^9\text{Li}$  background is reduced to the muon veto, and the fast neutron background is strongly reduced due to the fiducial volume cut.

<sup>2</sup> The peak in the atmospheric NC spectrum around 6 MeV is due to  $\gamma$ 's resulting from the atmospheric neutrino interactions:  ${}^{16}\text{O}(n,n){}^{16}\text{O}^*$  (6.13 MeV),  ${}^{16}\text{O}(n,2n){}^{15}\text{O}^*$  (6.18 MeV), and  ${}^{16}\text{O}(n,np){}^{15}\text{N}^*$  (6.32 MeV) [341].

Spectral contribution	100 kt-year exposure		
	Before Cuts	Muon Veto	Fiducial Volume Cut
DSNB signal	35.4	35.0	35.0
Reactor neutrinos	2240	2218	2218
Atmospheric CC	9.0	8.9	8.9
Atmospheric NC	1270	1253	1253
$\beta n$ -emitters ( ${}^9\text{Li}$ )	529	–	–
fast neutrons	131 (57)	130 (56)	2 (4)

Table 11.8: Rates of **DSNB** signal and backgrounds within the energy observation window ( $0-6000$ ) p.e., corresponding to an upper energy limit of  $\sim 46$  MeV for a live exposure of 100 kt yr. The cited fast neutron rate in the second column assumes a 2.5 m (1.5 m) fiducial volume cut of Theia100 (Theia25) or the presence of corresponding active shielding surrounding the target volume.

### 11.3.1 Cherenkov Ring Counting

The reconstruction of Cherenkov rings from final-state particles provides a further handle to discriminate background events. **DSNB** positron events provide exactly one Cherenkov ring. Contrariwise, atmospheric **NC** reactions may result in several particles, offering the possibility for several Cherenkov rings. Fig. 11.5 shows the number of Cherenkov rings in atmospheric **NC** events as a function of the visible scintillation energy. It is assumed that Cherenkov rings must contain at least 300 photoelectrons to be discernible. By limiting the signal acceptance to one-ring events, about half of the background events can be rejected without any relevant signal loss. It should be noted that these values set a lower limit for the discrimination power, as no detailed ring reconstruction is performed. The algorithm only counts if a produced initial particle creates Cherenkov light with at least 300 p.e. Some particles, especially high energy gammas, can create several secondary electrons, that would, therefore, make several Cherenkov rings. Moreover, the assumption of 300 p.e. threshold for ring reconstruction is very conservative, so that in reality, the ring counting process would be even better. So overall, in the signal energy range, the atmospheric **NC** amount can be reduced by 57%.

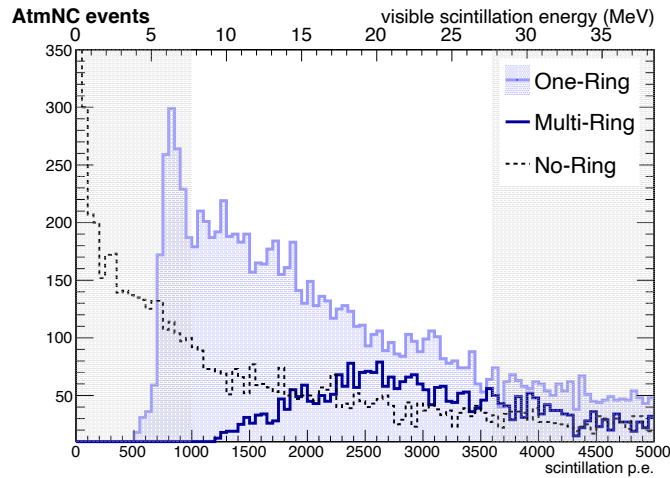
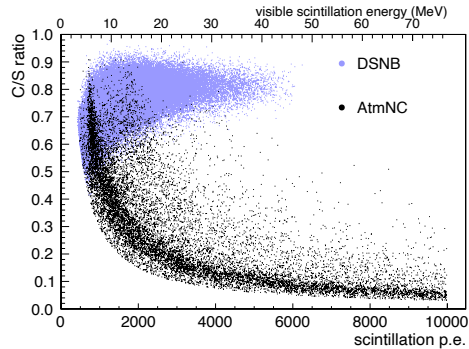


Figure 11.5: Number of Cherenkov rings for atmospheric  $\overline{\text{NC}}$  background events as a function of the promptly visible scintillation energy. The frequent occurrence of two or more rings allows for efficient discrimination against the single-ring  $\overline{\text{DSNB}}$  positron events. The grey box represents the inaccessible low energy window.

### 11.3.2 Cherenkov-to-Scintillation Ratio

A  $\overline{\text{WbLS}}$  detector will be able to detect both, the Cherenkov and the scintillation light. This feature can be used to identify different particle types by their Cherenkov light emission (or its absence). Background discrimination can be achieved by the application of a cut on the Cherenkov-to-scintillation ( $\overline{\text{C/S}}$ ) ratio of the photon signal. The  $\overline{\text{C/S}}$  parameter is defined as the ratio of photoelectrons arising from Cherenkov light to the scintillation light. In the present case, positron-like  $\overline{\text{IBDs}}$  can be separated from the mixed and largely hadronic prompt events in both atmospheric  $\overline{\text{NC}}$  and fast neutron interactions. Fig. 11.6 demonstrates the discrimination power by plotting the  $\overline{\text{C/S}}$  ratio of  $\overline{\text{DSNB}}$  signal and atmospheric  $\overline{\text{NC}}$  background as a function of the visible scintillation energy. For visible energies greater than  $\sim 8 \text{ MeV}$  ( $10^3 \text{ p.e.}$ ), the distributions of both species are sharply separated. The residual background contamination arises from  $\overline{\text{NC}}$  reactions in which gamma-rays are produced as a side-product. They may either originate from nuclear excitations directly induced by the reaction ( $E_\gamma \leq 20 \text{ MeV}$ ) or are often released in secondary neutron interactions with  $^{16}\text{O}$ , featuring typical energy of  $\sim 6 \text{ MeV}$ . The latter creates an easy-to-spot curved band in the distribution of atmospheric  $\overline{\text{NC}}$  events in Fig. 11.6. Due to these events, the discrimination is not perfect but provides a potent tool to reduce the atmospheric  $\overline{\text{NC}}$  neutrinos.



Abbildungen/Theia/CSvsScin\_zoom.pdf

Figure 11.6: The  $C/S$  ratio offers a powerful tool to discriminate prompt positrons of  $DSNB$  events (blue) and hadronic prompt events of atmospheric  $NC$  reactions (black). Atmospheric  $NC$  events lead to a significantly reduced emission of Cherenkov photons. The right plot presents a zoom-in for  $C/S$  values greater than 0.5. The gray shaded area corresponds to the  $DSNB$  energy window.

An energy-dependent cut on the  $C/S$  ratio is performed, and eight different cut strategies with varying amounts of surviving  $DSNB$  events ranging from 40% to 95% were developed. For instance,  $NC$  backgrounds can be reduced by 96.5% while maintaining a  $DSNB$  signal acceptance of 82%. The potential of a  $C/S$  cut is shown in Fig. 11.7, for Theia100 with a photo-coverage of 70%. The effect on the  $C/S$  cut efficiency with less coverage of 25% was also studied. With less coverage, every photoelectron has a minor chance ( $\sim 36\%$ ) to be detected by a light sensor. Therefore, the detection probability for every photoelectron was randomly evaluated. Based on the smaller amount of Cherenkov and scintillation photoelectrons, the  $C/S$  cut efficiency was determined in addition. The background rejection worsens slightly to 96.3%, corresponding to lower signal acceptance of 78%.<sup>3</sup>

Moreover, to estimate the cut efficiency on the fast neutron background,  $2 \times 10^3$  neutrons with energies of between 100 MeV and 110 MeV, corresponding to the mean energy of produced neutrons in the rock (102 MeV), were simulated [83]. It turned out that only  $\sim 1\%$  of fast neutron background events are surviving the  $C/S$  cut. Therefore, it is concluded that the background can be reduced to a minor level and is not considered in the following.

<sup>3</sup> The corresponding plot of cut efficiencies can be found in the appendix in Fig. A.9

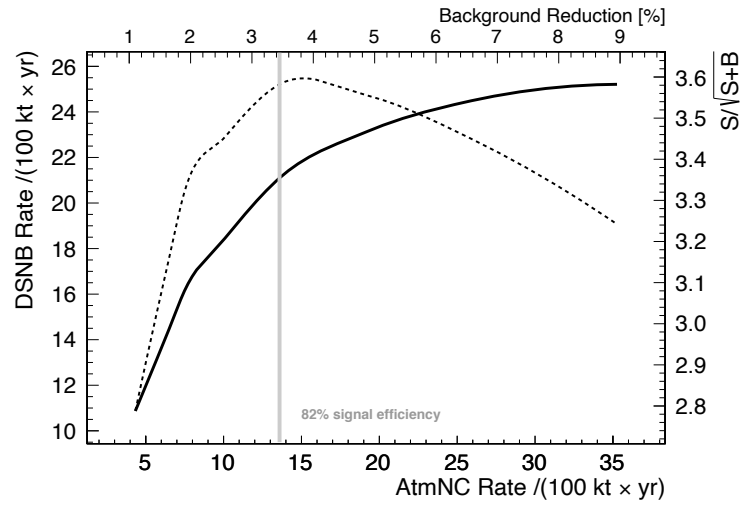


Figure 11.7: The potential of a  $C/S$  cut is shown. The residual amount of atmospheric  $NC$  events is shown to the amount of surviving  $DSNB$  signal events with a solid line. Besides, the significance  $S/\sqrt{S+B}$  is plotted as the dashed line corresponding to the right y-axis. To maximize the signal-to-background ratio, we chose the cut strategy with 82% signal efficiency, where the atmospheric  $NC$  background is reduced by nearly 97%.



### 11.3.3 Delayed Decay Triple Coincidence

A further means of background discrimination is provided by the fact that some of the nuclei in the final states of atmospheric **NC** reactions are radioactive. Their delayed decay provides the possibility to tag a triple coincidence signal from prompt **NC** signal, delayed neutron capture, plus the delayed decay of the isotope created. The dominant **NC** reaction partner of atmospheric neutrinos in **WbLS** is the oxygen nucleus, which turns out to be an advantage over organic **LS**, where interactions on carbon predominantly create the long-lived isotope  $^{11}\text{C}$ . Contrariwise, the amplest isotope created in **WbLS** is  $^{15}\text{O}$ , which is produced with a branching ratio of about 46% (cf. Tab. 11.7). The subsequent  $\beta^+$ -decay with an endpoint of 2.8 MeV and a lifetime of 2.9 min will be well visible in a **WbLS** detector and allows to remove about half of the **NC** background events by searching for a three-fold coincidence of prompt, delayed and a late  $^{15}\text{O}$  decay event [343]. While a similar argument can be made for the low-yield  $^{12}\text{B}$  ( $Q = 13.4$  MeV,  $\tau_{1/2} = 20.2$  ms), all other isotopes are either stable ( $^{14}\text{N}$ ,  $^{13}\text{C}$ ,  $^{12}\text{C}$ ,  $^{10}\text{B}$ ,  $^9\text{Be}$ ) or decaying too fast for a delayed tag ( $^8\text{Be}$ ) [344]. For  $\tau \sim 3$  min, and a veto time six times the lifetime of  $^{15}\text{O}$ , 99.75% of the reactions can be vetoed. Moreover, the dead time of this cut is well below 0.1%.<sup>4</sup> Hence, it is assumed that the atmospheric **NC** background can be reduced by about 48% by looking for the coincident decay of a radioactive isotope.<sup>5</sup>

<sup>4</sup> This depends (cf. section 9.2) on the achieved radioactive background level in the water, which might result in accidental coincidences with real **IBDs**, reducing the signal efficiency.

<sup>5</sup> Compared to **JUNO**, the muon rate of Theia is too low, to obtain significant contribution from cosmogenic  $^{15}\text{O}$  or  $^{12}\text{B}$  production.

## 11.4 Detection Significance

Based on [WbLS](#) Theia offers excellent background discrimination capabilities complementary to those of pure [WCD](#)s or organic [LS](#) detectors. Tab. [11.9](#) illustrates the impact of a sequence of event selection cuts that greatly reduce all backgrounds, including the most important one, i.e., atmospheric neutrino [NC](#) interactions, as described in section [11.2.2](#) and section [11.2.3](#). At the same time, the [DSNB](#) signal acceptance is hardly affected. The spectrum of signal and background events after applying the described cuts is shown in Fig. [11.8](#). Overall, circa nine background events per 100 kt yr are expected inside the detection window, while the [DSNB](#) predicts a rate of 21.1 events per 100 kt yr.

In order to assess the expected significance for positive detection of the [DSNB](#), it was assumed that the number of detected events equals the sum of the expected signal and background rate. Within a realistic scenario is that the expected background rate is only known with a certain precision. In this case, the detection significance can be calculated according to [\[322\]](#). By increasing the size of the confidence interval such that the lower limit is almost zero, the significance of the [DSNB](#) detection is calculated.

A prerequisite for positive detection of the [DSNB](#) is that the expected background rate is determined with high precision. The reactor and atmospheric  $\bar{\nu}_e$  rate can be extrapolated from the measured rate outside the detection window. As the fast neutron rate decreases with the radius of the fiducial volume, it can be determined by analyzing the dependence of the event rate on the radius of the reconstructed

Spectral contribution	100 kt yr exposure			
	before cuts	single-ring	C/S cut	delayed decays
DSNB signal	25.7	25.7	21.1 (20.7)	21.1 (20.7)
Atmospheric CC	2.0	2.0	1.7 (1.6)	1.7 (1.6)
Atmospheric NC	682	394	13.6 (14.6)	7.1 (7.6)
fast neutrons	0.8	0.8	–	–
Signal-to-background	0.04	0.07	1.4 (1.3)	2.4 (2.3)

Table 11.9: Rates of [DSNB](#) signal and backgrounds within the energy observation window (0–3600) p.e., corresponding to ( $\sim 8$ – $30$ ) MeV for a live exposure of 100 kt yr. While the first column represents the rates before cuts, the following columns apply a multi-ring event cut, [C/S](#) ratio cut, and delayed decay triple-coincidence cut. Background arising from reactor neutrinos is not present in the energy window, and  $\beta n$ -emitters are negligible due to the described muon veto. Values in brackets correspond to a smaller photo-coverage of 25%, assumed for Theia25.

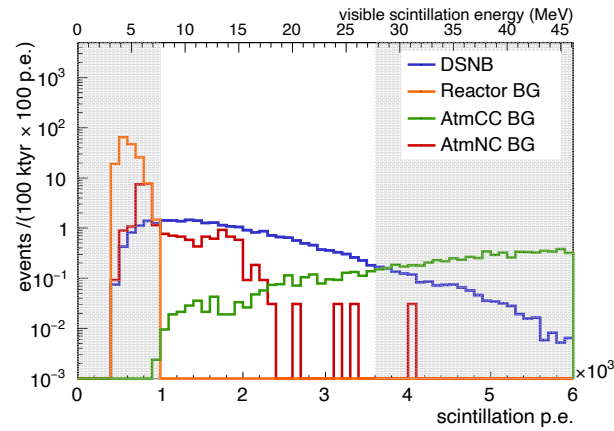


Figure 11.8: The visible scintillation energy spectrum expected for the **DSNB** signal and its ample backgrounds. The presented spectra include reactor neutrinos, atmospheric neutrino **CC** and **NC** interaction rates. The plot corresponds to the spectra the **IBD** event selection and after applying multi-ring event cut, **C/S** ratio cut, and delayed decay triple-coincidence cut.

position. The atmospheric **CC** background rate can likely be extrapolated from measurement outside the detection window with an uncertainty of 20%. Most critical is the **NC** atmospheric background. The different cut strategies reduce the background rate to  $\sim 1\%$  (cf. Tab. 11.9) in the considered energy window. In order to evaluate the number of remaining background events in the detection window, knowledge on the **NC** interaction rate and the cut efficiency is needed. A less unknown cut efficiency  $\epsilon_{cut} = 1\% \pm \delta_{cut}$ , increases the total uncertainty of the background events. Therefore, the effect on the detection sensitivity is studied. The relative uncertainty is varied by up to 20%, and the effect on the signal significance can be taken from the left panel of Fig. 11.9.

With a target mass several times the size of Super-Kamiokande (**SuperK**) or **JUNO**, Theia100 can obtain a  $5\sigma$  discovery of the **DSNB** in less than two years of data taking. Even the smaller Theia25 will profit considerably from the dual detection of Cherenkov and scintillation signals that offer a background discrimination capability unparalleled by Gd-doped water or pure organic scintillator. Thus, Theia25 will require about seven years of data taking to achieve a  $5\sigma$  discovery of the **DSNB** signal (assuming standard predictions for flux and spectral energy).

Moreover, the impact on the **DSNB** flux model is presented in the right panel of Fig. 11.9. Besides the detector performance, the sensitivity strongly depends on the signal rate, which is mainly determined by the actual **DSNB** flux and the detector size.

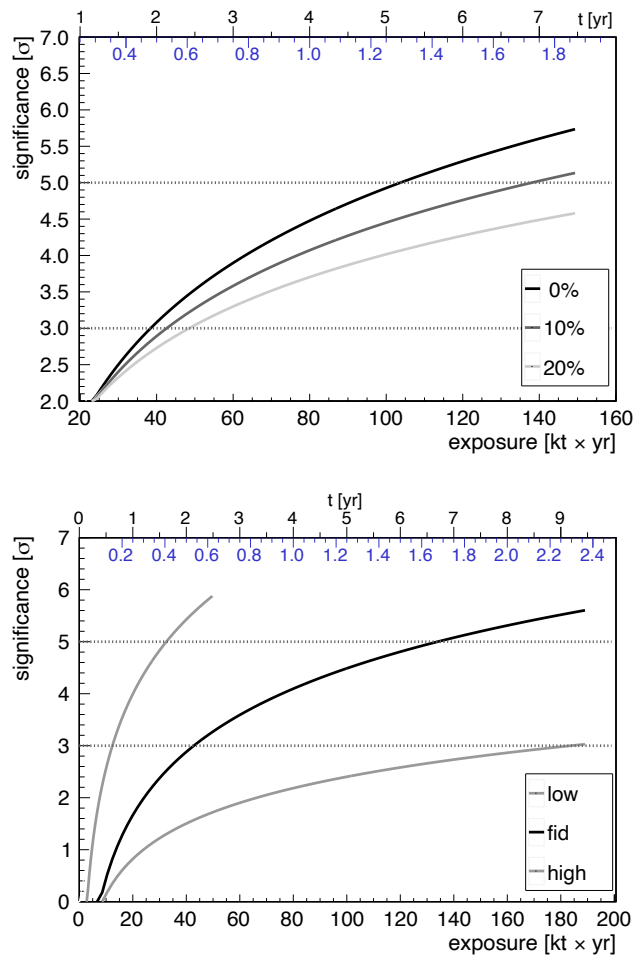


Figure 11.9: The significance of [DSNB](#) detection is given dependent on exposure. The upper black (blue) x-axis corresponds to the lifetime of Theia25 (Theia100). The uncertainty on the cut efficiency is varied up to 20%. A higher unknown uncertainty strongly reduces the detection sensitivity. The right panel corresponds to a variation of the [DSNB](#) flux model. The fiducial flux is shown in black, while the low and high flux models are given in gray. Note that the highest flux model is limited to the current [SuperK](#) limit.

All in all, it was shown that [WbLS](#) detectors offer a new great technology for neutrino observations. Even for low event rates, they provide excellent background suppression techniques to allow DSNB detection in the future. The perspective of a [DSNB](#) measurement is put in relation to other large (future) neutrino detectors within the next chapter.

## Chapter 12

### Comparison of Detection Techniques

The expected diffuse supernova neutrino background (DSNB) rate of approximately four events per year in the large volume scintillator experiment JUNO is too low to allow for spectral signal analysis within the next decade. Fortunately, several future large volume neutrino detectors are planned to be built and offer the possibility to merge DSNB data.

In the present chapter, three different future experiments are introduced and compared in the manner of DSNB detection. Therefore, the Gd-loaded water Cherenkov detector Super-Kamiokande and the proposed Hyper-Kamiokande detector are discussed in section 12.1 and section 12.2, respectively. Furthermore, the DSNB detection ability of the liquid argon detector DUNE will be presented in section 12.3. The results of the liquid scintillator experiment JUNO and the proposed water-based liquid scintillator detector Theia from chapter 10 and chapter 11, respectively, are adopted and merged in section 12.4. There, finally, the power of a combination of these four different detector technology experiments is shown. In the present chapter, the fiducial DSNB flux model (cf. section 4.3) is assumed, unless otherwise stated, to make signal expectations comparable.

## 12.1 Gd-loaded Super-Kamiokande

The Super-Kamiokande (SuperK) design (cf. section 2.1.1) is focussed on the measurements of proton decay, and atmospheric, accelerator, solar, and galactic supernova neutrinos. So while SuperK is with  $\sim 50$  kt large enough to have a few DSNB interactions per year, the detector design is not optimal for a DSNB measurement. Within SuperK, the observation of DSNB neutrinos by the inverse  $\beta$ -decay (IBD) is possible, but as the neutron capture signal is below the detection threshold, coincidence detection is difficult. Up to now, SuperK is mainly detecting electron antineutrinos ( $\bar{\nu}_e$ 's) from single positron events coming from IBD, for which there are enormous background rates present [116]. Although for a 2.2 MeV  $\gamma$ -ray detection efficiency of 20%, the background is much higher than the signal, positive detection is not possible [116, 345].

For SuperK, the energy window for observation is between 19 MeV to 35 MeV. Below 10 MeV, reactor neutrinos completely overwhelm the DSNB neutrino signal [346]. Above 10 MeV and below the observable energy window, the primary source of background is due to the solar neutrinos, radiation from outside the fiducial volume, and spallation-produced events due to the cosmic-ray muons in the detector [347]. Above 19 MeV, the background is primarily due to atmospheric muon (anti-)neutrinos, that produce invisible muons in the detector by interaction with the nucleons [287]. If these muons are produced with energies below the Cherenkov radiation threshold ( $\sim 53$  MeV), they cannot be detected. Subsequently, they produce decay electrons, with a maximum energy of 53 MeV. At energies higher than  $\sim 35$  MeV, the rapidly (exponentially) falling DSNB flux becomes smaller than the atmospheric  $\bar{\nu}_e$  flux.

In order to reduce the above-described backgrounds, the SuperK-Gd project was approved. By dissolving 0.2% gadolinium sulfate into SuperK's water, the detection efficiency of neutrons from neutrino interactions can be enhanced [117]. The proposed upgrade could reduce the invisible muon background substantially (by a factor five), and justifies the ongoing research and development effort [113, 159]. Furthermore, the spallation backgrounds can be removed between 10 MeV and 18 MeV, opening up the energy window for DSNB searches, but below 10 MeV, reactor  $\bar{\nu}_e$  would still overwhelm the DSNB signal [117]. The enrichment of SuperK with gadolinium is going to enhance the signal-over-background ratio drastically. The expected signal rate between 10.8 MeV and 30.8 MeV of neutrino energy is  $\sim 16.3 / (100 \text{ kt yr})$ , assuming a signal efficiency of 70% [345]. The background rate within this energy window is  $\sim 14 / (100 \text{ kt yr})$  and below the signal rate [326]. With a fiducial mass of 22.5 kt and expected start of data taking 2021, the DSNB sensitivity of SuperK+Gd is comparable with JUNO [117]. An even larger proposed project is the HyperK detector, which is the topic of the following section.

## 12.2 Hyper-Kamiokande

The Hyper-Kamiokande (HyperK) detector is proposed as a next-generation general-purpose neutrino detection experiment [113]. It will serve as a far detector of the long-baseline ( $\sim 295$  km) neutrino oscillation experiment T2HK for the J-PARC neutrino beam. Besides the beam neutrinos, the detector will be capable of observing proton decays, atmospheric and solar neutrinos as well as neutrinos from other astrophysical origins. HyperK comprises a cylindrical<sup>1</sup> (60 m high and 74 m in diameter) underground water Cherenkov detector containing a fiducial (total) mass of 187 kt (260 kt), making it more than 8 (5) times as large as the SuperK detector. The proposed location for HyperK is in the Tochibora mine,  $\sim 8$  km southern of SuperK, with an overburden corresponding to 1.75 km.w.e [348]. HyperK will benefit from  $\sim 40,000$  newly designed high-efficiency PMTs, thus reaching the same photo coverage ( $\sim 40\%$ ) as SuperK [348]. Together with attenuation lengths as high as  $\sim 100$  m (at 400 nm wavelength), which may be achievable through purification processes, an excellent detection efficiency can be guaranteed [113]. The enrichment of the nominal detector configuration with gadolinium sulfate is currently under discussion, according to the outcome of the SuperK gadolinium project [349]. With gadolinium added to water, greatly reduces backgrounds and opens up the DSNB energy window. The observable energy window of DSNB events in HyperK is comparable with the SuperK experiment, which is bounded by cosmic-ray induced spallation backgrounds at lower energies and invisible muon background from atmospheric neutrinos at higher energies.

It is assumed that HyperK will start data taking 2027 with 187 kt fiducial mass, while six years later, a second tank of the same size with gadolinium is assumed [350]. The expected signal rate between 10.8 MeV and 30.8 MeV of neutrino energy is  $15.6 / (100 \text{ kt yr})$  with gadolinium and a signal efficiency of 67% [351]. The background rate is assumed to be equal with the one estimated for SuperK-Gd (cf. section 12.1) with  $14 / (100 \text{ kt yr})$  [326].

Without gadolinium, the signal window is reduced to (20–30) MeV of energy deposition, corresponding to a signal rate of  $4.7 / (100 \text{ kt yr})$  without neutron tagging and signal selection efficiency of 90% [351]. Without gadolinium the amount of background events overwhelms with  $39.3 / (100 \text{ kt yr})$  the signal events by a factor of eight [113].

Nevertheless, due to the enormous target mass, high rates are expected, resulting in significantly higher statistics. However, the background rates have to become under control. Therefore, HyperK would clearly benefit from the Gd enrichment with a great chance to study the DSNB spectrum in detail.

<sup>1</sup> There are several options, also the possibility of two cylindrical tanks, each of them with 187 kt fiducial volume, under discussion.

### 12.3 Deep Underground Neutrino Experiment

In addition to liquid scintillator (LS) and water Cherenkov detectors (WCDs) (cf. chapter 2), the detectability of the DSNB using liquid argon (LAr) detectors will be shortly discussed. Although the detection of low energy neutrinos is challenging, the potential advantage of these detectors is that they are mainly sensitive to electron neutrinos ( $\nu_e$ 's) via charged current absorption of  $\nu_e$  on  $^{40}\text{Ar}$ :



The observables of this reaction are the electron and the de-excitation products from the excited  $K^*$  final state [352]. While LS and WCDs will be mainly sensitive to antineutrinos, the upcoming LAr Deep Underground Neutrino Experiment (DUNE) may detect the DSNB signal in the neutrino channel, providing complementary information [353].

DUNE is an upcoming long-baseline neutrino oscillation experiment aiming to determine the unknown oscillation parameters and explore new physics [352, 354]. The 1300 km baseline, stretching from the Long-Baseline Neutrino Facility (LBNF) facility at Fermilab to the Sanford Underground Research Facility in South Dakota, will result in high sensitivity for CP-violating phase, and neutrino mass ordering [354]. The design power of the LBNF beam is 1.2 MW and will comprise the world's highest-intensity neutrino beam [354]. The DUNE far detector will be a large modular LAr time projection chamber of 40 kt detector material located deep underground, which will provide comprehensive event statistics.

Background is also a severe issue for DSNB detection in DUNE. The irreducible solar neutrino background of hep and  $^8\text{B}$  neutrinos (cf. section 1.4.1) cannot be eliminated or tagged. Since the end tail of the hep neutrino flux is at 18.8 MeV, this will determine the lower bound of the DSNB search window. The upper bound is determined by the atmospheric  $\nu_e$  flux and is around 35 MeV. The main challenge for DSNB detection in a LAr time projection chamber is understanding how much of the spallation background from cosmic-ray interactions with the argon nucleus leaks into the search window. Some studies have been done, but more work is needed [355].

The expected number that could be observed in the DUNE detector is  $\sim 11.4 / (100 \text{ kt yr})$  between 16 MeV and 40 MeV of electron energy [356].<sup>2</sup> The estimated background rate is  $\sim 6 / (100 \text{ kt yr})$ , including background from solar and atmospheric neutrinos [356]. It is estimated that data taking will start 2026 with two caverns, while one (three) year(s) later, the third (fourth) chamber will be ready for detection [354].

<sup>2</sup> The event number is based on the assumptions made in [356], where the DSNB flux differs from the fiducial flux model of this thesis.



## 12.4 Comparison

In the previous sections, the WCDs SuperK and HyperK were presented in the manner of future DSNB detection. In addition, the neutrino detection technique using LAr was introduced on the example of the DUNE project. Now, the results for the LS detector JUNO and the proposed WbLS detector Theia from chapters 10 and 11, respectively, are transferred into this section. A summary of the individual experiments with their assumptions for signal and background rates are given in Tab. 12.1. Please note that DSNB signal assumptions were equal for all experiments, except for DUNE, where the signal expectation corresponds to a slightly weaker DSNB flux estimation. Nevertheless, the present comparison aims to show trends instead of making absolute statements.

Technology	Experiment	FM [kt]	Start	Energy-Window [MeV]	Signal [/(100 kt yr)]	BG
LS	JUNO	14.7	2021	12–34	14.4	8.1
	SuperK + Gd	22.5	2021	10–30	16.0	14.0
WCD	HyperK	187	2027	20–30	4.7	39.3
	HyperK + Gd	187	2033	10–30	15.6	14.0
WbLS	Theia25	20	2030	8–30	20.7	9.3
	Theia100	80			21.1	8.8
LAr	DUNE	20 (+20)	2026	16–40	11.4	6.0

Table 12.1: Overview of different future neutrino detectors that are probably able to detect the DSNB signal. The assumptions for fiducial mass (FM), start of data taking, and corresponding observation energy window are given. The expected signal and background rates are given for the LS experiment JUNO and the two proposed realizations of the WbLS experiment Theia. The two proposed options for Theia are given additionally. The WCDs: SuperK+Gd, HyperK, and HyperK+Gd, and the LAr project DUNE were also related [350,351,357]. DUNE is estimated to start data taking 2026 with two caverns ( $\sim 20$  kt), while the third and fourth chamber will be ready one and three year(s) later, respectively [354].

The lifetime evolution of expected **DSNB** events for each experiment is shown in the upper panel of Fig. 12.1. The curves of **JUNO** and Gd-loaded **SuperK** are quite similar due to the equal start of data taking in 2021. The apparent advantage for **SuperK** is mainly due to the larger fiducial volume, but the estimated background rates for **SuperK** are much higher. Therefore, it is concluded that the given values are not entirely optimized for **DSNB** detection. The proposed detector **HyperK** will overcome the amount of detected **DSNB** events at the beginning of 2030. If there will be a second tank present with Gd-loaded water, the event expectations rise noticeably. The smaller Theia realization (Theia25) will not be competitive in terms of rates. However, without Gd-loading in **HyperK**, the more massive proposed realization of Theia (Theia100) will take the leading position around 2035. The **LAr** experiment **DUNE** will not be a strong competitor in terms of signal rates, but with the third and fourth cavern, it will overcome the **JUNO** experiment only by exposure around 2033. However, as **DUNE** has some incomplete background knowledge, more studies are needed to give reliable statements about sensitivity. Moreover, it is of great interest, as it is the only experiment sensitive to the complementary neutrino channel.

The significance-like expression  $S/\sqrt{S+B}$  is plotted for the different experiments in the lower panel of Fig. 12.1. The relation between **JUNO**, **SuperK**+Gd and **DUNE** is almost the same as it is present for the **DSNB** rate comparison. Contrary to **HyperK** and Theia: **HyperK** without Gd is almost not sensitive to **DSNB** neutrinos, due to the overwhelming backgrounds. Therefore, Gd-loading is urgently needed to get access to this astrophysical neutrino source. The smaller Theia configuration has quite the same fiducial volume as **JUNO** and **SuperK**, but through the combination of both detection techniques, background suppression is more potent, resulting in a steeper sensitivity curve. The more extensive Theia100 configuration would dominate all other experiments in terms of sensitivity soon after its start.

All in all, there are luckily several neutrino experiments ready to start within the next years to search for the **DSNB** signal. A successful first detection could be performed in the future by the Gd-loaded **SuperK** detector or by the **LS** experiment **JUNO**, depending on detector performance and efficient background identification. Please note that all the previous comparisons were made with the fiducial **DSNB** flux model (cf. chapter 4) and that the timescale of **DSNB** detection beside detector performances also strongly depends on the actual signal strength. Nevertheless, the complementary detector techniques in combination with complementary neutrino channels offer great potential for joint analysis of **DSNB** measurements in the future.

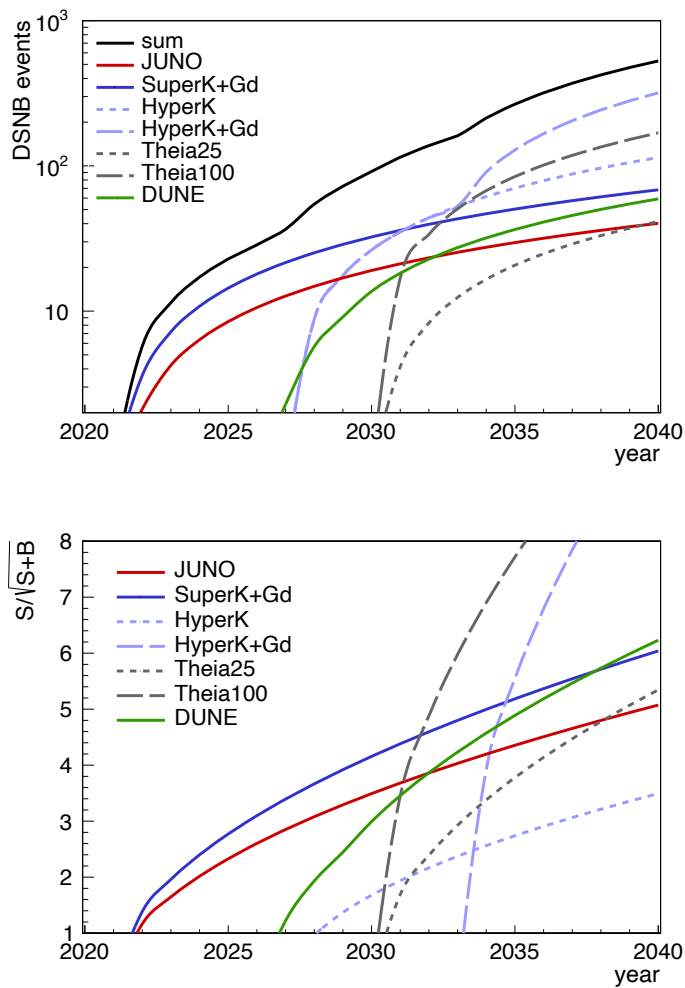


Figure 12.1: *Upper panel: Lifetime evolution of  $\overline{\text{DSNB}}$  events for different experiments. The curves of  $\overline{\text{JUNO}}$  and  $\overline{\text{SuperK}}+\text{Gd}$  are quite similar due to the same start in 2021, but with larger fiducial volume for  $\overline{\text{SuperK}}$ . The proposed detector  $\overline{\text{HyperK}}$  will overcome both experiments right after it has been started. With a second Gd-loaded water tank, the event expectations rise noticeably. The smaller Theia detector will not be competitive in terms of rates. However, without Gd-loaded  $\overline{\text{HyperK}}$ , the larger Theia100 will take the lead position around 2035. The  $\overline{\text{LAr}}$  experiment  $\overline{\text{DUNE}}$  will not be a strong competitor, but with the third and fourth cavern, it will overcome the  $\overline{\text{JUNO}}$  experiment only by volume. The shown sum corresponds to the most optimistic case with Gd-loaded  $\overline{\text{HyperK}}$  and Theia100. Lower panel: Comparison of significance. If no Gd-loading will be present for  $\overline{\text{HyperK}}$ , it is almost not sensitive to  $\overline{\text{DSNB}}$  neutrinos. Through the combination of both detection techniques in Theia, background suppression is more powerful, resulting in steeper sensitivity curves. Nevertheless, the larger Theia configuration would dominate all other experiments soon after its start, expected to be in the first quarter of 2030.*



## Conclusions

Since the first neutrino detection in 1956, many experiments have been built to examine the particle properties. Besides, these particles carry information about the environment in which they are created. Primarily through neutrino signals from supernova (SN) explosions, information about the explosion mechanism can be gained. A still unmeasured neutrino flux from stars is the so-called diffuse supernova neutrino background (DSNB), which is the average cumulate neutrino flux of all past core-collapse supernovae (CCSNe) in the visible universe. Contrary to observations of a single SN, a DSNB measurement would provide information on the average explosion of stars.

Within this work, the detection potential for the DSNB flux was studied for the Chinese multipurpose neutrino experiment named Jiangmen Underground Neutrino Observatory (JUNO). The JUNO detector is a 20 kt liquid scintillator (LS) detector currently under construction in southern China. Due to its large target mass and unprecedented energy resolution of 3% (at 1 MeV), a measurement of electron antineutrinos via the inverse  $\beta$ -decay (IBD) can be performed. The coincidence event signature of this reaction channel provides high-grade background suppression. With the two reactor complexes in 53 km distance to the detector, the neutrino mass ordering can be determined within the next years through a precision measurement of the energy-dependent survival probability of reactor neutrinos. Beyond, JUNO could be one of the first experiments to measure the DSNB successfully, as currently, only upper limits exist [3]. The DSNB flux predictions were refined from spherically symmetric SNe simulations performed over a wide range of progenitors [125]. The flux predictions were translated to observable neutrino signal spectra expected for JUNO, forecasting between 2.7 and 19.6 events per year in a fiducial volume of 14.7 kt. However, the highest flux model already exceeds the current flux limit by a factor of two. The DSNB spectrum depends on fundamental astrophysical source properties: the fraction of failed explosions, the mass threshold of black hole (BH) formation, and the CCSNe rate. A strong dependence of the spectrum at high neutrino energies on the maximum neutron star mass and BH fraction is present, with a spread of almost an order of magnitude. The fiducial flux model predicts 5.5 events per year ranging from 1.8 MeV to 40 MeV, assuming an amount of 17.3% of failed SNe, a BH (baryonic) mass threshold of  $2.7 M_{\odot}$ , and the fiducial CCSNe rate following [122].

---

Further, a variety of backgrounds are present for this measurement. The near distance to the nuclear power plants provides an enormous amount of reactor neutrinos, surpassing the **DSNB** signal by orders of magnitude. As the irreducible reactor neutrino background spectrum decreases exponentially, it defines the low energy threshold for **DSNB** detection. The reactor neutrino spectrum drops below the **DSNB** spectrum at  $\sim 10$  MeV.

Although the detector will be located underground with 650 m of rock overburden, around 3.5 muons per second still reach the central detector volume. The muons itself in the inner detector can be identified by a large amount of scintillation and Cherenkov light. However, cosmogenic muons can produce relatively long-lived radioactive isotopes, providing a background source. The  $\beta$ -decay of  ${}^9\text{Li}$  provides a Q-value large enough to reach in the **DSNB** signal noticeably. The production yield, measured by Borexino, was scaled to evaluate the expected background level arising from  ${}^9\text{Li}$  decays, resulting in  $\sim (1310 \pm 130)/(\text{kt yr})$  events. As there are spatial and temporal correlations between the spallation events and the parent muons, it is possible to veto the main of this background by vetoing a cylindrical volume around each reconstructed muon track. Assuming a muon detection efficiency of 99.8%, and a vetoed volume with  $r = 3$  m, which is vetoed for 1.2 s after each muon track, the background rate is reduced to  $(26.2 \pm 2.6)/(\text{kt yr})$ . This cut reduces the signal efficiency by 16%. The background rate still overwhelms the estimated signal below  $\sim 12$  MeV, setting an additional low energy threshold for **DSNB** detection.

Contrary to muons that traverse the inner detector, muons can pass the water Cherenkov veto volume or the surrounding rock. As muons in the outer detector can be vetoed, muons traversing the rock material can produce high energetic particles, like neutrons. Some of these, so-called, fast neutrons, can enter the inner detector volume without being tagged. The background rate was estimated to be  $\sim (2.4 \pm 0.5)/(\text{kt yr})$  in the total inner detector volume below 40 MeV. Because of the finite mean free path of neutrons, most of the events concentrate on the verge of the scintillator volume. Therefore, this background can be reduced significantly through a reduction of the fiducial detector volume. Reducing the fiducial radius by 1 m allows pushing the background already below the signal. Moreover, during experimental data taking, a radial dependent study of this background, matched with simulations, will help to understand the neutron background and allows for statistical subtraction.

The last group of background arises from atmospheric neutrinos. The atmospheric neutrino flux for the location of **JUNO** was approximated using two different simulations [5,6]. The charged current reactions of atmospheric electron antineutrinos on protons represent an indistinguishable background source. However, the atmospheric neutrino flux is increasing in energy, and defines, therefore, the

upper energy threshold on the detection window around 35 MeV. The atmospheric charged current rate was calculated to  $\sim (0.2 \pm 0.07)/(\text{kt yr})$  for  $E_\nu < 100 \text{ MeV}$ .

Also, neutral current (NC) reactions of atmospheric neutrinos and antineutrinos of all flavors pose a possible background for DSNB detection. In the reaction with the largest branching ratio, (anti-)neutrinos knock out a neutron of the  $^{12}\text{C}$  nucleus. The remaining nuclei are often left in an excited state, giving additional particles from the de-excitation. After thermalization, the neutron gets captured, providing the delayed signal for coincidence reaction. The total event rate of atmospheric NC interactions was calculated to  $\sim (30.8 \pm 0.31)/(\text{kt yr})$  for  $100 \text{ MeV} < E_\nu < 10 \text{ GeV}$ .

Signal and background events were simulated with JUNO's Offline Simulation Framework (IOSF) (Version J18v1r1) based on Geant4 (Version 9.4.p4) [202–205]. The interactions of atmospheric neutrinos with the LS target were simulated with GENIE (Version 2.12.4) and inserted in IOSF [70, 295]. The nuclear reaction program TALYS (Version 1.4) provides the particles emerging from excited nuclei that were additionally read into IOSF [296, 297]. After the simulation, event selection was performed to prove the coincidence event signature. The background, mainly the atmospheric NC background, overwhelms the DSNB signal in the interesting energy window by a factor of  $\sim 16$ .

Hence, techniques to identify background represents a decisive issue for a DSNB measurement, in order to possibly observe the tiny signal. Within this work, the powerful tool of pulse shape discrimination (PSD) was of particular interest. As just positrons create the prompt DSNB pulses, the atmospheric NC events arise mainly from much heavier protons and neutrons. Hence their light emission time profiles (pulse shapes) differ, allowing for disentanglement of background and signal events. The timing information of photons on the photocathodes was provided by IOSF and was modified to consider the photomultiplier tube and event reconstruction effects. Based on that, the timing profile of the light emission was reconstructed. Afterward, the simple tail-to-total ratio method was used to identify pulses, where information of the integral ratio of light emission times below 120 ns were compared. It was shown that the ratio is position-dependent, arising mainly from the enhanced probability for photon scattering in the inner detector volume. Furthermore, photons produced at the outer detector part show an increased probability for total reflection at the edge of the scintillator volume, resulting in a pulse form variation. In order to avoid the correction of these effects, events were simulated in the inner 16 m detector volume, where a minor chance of total reflection is present. To account for the scattering effects, the cut values are chosen position-dependent. The atmospheric NC background can be reduced to (0.5-3)%, with corresponding signal efficiencies ranging between 47% and 99%, relying on

---

the chosen cut strategy. The favored cut strategy is found through maximization of the significance like expression  $S/\sqrt{S+B}$ , providing 86.4% signal efficiency and background rejection of 98.4%. It is crucial to mention that the results strongly depend on the fluorescence timing parameters that determine the fractions of singlet and triplet states, determining the light emission time profiles. The results of the present work are based on Monte-Carlo tuning of Daya Bay data. It is inevitable to determine the fluorescence timing parameters for the JUNO scintillator separately and precisely in the future. Moreover, there is less knowledge on pulse shapes above  $\sim 10$  MeV of energy deposition, where the DSNB signal gets prominent, as scintillating time profiles were mostly measured with neutrons or  $\alpha$ -particles with lower energies. However, within the Borexino experiment, it was possible to identify atmospheric NC events through the application of PSD even in the higher energy region [308].

Additionally, a second background identification method to further suppress the atmospheric NC background events was discussed. The so-called triple coincidence veto based on the fact that some of the resulting nuclei are radioactive. Such a decay provides a third signal after the coincidence IBD and offers an additional veto strategy. The promising nuclei candidates are  $^{11}\text{C}$ ,  $^{10}\text{C}$ , and  $^8\text{Li}$ , as all other produced isotopes are either stable or decay almost instantly. Once the position of the IBD event is known, one needs to apply a cut in space and time around each candidate and veto events with corresponding energy deposition. It was proposed to divide the triple coincidence veto into three veto sections to account for the different Q-values and decay times of  $^{11}\text{C}$ ,  $^{10}\text{C}$ , and  $^8\text{Li}$ . It was proposed to veto (0.9–16.4) MeV of energy deposition for the first 8 s, which is followed by vetoing (0.9–3.8) MeV for 3 min, and lastly, vetoing the even smaller energy window (0.9–2.1) MeV for 1.5 h. It was found that for a vetoed mass of  $\sim 0.5$  t, the probability is  $\sim 80\%$  for the subsequent decay to happen inside. In that context, it was studied how big such a vetoed volume is allowed to be, to still guarantee an adequate signal efficiency. The probability of accidental events following signal events is estimated, concerning cosmogenic isotope production and signals arising from radioactivity. The overall signal efficiency is reduced by 6% due to the proposed triple coincidence cut but allows for an atmospheric NC background reduction by additional 30%.

Finally, based on the signal and background expectations, and considering the background suppression techniques of PSD and triple coincidence, the DSNB detection potential for the JUNO detector was estimated. Therefore, a detection strategy was proposed, explaining steps of data processing that have to be performed in order to obtain the signal out of the overwhelming background.



Supplementary, the detection significance was calculated based on an extension of the Feldman-Cousins method allowing to include uncertainty on the background prediction [322]. The optimal energy window was found to manifest between 12 MeV and 34 MeV, assuming the fiducial **DSNB** flux model and the background assumptions, made within this thesis. There,  $\sim 21$  **DSNB** events are expected after ten years of data taking, summing up with  $11.9 \pm 1.3$  estimated background events. With these assumptions,  $4.5\sigma$  of significance can be reachable.

The amount of predicted atmospheric **NC** events in the detection window relies on the precise knowledge of **PSD** cut efficiency. If the efficiency is less known, the uncertainty in the overall background rate increases, which strongly affects the significance. A relative uncertainty of 30% would lower the significance to  $3\sigma$ . Therefore it is stated that a relative uncertainty of 10% is required to allow for **DSNB** detection within the next years, manifesting at  $4\sigma$  after ten years.

Furthermore, the effect of the proposed triple coincidence veto on the sensitivity was studied. Assuming that this cut will introduce an additional relative uncertainty of 10%, increasing the error on the known background, and resulting in no positive effect on the detection significance.

Lastly, besides the detector performance, it was studied how the sensitivity depends on the **DSNB** flux itself. Therefore the failed SNe rate was fixed to 27.3%, and the CCSNe rate, as well as the **BH** forming mass threshold, were varied. It was shown that the actual values of the astrophysical parameters firmly influence the signal strength and, therefore, the significance. With **JUNO**, it is even possible to reach  $5\sigma$  after ten years with a parameter constellation that differs from the assumed fiducial one.

Moreover, it was shown, that the **BH** forming mass threshold and the amount of failed SNe, determine the decreasing slope of the **DSNB** spectrum. It is assumed that with the help of ongoing gravitational-wave measurements, more knowledge on the neutron star masses will be gained. This opens the possibility to determine the failed SNe rate directly through a spectral analysis of the **DSNB** measurement. Unfortunately, **JUNO** is not able to observe the difference in slope due to statistical limitations. However, there is hope for future extensive neutrino experiments and their joint analysis of **DSNB** data.

Supplementary, a future technique of neutrino detection, utilizing water-based liquid scintillators (**WbLSs**), is introduced on the example of the proposed Theia detector. This detector technique is of particular interest, as it will combine the two main approaches of neutrino detection: **LS** with a water Cherenkov detector (**WCD**), by introducing a small amount of **LS** into water. The **DSNB** detection significance was studied for the two proposed detector geometries, named Theia25

---

and Theia100, providing a fiducial volume of 20 kt and 80 kt, respectively. The background level was estimated, and subsequently, background rejection methods were studied. First, the possibility of Cherenkov ring counting reduces the atmospheric **NC** background by 57%. Furthermore, the Cherenkov-to-scintillation ratio cut allows reducing the atmospheric **NC** background by 96.5% (96.3%), maintaining a signal acceptance of 82% (78%) for Theia100 (Theia25). The triple coincidence veto searches for the delayed decay of  $^{15}\text{O}$  and  $^{12}\text{B}$  after each event candidate, reducing the atmospheric **NC** background by 48%. With a target mass several times the size of Super-Kamiokande (**SuperK**) or **JUNO**, Theia100 can obtain a  $5\sigma$  discovery of the **DSNB** in less than two years of data taking. Even the smaller Theia25 will profit considerably from the dual detection of Cherenkov and scintillation signals that offer a background discrimination capability unparalleled by Gd-doped water or pure organic scintillator. Thus, Theia25 will require about seven years of data taking to achieve a  $5\sigma$  discovery of the **DSNB** signal (assuming standard predictions for flux and spectral energy).

Finally, existing and future neutrino experiments with different detection techniques were discussed and compared in the manner of **DSNB** detection. The **WCDs** **SuperK** and the proposed Hyper-Kamiokande (**HyperK**), provide a fiducial volume of 22.5 kt and 187 kt, respectively. However, pure **WCDs** are not optimal for **DSNB** detection, as the delayed neutron capture signal is below the detection threshold, resulting in higher background rates. The possibility to dissolve gadolinium sulfate into the water enhances the detection efficiency of neutrons and reduces the invisible muon background by a factor of five. Furthermore, the Deep Underground Neutrino Experiment (**DUNE**) experiment with a fiducial volume of 40 kt allows for future **DSNB** measurement in a complementary neutrino channel as it measures electron neutrinos through the absorption on liquid argon (**LAr**). As there is more knowledge on the present background rates needed, predictions on the signal-to-background ratio are less reliable. A summary of the individual experiments with their assumptions for signal and background rates were given and related to the results obtained for **JUNO** and Theia to show trends. The experiments **JUNO** and Gd-loaded **SuperK** are quite comparable due to the equal start of data taking in 2021 with an advantage for **SuperK** due to the larger fiducial volume. As the background rates for **SuperK** are much higher, it was concluded that the given values not entirely optimized for **DSNB** detection. The proposed detector **HyperK** will overcome the amount of detected **DSNB** events with 187 kt at the beginning of 2030. However, without Gd-loading, **HyperK** is almost not sensitive to **DSNB** neutrinos, due to the overwhelming backgrounds. Therefore, Gd-loading is urgently needed in **WCDs** to get access to this astrophysical neutrino source. The smaller realization, Theia25, will not be competitive in terms of **DSNB** rates,

but through the combination of both detection techniques, background suppression is more potent, resulting in a steeper sensitivity curve. Without Gd-loading in **HyperK**, the more massive proposed realization of Theia would dominate all other experiments, in terms of sensitivity, soon after its start. The **LAr** experiment **DUNE** will not be a strong competitor, but with the third and fourth cavern, it will overcome the **JUNO** experiment only by exposure around 2033. However, as **DUNE** has some incomplete background knowledge, more studies are needed to give a reliable statement about sensitivity. Moreover, it is of great interest, as it is the only experiment sensitive to the complementary neutrino channel.

All in all, there are luckily several neutrino experiments ready to start within the next years to search for the **DSNB** signal. A successful first detection could be performed in the future by the Gd-loaded SuperK detector or by the **LS** experiment **JUNO**, depending on detector performance and efficient background identification. Note that all previous comparisons were made with the fiducial **DSNB** flux model and that the timescale of **DSNB** detection strongly depends on the actual signal strength. Nevertheless, the complementary detector techniques, in combination with complementary neutrino channels, offer great potential for joint analysis of **DSNB** measurements in the future. Prospective observations of the **DSNB** could probably probe the entire population of stellar core collapse in its full diversity and open the chance to constrain the cosmic core-collapse rate, as well as the fraction of failed SNe.



# APPENDIX



# Appendix A

## Additional Figures and Tables

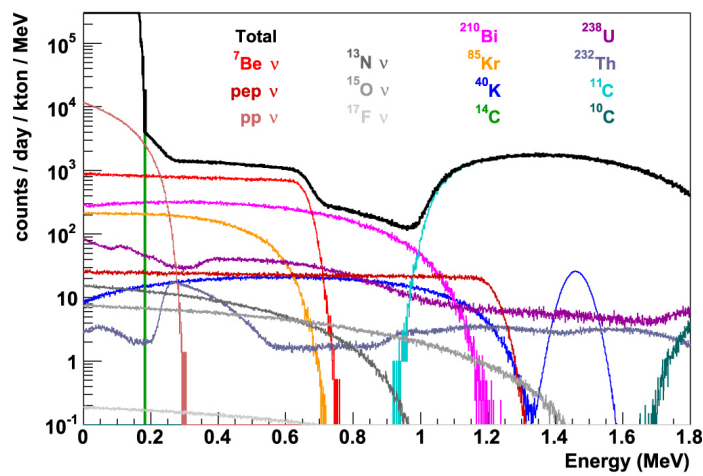


Figure A.1: The expected solar neutrino spectra in **JUNO** with radio-purity assumption from Borexino phase I [222]. Figure from [4].

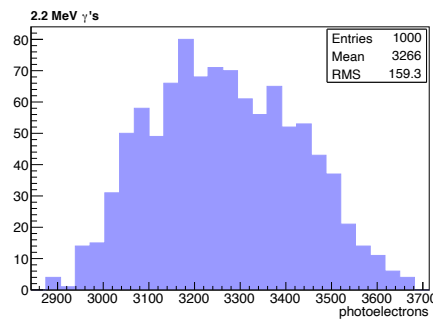


Figure A.2: The distribution of photoelectrons obtained from simulating  $10^3$  2.2 MeV- $\gamma$  events in the **JUNO** scintillator.

		events [/ (100 kt y)]			
threshold $E_\nu >$		1.8 MeV	9 MeV	10 MeV	11 MeV
DSNB	low	18.3	13.7	12.4	11.1
	high	133.4	110.7	104.0	96.8
	fiducial	37.7	29.0	26.6	24.1
reactor $\bar{\nu}_e$		$8.9 \times 10^4$	$37.6 \pm 1.9$	$2.0 \pm 0.1$	$0.04 \pm 0.002$

Table A.1: Total expected event rates for exposure of 100 kt y of reactor neutrinos and the three DSNB flux models. The reactor neutrino rate is obtained through integration of Eq. (5.1) using flux approximation of [282] up to neutrino energies  $E_\nu \leq 40$  MeV. The lower neutrino energy threshold is varied. Note that no detector response function is considered, and a 5% uncertainty in the high energy tail of the reactor spectrum is assumed [31].

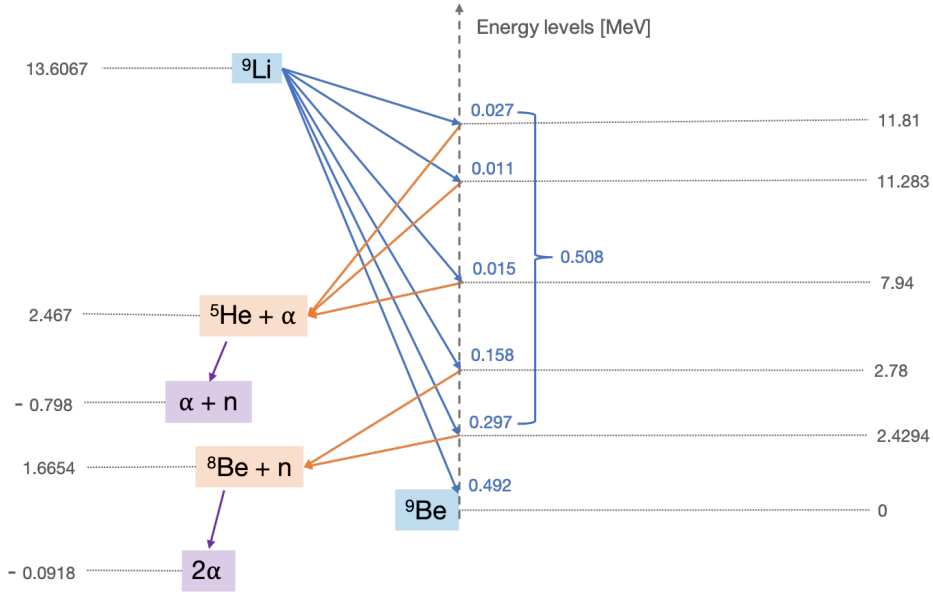


Figure A.3: Implemented decay scheme of the  $\beta^-$ -decay of  ${}^9\text{Li}$  to  ${}^9\text{Be}$  [299, 358]. The blue numbers correspond to the branching ratios of the  ${}^9\text{Li}$ -decay, and the energy levels are given in MeV. The excited state of  ${}^9\text{Be}$  can decay to  ${}^5\text{He}$  and  ${}^8\text{Be}$  (orange), which decay almost instantly into  $\alpha$ 's and neutrons (violet). Negative energy levels are given with respect to the ground state of  ${}^9\text{Be}$ .



Pulse Shape Discrimination					
Signal Efficiency [%]			Event Rate [ /100 kt yr]		
DSNB	AtmNC	FastN	DSNB	AtmNC	FastN
46.9	0.5	0.9	17.7	3.9	0.11
59.1	0.7	1.4	22.3	5.5	0.16
67.5	0.9	1.7	25.2	7.0	0.20
78.2	1.2	2.2	29.5	9.3	0.26
86.4	1.6	3.0	32.5	12.5	0.35
93.1	2.0	4.2	35.1	15.6	0.49
96.8	2.5	5.0	36.5	19.5	0.58
98.8	3.1	6.0	37.2	24.1	0.70

Table A.2: The PSD signal efficiencies and the event rates of the **DSNB** signal, atmospheric **NC** and fast neutron background events, given for different cut strategies. The efficiencies and rates are given for an energy deposition up to  $10^5$  prompt photoelectrons, corresponding to  $\sim 68$  MeV.

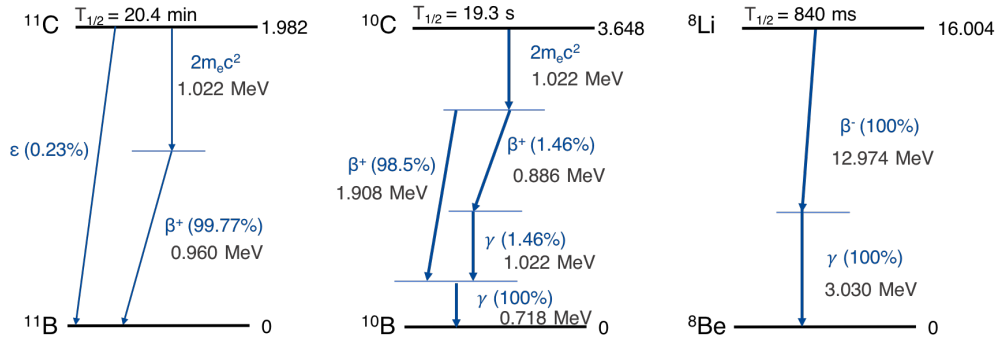


Figure A.4: The decay schemes of  $^{11}\text{C}$ ,  $^{10}\text{C}$ , and  $^8\text{Li}$  are shown from left to right, respectively, and sorted by their half-life times in decreasing order

Atmospheric NC Unstable Isotopes				
nuclei	decay	to	energy emission	life time $\tau$
$^{11}\text{C}$	$\beta+$	$^{11}\text{B}$	1.98 MeV	29.4 min
$^{10}\text{C}$	$\beta+$	$^{10}\text{B}$	3.65 MeV	27.8 s
$^9\text{B}$	$2\alpha$	$^1\text{H}$	0.28 MeV	$\mathcal{O}(\text{as})$
$^9\text{B}$	p	$^8\text{Be}$	0.18 MeV	$\mathcal{O}(\text{as})$
$^8\text{Be}$	$\alpha$	$^4\text{He}$	0.09 MeV	$\mathcal{O}(\text{as})$
$^8\text{Li}$	$\beta-$	$^8\text{Be}$	16.00 MeV	1.2 s
$^7\text{Be}$	$\beta+$	$^7\text{Li}$	0.86 MeV	76 d19 h
$^7\text{He}$	n	$^6\text{He}$	0.44 MeV	$\mathcal{O}(\text{zs})$
$^6\text{H}$	n	$^5\text{H}$	0.90 MeV	$\mathcal{O}(\text{ys})$
$^5\text{He}$	n	$^4\text{He}$	0.89 MeV	$\mathcal{O}(\text{zs})$

Table A.3: Decays of unstable isotopes resulting from atmospheric  $\text{NC}$  reactions. The highlighted nuclei are suitable for the in chapter 9 proposed triple coincidence veto, due to their appropriate life times [299, 358, 359].

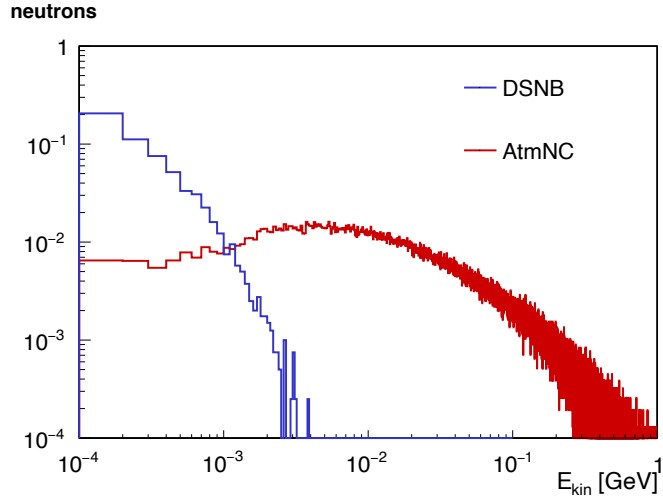


Figure A.5: Distribution of neutron's kinetic energy. Neutrons released in  $\text{IBD}$  reaction of  $\text{DSNB}$  events (blue) are less energetic than neutrons from atmospheric  $\text{NC}$  events (red).

Cut Efficiencies						
Cut	DSNB	AtmNC	AtmCC	FastN	Li9	Reactor
IBD	0.97	0.25	0.96	-	0.97	0.97
MuonVeto	0.84	0.84	0.84	0.84	0.02	0.84
PSD	0.93	0.02	0.93	0.93	0.93	0.04
Triple Coincidence	0.94	0.61	0.94	0.94	0.94	0.94

Table A.4: The table summarizes the cut efficiencies corresponding to different selection techniques for prompt energy deposition  $\lesssim 68$  MeV. The **IBD** selection criteria are described in section 4.4. The muon veto cut reduces mainly the cosmogenic  ${}^9\text{Li}$  background. The background rejection through **PSD** mainly affects the atmospheric **NC** and the fast neutron rate. Lastly, the effect of the triple coincidence cut on the event rate is given. Note that the background suppression methods are applied separately after the **IBD** cut and that the efficiency of reactor neutrinos corresponds to a lower energy threshold of 9 MeV.

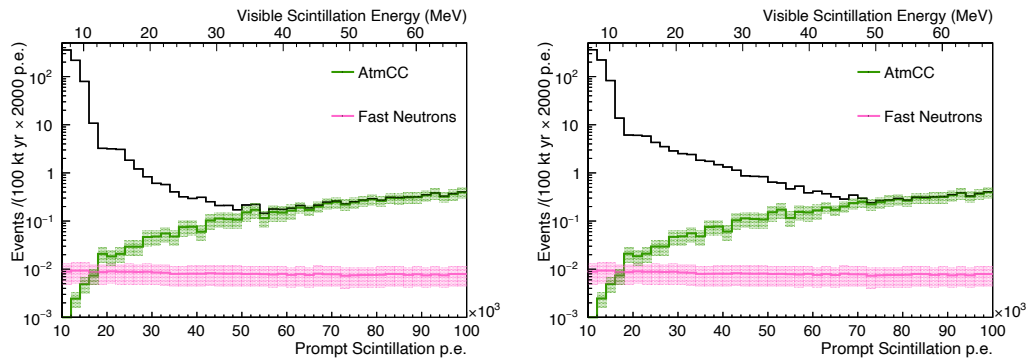


Figure A.6: Knowledge of the atmospheric **CC** interactions is gained from the analysis above a certain energy threshold, while below the background is obtained through extrapolation. The energy at which the atmospheric **CC** interactions surpass the **DSNB** signal depends on actual **DSNB** flux. The lower and upper flux models, correspond to left and right plot, respectively, and a higher **DSNB** flux shifts the energy threshold to higher energies.

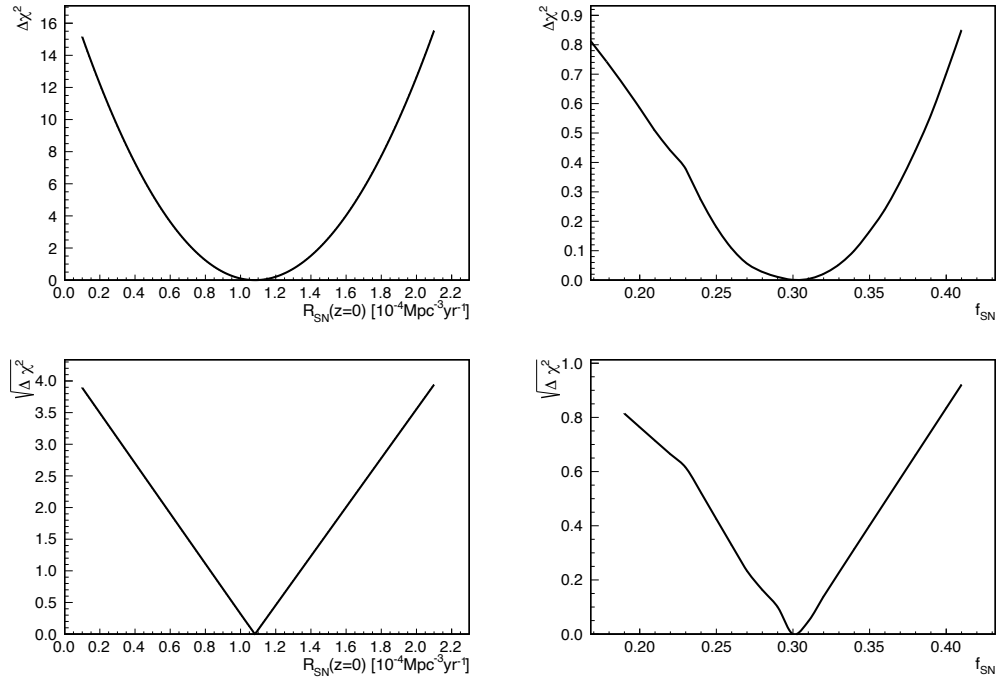


Figure A.7: Function for  $\Delta\chi^2$  (upper panels) and  $\sqrt{\Delta\chi^2}$  (lower panels) in dependence of the CCSNe rate  $R_{SN}$  (left) and the amount of failed SNe  $f_{SN}$  (right). The exposure was set to  $1000 \text{ kt yr}$  and the  $\chi^2$ -values were determined by keeping other parameters constant at their reference values.

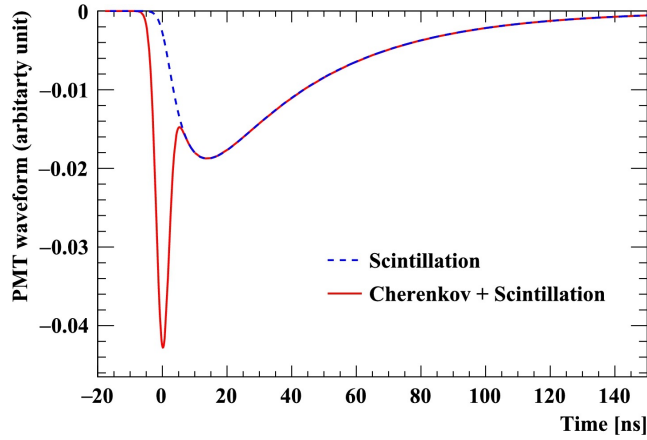


Figure A.8: Schematic diagram of **PMT** waveforms of Cherenkov and scintillation light as shown in [329]. The emission time constant of the scintillation light in **LAB** (dashed blue line) of  $\sim 37$  ns is much longer than the Cherenkov emission time ( $\lesssim 1$  ns) and the PMT response resolution ( $\sim 2$  ns). The red line represents the sum of scintillation and Cherenkov light. Figure from [326].

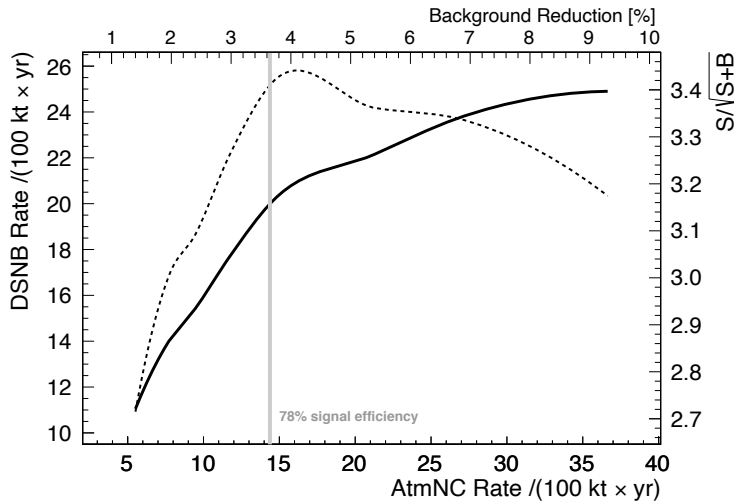


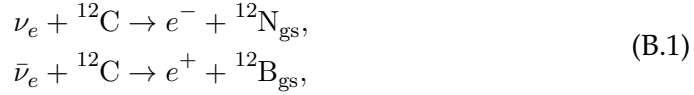
Figure A.9: The potential of a **C/S** cut is shown for detector coverage of 25%. The residual amount of atmospheric **NC** events is shown to the amount of surviving **DSNB** signal events with a solid line. Besides, the significance  $S/\sqrt{S+B}$  is plotted as the dashed line corresponding to the right y-axis. To maximize the signal-to-background ratio, the cut strategy with 78% signal efficiency is chosen, where the atmospheric **NC** background is reduced by nearly 96.3%.



## Appendix B

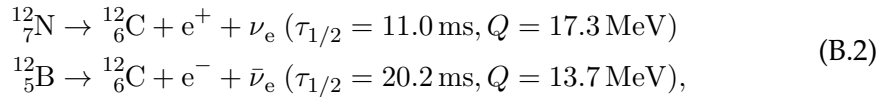
### Atmospheric Charged Current Background on $^{12}\text{C}$

Besides the known inverse  $\beta$ -decay (IBD) reaction of  $\bar{\nu}_e$  on free protons, there is also the possibility for a charged current (CC) reaction on  $^{12}\text{C}$ , where (anti-) electron neutrinos can produce  $^{12}\text{N}$  and  $^{12}\text{B}$ :



where  $gs$  denotes the ground state. The amount of reactions that produce  $^{12}\text{N}$  and  $^{12}\text{B}$  is estimated to  $0.67 / (\text{kt yr})$  and  $0.28 / (\text{kt yr})$ , respectively, calculated with GENIE cross-sections, which overestimates the result by 25% [338, 340, 360]. The maximum kinetic energies of the  $\beta$ -particles reach with 12.9 MeV and 16.8 MeV into the DSNEB detection window.

As there is no delayed neutron signal available, these reactions do not pass in principle the coincidence condition. Hence, the subsequent  $\beta$ -decay of  $^{12}\text{N}/^{12}\text{B}$



could provide the delayed signal, if the deposited energy match the delayed 2.2 MeV  $\gamma$ -signal. The amount of particles that decay within the time window of 1 ms is

$$N = 1 - \exp\left(-\ln 2 \times \frac{1 \text{ ms}}{\tau_{1/2}}\right)\tag{B.3}$$

and is 6% and 3% for  $^{12}\text{N}$  and  $^{12}\text{B}$ , respectively. The delayed energy window is defined in section 4.4. From the Fermi theory of  $\beta$ -decay, the shape of the energy

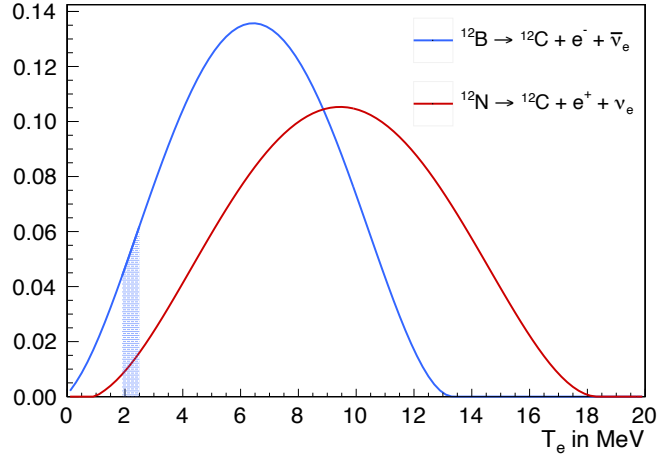


Figure B.1: Distribution of energy deposited by delayed  $\beta$ -decays of  $^{12}\text{B}$  (blue) and  $^{12}\text{N}$  (red). The allowed energy range of the delayed 2.2 MeV event is shown as the shaded area.

distribution is given approximately by the expression

$$\begin{aligned}
 N(T_e) \simeq & \sqrt{T_e^2 + 2T_e m_e c^2} \times (T_e + m_e c^2) \\
 & \times (Q - T_e) \sqrt{(Q - T_e)^2 - m_\nu^2 c^4} \times F(Z', T_e),
 \end{aligned} \tag{B.4}$$

where  $F(Z', T_e)$  is called the Fermi function,  $T_e$  here is the kinetic energy of the electron, and  $m_\nu$  the neutrino mass [361].  $Q$  represents the energy yield of the transition and as such is the upper bound on the kinetic energy of the electron. The energy distributions of the  $\beta$ -decays of  $^{12}\text{N}$  and  $^{12}\text{B}$  are shown in Fig. B.1. The delayed energy cut reduce these background rates below 1% and 3%, respectively, reducing both rates below 0.01 / (kt yr). Therefore the atmospheric CC reactions on  $^{12}\text{C}$  are not considered as a background for DSNB detection.



## List of Abbreviations

<b>BH</b>	black hole
<b>CC</b>	charged current
<b>C.L.</b>	confidence level
<b>CCSN</b>	core-collapse supernova
<b>C/S</b>	Cherenkov-to-scintillation
<b>DM</b>	dark matter
<b>DSNB</b>	diffuse supernova neutrino background
<b>DUNE</b>	Deep Underground Neutrino Experiment
$\nu_e$	electron neutrino
$\bar{\nu}_e$	electron antineutrino
$\nu_\mu$	muon neutrino
$\bar{\nu}_\mu$	muon antineutrino
$\nu_\tau$	tau neutrino
$\bar{\nu}_\tau$	tau antineutrino
<b>ES</b>	elastic scattering
<b>GUT</b>	Grand Unified Theory
<b>HyperK</b>	Hyper-Kamiokande
<b>IMF</b>	initial mass function
<b>IO</b>	inverted ordering
<b>IBD</b>	inverse $\beta$ -decay
<b>JUNO</b>	Jiangmen Underground Neutrino Observatory

**JOSF** JUNO's Offline Simulation Framework  
**LAB** linear alkylbenzene  
**LAr** liquid argon  
**LBNF** Long-Baseline Neutrino Facility  
**LS** liquid scintillator  
**LET** light-emission time  
**LY** light yield  
**MC** Monte-Carlo  
**MSW** Mikheyev-Smirnov-Wolfenstein  
**(k)m.w.e** (kilo)meter water equivalent  
**KamLAND** Kamioka Liquid-Scintillator Antineutrino Detector  
**NS** neutron star  
**NC** neutral current  
**NMO** neutrino mass ordering  
 **$0\nu\beta\beta$ -decay** neutrinoless double  $\beta$ -decay  
 **$2\nu\beta\beta$ -decay** two neutrino double  $\beta$ -decay  
**NPP** nuclear power plant  
**NO** normal ordering  
**PMNS** Pontecorvo-Maki-Nakagawa-Sakata  
**PNS** proto-neutron star  
**PMT** photomultiplier tube  
**Ps** positronium  
**p-Ps** parapositronium  
**o-Ps** orthopositronium  
**PSD** pulse shape discrimination

---

**SFH** star formation history  
**SuperK** Super-Kamiokande  
**SM** Standard Model  
**SN** supernova  
**SSM** Standard Solar Model  
**SNO** Sudbury Neutrino Observatory  
**TAO** Taishan Antineutrino Observatory  
**TOF** time of flight  
**TTR** tail-to-total ratio  
**TTS** transit time spread  
**TT** transit time  
**QEL** quasielastic  
**WbLS** water-based liquid scintillator  
**WIMP** weakly interacting massive particle  
**WCD** water Cherenkov detector



## List of Figures

1.1 Schematic representation of the neutrino mass ordering	13
1.2 Oscillation survival probability of reactor electron antineutrinos	14
1.3 Illustration of MSW effect	17
1.4 Energy dependent survival probability of solar electron neutrinos	18
1.5 Feynman graphs of charged current neutrino-nucleon interactions	20
1.6 Cross sections for reactions of electron neutrinos on $^{12}\text{C}$	21
1.7 Solar pp-chain	24
1.8 Solar CNO-cycle	25
1.9 Solar neutrino energy spectra	26
1.10 Core collapse supernova neutrino luminosities	30
1.11 DSNB flux range	35
2.1 Illustration of Cherenkov radiation	40
2.2 Jablonski diagram	46
3.1 Experimental site of JUNO	54
3.2 Detector concept of JUNO	55
3.3 Chemical structure of LAB	57
3.4 Serial simulation framework of the JUNO detector	60
3.5 JUNO's reactor neutrino spectrum for normal and inverted ordering	62
3.6 JUNO's reactor neutrino spectrum for different Birks parameters	63
3.7 Lifetime evolution of the neutrino mass ordering sensitivity of JUNO and IceCube	65
3.8 Expected solar neutrino spectra for JUNO	67
3.9 Expected sensitivities for JUNO to dark matter-nucleon cross-section	75
4.1 Progenitor mass dependent explodability of supernovae	81
4.2 Successful and failed supernova components on the DSNB flux	82
4.3 DSNB flux dependence on the black hole forming mass threshold	83
4.4 Red-shift dependent star formation rate function	85
4.5 Contributions to the DSNB flux from various redshift regions	86
4.6 DSNB flux energy spectrum arriving at Earth	88

List of Figures

---

4.7	Two-dimensional expected DSNB signal rates	89
4.8	Differential IBD cross-section	90
4.9	Sketch of multiplicity cut	92
4.10	Simulated prompt DSNB energy spectrum	92
5.1	Calculated reactor neutrino spectrum for JUNO	97
5.2	Dependence of reactor neutrino rate on lower energy threshold	98
5.3	Simulated reactor neutrino background spectrum	99
6.1	HKKM and Fluka atmospheric neutrino fluxes for JUNO location	102
6.2	Latitude dependent atmospheric neutrino flux scaling factor	103
6.3	Approximated atmospheric neutrino flux for JUNO	104
6.4	Calculated atmospheric charged current background spectrum.	107
6.5	Calculated spectrum of atmospheric neutral current reactions on $^{12}\text{C}$	109
6.6	Simple shell model of $^{12}\text{C}$ nucleus	110
6.7	Simulated spectrum of atmospheric neutral current background	113
7.1	Cylindrical fiducial volume cut around reconstructed muon tracks.	119
7.2	Simulated cosmogenic $^9\text{Li}$ background spectrum and energy threshold dependent event rate	120
7.3	Simulated fast neutron background spectrum and radial dependent event rate	122
8.1	Probability density function of the photon emission process	127
8.2	Sketch of reconstruction of the light emission time	129
8.3	Transit time spread distribution of 20inch PMTs	129
8.4	Time-of-flight calculation	130
8.5	Arbitrarily chosen pulse of a simulated DSNB event	131
8.6	Averaged prompt pulses of DSNB and AtmNC events	132
8.7	Normalized TTR distribution of AtmNC and DSNB events	134
8.8	Position-dependent TTR distribution of DSNB events	135
8.9	PSD cut efficiency versus signal efficiency	136
8.10	Effect of PSD on the signal and background event spectra	138
9.1	Basic triple coincidence veto	140
9.2	Advanced triple coincidence veto	141
9.3	Triple coincidence vetoed volume	142
9.4	Reconstructed positions of atmospheric NC event	142
9.5	Distribution of prompt and delayed event displacement	144
9.6	Angular distribution between positron and neutron of IBD	145
9.7	Prompt and delayed vertex position of DSNB and AtmNC event	145

9.8 Displacement of $^{11}\text{C}$ decay electron . . . . .	146
9.9 Radius dependent probability for a delayed decay to be vetoed . . . . .	147
9.10 Triple coincidence veto dead time . . . . .	148
9.11 Radioactivity spectra . . . . .	150
9.12 Triple coincidence background rejection for $t_V^1$ and $t_V^2$ . . . . .	151
9.13 $^{11}\text{C}$ background rejection . . . . .	153
9.14 Atmospheric NC background rejection for $t_V^3$ . . . . .	153
10.1 Prompt energy spectra of DSNB signal and backgrounds . . . . .	158
10.2 Prompt energy spectra of DSNB signal and backgrounds after muon veto cut and PSD . . . . .	159
10.3 IBD-like prompt event spectrum after muon veto cut . . . . .	160
10.4 Illustration of the proposed steps of data handling . . . . .	163
10.5 IBD-like prompt event spectrum after performing the described steps of data analysis . . . . .	164
10.6 DSNB detection significance in dependence of exposure . . . . .	168
10.7 Two-dimensional DSNB detection significance for 147 kt yr . . . . .	169
10.8 Maximum position and exponential spectral slope of DSNB spectra . . . . .	170
10.9 Astrophysical parameter exclusion plot from $\chi^2$ -analysis . . . . .	174
11.1 Scenarios of the proposed Theia detector design . . . . .	177
11.2 Theia's atmospheric neutrino flux . . . . .	181
11.3 Fast neutron background rates for Theia . . . . .	185
11.4 Theia's visible scintillation energy spectrum expected for the DSNB signal and its ample backgrounds . . . . .	188
11.5 Number of Cherenkov rings for atmospheric NC background events . . . . .	190
11.6 Cherenkov-to-scintillation ratio of DSNB and AtmNC events . . . . .	191
11.7 Cherenkov-to-scintillation cut efficiency . . . . .	192
11.8 Theia's visible scintillation energy spectrum after background suppression cuts . . . . .	195
11.9 Significance of DSNB detection in Theia . . . . .	196
12.1 Lifetime evolution of DSNB event rate and significance for different experiments . . . . .	203
A.1 JUNO's expected solar neutrino spectra for radio-purity of Borexino . . . . .	215
A.2 Photoelectron distribution of 2.2 MeV-gamma . . . . .	215
A.3 Decay scheme of $^9\text{Li}$ . . . . .	216
A.4 Decay schemes of $^{11}\text{C}$ , $^{10}\text{C}$ , and $^8\text{Li}$ . . . . .	217
A.5 Neutron's kinetic energy distribution of DSNB and AtmNC events . . . . .	218

List of Figures

---

A.6 Simulated atmospheric charged current interactions with low and high DSNB flux models . . . . .	219
A.7 Exemplary $\Delta\chi^2$ and $\sqrt{\Delta\chi^2}$ functions . . . . .	220
A.8 Schematic diagram of PMT waveforms of Cherenkov and scintillation light . . . . .	221
A.9 Cherenkov-to-scintillation cut efficiency for Theia25 . . . . .	221
B.1 Energy deposition of $\beta$ -particles from $^{12}\text{N}$ and $^{12}\text{B}$ decay . . . . .	224



## List of Tables

1.1	Global best fit values for oscillation parameters	12
1.2	Mean energies and pinching factors of CCSN neutrino spectra	31
2.1	Overview of current large volume neutrino experiments	39
3.1	Number of target atoms and protons of the JUNO scintillator	58
3.2	Expected achievable precision on the mixing parameters	65
3.3	Main neutrino detection channels of a CCSN	68
4.1	Definition of DSNB flux models	87
5.1	Power fractions and energy release for fissile reactor isotopes	96
6.1	Atmospheric charged current reactions in liquid scintillator	106
6.2	Reaction channels of atmospheric neutral current reactions on $^{12}\text{C}$	113
7.1	Cosmogenic $^9\text{Li}$ production yields of Borexino and KamLAND	118
8.1	Photon emission fluorescence parameters	126
9.1	Cosmogenic isotope production and radioactive event rates	149
9.2	Reaction channels of atmospheric neutral current reactions on $^{12}\text{C}$ after triple coincidence veto	154
10.1	DSNB signal and background event rates per 147 kt yr	159
10.2	Event rates per 147 kt yr for different PSD cut strategies	167
10.3	Maximum position and slope of the DSNB spectrum	171
10.4	Pull-term parameters of the $\chi^2$ -function	173
11.1	Comparison of neutrino detector technologies	176
11.2	Atmospheric charged current reactions on $^{16}\text{O}$	181
11.3	Cosmogenic $^9\text{Li}$ production yield of Borexino and SuperK	182
11.4	Fast neutron background rates for Theia	184
11.5	Atmospheric neutral current interaction rates in Theia	186

List of Tables

---

11.6 Atmospheric neutral current reaction channels on oxygen . . . . .	187
11.7 IBD-like atmospheric neutral current reactions in Theia . . . . .	187
11.8 DSNB signal and background rates for Theia . . . . .	189
11.9 DSNB signal and background rates after background suppression . .	194
12.1 DSNB signal and background rates for different (future) neutrino detectors . . . . .	201
A.1 Reactor neutrino background rates for JUNO . . . . .	216
A.2 PSD signal efficiencies and event rates in JUNO . . . . .	217
A.3 Unstable isotopes from atmospheric neutral current reactions . . . .	218
A.4 Cut efficiencies for different selection techniques in JUNO . . . . .	219

## Bibliography

- [1] Reines, F., *et al.* [The neutrino](#). *Nature*, 178:446–449 (1956).
- [2] Bionta, R. M., *et al.* [Observation of a Neutrino Burst in Coincidence with Supernova SN 1987a in the Large Magellanic Cloud](#). *Phys. Rev. Lett.*, 58:1494 (1987).
- [3] Bays, K., *et al.* (Super-Kamiokande). [Supernova Relic Neutrino Search at Super-Kamiokande](#). *Phys. Rev.*, D85:052007 (2012).
- [4] An, F., *et al.* (JUNO). [Neutrino Physics with JUNO](#). *J. Phys.*, G43(3):030401 (2016).
- [5] Pauli, W. Collected scientific papers. Number 2 in Collected Scientific Papers. Interscience Publishers (1964).
- [6] Danby, G., *et al.* [Observation of High-Energy Neutrino Reactions and the Existence of Two Kinds of Neutrinos](#). *Phys. Rev. Lett.*, 9:36–44 (1962).
- [7] Weinberg, S. [A Model of Leptons](#). *Phys. Rev. Lett.*, 19:1264–1266 (1967).
- [8] Perl, M. L., *et al.* [Evidence for Anomalous Lepton Production in  \$e^+ - e^-\$  Annihilation](#). *Phys. Rev. Lett.*, 35:1489–1492 (1975).
- [9] Kodama, K., *et al.* (DONUT). [Observation of tau neutrino interactions](#). *Phys. Lett.*, B504:218–224 (2001).
- [10] Tanabashi, M., *et al.* (Particle Data Group). [Review of Particle Physics](#). *Phys. Rev.*, D98(3):030001 (2018).
- [11] Donoghue, J. F. [The effective field theory treatment of quantum gravity](#). *AIP Conf. Proc.*, 1483:73–94 (2012).
- [12] Landau, L. D. [On the conservation laws for weak interactions](#). *Nucl. Phys.*, 3:127–131 (1957).
- [13] Lee, T. D., *et al.* [Parity Nonconservation and a Two Component Theory of the Neutrino](#). *Phys. Rev.*, 105:1671–1675 (1957).

- [14] Salam, A. [On parity conservation and neutrino mass](#). *Nuovo Cim.*, 5:299–301 (1957).
- [15] Bilenky, S. [Neutrino. History of a unique particle](#). *Eur.Phys.J.*, H38:345–404 (2013).
- [16] Fermi, E. [An attempt of a theory of beta radiation. I](#). *Z. Phys.*, 88:161–177 (1934).
- [17] Alimonti, G., *et al.* (Borexino). [Science and technology of Borexino: a real time detector for low-energy solar neutrinos](#). *Astropart.Phys.*, 16:205–234 (2002).
- [18] Araki, T., *et al.* (KamLAND). [Measurement of neutrino oscillation with KamLAND: Evidence of spectral distortion](#). *Phys. Rev. Lett.*, 94:081801 (2005).
- [19] Gell-Mann, M., *et al.* [Behavior of neutral particles under charge conjugation](#). *Phys. Rev.*, 97:1387–1389 (1955).
- [20] Pontecorvo, B. Mesonium and anti-mesonium. *Sov.Phys.JETP*, 6:429 (1957).
- [21] Maki, Z., *et al.* [Remarks on the unified model of elementary particles](#). *Prog. Theor. Phys.*, 28:870–880 (1962).
- [22] Davis, R. [A review of the Homestake solar neutrino experiment](#). *Progress in Particle and Nuclear Physics*, 32:13 – 32 (1994). ISSN 0146-6410.
- [23] Bahcall, J. N., *et al.* [A Solution of the solar neutrino problem](#). *Phys. Rev. Lett.*, 65:2233–2235 (1990).
- [24] Cleveland, B. T., *et al.* [Measurement of the solar electron neutrino flux with the Homestake chlorine detector](#). *Astrophys. J.*, 496:505–526 (1998).
- [25] Hampel, W., *et al.* (GALLEX). [GALLEX solar neutrino observations: Results for GALLEX IV](#). *Phys. Lett.*, B447:127–133 (1999).
- [26] Altmann, M., *et al.* (GNO). [Complete results for five years of GNO solar neutrino observations](#). *Phys. Lett.*, B616:174–190 (2005).
- [27] Hosaka, J., *et al.* (Super-Kamiokande). [Solar neutrino measurements in super-Kamiokande-I](#). *Phys. Rev.*, D73:112001 (2006).
- [28] Aharmim, B., *et al.* (SNO). [Combined Analysis of all Three Phases of Solar Neutrino Data from the Sudbury Neutrino Observatory](#). *Phys.Rev.*, C88:025501 (2013).
- [29] Eguchi, K., *et al.* (KamLAND). [First results from KamLAND: Evidence for reactor anti-neutrino disappearance](#). *Phys.Rev.Lett.*, 90:021802 (2003).

- 
- [30] Abe, Y., *et al.* (Double Chooz). [Indication for the disappearance of reactor electron antineutrinos in the Double Chooz experiment](#). *Phys. Rev. Lett.*, 108:131801 (2012).
- [31] An, F. P., *et al.* (Daya Bay). [Observation of electron-antineutrino disappearance at Daya Bay](#). *Phys. Rev. Lett.*, 108:171803 (2012).
- [32] Ahn, J. K., *et al.* (RENO). [Observation of Reactor Electron Antineutrino Disappearance in the RENO Experiment](#). *Phys. Rev. Lett.*, 108:191802 (2012).
- [33] Abe, K., *et al.* (T2K). [Evidence of Electron Neutrino Appearance in a Muon Neutrino Beam](#). *Phys. Rev.*, D88(3):032002 (2013).
- [34] Bilenky, S. M. [Majorana neutrino mixing](#). *J. Phys.*, G32:R127 (2006).
- [35] Kayser, B. [Neutrino Mass, Mixing, and Flavor Change](#) (2008). [arXiv:hep-ph/0804.1497].
- [36] Bilenky, S. M. [On the phenomenology of neutrino oscillations in vacuum](#) (2012). [arXiv:hep-ph/1208.2497].
- [37] Schael, S., *et al.* [Precision electroweak measurements on the  \$Z\$  resonance](#). *Phys. Rept.*, 427:257–454 (2006).
- [38] Chau, L.-L., *et al.* [Comments on the Parametrization of the Kobayashi-Maskawa Matrix](#). *Phys. Rev. Lett.*, 53:1802 (1984).
- [39] Bilenky, S. M., *et al.* [On Oscillations of Neutrinos with Dirac and Majorana Masses](#). *Phys. Lett.*, 94B:495–498 (1980).
- [40] Langacker, P., *et al.* [On the Mikheev-Smirnov-Wolfenstein \(MSW\) Mechanism of Amplification of Neutrino Oscillations in Matter](#). *Nucl. Phys.*, B282:589–609 (1987).
- [41] Stodolsky, L. [The Unnecessary wave packet](#). *Phys. Rev.*, D58:036006 (1998).
- [42] Akhmedov, E. K., *et al.* [Paradoxes of neutrino oscillations](#). *Phys. Atom. Nucl.*, 72:1363–1381 (2009).
- [43] Zralek, M. [From kaons to neutrinos: Quantum mechanics of particle oscillations](#). *Acta Phys. Polon.*, B29:3925–3956 (1998).
- [44] Aker, M., *et al.* (KATRIN). [Improved Upper Limit on the Neutrino Mass from a Direct Kinematic Method by KATRIN](#). *Phys. Rev. Lett.*, 123(22):221802 (2019).

- [45] Dolgov, A. D., *et al.* [Bounds on Dirac neutrino masses from nucleosynthesis](#). *Phys. Rev.*, D51:4129–4133 (1995).
- [46] Hannestad, S., *et al.* [Cosmological constraints on neutrino plus axion hot dark matter](#). *JCAP*, 0708:015 (2007).
- [47] Baudis, L., *et al.* [Limits on the Majorana neutrino mass in the 0.1 eV range](#). *Phys. Rev. Lett.*, 83:41–44 (1999).
- [48] Abe, K., *et al.* (T2K). [Measurement of neutrino and antineutrino oscillations by the T2K experiment including a new additional sample of  \$\nu\_e\$  interactions at the far detector](#). *Phys. Rev.*, D96(9):092006 (2017). [Erratum: *Phys. Rev.*, D98(1):019902 (2018)].
- [49] Abe, K., *et al.* (Super-Kamiokande). [Solar Neutrino Measurements in Super-Kamiokande-IV](#). *Phys. Rev.*, D94(5):052010 (2016).
- [50] Gando, A., *et al.* (KamLAND). [Reactor On-Off Antineutrino Measurement with KamLAND](#). *Phys. Rev.*, D88(3):033001 (2013).
- [51] An, F. P., *et al.* (Daya Bay). [Measurement of electron antineutrino oscillation based on 1230 days of operation of the Daya Bay experiment](#). *Phys. Rev.*, D95(7):072006 (2017).
- [52] Schlattl, H. [Can three flavor oscillations solve the solar neutrino problem?](#) *Phys. Rev.*, D64:013009 (2001).
- [53] Zhan, L., *et al.* [Experimental Requirements to Determine the Neutrino Mass Hierarchy Using Reactor Neutrinos](#). *Phys. Rev.*, D79:073007 (2009).
- [54] Mohapatra, R., *et al.* [Neutrino Mass and New Physics](#). *Ann. Rev. Nucl. Part. Sci.*, 56:569–628 (2006).
- [55] Learned, J., *et al.* [Determination of neutrino mass hierarchy and  \$\theta\_{13}\$  with a remote detector of reactor antineutrinos](#). *Phys. Rev.*, D78:071302 (2008).
- [56] Cahn, R. N., *et al.* [White Paper: Measuring the Neutrino Mass Hierarchy](#). In Proceedings, Community Summer Study on the Future of U.S. Particle Physics, USA (2013).
- [57] Qian, X., *et al.* [Neutrino Mass Hierarchy](#). *Prog. Part. Nucl. Phys.*, 83:1–30 (2015).
- [58] Kayser, B. [Neutrino Oscillation Phenomenology](#). In Neutrinos in particle physics, astrophysics and cosmology. Proceedings, 61st Scottish Universities Summer School in Physics, pp. 51–64 (2008). [arXiv:hep-ph/0804.1121].

- [59] Akhmedov, E. K., *et al.* [A simple analytic three flavor description of the day night effect in the solar neutrino flux](#). *JHEP*, 05:057 (2004).
- [60] Blennow, M., *et al.* [Day-night effect in solar neutrino oscillations with three flavors](#). *Phys. Rev.*, D69:073006 (2004).
- [61] de Holanda, P. C., *et al.* [Toward precision measurements in solar neutrinos](#). *Nucl. Phys.*, B702:307–332 (2004).
- [62] Wolfenstein, L. [Neutrino Oscillations and Stellar Collapse](#). *Phys. Rev.*, D20:2634–2635 (1979).
- [63] Mikheev, S. P., *et al.* Resonance Amplification of Oscillations in Matter and Spectroscopy of Solar Neutrinos. *Sov. J. Nucl. Phys.*, 42:913–917 (1985).
- [64] Agostini, M., *et al.* (Borexino). [First Simultaneous Precision Spectroscopy of  \$pp\$ ,  \${}^7\text{Be}\$ , and  \$pep\$  Solar Neutrinos with Borexino Phase-II](#). *Phys. Rev.*, D100(8):082004 (2019).
- [65] Agostini, M., *et al.* (Borexino). [Improved measurement of  \${}^8\text{B}\$  solar neutrinos with 1.5 kt-y of Borexino exposure](#). *Phys. Rev.*, D101(6):062001 (2020).
- [66] Geytenbeek, B., *et al.* [Effect of electromagnetic dipole dark matter on energy transport in the solar interior](#). *JCAP*, 1703:029 (2017).
- [67] Bergstrom, J., *et al.* [Updated determination of the solar neutrino fluxes from solar neutrino data](#). *JHEP*, 03:132 (2016).
- [68] Bilenky, S. M., *et al.* [Phenomenology of neutrino oscillations](#). *Prog. Part. Nucl. Phys.*, 43:1–86 (1999).
- [69] de Holanda, P. C., *et al.* [Solar neutrino spectrum, sterile neutrinos and additional radiation in the Universe](#). *Phys. Rev.*, D83:113011 (2011).
- [70] Andreopoulos, C., *et al.* [The GENIE Neutrino Monte Carlo Generator](#). *Nucl. Instrum. Meth.*, A614:87–104 (2010).
- [71] Akimov, D., *et al.* (COHERENT). [Observation of Coherent Elastic Neutrino-Nucleus Scattering](#). *Science*, 357(6356):1123–1126 (2017).
- [72] Freedman, D. Z. [Coherent Neutrino Nucleus Scattering as a Probe of the Weak Neutral Current](#). *Phys. Rev.*, D9:1389–1392 (1974).
- [73] Adelberger, E. G., *et al.* [Solar fusion cross sections II: the  \$pp\$  chain and CNO cycles](#). *Rev. Mod. Phys.*, 83:195 (2011).

- [74] Bethe, H. A. [Energy production in stars](#). *Phys. Rev.*, 55:434–456 (1939).
- [75] Bahcall, J. N., *et al.* [What do we \(not\) know theoretically about solar neutrino fluxes?](#) *Phys. Rev. Lett.*, 92:121301 (2004).
- [76] Serenelli, A. M., *et al.* [Solar models with accretion. I. Application to the solar abundance problem](#). *Astrophys. J.*, 743:24 (2011).
- [77] Villante, F. L. [ecCNO Solar Neutrinos: A Challenge for Gigantic Ultra-Pure Liquid Scintillator Detectors](#). *Phys. Lett.*, B742:279–284 (2015).
- [78] Serenelli, A. [Alive and well: a short review about standard solar models](#). *Eur. Phys. J.*, A52(4):78 (2016).
- [79] Bellini, G., *et al.* (Borexino). [First evidence of pep solar neutrinos by direct detection in Borexino](#). *Phys. Rev. Lett.*, 108:051302 (2012).
- [80] Asplund, M., *et al.* [The Solar chemical composition](#). *Nucl. Phys.*, A777:1–4 (2006). [ASP Conf. Ser.336,25(2005)].
- [81] Grevesse, N., *et al.* [Standard Solar Composition](#). *Space Sci. Rev.*, 85:161–174 (1998).
- [82] Bellini, G., *et al.* [Precision measurement of the  \${}^7\text{Be}\$  solar neutrino interaction rate in Borexino](#). *Phys. Rev. Lett.*, 107:141302 (2011).
- [83] Aharmim, B., *et al.* (SNO). [Measurement of the  \$\nu\_e\$  and Total  \${}^8\text{B}\$  Solar Neutrino Fluxes with the Sudbury Neutrino Observatory Phase-III Data Set](#). *Phys. Rev.*, C87(1):015502 (2013).
- [84] Bellini, G., *et al.* (Borexino). [Measurement of the solar  \${}^8\text{B}\$  neutrino rate with a liquid scintillator target and 3 MeV energy threshold in the Borexino detector](#). *Phys. Rev.*, D82:033006 (2010).
- [85] Gaisser, T. K., *et al.* *Cosmic Rays and Particle Physics*. Cambridge University Press, 2 edition (2016).
- [86] Stettner, J. (IceCube). [Measurement of the Diffuse Astrophysical Muon-Neutrino Spectrum with Ten Years of IceCube Data](#). *PoS*, ICRC2019:1017 (2020).
- [87] Abraham, J., *et al.* (Pierre Auger). [Measurement of the energy spectrum of cosmic rays above  \$10^{18}\$  eV using the Pierre Auger Observatory](#). *Phys. Lett.*, B685:239–246 (2010).



- 
- [88] Greisen, K. [End to the cosmic ray spectrum?](#) *Phys. Rev. Lett.*, 16:748–750 (1966).
- [89] Zatsepin, G. T., *et al.* Upper limit of the spectrum of cosmic rays. *JETP Lett.*, 4:78–80 (1966).
- [90] Gaisser, T. K. [Atmospheric Neutrinos.](#) *AIP Conf. Proc.*, 944:140–142 (2007).
- [91] Gaisser, T. K. [Fluxes of atmospheric neutrinos and related cosmic rays.](#) *Nucl. Phys. Proc. Suppl.*, 77:133–139 (1999).
- [92] Honda, M., *et al.* [Atmospheric neutrino flux calculation using the NRLMSISE-00 atmospheric model.](#) *Phys. Rev.*, D92(2):023004 (2015).
- [93] Honda, M. [Uncertainty of the atmospheric neutrino fluxes.](#) *Nucl. Phys. Proc. Suppl.*, 77:140–145 (1999).
- [94] Hirata, K. S., *et al.* (Kamiokande-II). [Observation of a small atmospheric  \$\nu\_\mu/\nu\_e\$  ratio in Kamiokande.](#) *Phys. Lett.*, B280:146–152 (1992).
- [95] Burrows, A. [Colloquium: Perspectives on core-collapse supernova theory.](#) *Rev. Mod. Phys.*, 85:245 (2013).
- [96] Smartt, S. J. [Progenitors of core-collapse supernovae.](#) *Ann. Rev. Astron. Astrophys.*, 47:63–106 (2009).
- [97] Heger, A., *et al.* [How massive single stars end their life.](#) *Astrophys. J.*, 591:288–300 (2003).
- [98] Janka, H.-T. [Neutrino Emission from Supernovae.](#) *Handbook of Supernovae*, pp. 1575–1604 (2017).
- [99] Hamuy, M. [Observed and physical properties of core-collapse supernovae.](#) *Astrophys. J.*, 582:905–914 (2003).
- [100] Kotake, K., *et al.* [Explosion mechanism, neutrino burst, and gravitational wave in core-collapse supernovae.](#) *Rept. Prog. Phys.*, 69:971–1144 (2006).
- [101] Keil, M. T., *et al.* [Monte Carlo study of supernova neutrino spectra formation.](#) *Astrophys. J.*, 590:971–991 (2003).
- [102] Thompson, T. A., *et al.* [Shock breakout in core-collapse supernovae and its neutrino signature.](#) *Astrophys. J.*, 592:434 (2003).
- [103] Yoshida, T., *et al.* [Neutrino-Nucleus Reaction Cross Sections for Light Element Synthesis in Supernova Explosions.](#) *Astrophys. J.*, 686:448–466 (2008).

- [104] Yuksel, H., *et al.* [Neutrino Spectrum from SN 1987A and from Cosmic Supernovae](#). *Phys. Rev.*, D76:083007 (2007).
- [105] Ando, S., *et al.* [Relic neutrino background from cosmological supernovae](#). *New J. Phys.*, 6:170 (2004).
- [106] Chakraborty, S., *et al.* [Effect of Collective Flavor Oscillations on the Diffuse Supernova Neutrino Background](#). *JCAP*, 0809:013 (2008).
- [107] Tamborra, I., *et al.* [High-resolution supernova neutrino spectra represented by a simple fit](#). *Phys. Rev.*, D86:125031 (2012).
- [108] Fukuda, S., *et al.* (Super-Kamiokande). [Determination of solar neutrino oscillation parameters using 1496 days of Super-Kamiokande I data](#). *Phys. Lett.*, B539:179–187 (2002).
- [109] Ahmed, S. N., *et al.* (SNO). [Measurement of the total active  \$^8\text{B}\$  solar neutrino flux at the Sudbury Neutrino Observatory with enhanced neutral current sensitivity](#). *Phys. Rev. Lett.*, 92:181301 (2004).
- [110] Fukuda, Y., *et al.* (Super-Kamiokande). [Measurement of the flux and zenith angle distribution of upward through going muons by Super-Kamiokande](#). *Phys. Rev. Lett.*, 82:2644–2648 (1999).
- [111] Hirata, K., *et al.* (Kamiokande-II). [Observation of a Neutrino Burst from the Supernova SN 1987a](#). *Phys. Rev. Lett.*, 58:1490–1493 (1987).
- [112] Laha, R., *et al.* [Gadolinium in water Cherenkov detectors improves detection of supernova  \$\nu\_e\$](#) . *Phys. Rev.*, D89:063007 (2014).
- [113] Abe, K., *et al.* [Letter of Intent: The Hyper-Kamiokande Experiment — Detector Design and Physics Potential —](#) (2011). [arXiv:hep-ex/1109.3262].
- [114] Horiuchi, S., *et al.* [The Diffuse Supernova Neutrino Background is detectable in Super-Kamiokande](#). *Phys. Rev.*, D79:083013 (2009).
- [115] Beacom, J. F. [The Diffuse Supernova Neutrino Background](#). *Ann. Rev. Nucl. Part. Sci.*, 60:439–462 (2010).
- [116] Malek, M., *et al.* (Super-Kamiokande). [Search for supernova relic neutrinos at Super-Kamiokande](#). *Phys. Rev. Lett.*, 90:061101 (2003).
- [117] Beacom, J. F., *et al.* [GADZOOKS! Anti-neutrino spectroscopy with large water Cherenkov detectors](#). *Phys. Rev. Lett.*, 93:171101 (2004).

- 
- [118] Ando, S. [Cosmic star formation history and the future observation of supernova relic neutrinos](#). *Astrophys. J.*, 607:20–31 (2004).
- [119] Keehn, J. G., *et al.* [Neutrinos from failed supernovae at future water and liquid argon detectors](#). *Phys. Rev.*, D85:043011 (2012).
- [120] Totani, T., *et al.* [Future detection of supernova neutrino burst and explosion mechanism](#). *Astrophys. J.*, 496:216–225 (1998).
- [121] Lunardini, C. [Diffuse supernova neutrinos at underground laboratories](#). *Astropart. Phys.*, 79:49–77 (2016).
- [122] Mathews, G. J., *et al.* [Supernova Relic Neutrinos and the Supernova Rate Problem: Analysis of Uncertainties and Detectability of ONeMg and Failed Supernovae](#). *Astrophys. J.*, 790:115 (2014).
- [123] Nakazato, K., *et al.* [Spectrum of the Supernova Relic Neutrino Background and Metallicity Evolution of Galaxies](#). *Astrophys. J.*, 804(1):75 (2015).
- [124] Baldry, I. K., *et al.* [Constraints on a universal IMF from UV to near-IR galaxy luminosity densities](#). *Astrophys. J.*, 593:258–271 (2003).
- [125] Kresse, D. [Stellar Collapse Diversity and the Diffuse Supernova Neutrino Background](#). *Master's thesis*, Technische Universität München (2018).
- [126] Goldberg, H., *et al.* [Mini Z' burst from relic supernova neutrinos and late neutrino masses](#). *JHEP*, 11:023 (2006).
- [127] Lunardini, C. [Diffuse neutrino flux from failed supernovae](#). *Phys. Rev. Lett.*, 102:231101 (2009).
- [128] Horiuchi, S., *et al.* [Diffuse Supernova Neutrino Background from extensive core-collapse simulations of 8–100  \$M\_{\odot}\$  progenitors](#). *Mon. Not. Roy. Astron. Soc.*, 475:1363 (2018).
- [129] Bratton, C. B., *et al.* (IMB). [Angular Distribution of Events From SN1987A](#). *Phys. Rev.*, D37:3361 (1988).
- [130] Vissani, F. [Comparative analysis of SN1987A antineutrino fluence](#). *J. Phys.*, G42:013001 (2015).
- [131] Priya, A., *et al.* [Diffuse neutrinos from luminous and dark supernovae: prospects for upcoming detectors at the  \$O\(10\)\$  kt scale](#). *JCAP*, 1711(11):031 (2017).

- [132] Ando, S. [Decaying neutrinos and implications from the supernova relic neutrino observation](#). *Phys. Lett.*, B570:11 (2003).
- [133] Fogli, G. L., *et al.* [Three generation flavor transitions and decays of supernova relic neutrinos](#). *Phys. Rev.*, D70:013001 (2004).
- [134] Abbott, B. P., *et al.* (Virgo, LIGO Scientific). [Observation of Gravitational Waves from a Binary Black Hole Merger](#). *Phys. Rev. Lett.*, 116(6):061102 (2016).
- [135] Schultz, P. J., *et al.* [Interaction of positron beams with surfaces, thin films, and interfaces](#). *Rev. Mod. Phys.*, 60:701–779 (1988).
- [136] Deutsch, M. [Evidence for the Formation of Positronium in Gases](#). *Phys. Rev.*, 82:455–456 (1951).
- [137] Schwarz, M., *et al.* [Measurements of the Lifetime of Orthopositronium in the LAB-Based Liquid Scintillator of JUNO](#). *Nucl. Instrum. Meth.*, A922:64–70 (2019).
- [138] Al-Ramadhan, A. H., *et al.* [New precision measurement of the decay rate of singlet positronium](#). *Phys. Rev. Lett.*, 72:1632–1635 (1994).
- [139] Mughabghab, S., *et al.* [Preface](#). In *Neutron Resonance Parameters and Thermal Cross Sections*, pp. 7–8. Academic Press (1981). ISBN 978-0-12-509701-7.
- [140] Reedy, R. C., *et al.* [Prompt Gamma Rays From Radiative Capture of Thermal Neutrons by Elements from Hydrogen through Zinc](#). *Atom. Data Nucl. Data Tabl.*, 80:1–34 (2002).
- [141] Strumia, A., *et al.* [Precise quasielastic neutrino/nucleon cross-section](#). *Phys. Lett.*, B564:42–54 (2003).
- [142] Antonelli, V., *et al.* (JUNO). [Status and potentialities of the JUNO experiment](#). *PoS*, NEUTEL2017:056 (2018).
- [143] Alimonti, G., *et al.* (Borexino). [The Borexino detector at the Laboratori Nazionali del Gran Sasso](#). *Nucl. Instrum. Meth.*, A600:568–593 (2009).
- [144] Dunger, J. *The SNO+ Experiment*, pp. 47–67. Springer International Publishing, Cham (2019). ISBN 978-3-030-31616-7.
- [145] Suzuki, A. [Antineutrino Science in KamLAND](#). *Eur. Phys. J.*, C74(10):3094 (2014).
- [146] Fukuda, Y., *et al.* (Super-Kamiokande). [The Super-Kamiokande detector](#). *Nucl. Instrum. Meth.*, A501:418–462 (2003).

- [147] Aartsen, M. G., *et al.* (IceCube). [Energy Reconstruction Methods in the IceCube Neutrino Telescope](#). *JINST*, 9:P03009 (2014).
- [148] Lomon, E. L. [Classical Electrodynamics](#). *Science*, 136(3521):1046–1047 (1962). ISSN 0036-8075.
- [149] Wurm, M. Cosmic Background Discrimination for the Rare Neutrino Event Search in BOREXINO and LENA. *Ph.D. thesis*, Technische Universität München (2009).
- [150] Bellerive, A., *et al.* (SNO). [The Sudbury Neutrino Observatory](#). *Nucl. Phys.*, B908:30–51 (2016).
- [151] Abe, K., *et al.* [Calibration of the Super-Kamiokande Detector](#). *Nucl. Instrum. Meth.*, A737:253–272 (2014).
- [152] Fukuda, Y., *et al.* (Super-Kamiokande). [Evidence for oscillation of atmospheric neutrinos](#). *Phys.Rev.Lett.*, 81:1562–1567 (1998).
- [153] Fukuda, Y., *et al.* (Super-Kamiokande). [Measurements of the solar neutrino flux from Super-Kamiokande's first 300 days](#). *Phys. Rev. Lett.*, 81:1158–1162 (1998). [Erratum: *Phys. Rev. Lett.*,81:4279(1998)].
- [154] Fukuda, Y., *et al.* (Super-Kamiokande). [Measurement of the solar neutrino energy spectrum using neutrino electron scattering](#). *Phys. Rev. Lett.*, 82:2430–2434 (1999).
- [155] Shiozawa, M., *et al.* (Super-Kamiokande). [Search for proton decay via  \$p \rightarrow e^+ \pi^0\$  in a large water Cherenkov detector](#). *Phys. Rev. Lett.*, 81:3319–3323 (1998).
- [156] Hayato, Y., *et al.* (Super-Kamiokande). [Search for proton decay through  \$p \rightarrow \bar{\nu} K^+\$  in a large water Cherenkov detector](#). *Phys. Rev. Lett.*, 83:1529–1533 (1999).
- [157] Zhang, H., *et al.* (Super-Kamiokande). [Supernova Relic Neutrino Search with Neutron Tagging at Super-Kamiokande-IV](#). *Astropart. Phys.*, 60:41–46 (2015).
- [158] Nakano, Y. (Super-Kamiokande). [Highlight Talk from Super-Kamiokande](#). *Universe*, 5(1):20 (2019).
- [159] Xu, C. (Super-Kamiokande). [Current status of SK-Gd project and EGADS](#). *J. Phys. Conf. Ser.*, 718(6):062070 (2016).
- [160] Aartsen, M. G., *et al.* (IceCube). [The IceCube Neutrino Observatory: Instrumentation and Online Systems](#). *JINST*, 12(03):P03012 (2017).

- [161] Aartsen, M. G., *et al.* (IceCube). [Measurement of South Pole ice transparency with the IceCube LED calibration system](#). *Nucl. Instrum. Meth.*, A711:73–89 (2013).
- [162] Aartsen, M. G., *et al.* (IceCube PINGU). [Letter of Intent: The Precision IceCube Next Generation Upgrade \(PINGU\)](#) (2014). [arXiv:physics.ins-det/1401.2046].
- [163] Aartsen, M. G., *et al.* (IceCube). [Evidence for High-Energy Extraterrestrial Neutrinos at the IceCube Detector](#). *Science*, 342:1242856 (2013).
- [164] Aartsen, M. G., *et al.* (IceCube). [Neutrino emission from the direction of the blazar TXS 0506+056 prior to the IceCube-170922A alert](#). *Science*, 361(6398):147–151 (2018).
- [165] Ishihara, A. (IceCube). [The IceCube Upgrade – Design and Science Goals](#). *PoS*, ICRC2019:1031 (2020).
- [166] van Santen, J. (IceCube Gen2). [IceCube-Gen2: the next-generation neutrino observatory for the South Pole](#). *PoS*, ICRC2017:991 (2018).
- [167] Birks, J. B. *The Theory and practice of scintillation counting* (1964).
- [168] Voltz, R., *et al.* [Radioluminescence des milieux organiques I. Étude cinétique](#). *Journal de Physique*, 29(2-3):159–166 (1968).
- [169] Kasha, M. [Characterization of electronic transitions in complex molecules](#). *Discuss. Faraday Soc.*, 9:14–19 (1950).
- [170] Birks, J. B. [Scintillations from Organic Crystals: Specific Fluorescence and Relative Response to Different Radiations](#). *Proc. Phys. Soc.*, A64:874–877 (1951).
- [171] Schweizer, K. *Determination of the Nonlinearity Parameter for LAB-based Liquid Scintillators*. *Master's thesis*, Technische Universität München (2017).
- [172] Hackspacher, P. C. *Studies of Light Quenching Effects in Liquid Scintillators and Parameter Determination of the Buffer and Veto Fluids of the Double Chooz Near Detector*. *Master's thesis*, Technische Universität München (2014).
- [173] Lewke, T. *Studies of Scintillator Optical Properties, Electronics Simulation and Data Analysis for the BOREXINO Neutrino Experiment*. *Ph.D. thesis*, Technische Universität München (2013).
- [174] Povh, B. *Eine Einführung in die physikalischen Konzepte*. Springer (2004).

- [175] Seltzer, S. M., *et al.* Evaluation of the collision stopping power of elements and compounds for electrons and positrons. *Int. J. Appl. Radiat. Isotopes*, 33:1189–1218 (1982).
- [176] Apollonio, M., *et al.* (CHOOZ). Search for neutrino oscillations on a long baseline at the CHOOZ nuclear power station. *Eur. Phys. J.*, C27:331–374 (2003).
- [177] Ahn, J. K., *et al.* (RENO). RENO: An Experiment for Neutrino Oscillation Parameter  $\theta_{13}$  Using Reactor Neutrinos at Yonggwang (2010). [arXiv:hep-ex/1003.1391].
- [178] An, F. P., *et al.* (Daya Bay). A side-by-side comparison of Daya Bay antineutrino detectors. *Nucl. Instrum. Meth.*, A685:78–97 (2012).
- [179] Arpesella, C., *et al.* (Borexino). First real time detection of  $^7\text{Be}$  solar neutrinos by Borexino. *Phys. Lett.*, B658:101–108 (2008).
- [180] Bellini, G., *et al.* (Borexino). Neutrinos from the primary proton–proton fusion process in the Sun. *Nature*, 512(7515):383–386 (2014).
- [181] Boger, J., *et al.* (SNO). The Sudbury neutrino observatory. *Nucl. Instrum. Meth.*, A449:172–207 (2000).
- [182] Andringa, S. (SNO+). SNO+ present status and prospects. *J. Phys. Conf. Ser.*, 1137(1):012053 (2019).
- [183] Anderson, M., *et al.* (SNO+). Search for invisible modes of nucleon decay in water with the SNO+ detector. *Phys. Rev.*, D99(3):032008 (2019).
- [184] Anderson, M., *et al.* (SNO+). Measurement of the  $^8\text{B}$  solar neutrino flux in SNO+ with very low backgrounds. *Phys. Rev.*, D99(1):012012 (2019).
- [185] Alduino, C., *et al.* (CUORE). CUORE sensitivity to  $0\nu\beta\beta$  decay. *Eur. Phys. J.*, C77(8):532 (2017).
- [186] Manecki, S. SNO+ Tellurium Loading for Neutrinoless Double Beta Decay (2018). <https://doi.org/10.5281/zenodo.1300697>.
- [187] Leming, E. (SNO+). SNO+: Current Results and Future Prospects. *PoS*, NOW2018:027 (2019).
- [188] Gando, A., *et al.* (KamLAND).  $^7\text{Be}$  Solar Neutrino Measurement with KamLAND. *Phys. Rev.*, C92(5):055808 (2015).



- [189] Araki, T., *et al.* [Experimental investigation of geologically produced antineutrinos with KamLAND](#). *Nature*, 436:499–503 (2005).
- [190] Google Earth (Version 7.1.2.2041) [Software]. 02.10.2014.
- [191] [https://de.nucleopedia.org/wiki/kernkraftwerk\\_taishan](https://de.nucleopedia.org/wiki/kernkraftwerk_taishan). 12.06.2019.
- [192] Genster, C., *et al.* [Muon reconstruction with a geometrical model in JUNO](#). *JINST*, 13(03):T03003 (2018).
- [193] Djurcic, Z., *et al.* (JUNO). [JUNO Conceptual Design Report](#) (2015). [arXiv:physics.ins-det/1508.07166].
- [194] He, M. (JUNO). [Double Calorimetry System in JUNO](#). In Proceedings of International Conference on Technology and Instrumentation in Particle Physics (TIPP2017) (2017). [arXiv:physics.ins-det/1706.08761].
- [195] Adam, T., *et al.* [The OPERA experiment target tracker](#). *Nucl. Instrum. Meth.*, A577:523–539 (2007).
- [196] Huang, Q., *et al.* Current status of JUNO Top Tracker. *PoS*, EPS-HEP2019 (2019). *in preparation*.
- [197] Undagoitia, T. M. Measurement of light emission in organic liquid scintillators and studies towards the search for proton decay in the future large-scale detector LENA. *Ph.D. thesis*, Technische Universität München (2008).
- [198] Absorption and Scattering of Light by Small Particles. C. F. Bohren, D. R. Huffman (1983).
- [199] Vogel, H. Gerthsen Physik. Springer-Verlag (1995).
- [200] Zhou, X., *et al.* [Rayleigh scattering of linear alkylbenzene in large liquid scintillator detectors](#). *Rev. Sci. Instrum.*, 86(7):073310 (2015).
- [201] Franke, S. Optical Purification Study of the LAB-based Liquid Scintillator for the JUNO Experiment. *Ph.D. thesis*, Technische Universität München (2019).
- [202] Agostinelli, S., *et al.* (GEANT4). [GEANT4: A Simulation toolkit](#). *Nucl. Instrum. Meth.*, A506:250–303 (2003).
- [203] Allison, J., *et al.* [Geant4 developments and applications](#). *IEEE Trans. Nucl. Sci.*, 53:270 (2006).
- [204] Lin, T., *et al.* (JUNO). [Parallelized JUNO simulation software based on SNIPEr](#). *J. Phys. Conf. Ser.*, 1085(3):032048 (2018).



- [205] Lin, T., *et al.* (JUNO). [The Application of SNIpER to the JUNO Simulation](#). *J. Phys. Conf. Ser.*, 898(4):042029 (2017).
- [206] Zou, J. H., *et al.* [SNIpER: an offline software framework for non-collider physics experiments](#). *J. Phys. Conf. Ser.*, 664(7):072053 (2015).
- [207] Huang, X., *et al.* (JUNO). [Offline Data Processing Software for the JUNO Experiment](#). *PoS, ICHEP2016*:1051 (2017).
- [208] Vorobel, V. LS nonlinearity measurement in Prague. *JUNO DocDB*, 2216 (2017).
- [209] Dwyer, D. A., *et al.* [Spectral Structure of Electron Antineutrinos from Nuclear Reactors](#). *Phys. Rev. Lett.*, 114(1):012502 (2015).
- [210] Von Feilitzsch, F., *et al.* [Eperimental beta-spectra from  \$^{239}\text{Pu}\$  and  \$^{235}\text{U}\$  thermal neutron fission products and their correlated antineutrino spectra](#). *Phys. Lett.*, B118:162–166 (1982).
- [211] Schreckenbach, K., *et al.* [Determination of the antineutrino spectrum from  \$^{235}\text{U}\$  thermal neutron fission products up to 9.5 MeV](#). *Phys. Lett.*, B160:325–330 (1985).
- [212] Hahn, A. A., *et al.* [Anti-neutrino Spectra From  \$^{241}\text{Pu}\$  and  \$^{239}\text{Pu}\$  Thermal Neutron Fission Products](#). *Phys. Lett.*, B218:365–368 (1989).
- [213] Fallot, M., *et al.* [New antineutrino energy spectra predictions from the summation of beta decay branches of the fission products](#). *Phys. Rev. Lett.*, 109:202504 (2012).
- [214] Forero, D. V., *et al.* [The benefits of a near detector for JUNO](#) (2017). [arXiv:hep-ph/1710.07378].
- [215] Wang, W. [Taishan Antineutrino Observatory](#). *Talk at International Workshop on Next generation Nucleon Decay and Neutrino Detectors (NNN)*, Columbia (2019).
- [216] Capozzi, F., *et al.* [PINGU and the neutrino mass hierarchy: Statistical and systematic aspects](#). *Phys. Rev.*, D91:073011 (2015).
- [217] Aartsen, M. G., *et al.* (IceCube, JUNO). [Combined sensitivity to the neutrino mass ordering with JUNO, the IceCube Upgrade, and PINGU](#). *Phys. Rev.*, D101(3):032006 (2020).

- [218] Adey, D., *et al.* (Daya Bay). [Measurement of the Electron Antineutrino Oscillation with 1958 Days of Operation at Daya Bay](#). *Phys. Rev. Lett.*, 121(24):241805 (2018).
- [219] Abe, K., *et al.* (T2K). [Search for CP Violation in Neutrino and Antineutrino Oscillations by the T2K Experiment with  \$2.2 \times 10^{21}\$  Protons on Target](#). *Phys. Rev. Lett.*, 121(17):171802 (2018).
- [220] He, M. [Future Reactor Experiments](#). In 15th International Workshop on Neutrino Factories, Super Beams and Beta Beams (NuFact2013) (2013). [arXiv:physics.ins-det/1310.7343].
- [221] Antusch, S., *et al.* [Unitarity of the Leptonic Mixing Matrix](#). *JHEP*, 0610:084 (2006).
- [222] Bellini, G., *et al.* (Borexino). [Final results of Borexino Phase-I on low energy solar neutrino spectroscopy](#). *Phys. Rev.*, D89(11):112007 (2014).
- [223] Bellini, G., *et al.* [Geo-neutrinos](#). *Prog. Part. Nucl. Phys.*, 73:1–34 (2013).
- [224] Sramek, O., *et al.* [Geophysical and geochemical constraints on geoneutrino fluxes from Earth's mantle](#). *Earth Planet. Sci. Lett.*, 361:356–366 (2013).
- [225] Agostini, M., *et al.* (Borexino). [Spectroscopy of geoneutrinos from 2056 days of Borexino data](#). *Phys. Rev.*, D92(3):031101 (2015).
- [226] Minkowski, P.  [\$\mu \rightarrow e\gamma\$  at a Rate of One Out of  \$10^9\$  Muon Decays?](#) *Phys. Lett.*, 67B:421–428 (1977).
- [227] Mohapatra, R. N., *et al.* [Neutrino Mass and Spontaneous Parity Nonconservation](#). *Phys. Rev. Lett.*, 44:912 (1980).
- [228] Schechter, J., *et al.* [Neutrino Masses in  \$SU\(2\) \times U\(1\)\$  Theories](#). *Phys. Rev.*, D22:2227 (1980).
- [229] Fukugita, M., *et al.* [Baryogenesis Without Grand Unification](#). *Phys. Lett.*, B174:45–47 (1986).
- [230] Davidson, S., *et al.* [Leptogenesis](#). *Phys. Rept.*, 466:105–177 (2008).
- [231] Kusenko, A. [Sterile neutrinos: The Dark side of the light fermions](#). *Phys. Rept.*, 481:1–28 (2009).
- [232] Abazajian, K. N., *et al.* [Neutrino Physics from the Cosmic Microwave Background and Large Scale Structure](#). *Astropart. Phys.*, 63:66–80 (2015).

- [233] Gariazzo, S., *et al.* [Light sterile neutrinos](#). *J. Phys.*, G43:033001 (2016).
- [234] Aguilar-Arevalo, A. A., *et al.* (MiniBooNE). [Event Excess in the MiniBooNE Search for  \$\bar{\nu}\_\mu \rightarrow \bar{\nu}\_e\$  Oscillations](#). *Phys. Rev. Lett.*, 105:181801 (2010).
- [235] Aguilar-Arevalo, A., *et al.* (LSND). [Evidence for neutrino oscillations from the observation of  \$\bar{\nu}\_e\$  appearance in a  \$\bar{\nu}\_\mu\$  beam](#). *Phys. Rev.*, D64:112007 (2001).
- [236] Huber, P. [On the determination of anti-neutrino spectra from nuclear reactors](#). *Phys. Rev.*, C84:024617 (2011). [Erratum: *Phys. Rev.*, C85:029901(2012)].
- [237] Mention, G., *et al.* [The Reactor Antineutrino Anomaly](#). *Phys. Rev.*, D83:073006 (2011).
- [238] Armbruster, B., *et al.* (KARMEN). [Upper limits for neutrino oscillations  \$\bar{\nu}\_\mu \rightarrow \bar{\nu}\_e\$  from muon decay at rest](#). *Phys. Rev.*, D65:112001 (2002).
- [239] Astier, P., *et al.* (NOMAD). [Search for  \$\nu\_\mu \rightarrow \nu\_e\$  oscillations in the NOMAD experiment](#). *Phys. Lett.*, B570:19–31 (2003).
- [240] Antonello, M., *et al.* (ICARUS). [Search for anomalies in the  \$\nu\_e\$  appearance from a  \$\nu\_\mu\$  beam](#). *Eur. Phys. J.*, C73:2599 (2013).
- [241] Agafonova, N., *et al.* (OPERA). [Search for  \$\nu\_\mu \rightarrow \nu\_e\$  oscillations with the OPERA experiment in the CNGS beam](#). *JHEP*, 07:004 (2013). [Addendum: *JHEP*, 07:085(2013)].
- [242] Sousa, A. B. (MINOS, MINOS+). [First MINOS+ Data and New Results from MINOS](#). *AIP Conf. Proc.*, 1666(1):110004 (2015).
- [243] Conrad, J. M., *et al.* [Electron Antineutrino Disappearance at KamLAND and JUNO as Decisive Tests of the Short Baseline  \$\bar{\nu}\_\mu \rightarrow \bar{\nu}\_e\$  Appearance Anomaly](#). *Phys. Rev.*, D89(5):057301 (2014).
- [244] Bakhti, P., *et al.* [Constraining Super-light Sterile Neutrino Scenario by JUNO and RENO-50](#). *JHEP*, 10:200 (2013).
- [245] Girardi, I., *et al.* [Constraining Sterile Neutrinos Using Reactor Neutrino Experiments](#). *JHEP*, 08:057 (2014).
- [246] Sakharov, A. D. Quark - Muonic Currents and Violation of CP Invariance. *JETP Lett.*, 5:27–30 (1967).
- [247] Abe, K., *et al.* (Super-Kamiokande). [Search for proton decay via  \$p \rightarrow e^+ \pi^0\$  and  \$p \rightarrow \mu^+ \pi^0\$  in 0.31 megaton-years exposure of the Super-Kamiokande water Cherenkov detector](#). *Phys. Rev.*, D95(1):012004 (2017).

- [248] Abe, K., *et al.* (Super-Kamiokande). Search for proton decay via  $p \rightarrow \nu K^+$  using 260 kiloton-year data of Super-Kamiokande. *Phys. Rev.*, D90(7):072005 (2014).
- [249] Undagoitia, T. M., *et al.* Search for the proton decay  $p \rightarrow K^+ \bar{\nu}$  in the large liquid scintillator low energy neutrino astronomy detector LENA. *Phys. Rev.*, D72:075014 (2005).
- [250] Stefan, D., *et al.* Nuclear effects in proton decay. *Acta Phys. Polon.*, B40:671–674 (2009).
- [251] Bueno, A., *et al.* Nucleon decay searches with large liquid argon TPC detectors at shallow depths: Atmospheric neutrinos and cosmogenic backgrounds. *JHEP*, 04:041 (2007).
- [252] Jungman, G., *et al.* Supersymmetric dark matter. *Phys. Rept.*, 267:195–373 (1996).
- [253] Rubin, V. C., *et al.* Rotation of the Andromeda Nebula from a Spectroscopic Survey of Emission Regions. *Astrophys. J.*, 159:379–403 (1970).
- [254] Ade, P. A. R., *et al.* (Planck). Planck 2015 results. XIII. Cosmological parameters. *Astron. Astrophys.*, 594:A13 (2016).
- [255] Guo, W.-L. Search for solar dark matter annihilation with JUNO. *J. Phys. Conf. Ser.*, 1056(1):012025 (2018).
- [256] Janka, H.-T., *et al.* Theory of Core-Collapse Supernovae. *Phys. Rept.*, 442:38–74 (2007).
- [257] Ertl, T., *et al.* A two-parameter criterion for classifying the explodability of massive stars by the neutrino-driven mechanism. *Astrophys. J.*, 818(2):124 (2016).
- [258] Woosley, S. E., *et al.* The Remarkable Deaths of 9-11 Solar Mass Stars. *Astrophys. J.*, 810(1):34 (2015).
- [259] Sukhbold, T., *et al.* The Compactness of Presupernova Stellar Cores. *Astrophys. J.*, 783:10 (2014).
- [260] Woosley, S. E., *et al.* Nucleosynthesis and Remnants in Massive Stars of Solar Metallicity. *Phys. Rept.*, 442:269–283 (2007).
- [261] Sukhbold, T., *et al.* Core-Collapse Supernovae from 9 to 120 Solar Masses Based on Neutrino-powered Explosions. *Astrophys. J.*, 821(1):38 (2016).

- [262] Smith, N. [The Crab Nebula and the class of Type II<sub>n</sub>-P supernovae caused by sub-energetic electron capture explosions](#). *Mon. Not. Roy. Astron. Soc.*, 434:102 (2013).
- [263] Tominaga, N., *et al.* [Supernova Explosions of Super-Asymptotic Giant Branch Stars: Multicolor Light Curves of Electron-Capture Supernovae](#). *Astrophys. J.*, 771:L12 (2013).
- [264] Yang, H., *et al.* [Evolution of the Crab nebula in a low energy supernova](#). *Astrophys. J.*, 806(2):153 (2015).
- [265] Sumiyoshi, K., *et al.* [Neutrino signals from the formation of black hole: A probe of equation of state of dense matter](#). *Phys. Rev. Lett.*, 97:091101 (2006).
- [266] Sumiyoshi, K., *et al.* [Dynamics and neutrino signal of black hole formation in non-rotating failed supernovae. II. progenitor dependence](#). *Astrophys. J.*, 688:1176 (2008).
- [267] O'Connor, E., *et al.* [Black Hole Formation in Failing Core-Collapse Supernovae](#). *Astrophys. J.*, 730:70 (2011).
- [268] Horiuchi, S., *et al.* [The red supergiant and supernova rate problems: implications for core-collapse supernova physics](#) (2014). [arXiv:astro-ph.HE/1409.0006].
- [269] Nakamura, K., *et al.* [Systematic Features of Axisymmetric Neutrino-Driven Core-Collapse Supernova Models in Multiple Progenitors](#). *Publ. Astron. Soc. Jap.*, 67(6):107 (2015).
- [270] Demorest, P., *et al.* [Shapiro Delay Measurement of A Two Solar Mass Neutron Star](#). *Nature*, 467:1081–1083 (2010).
- [271] Antoniadis, J., *et al.* [A Massive Pulsar in a Compact Relativistic Binary](#). *Science*, 340:6131 (2013).
- [272] Özel, F., *et al.* [The Dense Matter Equation of State from Neutron Star Radius and Mass Measurements](#). *Astrophys. J.*, 820(1):28 (2016).
- [273] Abbott, B. P., *et al.* [Multi-messenger Observations of a Binary Neutron Star Merger](#). *Astrophys. J.*, 848(2):L12 (2017).
- [274] Margalit, B., *et al.* [Constraining the Maximum Mass of Neutron Stars From Multi-Messenger Observations of GW170817](#). *Astrophys. J.*, 850(2):L19 (2017).
- [275] Kennicutt, R. C., Jr. [Star formation in galaxies along the Hubble sequence](#). *Ann. Rev. Astron. Astrophys.*, 36:189–231 (1998).

- [276] Smartt, S. J., *et al.* [The death of massive stars - I. Observational constraints on the progenitors of type II-P supernovae](#). *Mon. Not. Roy. Astron. Soc.*, 395:1409 (2009).
- [277] Hopkins, A. M., *et al.* [On the normalisation of the cosmic star formation history](#). *Astrophys. J.*, 651:142–154 (2006).
- [278] Reddy, N. A., *et al.* [Multi-Wavelength Constraints on the Cosmic Star Formation History from Spectroscopy: The Rest-Frame UV, H-alpha, and Infrared Luminosity Functions at Redshifts  \$1.9 < z < 3.4\$](#) . *Astrophys. J. Suppl.*, 175(48) (2008).
- [279] Rujopakarn, W., *et al.* [The Evolution of the Star Formation Rate of Galaxies at  \$0.0 < z < 1.2\$](#) . *Astrophys. J.*, 718:1171–1185 (2010).
- [280] Yuksel, H., *et al.* [Revealing the High-Redshift Star Formation Rate with Gamma-Ray Bursts](#). *Astrophys. J.*, 683:L5–L8 (2008).
- [281] Vogel, P., *et al.* [Angular distribution of neutron inverse beta decay,  \$\bar{\nu}\_e + p \rightarrow e^+ + n\$](#) . *Phys. Rev.*, D60:053003 (1999).
- [282] Mueller, T. A., *et al.* [Improved Predictions of Reactor Antineutrino Spectra](#). *Phys. Rev.*, C83:054615 (2011).
- [283] Vogel, P., *et al.* [Reactor Anti-neutrino Spectra and Their Application to Anti-neutrino Induced Reactions. II](#). *Phys. Rev.*, C24:1543–1553 (1981).
- [284] Kopeikin, V., *et al.* [Reactor as a source of antineutrinos: Thermal fission energy](#). *Phys. Atom. Nucl.*, 67:1892–1899 (2004).
- [285] Battistoni, G., *et al.* [The atmospheric neutrino flux below 100-MeV: The FLUKA results](#). *Astropart. Phys.*, 23:526–534 (2005).
- [286] Wurm, M., *et al.* [Detection potential for the diffuse supernova neutrino background in the large liquid-scintillator detector LENA](#). *Phys. Rev.*, D75:023007 (2007).
- [287] Gaisser, T. K., *et al.* [Cosmic Ray Neutrinos in the Atmosphere](#). *Phys. Rev.*, D38:85 (1988).
- [288] Measday, D. F. [The nuclear physics of muon capture](#). *Phys. Rept.*, 354:243–409 (2001).
- [289] Guo, W.-L. [Low energy neutrinos from stopped muons in the Earth](#). *Phys. Rev.*, D99(7):073007 (2019).

- [290] Gando, A., *et al.* (KamLAND). [A study of extraterrestrial antineutrino sources with the KamLAND detector](#). *Astrophys. J.*, 745:193 (2012).
- [291] Kamyshev, Y. A., *et al.* [Signatures of nucleon disappearance in large underground detectors](#). *Phys. Rev.*, D67:076007 (2003).
- [292] Auerbach, N., *et al.* [Neutrino - nucleus reactions on C-12 and O-16](#). *Phys. Rev.*, C56:R2368–R2372 (1997).
- [293] Kolbe, E., *et al.* [Weak reactions on C-12 within the continuum random phase approximation with partial occupancies](#). *Nucl. Phys.*, A652:91–100 (1999).
- [294] Cheng, J. Update on atmospheric neutrino background calculation: going beyond the simple shell model. *JUNO DocDB*, 3637 (2018).
- [295] Andreopoulos, C., *et al.* [The GENIE Neutrino Monte Carlo Generator: Physics and User Manual](#) (2015). [arXiv:hep-ph/1510.05494].
- [296] Möllenberg, R. Monte Carlo Study of Solar  $^8\text{B}$  Neutrinos and the Diffuse Supernova Neutrino Background in LENA. *Ph.D. thesis*, Technische Universität München (2013).
- [297] Koning, A. J., *et al.* [Modern Nuclear Data Evaluation with the TALYS Code System](#). *Nucl. Data Sheets*, 113:2841–2934 (2012).
- [298] Firestone, R. B., *et al.* (editors). Table of Isotopes. A Wiley–Interscience Publication, John Wiley and Sons Inc., 8 edition (1999).
- [299] Tilley, D. R., *et al.* [Energy levels of light nuclei A=8,9,10](#). *Nucl. Phys.*, A745:155–362 (2004).
- [300] Bellini, G., *et al.* (Borexino). [Cosmogenic Backgrounds in Borexino at 3800 m water-equivalent depth](#). *JCAP*, 1308:049 (2013).
- [301] Abe, S., *et al.* (KamLAND). [Production of Radioactive Isotopes through Cosmic Muon Spallation in KamLAND](#). *Phys.Rev.*, C81:025807 (2010).
- [302] Li, S. W., *et al.* [First calculation of cosmic-ray muon spallation backgrounds for MeV astrophysical neutrino signals in Super-Kamiokande](#). *Phys. Rev.*, C89:045801 (2014).
- [303] Hagner, T., *et al.* [Muon induced production of radioactive isotopes in scintillation detectors](#). *Astropart. Phys.*, 14:33–47 (2000).
- [304] Cheng, J. Status of Fast Neutron Simulation at JUNO. *JUNO DocDB*, 2274 (2017).



- [305] An, F., *et al.* (Daya Bay). [Improved Measurement of Electron Antineutrino Disappearance at Daya Bay](#). *Chin.Phys.*, C37:011001 (2013).
- [306] Cao, G. private communication.
- [307] Bo-Xiang, Y. The measurment of LS optical performance. *JUNO DocDB*, 113 (2013).
- [308] Jeschke, D. Modulations of the Cosmic Muon Flux & Identification of Atmospheric Neutrino Interactions in Borexino. *Ph.D. thesis*, Technische Universität München (2018).
- [309] Wu, C.-W. Pulse Shape Discrimination Application to Supernova Neutrino Events in JUNO. *JUNO DocDB*, 3040 (2017).
- [310] K.K., H. P. Hamamatsu Large Photocathode Area Photomultiplier Tubes (2019). Data sheet.
- [311] Gao, F., *et al.* (MCP-PMT workgroup). [Status of the 20 inch MCP-PMT prototype development for JUNO experiment](#). *J. Phys. Conf. Ser.*, 888(1):012050 (2017).
- [312] Schever, M. [Waveform Reconstruction of IBD and Muon Events in JUNO](#) (2018). 10.5281/zenodo.1300922.
- [313] Lin, T. Calculating TOF with the Optical Boundary and the simulation software update note. *JUNO DocDB*, 887 (2015).
- [314] Gatti, E., *et al.* A new linear method of discrimination between elementary particles in scintillation counters, volume 2 of *Nuclear Electronics*. IAEA (1962).
- [315] Griffiths, J., *et al.* [Pulse Shape Discrimination and Exploration of Scintillation Signals Using Convolutional Neural Networks](#) (2018). [arXiv:physics.ins-det/1807.06853].
- [316] Punzi, G. [Sensitivity of searches for new signals and its optimization](#). *eConf*, C030908:MODT002 (2003).
- [317] Galbiati, C., *et al.* [Cosmogenic C-11 production and sensitivity of organic scintillator detectors to pep and CNO neutrinos](#). *Phys. Rev.*, C71:055805 (2005).
- [318] Shirai, J. (KamLAND). [Start of KamLAND](#). *Nucl. Phys. Proc. Suppl.*, 118:15–22 (2003).
- [319] Zhao, J. B8 solar neutrino analysis cross check. *JUNO DocDB*, 4739 (2019).



- 
- [320] Klein, J. R., *et al.* [Blind analysis in nuclear and particle physics](#). *Ann. Rev. Nucl. Part. Sci.*, 55:141–163 (2005).
- [321] Feldman, G. J., *et al.* [A Unified approach to the classical statistical analysis of small signals](#). *Phys. Rev.*, D57:3873–3889 (1998).
- [322] Rolke, W. A., *et al.* [Limits and confidence intervals in the presence of nuisance parameters](#). *Nucl. Instrum. Meth.*, A551:493–503 (2005).
- [323] Blennow, M., *et al.* [Quantifying the sensitivity of oscillation experiments to the neutrino mass ordering](#). *JHEP*, 03:028 (2014).
- [324] Orebi Gann, G. D. (THEIA Interest Group). [Physics Potential of an Advanced Scintillation Detector: Introducing THEIA](#) (2015).
- [325] Yeh, M., *et al.* [A new water-based liquid scintillator and potential applications](#). *Nucl. Instrum. Meth.*, A660:51–56 (2011).
- [326] Wei, H., *et al.* [Discovery potential for supernova relic neutrinos with slow liquid scintillator detectors](#). *Phys. Lett.*, B769:255–261 (2017).
- [327] Alonso, J. R., *et al.* [Advanced Scintillator Detector Concept \(ASDC\): A Concept Paper on the Physics Potential of Water-Based Liquid Scintillator](#) (2014). [arXiv:physics.ins-det/1409.5864].
- [328] Aberle, C., *et al.* [Measuring Directionality in Double-Beta Decay and Neutrino Interactions with Kiloton-Scale Scintillation Detectors](#). *JINST*, 9:P06012 (2014).
- [329] Li, M., *et al.* [Separation of Scintillation and Cherenkov Lights in Linear Alkyl Benzene](#). *Nucl. Instrum. Meth.*, A830:303–308 (2016).
- [330] Caravaca, J., *et al.* [Experiment to demonstrate separation of Cherenkov and scintillation signals](#). *Phys. Rev.*, C95(5):055801 (2017).
- [331] Askins, M., *et al.* [Theia: An advanced optical neutrino detector](#) (2019). [arXiv:physics.ins-det/1911.03501].
- [332] Barna, A., *et al.* [Global Antineutrino Modeling: A Web Application](#) (2015). [arXiv:physics.ins-det/1510.05633].
- [333] Mei, D., *et al.* [Muon-induced background study for underground laboratories](#). *Phys. Rev.*, D73:053004 (2006).
- [334] Zhang, Y., *et al.* (Super-Kamiokande). [First measurement of radioactive isotope production through cosmic-ray muon spallation in Super-Kamiokande IV](#). *Phys. Rev.*, D93(1):012004 (2016).

- [335] Li, S. W., *et al.* Spallation Backgrounds in Super-Kamiokande Are Made in Muon-Induced Showers. *Phys. Rev.*, D91(10):105005 (2015).
- [336] Möllenberg, R., *et al.* Detecting the Diffuse Supernova Neutrino Background with LENA. *Phys. Rev.*, D91(3):032005 (2015).
- [337] Aglietta, M., *et al.* (LVD). Measurement of the neutron flux produced by cosmic ray muons with LVD at Gran Sasso. In Proceedings, 26th International Cosmic Ray Conference (ICRC), pp. 44–47 (1999). [arXiv:hep-ex/9905047].
- [338] Ahrens, L. A., *et al.* Measurement of Neutrino - Proton and anti-neutrino - Proton Elastic Scattering. *Phys. Rev.*, D35:785 (1987).
- [339] Paschos, E. A., *et al.* Neutrino interactions in oscillation experiments. *Phys. Rev.*, D65:033002 (2002).
- [340] Rein, D., *et al.* Neutrino Excitation of Baryon Resonances and Single Pion Production. *Annals Phys.*, 133:79–153 (1981).
- [341] Abe, K., *et al.* (T2K). Measurement of the neutrino-oxygen neutral-current interaction cross section by observing nuclear deexcitation  $\gamma$  rays. *Phys. Rev.*, D90(7):072012 (2014).
- [342] Ejiri, H. Nuclear deexcitations of nucleon holes associated with nucleon decays in nuclei. *Phys. Rev.*, C48:1442–1444 (1993).
- [343] Ajzenberg-Selove, F. Energy levels of light nuclei  $A = 13-15$ . *Nucl. Phys.*, A523:1–196 (1991).
- [344] Ajzenberg-Selove, F. Energy levels of light nuclei  $A = 11-12$ . *Nucl. Phys.*, A506:1–158 (1990).
- [345] Watanabe, H., *et al.* (Super-Kamiokande). First Study of Neutron Tagging with a Water Cherenkov Detector. *Astropart. Phys.*, 31:320–328 (2009).
- [346] Lagage, P. O. Nuclear power stations as a background source for antineutrino astronomy. *Nature*, 316:420–421 (1985).
- [347] Zhang, W., *et al.* Experimental Limit on the Flux of Relic Anti-neutrinos From Past Supernovae. *Phys. Rev. Lett.*, 61:385–388 (1988).
- [348] Migenda, J. (Hyper-Kamiokande Proto). Astroparticle Physics in Hyper-Kamiokande. *PoS*, EPS-HEP2017:020 (2017).
- [349] Sekiya, H. (Super-Kamiokande). The Super-Kamiokande Gadolinium Project. *PoS*, ICHEP2016:982 (2016).

- 
- [350] Takatomi, Y. [Astrophysical neutrinos at Hyper-Kamiokande](#). *Talk at Topics in Astroparticle and Underground Physics (TAUP)*, Japan (2019).
- [351] Abe, K., *et al.* (Hyper-Kamiokande). [Hyper-Kamiokande Design Report](#) (2018). [arXiv:physics.ins-det/1805.04163].
- [352] Acciarri, R., *et al.* (DUNE). [Long-Baseline Neutrino Facility \(LBNF\) and Deep Underground Neutrino Experiment \(DUNE\)](#) (2015). [arXiv:physics.ins-det/1512.06148].
- [353] Acciarri, R., *et al.* (DUNE). [Long-Baseline Neutrino Facility \(LBNF\) and Deep Underground Neutrino Experiment \(DUNE\)](#) (2016). [arXiv:physics.ins-det/1601.05471].
- [354] Abi, B., *et al.* (DUNE). [The DUNE Far Detector Interim Design Report Volume 1: Physics, Technology and Strategies](#) (2018). [arXiv:physics.ins-det/1807.10334].
- [355] Barker, D., *et al.* [Muon-Induced Background Study for an Argon-Based Long Baseline Neutrino Experiment](#). *Phys. Rev.*, D86:054001 (2012).
- [356] Cocco, A. G., *et al.* [Supernova relic neutrinos in liquid argon detectors](#). *JCAP*, 0412:002 (2004).
- [357] Vagins, M. R. [Preparing for a Gd-loaded Super-K](#). *Talk at Revealing the History of the Universe with Underground Particle and Nuclear Research*, Japan (2019).
- [358] Tilley, D. R., *et al.* [Energy levels of light nuclei A=5, A=6, A=7](#). *Nucl. Phys.*, A708:3–163 (2002).
- [359] Kelley, J. H., *et al.* [Energy levels of light nuclei](#). *Nucl. Phys.*, A880:88–195 (2012).
- [360] Lai, K.-C., *et al.* [Probing Neutrino Mass Hierarchy by Comparing the Charged-Current and Neutral-Current Interaction Rates of Supernova Neutrinos](#). *JCAP*, 1607(07):039 (2016).
- [361] Krane, K. S. *Introductory nuclear physics*. Wiley, New York, NY (1988).